SUPER-RESOLUTION SPECTRAL ESTIMATION METHODS FOR BURIED AND THROUGH-THE-WALL OBJECT DETECTION

by

Erman ÖZDEMİR

B.S., Electrical and Electronics Engineering, Middle East Technical University, 2005

Submitted to the Institute for Graduate Studies in
Science and Engineering in partial fulfillment of
the requirements for the degree of
Master of Science

Graduate Program in Electrical and Electronics Engineering
Boğaziçi University

2008

SUPER-RESOLUTION SPECTRAL ESTIMATION METHODS FOR BURIED AND THROUGH-THE-WALL OBJECT DETECTION

APPROVED BY:

Assist. Prof. M. Kıvanç Mıhçak ..... (Thesis Supervisor)

Prof. Emin Anarım ..... (Thesis Cosupervisor)

Assoc. Prof. Fatih Alagöz .....

Assist. Prof. Mutlu Koca .....

Assist. Prof. S. Serdar Kozat .....

DATE OF APPROVAL: .....

ACKNOWLEDGEMENTS

I would like to thank my thesis supervisor, Assist. Prof. Dr. M. Kıvanç Mıhçak for his continuous support, guidance and encouragement he provided in all stages of this thesis. Without his assistance and suggestions this thesis could not have been completed. I would also like to thank my cosupervisor Prof. Dr. Emin Anarım for his encouragement and motivation throughout my study.

Finally, I would like to thank my family for their support and motivation during the period of this study.

ABSTRACT

SUPER-RESOLUTION SPECTRAL ESTIMATION METHODS FOR BURIED AND THROUGH-THE-WALL OBJECT DETECTION

Seeing the targets behind and inside visually opaque obstacles such as walls using microwave signals is considered as a powerful tool for a variety of applications in both military and commercial paradigms.

The ultimate goal in Through-the-Wall Object Detection (TWOD) and Buried Object Detection (BOD) systems is to achieve High Range Resolution (HRR). HRR provides the ability of resolving closely spaced targets in range, improves the accuracy of range estimates and aids in target recognition and classification.

HRR can be achieved using impulsive waveforms which use extremely narrow pulses, frequency modulated waveforms which increase the instantaneous bandwidth by applying frequency modulation to each transmitted pulse, stepped-frequency waveform, and signal processing techniques.

The range resolution of stepped-frequency and frequency modulated continuous wave (FMCW) radar systems is limited by the Inverse Fast Fourier Transform (IFFT) and Fast Fourier Transform (FFT), respectively. FFT provides poor range resolution for data with a small bandwidth and when the data size is small. On the other hand, it is well known that parametric spectral estimation methods provide super-resolved range profiles of the targets compared with FFT for the same frequency bandwidth.

This thesis studies the target detection and range extraction performance of ESPRIT, Root-MUSIC, Higher Order Yule-Walker, Minimum-Norm, Yule-Walker, and Least-Squares methods in BOD and TWOD applications using synthetic stepped-frequency and FMCW radar signals and experimental stepped-frequency radar data.

ÖZET

SUPER-RESOLUTION SPECTRAL ESTIMATION METHODS FOR BURIED AND THROUGH-THE-WALL OBJECT DETECTION

Mikrodalga sinyalleri kullanarak duvar gibi saydam olmayan engellerin arkasını ve içeriğini görüntülemek, askeri ve ticari alanlardaki uygulamalar için kuvvetli bir araç olarak görülmektedir.

Duvar Arkası Cisim Tespiti (DACT) ve Gömülü Cisim Tespiti (GCT) sistemlerindeki ana hedef, Yüksek Menzil Çözünürlüğü (YMÇ) sağlamaktır. YMÇ, menzil içerisinde birbirine yakın hedefleri ayırabilme kabiliyetini sağlar, menzil kestirimlerinin doğruluğunu arttırır ve hedef tanıma ve sınıflandırmaya yardımcı olur.

YMÇ, çok dar vurum kullanan dürtün dalgabiçimi, anlık bant genişliğini gönderilen herbir vuruma frekans kipleme uygulayarak arttıran frekans kipli dalgabiçimi, adım-frekans dalgabiçimi ve sinyal işleme teknikleri kullanılarak elde edilebilir.

Adım frekans ve frekans kipli sürekli dalga (FKSD) radar sistemlerinin menzil çözünürlük kabiliyeti Ters Hızlı Fourier Dönüşümü (THFT) ve Hızlı Fourier Dönüşümü (HFT) ile sınırlıdır. HFT, küçük bant genişliğine sahip veriler için ve veri boyutu küçük olduğunda düşük çözünürlük sağlar. Diğer yandan, parametrik spektral kestirim metodlarının, aynı frekans bant genişliğinde HFT ile kıyaslandığında, yüksek çözünülürlükte menzil profil kestirimi sağladığı bilinmektedir.

Bu tez çalışması ile DACT ve GCT uygulamalarında hedef tanıma ve menzil özütlemesi için ESPRIT, Root-MUSIC, Yüksek Dereceli Yule-Walker, En Küçük Norm, Yule Walker ve En Küçük Kareler metodlarının performanslarını sentetik adım-frekans ve FKSD radar sinyalleri ve deneysel adım frekans radar verileri kullanarak belirlemektir.

TABLE OF CONTENTS

LIST OF FIGURES

LIST OF TABLES

LIST OF SYMBOLS / ABBREVIATIONS

$\boldsymbol{a}$	Auto-regressive model coefficients vector
A	Radar cross section of target
$\boldsymbol{b}$	Moving average model coefficients vector
B	Bandwidth
B_{eff}	Efficient bandwidth
B_{inst}	Instantaneous bandwidth
c	speed of light
$\boldsymbol{e}$	Noise vector
E	Maximum target extend
f_0	Carrier frequency
f_b	Beat frequency
f_{STALO}	Frequency of stable oscillator
f_{COHO}	Frequency of coherent oscillator
$\boldsymbol{g}$	Eigenvector associated with noise eigenvalue
$\boldsymbol{h}$	Impulse response of filter
$\boldsymbol{I}$	Identity Matrix
I	Inphase component
k_f	Frequency sensitivity of modulator
L	Number of subarrays
M	Number of elements in subarrays
N	Number of frequency steps
p	Auto-regressive model order
$\boldsymbol{P}$	Signal power matrix
P_{ref}	Reflected power
P	Upper bound for model order
P_i	Incident power
q	Moving average model order

Q	Quadrature component
$\boldsymbol{r}$	Autocorrelation sequence
$\hat{\boldsymbol{r}}$	Autocorrelation sequence estimate
$\hat{\boldsymbol{r}}^{b}$	Biased autocorrelation sequence estimate
$\hat{\boldsymbol{r}}^{U}$	Unbiased autocorrelation sequence estimate
R	Range to the target
$\boldsymbol{R}$	Covariance matrix
$\hat{\boldsymbol{R}}$	Sample covariance matrix
R_U	Unambiguous range
$\boldsymbol{s}$	Eigenvector associated with signal eigenvalue
T	Pulse period
$\boldsymbol{U}$	Unitary matrix for SVD factorization
$\boldsymbol{V}$	Unitary matrix for SVD factorization
w	Angular frequency
$\boldsymbol{x}$	Noise-free complex valued sinusoidal signal vector
X	Fourier transform of x
$\boldsymbol{y}$	Noisy complex valued sinusoidal signal vector
σ	Radar cross section
σ_e	Variance of noise
δ	Dirac delta
Δf	Frequency step size
ϕ	Power spectral density
$\hat{\phi}_P$	Periodogram power spectral density estimate
$\hat{\phi}_C$	Correlogram power spectral density estimate
$\hat{\phi}_B$	Bartlett power spectral density estimate
$\hat{\phi}_{BT}$	Blackman-Tukey power spectral density estimate
$\hat{\phi}_W$	Welch power spectral density estimate
φ	Phase of sinusoidal signal
τ	Pulse width

ACS	Auto-Covariance Sequence
ADC	Analog-to-Digital Converter
AIC	Akaike Information Criterion
AR	Auto-Regressive
ARMA	Auto-Regressive Moving Average
BOD	Buried Object Detection
BW	Bandwidth
COHO	Coherent Oscillator
CPI	Coherent Processing Interval
CW	Continuous Wave
DTFT	Discrete Time Fourier Transform
ESD	Energy Spectral Density
ESPRIT	Estimation of Signal Parameters via Rotational Invariance Technique
EVD	Eigenvalue Decomposition
FFT	Fast Fourier Transform
FM	Frequency Modulation
FMCW	Frequency Modulate Continuous Wave
GUI	Graphical User Interface
HOYW	Higher-Order Yule Walker
HRR	High Range Resolution
IDTFT	Inverse Discrete Time Fourier Transform
IFFT	Inverse Fast Fourier Transform
LFM	Linear Frequency Modulation
LNA	Low Noise Amplifier
LO	Local Oscillator
LS	Least Squares
LTI	Linear Time Invariant
MA	Moving Average
MDL	Minimum Description Length
MSSP	Modified Spatial Smoothing Process
MUSIC	Multiple Signal Classification
PD	Phase Detector

PRF	Pulse Repetition Frequency
PRI	Pulse Repetition Interval
PSD	Power Spectral Density
RADAR	Radio Detection and Ranging
RCS	Radar Cross Section
RF	Radio frequency
SCR	Signal-to-Clutter Ratio
SFCW	Stepped-Frequency Continuous Wave
SFG	Sweep Frequency Generator
SFS	Stepped-Frequency-Synthesizer
SNR	Signal-to-Noise Ratio
SSP	Spatial Smoothing Process
STALO	Stable Oscillator
SVD	Singular Value Decomposition
TLS	Total Least Squares
TWOD	Through-the-Wall Object Detection
WSS	White-Sense Stationary
YW	Yule-Walker

1. INTRODUCTION

1.1. Motivation

The ability to "see" the targets behind and inside obstacles such as walls, doors, and other visually opaque materials, using microwave signals is considered as a powerful tool for a variety of applications in both military and commercial paradigms. Search-and-rescue workers, counter-terrorism and counter-intelligence agents encounter situations where they need to detect, locate, and identify building occupants and hidden objects from stand-off location. Specialized devices using electromagnetic waves can provide significant help in these applications[1-8].

The ultimate goal in Through-the-Wall Object Detection (TWOD) and Burried Object Detection (BOD) systems is to achieve high range and cross range resolutions. High Range Resolution (HRR) capability is one of the key parameters in the radar system design which provides many advantages. It provides the ability of resolving closely spaced targets in range, improves the range accuracy, reduces the amount of clutter within the range cell, reduces multi-path, and aids in target recognition and classification. HRR is also very useful in detection of targets with low radar cross sections (RCS) embedded in high clutter. It increases signal-to-clutter ratio (SCR) which makes targets with low RCS visible [9-13].

HRR techniques can be grouped in four main categories: impulsive waveforms, intrapulse pulse compression techniques, interpulse pulse compression techniques, and signal processing techniques [9-13].

Impulsive waveforms achieve HRR via extremely narrow pulses (on the order of nanoseconds). Such a short pulse width can be obtained at very low power levels due to its stability problems, i.e., wide bandwidth and high power can not be achieved simultaneously. Also, the large instantaneous bandwidth imposes severe constraints on the analog to digital conversion process, which in turn degrades some other radar capabilities.

Intrapulse pulse compression techniques increase the instantaneous bandwidth by applying either frequency or phase modulation to each transmitted signal instead of decreasing their time duration. Modulation is applied within individual pulses. Advantage of these techniques over impulsive waveforms is that they increase the bandwidth without decreasing the power level. Linear Frequency Modulation (LFM) technique is one of frequency coding techniques.

Stepped-frequency waveform can be viewed as an interpulse modulated pulse compression waveform in which modulation is applied across the pulses instead of within individual pulses. The key advantage of the stepped frequency method compared to other pulse compression techniques is that the HRR is achieved while still maintaining the instantaneous bandwidth of the receiver narrow, which increases sensitivity and provides jam-immunity.

The drawbacks of the impulsive waveforms can be eliminated using linear frequency modulated or stepped-frequency waveforms. However, the range resolution of stepped-frequency and frequency modulated continuous wave (FMCW) radar systems is limited by the Inverse Fast Fourier Transform (IFFT) and Fast Fourier Transform (FFT), respectively. Although the FFT and IFFT are computationally-efficient, they provide poor range resolution for data with a small bandwidth and when the data size is small. Moreover, the range estimates have large bias. On the other hand, it is well known that parametric spectral estimation methods provide superresolved range profiles of the targets compared with conventional Fourier transform for the same frequency bandwidth. Of course, the computational complexity of the parametric methods is much larger than FFT and IFFT, but the recent developments in the digital signal processors and field programmable gate arrays makes it possible to implement parametric methods within real time. So, parametric spectral estimation methods can be viewed as the fourth technique of achieving HRR.

Motivation of this thesis is to investigate the potential use of the parametric spectral estimation methods for range extraction in frequency modulated continuous wave and stepped frequency radar systems for buried and through-the-wall object detection. Synthetic stepped-frequency and FMCW radar signals and experimental stepped-frequency radar data are used to study the performances of the Yule-Walker, Least-Squares,

Minimum-Norm, Higher-Order Yule-Walker, Root-MUSIC, and ESPRIT methods in BOD and TWOD applications.

1.2. Outline of the Thesis

The thesis is organized as follows: The most common terms used in the radar systems and pulse, stepped-frequency and frequency modulated continuous wave radar priciples are introduced in Chapter 2.

In Chapter 3, non-parametric and parametric spectral estimation methods are explained.

The performance of non-parametric and parametric spectral estimation methods for range extraction in stepped-frequency and FMCW radar systems is investigated in Chapter 4.

Chapter 5 investigates the potential use of the parametric spectral estimation methods for range extraction in BOD and TWOD applications using experimental stepped-frequency radar data.

Chapter 6 concludes the thesis emphasizing the super-resolving capability of parametric spectral estimation methods.

2. RADARS

2.1. Radar Basics

Radar is an abbreviation for RAdio Detection And Ranging. Radar systems use special waveforms and directive antennas to transmit electromagnetic energy into a specific direction to search for targets. Targets in the search area reflect some of this energy back to the radar. These returns are then processed by the receiver to extract some target information, depending on the radar type.

Radars are most often classified by the types of waveforms they use, or by their functionality. Considering the waveforms, radars can be classified as Continuous Wave (CW) or Pulse Radars. Continuous Wave radars continuously emit electromagnetic energy whereas pulse radars transmit a train of pulses. Moreover, CW operation means that the radar transmits and receives at the same time while pulse radars transmits and receives in different time slots. Another classification is based on the functionality of the radars, which includes weather, early warning, over the horizon, ground penetrating, and through the wall radars where the last two ones are the subject of this thesis [9].

This section will explain the terms that will be frequently used in the following chapters such as range, down-range resolution, cross-range resolution, high range resolution, monostatic and bistatic operation and radar cross section.

2.1.1. Range

Radars compute the target range, R, by measuring the time difference, Δt, that is, the time it takes the radar signal to travel the two-way path between the target and the radar. The range is given as

$$R = \frac{c\,\Delta t}{2} \tag{2.1}$$

where c is the speed, $3x10^8$ *m/sec*.

2.1.2. Down-Range Resolution

Down-range resolution, denoted as ΔR, describes the radars ability to distinguish targets that are close in down range as distinct objects. The down-range term is used for the distance in the line-of-sight direction of the radar as shown in figure 2.1. Radars are designed to operate between a minimum down-range R_{min}, and a maximum down-range R_{max}. The distance between R_{max} and R_{min} is divided into N range bins, each of width ΔR, i.e,

$$\Delta R = \frac{R_{\max} - R_{\min}}{N} \tag{2.2}$$

Targets separated in down-range less than ΔR will be evaluated as a single target. So, down-range resolution is one of the most important design parameter for a radar system. Several techniques have been developed to improve the down-range resolution which can be employed both in hardware and software. Radars generally use pulse waveforms for extracting range. The shorter the pulse, the larger the bandwidth, and the more precise the range measurement is.

The effect of a short pulse can be obtained with a long pulse whose bandwidth has been increased by phase or frequency modulation. When passed through a *matched filter,* the output is a compressed pulse whose duration is approximately the reciprocal of the bandwidth of the modulated long pulse. This is called *pulse compression* and allows the resolution of a short pulse with the energy of a long pulse. CW waveform with frequency or phase modulation also can provide accurate range measurement. It is also possible to measure the range of a single target by comparing the phase difference between two or more CW frequencies (multi-frequency radar).

The methods explained so far depend on the radar hardware and should be decided before designing the radar. However, there are also some signal processing techniques that can be used to improve the down-range resolution without any or with some minor changes in radar hardware and they will be explained in detail in chapter three, implemented on synthetic radar return signals in chapter four and on real radar data in chapter five.

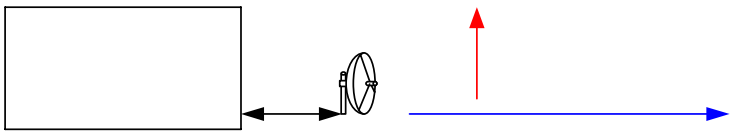

Figure 2.1. Down-Range and Cross-Range directions

2.1.3. Cross-Range Resolution

Cross-range resolution, denoted as ΔR_C and defined similar to downrange resolution, describes the radars ability to distinguish targets that are close in cross range as distinct objects. Cross-range direction is used for the direction that is perpendicular to the down-range as shown in figure 2.1. Cross-range resolution is an important radar parameter, especially in radar imaging. Radars must have a good cross-range resolution to construct a two dimensional image of the scene illuminated by the radar.

The resolution in the cross range can only be achieved by varying the illumination over the field of view. It is necessary to make a set of linearly independent observations in the cross range direction to improve cross-range resolution. Sweeping the beam of the very narrow beam of antenna over the field of view is the preferred method. However, it is sometimes not feasible or possible to design very narrow beam antennas especially in wideband systems or at low frequencies.

Another method to vary illumination over the field of view is to move the radar taking data at different locations, and then synthesize an aperture to obtain cross-range resolution. Also, antenna array can be used to synthesize an aperture in cases where it is not desired or possible to move the antenna. An array where only one antenna transmits and all other receive simultaneously is called a real array and the array where only one antenna transmits and only one antenna receives and this transceiver pair is scanned from end to end is called synthetic array. Also, some signal processing techniques can be used together with the methods explained above, such as beamforming and high resolution spectral estimation methods, to improve the resolution in cross range.

2.1.4. High Range Resolution

High Range Resolution (HRR) capability is one of the key parameters in the radar system design which provides many advantages. It provides the ability of resolving closely spaced targets in range, improves the range accuracy, reduces the amount of clutter within the range cell, reduces multi-path, and aids in target recognition and classification. HRR is also very useful in detection of targets with low radar cross sections embedded in high clutter. It increases signal-to-clutter ratio which in turn makes targets with low RCS visible.

HRR techniques can be grouped in four main categories and they are explained in the following subsections [9-13].

2.1.4.1. Impulsive Waveforms. This technique achieves HRR via extremely narrow pulses (on the order of nanoseconds). The bandwidth of the waveform can be increased by shrinking the pulse width, which degrades the radar sensitivity. Such a short pulse width can be obtained at very low power levels due to its stability problems, i.e., wide bandwidth and high power can not be achieved simultaneously. Also, the large instantaneous bandwidth imposes severe constraints on the analog to digital conversion process, which in turn degrades some other radar capabilities.

2.1.4.2. Intrapulse Pulse Compression Techniques. These techniques increase the instantaneous bandwidth by applying either frequency or phase modulation to each transmitted signal instead of decreasing their time duration. Modulation is applied within individual pulses. Advantage of these techniques over impulsive waveforms is that they increase the bandwidth without decreasing the power level. Linear Frequency Modulation (LFM) technique is one of frequency coding techniques and it will be explained in detail in section 2.4.

2.1.4.3. Interpulse Pulse Compression Techniques. Stepped frequency waveform can be viewed as an interpulse modulated pulse compression waveform in which modulation is applied across the pulses instead of within individual pulses. The key advantage of the stepped frequency method compared to other pulse compression techniques is that the range resolution is increased while still maintaining the instantaneous bandwidth of the receiver narrow, which increases sensitivity. Stepped frequency radar will be explained in detail in section 2.3.

2.1.4.4. Signal Processing Techniques. Range resolution can also be increased via signal processing techniques. A number of high resolution techniques have been developed which provide superior performance than classical methods. These techniques use high-resolution estimation methods to improve range resolution and they will be explained in detail in chapter three.

2.1.5. Bistatic and Monostatic Operation

A radar is called bistatic if it uses separate antennas for transmission and reception, and monostatic if it uses same antenna for transmission and reception. Pulsed radars can use same antenna for transmission and reception since different time slots are allocated for transmission and reception [9]. However, in CW operation, since CW radars transmits and receives at the same time, it is difficult to use same antenna to simultaneously transmit and receive because of the leakage between transmitter and receiver. Receiver sensitivity is set by the level of the transmitted signal that directly gets into the receiver. This situation is similar to that of someone shouting next to you while you are trying to hear someone else far away from you. Providing sufficient isolation over a wide frequency range is not possible, so the easiest method is to separate the transmit and receive antennas.

2.1.6. Radar Cross Section

Radar Cross Section (RCS) is defined as the amount of the power scattered from the target when target is illuminated by RF energy. RCS fluctuates depending on the frequency, aspect angle and polarization of the RF field.

Let P_i denote the power density of a wave incident on a target that is is located at a range R from the radar. The amount of power reflected from the target is

$$P_{ref} = \sigma P_i \tag{2.3}$$

where σ denotes the RCS. Let P_{rec} denote the power of the reflected waves at the receiving antenna. It follows that

$$P_{rec} = \frac{P_{ref}}{4\pi R^2} \tag{2.4}$$

$$\Rightarrow \quad \sigma = 4\pi R^2 \frac{P_{rec}}{P_i} \tag{2.5}$$

And ensuring that the radar receive antenna is in the far field of the target, RCS is given as follows:

$$\sigma = 4\pi R^2 \lim_{R \to \infty} \frac{P_{rec}}{P_i} \tag{2.6}$$

Note that, in practice, the RCS is not a target-specific constant. Different targets may have similar RCS values since RCS fluctuates with aspect angle, frequency and polarization [9].

2.2. Pulse Radar

This section covers the block diagram, waveform, phase detector and important parameters of pulse radars. This chapter will also be used a basis while explaining other waveforms.

Pulse radars transmit and receive a train of modulated pulses. Range is extracted directly from the two-way time delay between a transmitted and received pulse. Carrier frequency (which depends on the design requirements and radar mission), pulse width (defines the range resolution), modulation (which improves range resolution), and the pulse repetition frequency (PRF) are the parameters used to characterize the pulse radar [9-13]. Modulation enhances radar performance. The PRF must be chosen to avoid Doppler and range ambiguities as well as to maximize the average transmitted power. These parameters will not be explained in detail since pulse radar is not the main focus in the thesis. Instead, to construct a basis for the next sections, block diagram, waveform, and important parameters will be explained briefly.

2.2.1. Block Diagram

Simplified block diagram of pulse radar is shown in figure 2.2. In this configuration, Coherent Oscillator (COHO) is used as a reference for the Phase Detector (PD). In transmitter side, COHO output is mixed with Stable Local Oscillator (STALO) output to produce the signal which will upconvert the baseband pulse to the frequency $f_{COHO} + f_{STALO}$. After filtering to eliminate the images and intermodulation products, the output of the mixer is amplified by the power amplifier, pulse modulated and transmitted.

In receive part, the received signal is downconverted to f_{IF} , which is equal to f_{COHO} , by mixing the received signal, which is at frequency $f_{COHO} + f_{STALO}$, with STALO. Then, the intermediate-frequeny (IF) signal is fed to the IF amplifier which has a bandwidth of inverse of pulse width whose output is IQ demodulated in phase detector using COHO signal to produce Inphase(I) and Quadrature(Q) signals.

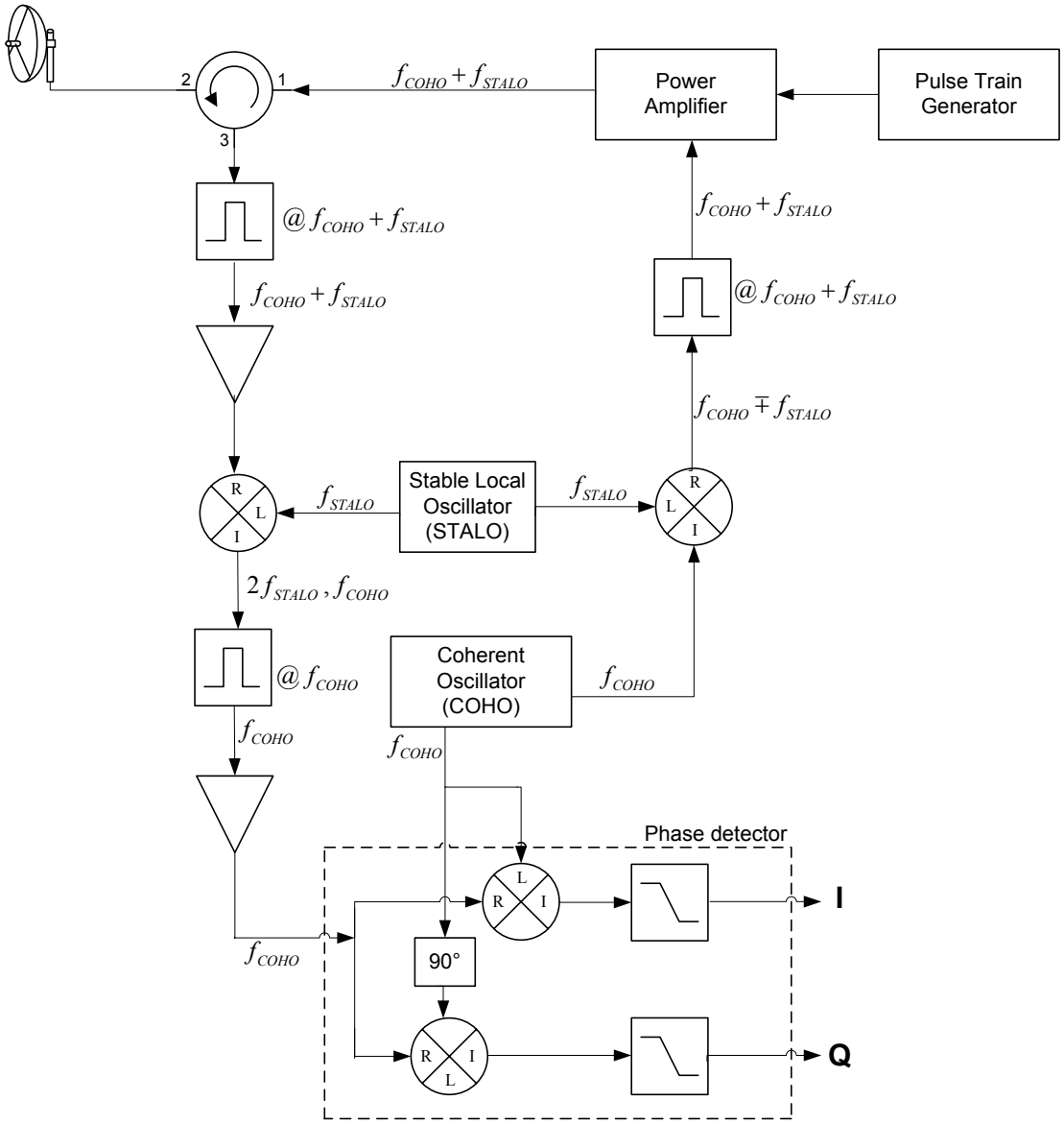

Figure 2.2. Block diagram of monostatic pulse radar

Bandpass and low pass analog filters in the radar diagram are used to suppress the unwanted intermodulation products of the mixers. Note that radar system does not add any phase ambiguity to the radar signal since the COHO and STALO are the Local Oscillators (LO) of both transmit and receive parts. Phase detector outputs are used to extract the phase difference between transmitted and received signals.

2.2.2. Pulse Radar Waveform

Simplified representation of pulse radar waveform is shown in figure 2.3 and 2.4.

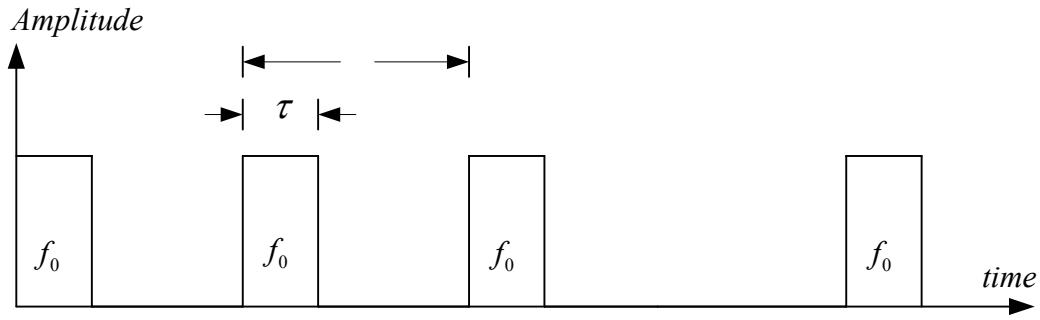

Figure 2.3. Pulse radar waveform

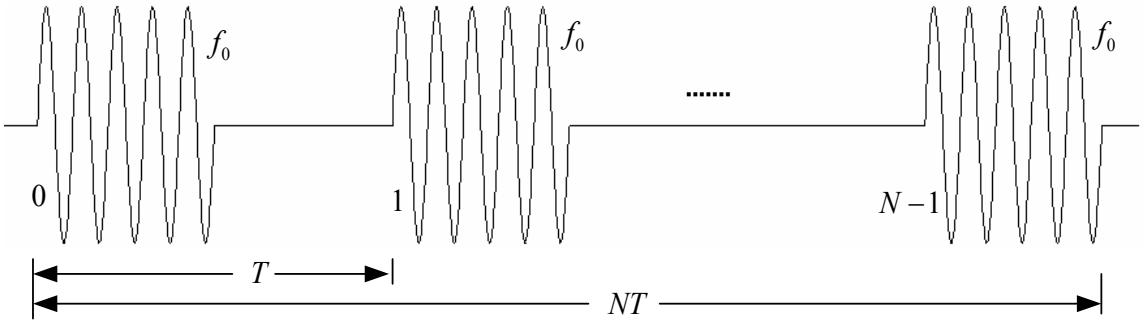

Figure 2.4. Pulse Radar Waveform

Pulse radar waveform can be written as

$$s(t)=\sum_{n=0}^{N-1} A\,rect(\frac{t-nT}{\tau})\cos(2\pi f_0 t) \tag{2.7}$$

The Fourier pairs given below will be used to obtain the frequency spectrum of pulse radar waveform.

$$F\{Cos(2\pi f_0 t)\}=\frac{1}{2}[\delta(f-f_0)+\delta(f+f_0)] \tag{2.8}$$

$$F\{A\,rect(\frac{t}{\tau})\} = A\tau\,Sinc(f\tau) \tag{2.9}$$

$$F\{x(t)\,y(t)\}=\int_{-\infty}^{+\infty} X(f')\,Y(f-f')\,df' \tag{2.10}$$

Let

$$g(t)=\sum_{n=-\infty}^{\infty} A\,rect(\frac{t-nT}{\tau}) \tag{2.11}$$

Using complex exponential Fourier series, $g(t)$ can be written as

$$g(t)=\sum_{n=-\infty}^{\infty} \frac{A\tau}{T} Sinc(\frac{\pi n\tau}{T}) \exp\left(\frac{j2\pi nt}{T}\right) \tag{2.12}$$

It follows that the Fourier transform of $g(t)$ is

$$G(f)=\sum_{n=-\infty}^{\infty} \frac{A\tau}{T} Sinc(\frac{\pi n\tau}{T})\,\delta(f-\frac{n}{T}) \tag{2.13}$$

Let

$$f(t)=\sum_{n=0}^{N} A\,rect(\frac{t-nT}{\tau}) \tag{2.14}$$

Then, the Fourier transform of $f(t)$ is

$$F(f)=AN\tau\left(Sinc(fNT)*\sum_{n=-\infty}^{\infty} Sinc(\frac{N\tau}{2T})\delta(f-\frac{n}{T})\right) \tag{2.15}$$

The multiplication of *F(f)* by $Cos(2\pi f_0 t)$ shifts the spectrum given above by f_0. Figure 2.5 shows the envelope of the amplitude spectrum of a coherent pulse train of finite length [9].

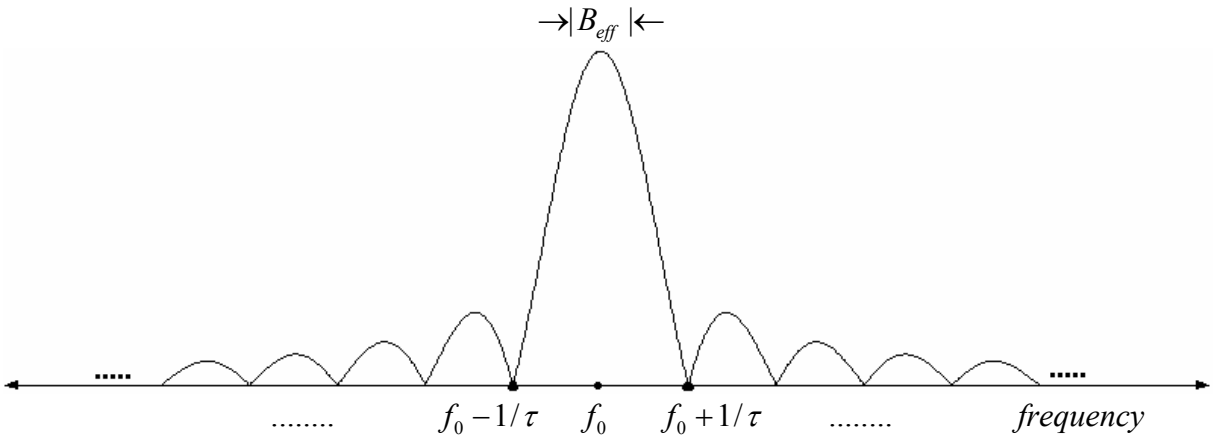

Figure 2.5. Envelope of spectrum of pulse radar waveform

2.2.3. Signal Flow & Phase Detector

Pulse radars transmit *N* pulses each of which has same duration and amplitude. Each pulse is transmitted at the same carrier frequency, $f_0 = f_{STALO} + f_{COHO}$.

Let the transmitted pulse signal be

$$s_1(t) = A_1 Cos(2\pi f_0 t) \tag{2.16}$$

If the range of the target to the radar is *R,* the signal received after a time delay of $2R/c$ is

$$s_2(t) = A_2 Cos(2\pi f_0 (t - 2R/c)) \tag{2.17}$$

Mixing the received signal with $s_{STALO}(t) = 2A_S Cos(2\pi f_{STALO} t)$, we have,

$$\begin{aligned} s_2(t)s_{STALO}(t) &= 2A_2 A_S Cos[2\pi f_0 (t - 2R/c)] Cos(2\pi f_{STALO} t) \\ &= 2A_2 A_S Cos[2\pi (f_{COHO} + f_{STALO})(t - 2R/c)] Cos(2\pi f_{STALO} t) \\ &= 2A_2 A_S Cos\{2\pi f_{COHO} t + 2\pi f_{STALO} t - [2\pi (f_{COHO} + f_{STALO})(2R/c)]\} \\ &\quad x Cos(2\pi f_{STALO} t) \\ &= A_2 A_S Cos\{2\pi f_{COHO} t - [2\pi (f_{COHO} + f_{STALO})(2R/c)]\} \\ &\quad + A_2 A_S Cos\{2\pi f_{COHO} t + 4\pi f_{STALO} t - [2\pi (f_{COHO} + f_{STALO})(2R/c)]\} \end{aligned} \tag{2.18}$$

The second component, which is high frequency term is filtered out by a bandpass filter with center frequency at f_{COHO}. Therefore, the output of the mixer is

$$s_3(t) = A_2 A_S Cos\{2\pi f_{COHO} t - [2\pi (f_{COHO} + f_{STALO})(2R/c)]\} \tag{2.19}$$

Then, $s_3(t)$ is mixed with $s_{COHO,I}(t) = 2A_C Cos(2\pi f_{COHO} t)$ and $s_{COHO,Q}(t) = 2A_C Sin(2\pi f_{COHO} t)$ and then low pass filtered to produce inphase and quadrature components at the output of phase detector.

Mixing $s_3(t)$ with $s_{COHO,I}(t) = 2A_C\, Cos(2\pi f_{COHO}t)$, we have,

$$\begin{aligned} s_3(t)\, s_{COHO,I}(t) &= 2A_2\, A_S\, A_c\, Cos\{2\pi f_{COHO}t - [2\pi(f_{COHO} + f_{STALO})(2R/c)]\} \\ &\quad x\ Cos(2\pi f_{COHO}t) \\ &= A_2\, A_S\, A_c\, Cos[2\pi(f_{COHO} + f_{STALO})(2R/c)] \\ &\quad + A_2\, A_S\, A_c\, Cos\{4\pi f_{COHO}t - [2\pi(f_{COHO} + f_{STALO})(2R/c)]\} \end{aligned} \tag{2.20}$$

The second component, which is high frequency term is filtered out by lowpass filter.

$$\begin{aligned} \Rightarrow I &= A_2\, A_S\, A_c\, Cos[2\pi(f_{COHO} + f_{STALO})(2R/c)] \\ I &= A\, Cos[2\pi f_0(2R/c)] \end{aligned} \tag{2.21}$$

Mixing $s_3(t)$ with $s_{COHO,Q}(t) = 2A_C\, Sin(2\pi f_{COHO}t)$, we have,

$$\begin{aligned} s_3(t)\, s_{COHO,Q}(t) &= 2A_2\, A_S\, A_c\, Cos\{2\pi f_{COHO}t - [2\pi(f_{COHO} + f_{STALO})(2R/c)]\} \\ &\quad x\ Sin(2\pi f_{COHO}t) \\ &= A_2\, A_S\, A_c\, Sin[-2\pi(f_{COHO} + f_{STALO})(2R/c)] \\ &\quad + A_2\, A_S\, A_c\, Sin\{4\pi f_{COHO}t - [2\pi(f_{COHO} + f_{STALO})(2R/c)]\} \end{aligned} \tag{2.22}$$

The second component, which is high frequency term is filtered out by lowpass filter.

$$\begin{aligned} \Rightarrow Q &= A_2\, A_S\, A_c\, Sin[-2\pi(f_{COHO} + f_{STALO})(2R/c)] \\ Q &= A\, Sin[-2\pi f_0(2R/c)] \end{aligned} \tag{2.23}$$

2.2.4. Important Parameters

2.2.4.1. Instantaneous Bandwidth. Instantaneous bandwidth of the pulse radar is approximately equal to inverse of the pulse width.

$$B_{inst} = \frac{1}{\tau} \tag{2.24}$$

Analog-to-Digital Converter (ADC) sampling rate is determined according to instantaneous bandwidth and since the pulse radars use very short duration (on the order of nanoseconds) pulses, they require high sampling rates which degrades the radar performance.

2.2.4.2. Effective Bandwidth. The effective bandwidth of the pulse radar is given by,

$$B_{eff} = \frac{1}{\tau} \tag{2.25}$$

which is equal to instantaneous bandwidth. Range resolution of the radars is directly related to effective bandwidth. The larger the value of effective bandwidth, the higher the range resolution is and the more accurate the range measurement is.

2.2.4.3. Range Resolution. Range resolution is determined from the overall system bandwidth. Therefore, the range resolution of the pulse radar is

$$\Delta R = \frac{c}{2B_{eff}} = \frac{c\tau}{2} \tag{2.26}$$

2.2.4.4. Maximum Unambiguous Range. Once a pulse is transmitted from the radar, sufficient length of time must elapse to allow any echo signals to be received before the next pulse is transmitted. Therefore, the maximum range at which the targets are expected determines the rate at which the pulses are transmitted. If the pulse repetition frequency is too high, echo signals from some targets might arrive after the transmission of next pulse. Such echo signals are called multiple-time-around echo and they appear to be at a much shorter range than the actual and might cause false alarms if they were not known to be multiple-time-around echo. The range beyond which the targets are accepted as second-time-around echo is called maximum unambiguous range [9]. The maximum unambiguous range of the pulse radar is

$$R_U = \frac{cT}{2} \tag{2.27}$$

2.3. Stepped-Frequency Radar

Radars employing stepped-frequency waveform increase the frequency of successive pulses linearly in discrete steps. Stepped-frequency waveform can be viewed as an interpulse pulse compression technique in which modulation is applied across the pulses instead of within individual pulses. High range resolution capability of stepped-frequency radar is used to solve the difficult problem of detection of low-RCS targets in the presence of large clutter such as detection of cruise missiles and buried mines.

Stepped-frequency radar has a narrow instantaneous bandwidth (corresponding to individual pulse) and attains a large effective bandwidth (corresponding to frequency spread of pulses within a burst). As a result, the hardware requirements become less stringent. Lower-speed ADCs and slower processors can be used. The receiver bandwidth would be smaller, resulting in lower noise bandwidth and a higher signal-to-noise ratio.

Stepped-frequency waveform also provides some technical advantages. Being able to select frequencies gives radar the flexibility to change its range resolution, avoid transmitting on critical communication frequencies, and optimize its waveform to enhance the performance of signal processing algorithms.

CW operation also provides the radar some advantages. Since the frequency of the transmitted signal is known, it is possible to use narrowband detection techniques to improve signal to noise ratio and improve the ability to reject signals in adjacent bands (jam immunity). A sample of transmitted signals is sent to the receiver and used as a phase reference for the received signal. This allows radar to demodulate the received signal into inphase and quadrature components without any phase ambiguity and results in a coherent system which means that from frequency to frequency and sweep to sweep, the received signals from all of the stationary objects in the range can be added to improve system signal to noise ratio.

However, these advantages are obtained at the expense of longer operation time. It would require longer time to transmit, receive, and process of a group of pulses. Actually,

this could be a limiting factor in real time operation but, thanks to the development in high speed Direct Digital Synthesis (DDS) and digital receiver technologies, this does not seem to be a limiting factor any more.

2.3.1. Block Diagram

Stepped-frequency radar waveform consists of a group of N coherent pulses whose frequencies are increased from pulse to pulse by a fixed frequency increment Δf. The frequency of the n^{th} pulse of the stepped frequency radar waveform can be written as

$$f_n = f_0 + n\Delta f, \quad n = 0,1,...,N-1 \tag{2.28}$$

where $f_0 = f_{COHO} + f_{STALO}$ is the starting carrier frequency and Δf is the frequency step size, that is, the change in frequency from pulse to pulse. The change in carrier frequency is achieved by the Stepped Frequency Synthesizer (SFS) which produces $f_s = n\Delta f$, $n = 0,1...N-1$. Figure 2.6 shows the block diagram of bistatic stepped-frequency radar.

On the transmit side, first COHO and SFS frequencies are added in a mixer. The mixer output is filtered by an appropriate bandpass filter to suppress unwanted intermodulation products. After suppressing the LO leakage and high order intermodulation products, the sum of the two frequencies is up converted to RF by mixing with STALO. The resulting signal, consisting of the sum of the STALO, COHO, and SFS frequencies, is amplified and transmitted. Thus, the frequency of the n^{th} transmitted pulse within the burst of N pulses is given by

$$f_n = f_{COHO} + f_{STALO} + n\Delta f, \quad n = 0,1,...,N-1 \tag{2.29}$$

On the receive side, where the receiver is a three stage receiver, the received signal is amplified and down-converted to first IF, f_{IF1}, by mixing it with the STALO output, which is then band limited by a bandpass filter. In the second stage, the first IF signal is further

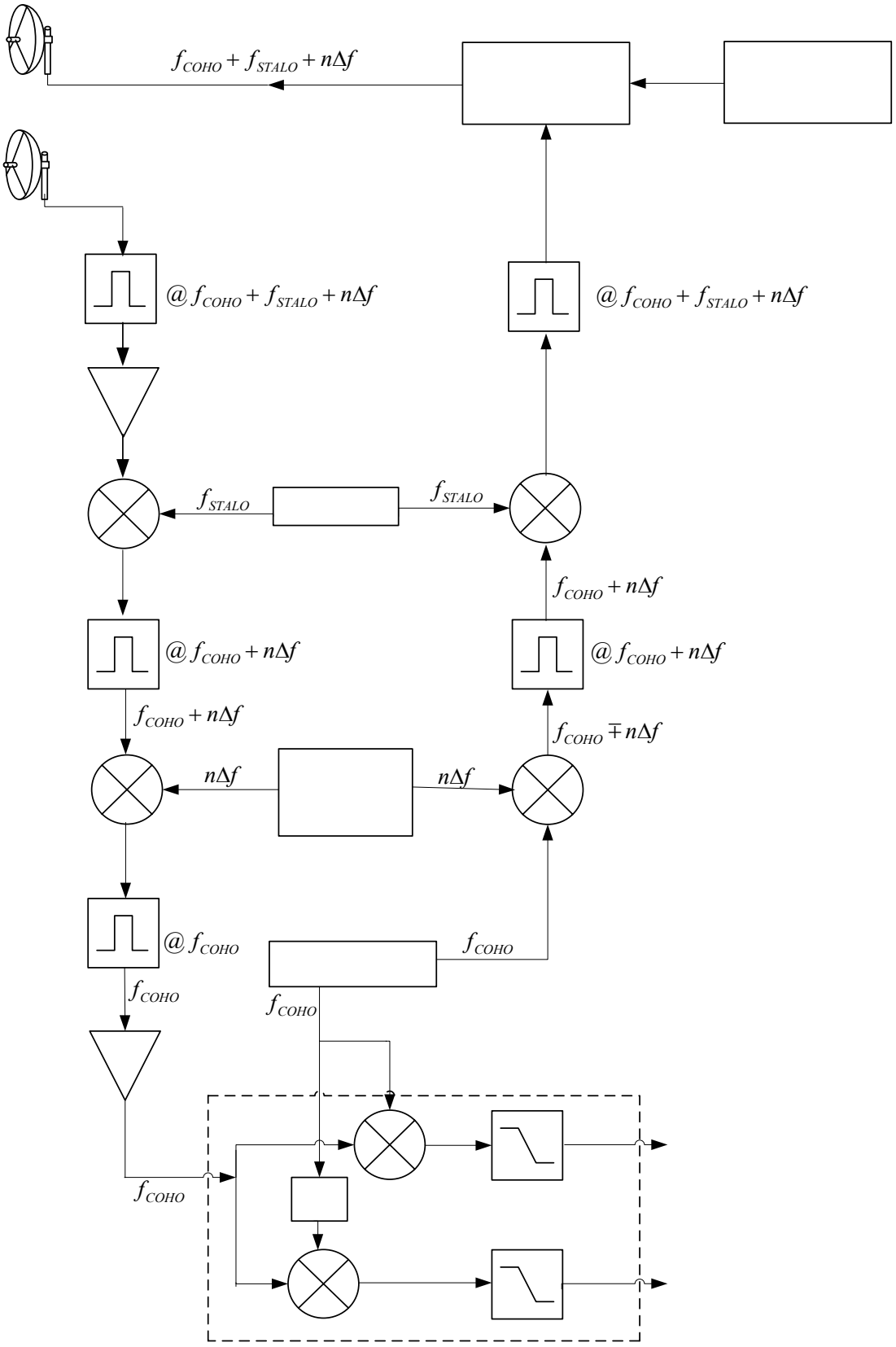

Figure 2.6. Block diagram of a bistatic stepped-frequency continuous wave radar

down converted to second IF, f_{IF2}, by mixing it with the output of the SFS, which is then band limited by a bandpass filter with center frequency f_{COHO}. At the last stage, the output of the second IF filter is down converted to baseband in phase detector. Phase detector mixes the IF signal with two 90° phase-shifted outputs from COHO, producing inphase and quadrature outputs which will be used to extract the phase difference between transmitted and received signals.

2.3.2. Stepped-Frequency Radar Waveform

The frequency of the n^{th} pulse of the stepped frequency radar waveform was given as

$$f_n = f_0 + n\Delta f, \qquad n = 0,1,...N-1 \tag{2.30}$$

where $f_0 = f_{COHO} + f_{STALO}$. Pictorial representation of stepped-frequency waveform is shown in figures 2.7 and 2.8. Each pulse has duration of τ seconds. Group of *N* pulses is called as *burst.* The *burst time,* i.e., the time corresponding to transmission of *N* pulses, is called as coherent processing interval (CPI) [10].

Note that the frequency is constant within each pulse. So, its instantaneous bandwidth is approximately equal to the inverse of pulse width and since pulses do not have short time duration, instantaneous bandwidth of the radar is narrow.

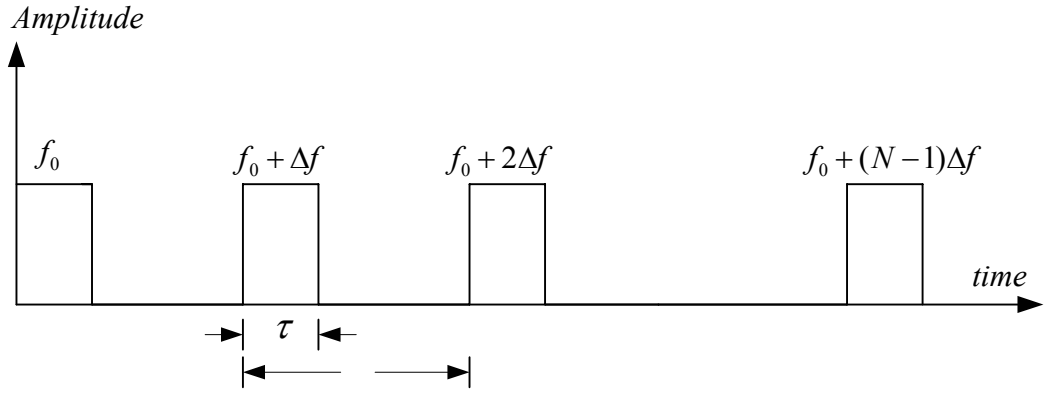

Figure 2.7. Stepped-frequency radar waveform

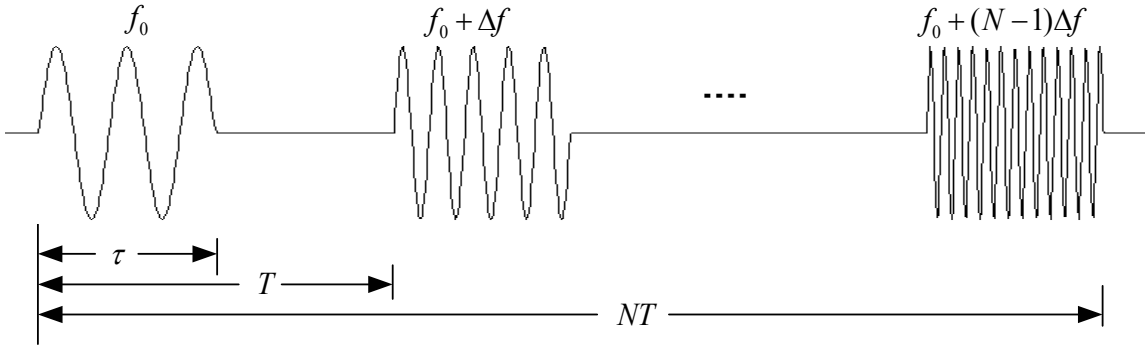

Figure 2.8. Stepped-frequency radar waveform

Stepped-frequency radar achieves high range resolution by processing *N* pulses, each of which has narrow instantaneous bandwidths, in a CPI, instead of using wideband, short duration pulses as in pulse radar.

Stepped-frequency waveform can be written as

$$s(t) = \sum_{n=0}^{N-1} A\,rect\left(\frac{t - nT}{\tau}\right) Cos(2\pi f_n t) \tag{2.31}$$

Frequency spectrum of stepped-frequency waveform can be obtained using the Fourier transform pairs given in section 2.2.2. A pictorial representation of the envelope of the spectrum of stepped-frequency radar pulses is shown in figure 2.9. Note that pulses have different carrier frequencies, low instantaneous bandwidths, and large effective bandwidth.

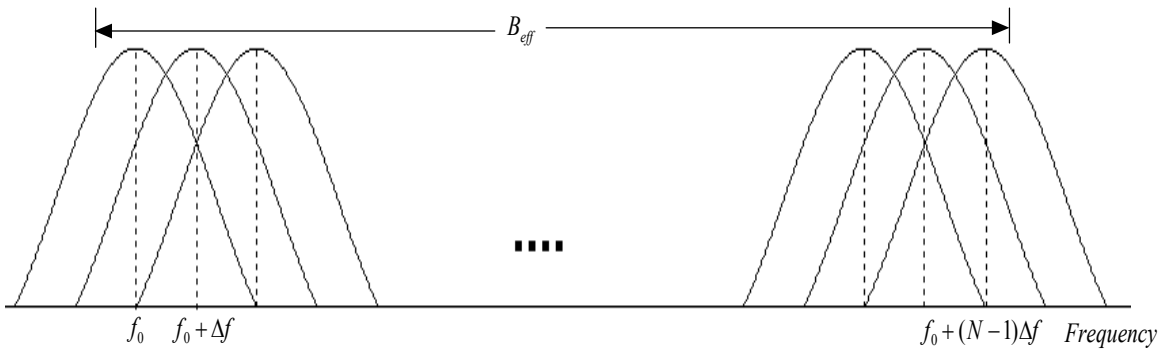

Figure 2.9. Envelope of spectrum of stepped-frequency waveform

2.3.3. Signal Flow & Phase Detector

Let the transmitted signal be

$$\begin{aligned} s_T(t) &= A_1 Cos(2\pi f_n t) \\ &= A_1 Cos[2\pi (f_{COHO} + f_{STALO} + n\Delta f)t] \end{aligned} \tag{2.32}$$

If the range of the target to the radar is *R,* the signal received after a time delay of $2R/c$ is

$$\begin{aligned} s_R(t) &= A_n Cos[2\pi (f_{COHO} + f_{STALO} + n\Delta f)(t - 2R/c)] \\ &= A_n Cos[2\pi f_{COHO}t + 2\pi f_{STALO}t + 2\pi n\Delta f t \\ &\quad - 2\pi (f_{COHO} + f_{STALO} + n\Delta f)(2R/c)] \end{aligned} \tag{2.33}$$

Mixing the received signal with $s_{STALO}(t) = 2A_S Cos(2\pi f_{STALO}t)$ yields

$$\begin{aligned} s_R(t)\, s_{STALO}(t) &= 2A_S A_n Cos[2\pi (f_{COHO} + f_{STALO} + n\Delta f)(t - 2R/c)]\ Cos(2\pi f_{STALO}t) \\ &= A_S A_n Cos[2\pi f_{COHO}t + 2\pi n\Delta f t - 2\pi (f_{COHO} + f_{STALO} + n\Delta f)(2R/c)] \\ &\quad + A_S A_n Cos[2\pi f_{COHO}t + 4\pi f_{STALO}t + 2\pi n\Delta f t \\ &\quad - 2\pi (f_{COHO} + f_{STALO} + n\Delta f)(2R/c)] \end{aligned} \tag{2.34}$$

The second component, which is high frequency term is filtered out by a bandpass filter. Therefore, the first IF signal is

$$s_{IF1}(t) = A_S A_n Cos[2\pi f_{COHO}t + 2\pi n\Delta f t - 2\pi (f_{COHO} + f_{STALO} + n\Delta f)(2R/c)] \tag{2.35}$$

Then, $s_{IF1}(t)$ is mixed with SFS output, $s_{SFS}(t) = 2A_{SFS} Cos(2\pi n\Delta f t)$, i.e.,

$$\begin{aligned} s_{IF1}(t)\, s_{SFS}(t) &= 2A_{SFS} A_S A_n Cos[2\pi f_{COHO}t + 2\pi n\Delta f t - 2\pi (f_0 + n\Delta f)(2R/c)]\ Cos(2\pi n\Delta f t) \\ &= A_{SFS} A_S A_n Cos[2\pi f_{COHO}t - 2\pi (f_0 + n\Delta f)(2R/c)] \\ &\quad + A_{SFS} A_S A_n Cos[2\pi f_{COHO}t + 4\pi n\Delta f t - 2\pi (f_0 + n\Delta f)(2R/c)] \end{aligned} \tag{2.36}$$

The second component, which is high frequency term is filtered out by a bandpass filter. Therefore, the second intermediate frequency signal is

$$s_{IF2} = A_{SFS} A_S A_n \, Cos[2\pi f_{COHO} t - 2\pi (f_0 + n\Delta f)(2R/c)] \tag{2.37}$$

Then, $s_{IF2}(t)$ is mixed with $s_{COHO,I}(t) = 2A_C \, Cos(2\pi f_{COHO} t)$ and $s_{COHO,Q}(t) = 2A_C \, Sin(2\pi f_{COHO} t)$ and then low pass filtered to produce inphase and quadrature components at the output of phase detector.

Mixing $s_{IF2}(t)$ with $s_{COHO,I}(t) = 2A_C \, Cos(2\pi f_{COHO} t)$ yields

$$\begin{aligned} s_{IF2}(t)\, s_{COHO,I}(t) = {} & 2A_{SFS} A_S A_n \, A_C \, Cos[2\pi f_{COHO} t - 2\pi (f_0 + n\Delta f)(2R/c)] \;\; Cos(2\pi f_{COHO} t) \\ = {} & A_{SFS} A_S A_n \, A_C \, Cos[-2\pi (f_0 + n\Delta f)(2R/c)] \\ & + A_{SFS} A_S A_n \, A_C \, Cos\{4\pi f_{COHO} t - [2\pi (f_0 + n\Delta f)(2R/c)]\} \end{aligned} \tag{2.38}$$

The second component, which is high frequency term is filtered out by lowpass filter.

$$I = A_{SFS} A_S A_n \, A_C \, Cos[-2\pi (f_0 + n\Delta f)(2R/c)]$$

$$I = A \, Cos[-2\pi \, (f_0 + n\Delta f) \, (2R/c)] \tag{2.39}$$

Mixing $s_{IF2}(t)$ with $s_{COHO,Q}(t) = 2A_C \, Sin(2\pi f_{COHO} t)$ yields

$$\begin{aligned} s_{IF2}(t)\, s_{COHO,Q}(t) = {} & 2A_{SFS} A_S A_n \, A_C \, Cos[2\pi f_{COHO} t - 2\pi (f_0 + n\Delta f)(2R/c)] \;\; Sin(2\pi f_{COHO} t) \\ = {} & A_{SFS} A_S A_n \, A_C \, Sin[-2\pi (f_0 + n\Delta f)(2R/c)] \\ & + A_{SFS} A_S A_n \, A_C \, Sin\{4\pi f_{COHO} t - [2\pi (f_0 + n\Delta f)(2R/c)]\} \end{aligned} \tag{2.40}$$

The second component, which is high frequency term is filtered out by lowpass filter.

$$Q = A_{SFS} A_S A_n \, A_C \, Sin[2\pi (f_0 + n\Delta f)(2R/c)]$$

$$Q = A \, Sin[-2\pi \, (f_0 + n\Delta f) \, (2R/c)] \tag{2.41}$$

Therefore, the output of IQ phase detector can be written as

$$S_n = A e^{-j\phi_n} \tag{2.42}$$

where

$$\phi_n = 2\pi (f_0 + n\Delta f)\frac{2R}{c} \tag{2.43}$$

and it can be expanded as

$$\phi_n = 2\pi f_0 \frac{2R}{c} + 2\pi\, n\Delta f \frac{2R}{c} \tag{2.44}$$

The first term represents a constant phase shift which is not any of practical significance. It is the second component that provides the desired range resolution which represents the phase shift due to the frequency rate of change multiplied by round-trip delay time [10]. This is also called as induced phase shift.

2.3.4. Important Parameters

2.3.4.1. Instantaneous Bandwidth. Instantaneous bandwidth of the stepped-frequency waveform is the same as the pulse radar waveform and approximately equal to inverse of the pulse width.

$$B_{inst} = \frac{1}{\tau} \tag{2.45}$$

Note that the pulse width that is used in stepped frequency radar is much larger than that is used in pulse radar. Therefore, the instantaneous bandwidth of stepped frequency waveform is much smaller which enables the ADCs with low sampling rates to be used.

2.3.4.2. Effective Bandwidth. The effective bandwidth of the stepped frequency waveform is given by,

$$B_{eff} = N\Delta f \tag{2.46}$$

Since the range resolution of the radars is proportional to effective bandwidth, stepped frequency waveform provides high range resolution while keeping the instantaneous bandwidth small.

2.3.4.3. Range Resolution. Output of IQ phase detector was shown to be

$$\phi_n = 2\pi f_0 \frac{2R}{c} + 2\pi\, n\Delta f \frac{2R}{c} \tag{2.47}$$

The second term in this expression, which is called as induced phase shift, can be written as

$$\phi_{ind} = 2\pi\, n\Delta f \frac{2R}{c} = 2\pi \frac{\Delta f}{T} \frac{2R}{c} nT \tag{2.48}$$

The rate at which the phase changes is called induced frequency shift and given by

$$f_{ind} = \frac{\Delta f}{T} \frac{2R}{c} \tag{2.49}$$

Rewriting R in terms of f_{ind}

$$R = \frac{c}{2} \frac{T}{\Delta f} f_{ind} \tag{2.50}$$

Taking the differential of both sides, we have,

$$\Delta R = \frac{c}{2} \frac{T}{\Delta f} \Delta f_{ind} \tag{2.51}$$

The above equation expresses the range resolution in terms of frequency resolution. Since the frequency resolution obtained from DFT is

$$\Delta f_{ind} = \frac{1}{NT} \tag{2.52}$$

From equations (2.50) and (2.51), the range resolution is obtained as

$$\Delta R = \frac{c}{2N\Delta f} = \frac{c}{2B_{eff}} \tag{2.53}$$

Stepped frequency waveform increases the range resolution since it subdivides the conventional range bin into smaller parts [10].

2.3.4.4. Maximum Unambiguous Range. Stepped-Frequency radar employing DFT achieves range resolution by the Fourier transform of the *N* samples from *N* pulses from a range bin. Fourier transform divides the maximum unambiguous range into *N* equal parts. Therefore, maximum unambiguous range of stepped frequency waveform is given as follows,

$$R_U = N.\Delta R = \frac{c}{2\Delta f} \tag{2.54}$$

Stepped-frequency radar can not measure absolute ranges to individual scatterers. Any target within a range which is a multiple of unambiguous range will be folded into range profile causing range ambiguity [9]. For instance, if Δf is 10 MHz, the unambiguous range is 15 meters and the targets at ranges 5 ($R_U - 10$), 20($2R_U - 10$) and 35($3R_U - 10$) meters will be observed at the same location in the HRR profile. This range fold-over problem is similar to the fold-over problem that occurs when FFT is used to estimate the frequency spectrum [9]. For example, if the sampling rate is 1 kHz, a sine-wave tone at 1200 Hz and 200 Hz will be observed at the same bin in the spectrum.

In order to avoid the range fold-over, Δf and τ must be chosen such that

$$\Delta f \le \frac{c}{2E} \qquad \text{,i.e,} \qquad E \le R_U \tag{2.55}$$

where *E* is the maximum target extent (maximum range the radar will detect targets) in meters. Also, note that the ratio of range bin to the maximum unambiguous range is

$$\frac{c\tau/2}{R_U}=\frac{c\tau/2}{c/2\Delta f}=\tau\Delta f \tag{2.56}$$

Therefore, $\tau\Delta f$ plays an important role in the stepped frequency waveform design, and three cases for $\tau\Delta f$ will be explained in detail in next section.

2.3.5. Signal Processing

As explained in section 2.2.1., the output of the second IF stage is down converted to baseband in phase detector. Phase detector mixes the IF signal with two 90° phase-shifted outputs from COHO, producing Inphase(I) and Quadrature(Q) outputs which will be used in signal processing to extract the HRR profile. When the radar transmits a pulse, the phase detector output is sampled, digitized, and stored. Samples from the *I* and *Q* channels form a complex sample consisting of real and imaginary components, i.e., $A=I+jQ$. The typical sampling rate is one complex sample per pulse width. Each complex sample is termed a *range bin,* as it represents the signal from a range window of length $c\tau/2$ where τ is the pulse width. The phase detector output for all range bins of interest due to all *N* pulses in a burst is collected prior to performing any processing [10].

Complex samples from *N* frequency-stepped pulses are processed by taking their DFT, and these DFT coefficients represent resolution of range R_U into *N* subdivisions, each of width $c/2N\Delta f$. The equation

$$\Delta R=\frac{c}{2N\Delta f}=\frac{c\tau/2}{N\tau\Delta f}=\frac{R_U}{N} \tag{2.57}$$

implies that the range bin of $c\tau/2$ is resolved in $N\tau\Delta f$ parts with range resolution of $c/2N\Delta f$ [10].

As explained in the last section, $\tau\Delta f$ plays an important role in the stepped frequency waveform design and these are the three cases for $\tau\Delta f$ [10]:

2.3.5.1. Case-1. In this case the original range bin is equal to the unambiguous range window R_U. The range bin of width $c\tau/2$ is resolved into *N* parts with an effective range resolution of $c\tau/2N$. This case can be used to detect stationary targets or rotating targets with no translational motion but it is unacceptable for detecting moving targets since the target and the clutter coexist in the range cell and there is no clutter-free space for moving targets. This case is shown in figure 2.10.

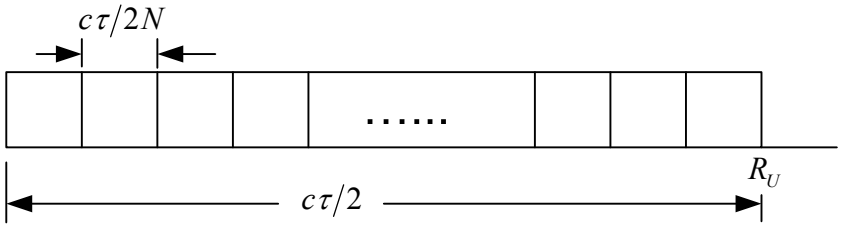

Figure 2.10. Case-1 : $\tau\Delta f = 1$

2.3.5.1. Case-2. In this case, the range bin accommodates only a fraction of unambiguous range window. The range resolution, $c\tau/2N\tau\Delta f$, is worse than the first case; however, there is a clutter free space available for detecting moving targets. This case is shown in figure 2.11.

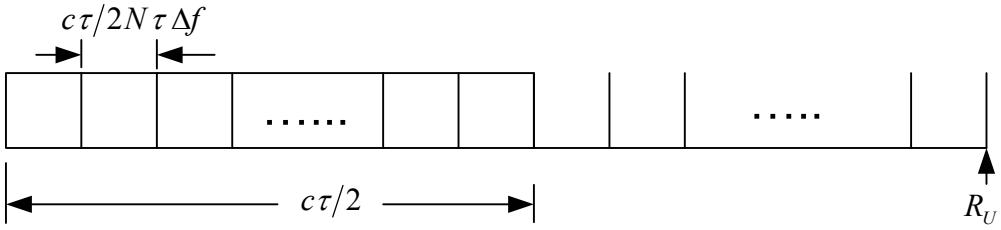

Figure 2.11. Case-2 : $\tau\Delta f < 1$

2.3.5.2. Case-3. In this case, the range bin is larger than the unambiguous range window, and, the range profile is aliased and fold-over will occur. Therefore, this case should be avoided.

After eliminating the range fold-over problem by choosing appropriate values for Δf and τ, we have N complex samples from N frequency-stepped pulses that can be used for range extraction.

From equation (2.48), we have

$$\phi_{ind} = 2\pi\, n\Delta f \frac{2R}{c} = 2\pi \frac{\Delta f}{T} \frac{2R}{c} nT \tag{2.58}$$

The second term, which is the multiplication of the rate of change of frequency $\Delta f / T$ with the round-trip time $2R/c$, represents a shift in frequency during the round-trip time. Thus, the range (or the round-trip time) is converted into a frequency shift (which is analogous to conversion of range to frequency in linear frequency-modulated CW radar as explained in section 2.4). Therefore, it is possible to resolve and measure the range by resolving the frequency, which can be done by taking the DFT of the received signal from N frequency-stepped pulses [10]. Since the range is measured by taking the DFT, the range measurement will have the same limitations as the frequency measurement by DFT. Thus, the range resolution ΔR is dependent on the frequency resolution. In order to improve the range resolution, high resolution spectral estimators which provide superior performance than DFT in frequency estimation can be used. High resolution spectral estimators will be explained in detail in chapter three and they will be tested using synthetic stepped-frequency radar returns in chapter four and using real stepped-frequency radar returns in chapter five.

2.4. Frequency Modulated Continuous Wave (FMCW) Radar

Frequency modulated waveform is a widely used pulse-compression technique to achieve wide operating bandwidths. Among the modulation techniques, Linear Frequency Modulation (LFM) is the most commonly used one. LFM pulses are also called as chirp pulses. In the LFM, the frequency is swept linearly across the pulse width, either upward (up-chirp) or downward (down-chirp). Another way of sweeping the frequency is using two chirp signals, one having up, and the other down, called triangular LFM. Frequency variation of up-chirp and triangular LFM can be seen in figures 2.12 and 2.13, respectively, and figure 2.14 shows the time variation of up-chirp LFM.

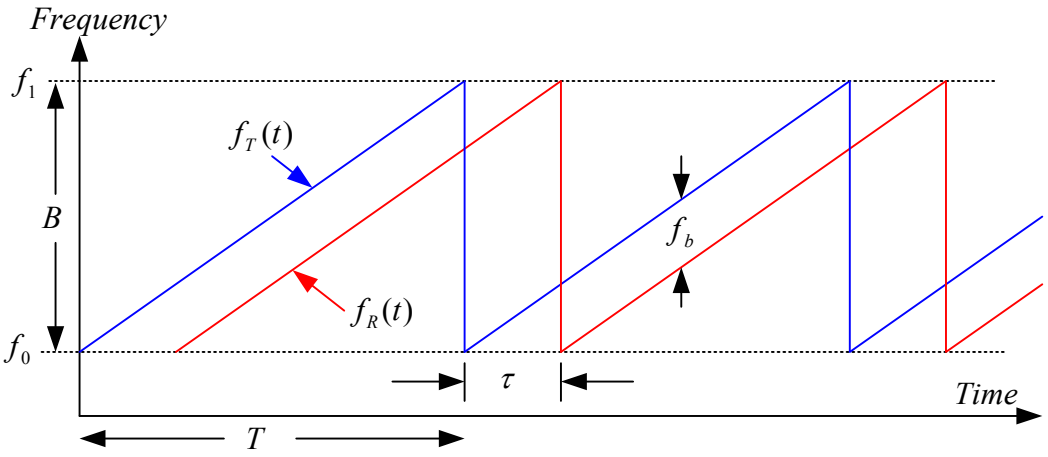

Figure 2.12. Frequency variation of up-chirp LFM waveform

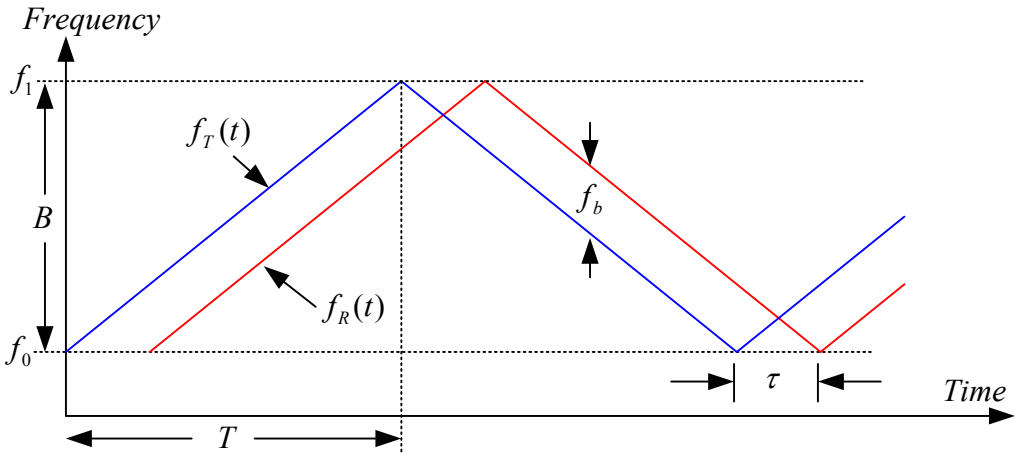

Figure 2.13. Frequency variation of triangular LFM waveform

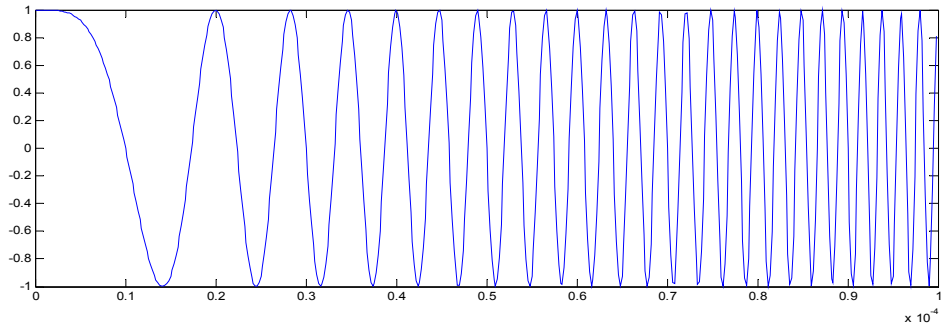

Figure 2.14. Up-chirp LFM waveform

2.4.1. Block Diagram

As explained in section 2.3., the frequencies of the pulses of the stepped-frequency radar are increased from pulse to pulse by a fixed frequency increment Δf by the stepped frequency synthesizer (SFS). In FMCW radar, the frequency is swept linearly across the pulse width by a Sweep Frequency Generator (SFG). Block diagram of the bistatic FMCW radar is shown in figure 2.15.

On the transmit side, first STALO and SFG frequencies are added in a mixer. SFG output provides the frequency sweep in the FMCW waveform and STALO is used to upconvert the sweep waveform to RF. SFG output is a sweep signal where the frequency changes between f_0 and f_1 . The mixer output is filtered by an appropriate bandpass filter to suppress undesired intermodulation products. The resulting signal, consisting of the sum of the STALO and SFG frequencies, is amplified and transmitted. Note that a sample of the transmitted signal is fed through the receive part via coupler.

On the receive side, received signal is first band limited by a bandpass filter and then amplified by a Low Noise Amplifier. The output of the LNA is compared with the transmitted signal in the mixer. The output of the mixer is low pass filtered to eliminate images and intermodulation products. The output of the low pass filter is called the IF or beat signal.

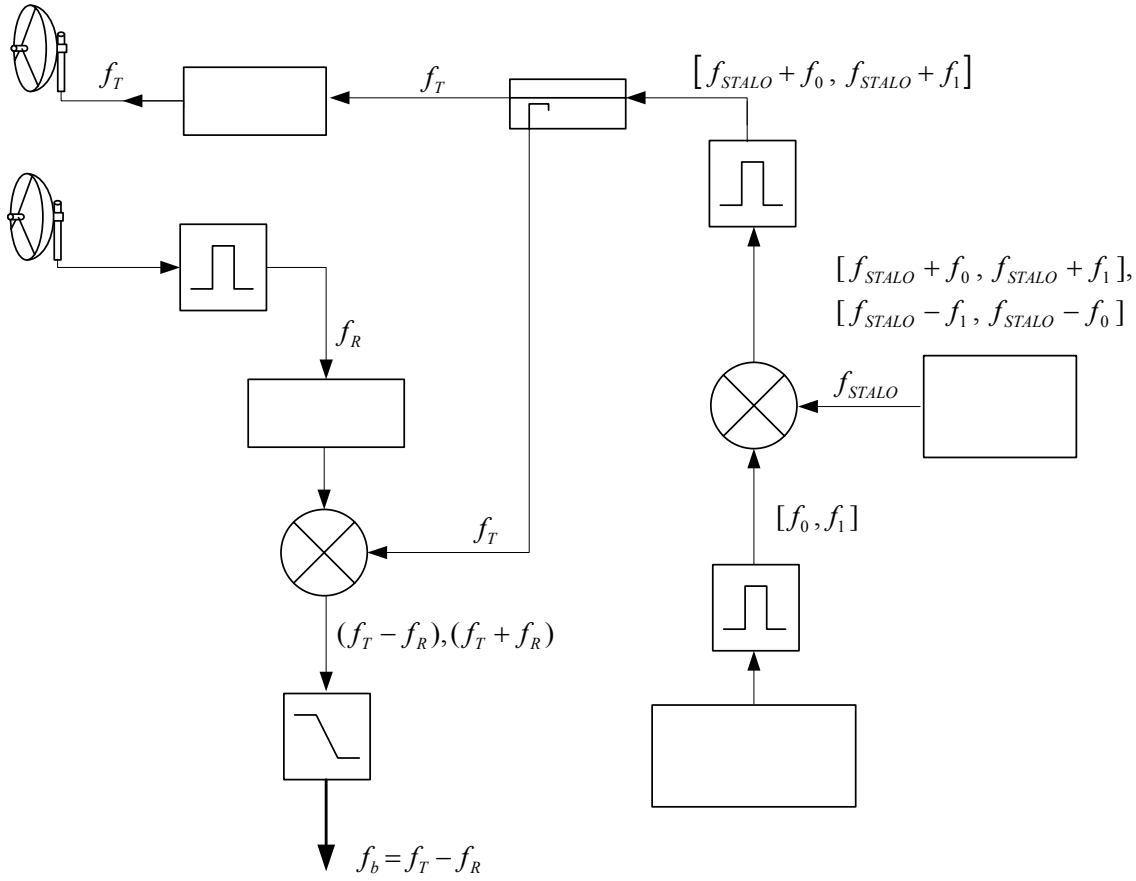

Figure 2.15. Block diagram of a bistatic FMCW radar

2.4.2. Waveform

In this section, first, Frequency Modulation (FM) will be explained in order to make it easier to understand the LFM waveform, then, the time domain representation and spectrum of LFM waveform will be explained in detail.

2.4.2.1. Frequency Modulation. Let θ_i denote the angle of the modulated carrier which is a function of the message signal. Thus, the angle modulated signal can be expressed as

$$s(t) = Cos[\theta_i(t)] \tag{2.59}$$

where the amplitude of the carrier is assumed to be unity.

The average frequency over an interval from t to $t + \Delta t$ is given by,

$$f_{\Delta t} = \frac{\theta_i(t+\Delta t) - \theta_i(t)}{2\pi \Delta t} \tag{2.60}$$

Thus, the instantaneous frequency of the angle modulated signal can be written as follows:

$$\begin{aligned} f_i(t) &= \lim_{\Delta t \to 0} f_{\Delta t} \\ &= \lim_{\Delta t \to 0} \left[\frac{\theta_i(t+\Delta t) - \theta_i(t)}{2\pi \Delta t} \right] \\ &= \frac{1}{2\pi} \frac{d\theta_i}{dt} \end{aligned} \tag{2.61}$$

Frequency modulation is a form of angle modulation in which the instantaneous frequency is varied linearly with the message signal, as shown by,

$$f_i(t) = f_0 + k_f\, m(t) \tag{2.62}$$

where f_0 represents the frequency of the unmodulated carrier and k_f represents the frequency sensitivity of the modulator. So, the instantaneous frequency can be expressed as

$$\begin{aligned} f_i(t) = \frac{1}{2\pi} \frac{d\theta_i}{dt} \quad \Rightarrow \quad \theta_i &= 2\pi \int_0^t f_i(t)\, dt \\ &= 2\pi \int_0^t [f_0 + k_f\, m(t)]\, dt \\ &= 2\pi f_0 t + 2\pi k_f \int_0^t m(t)\, dt \end{aligned} \tag{2.63}$$

Therefore, the time domain representation of the frequency modulated signal is

$$s(t) = Cos\, [\, 2\pi f_0 t + 2\pi k_f \int_0^t m(t)\, dt\,] \tag{2.64}$$

In the rest of this chapter, k_f is assumed to be unity.

2.4.2.2. Linear Frequency Modulation. In up-chirp LFM waveform, instantaneous frequency is increased linearly with the message signal where the message signal is

$$m(t) = \alpha t \tag{2.65}$$

where

$$\alpha = B/T \tag{2.66}$$

and B represents the bandwidth, and T represents the pulse width.

So, the transmitted up-chirp LFM signal can be written as, in time domain,

$$\begin{aligned} s_T(t) &= Cos\,[\,2\pi f_0 t + 2\pi \int_0^t m(t)\,dt\,] \\ &= Cos\,[\,2\pi f_0 t + 2\pi \int_0^t \alpha t\,dt\,] \\ &= Cos\,[\,2\pi f_0 t + 2\pi(\alpha \frac{t^2}{2})] \\ \Rightarrow \quad \theta_i(t) &= 2\pi(f_0 t + \alpha \frac{t^2}{2}) \end{aligned} \tag{2.67}$$

Thus, the instantaneous frequency is

$$f(t) = f_0 + \alpha t \tag{2.68}$$

Transmitted up-chirp LFM signal can be expressed in complex notation by

$$\begin{aligned} s_T(t) &= rect\,(\frac{t}{T})\exp[\,j2\pi(f_0 t + \frac{1}{2}\alpha t^2)] \\ &= rect\,(\frac{t}{T})\exp(j\pi\alpha t^2)\exp(j2\pi f_0 t) \\ &= s(t)\exp(j2\pi f_0 t) \end{aligned} \tag{2.69}$$

where

$$s(t) = rect\,(\frac{t}{T})\exp(j\pi\alpha t^2) \tag{2.70}$$

The spectrum of the transmitted signal is determined from the envelope of *s(t)*. Since the multiplication of *s(t)* with $\exp(j2\pi f_0 t)$ shifts the spectrum of *s(t)* by f_0, it is enough to find the spectrum of *s(t)* [9] .

$$\begin{aligned} S(w) &= \int_{-\infty}^{\infty} s(t) e^{-jwt} \\ &= \int_{-\infty}^{\infty} rect(\frac{t}{T}) \exp(j\pi\alpha t^2) \exp(-jwt)\, dt \\ &= \int_{-T/2}^{T/2} \exp(\frac{j2\pi\alpha t^2}{2}) \exp(-jwt)\, dt \end{aligned} \tag{2.71}$$

Let

$$\alpha' = 2\pi\alpha = 2\pi B/T \tag{2.72}$$

changing the integration variable as

$$\beta = \sqrt{\frac{\alpha'}{\pi}}\left(t - \frac{w}{\alpha'}\right) \quad ; \quad d\beta = \sqrt{\frac{\alpha'}{\pi}}\, dt \quad \Rightarrow dt = \sqrt{\frac{\pi}{\alpha'}}\, d\beta \tag{2.73}$$

we have

$$\begin{aligned} S(w) &= \sqrt{\frac{\pi}{\alpha'}} \exp(\frac{-jw^2}{2\alpha'}) \int_{-\beta_1}^{\beta_2} \exp(\frac{j\pi\beta^2}{2}) d\beta \\ &= \sqrt{\frac{\pi}{\alpha'}} \exp(\frac{-jw^2}{2\alpha'}) \left\{ \int_0^{\beta_2} \exp(\frac{j\pi\beta^2}{2}) d\beta - \int_0^{-\beta_1} \exp(\frac{j\pi\beta^2}{2}) d\beta \right\} \end{aligned} \tag{2.74}$$

where

$$\begin{aligned} \beta_1 &= \sqrt{\frac{\pi}{\alpha'}}\left(\frac{T}{2} + \frac{w}{\alpha'}\right) = \sqrt{\frac{BT}{2}}\left(1 + \frac{f}{B/2}\right) \\ \beta_2 &= \sqrt{\frac{\pi}{\alpha'}}\left(\frac{T}{2} - \frac{w}{\alpha'}\right) = \sqrt{\frac{BT}{2}}\left(1 - \frac{f}{B/2}\right) \end{aligned} \tag{2.75}$$

Remembering the Freshnel Integrals, $S(x)$ and $C(x)$, defined by

$$C(\beta) = \int_0^{\beta} Cos(\frac{\pi x^2}{2}) dx \tag{2.76}$$

$$S(\beta) = \int_0^{\beta} Sin(\frac{\pi x^2}{2}) dx \tag{2.77}$$

The spectrum of *s(t)* can be written as follows:

$$S(w) = \sqrt{\frac{\pi}{\alpha'}} \exp(\frac{-jw^2}{2\alpha'}) \left\{ \begin{array}{l} \int_0^{\beta_2} Cos(\frac{\pi x^2}{2}) dx + j \int_0^{\beta_2} Sin(\frac{\pi x^2}{2}) dx \\ - \int_0^{-\beta_1} Cos(\frac{\pi x^2}{2}) dx - j \int_0^{-\beta_1} Sin(\frac{\pi x^2}{2}) dx \end{array} \right\}$$

$$= \sqrt{\frac{\pi}{\alpha'}} \exp(\frac{-jw^2}{2\alpha'}) \left\{ C(\beta_2) + j\, S(\beta_2) - C(-\beta_1) - j\, S(-\beta_1) \right\} \tag{2.78}$$

Fresnel Integrals can be approximated by

$$C(x) \cong \frac{1}{2} + \frac{1}{\pi\beta} Sin(\frac{\pi\beta^2}{2}) \quad ; \quad \beta >> 1 \tag{2.79}$$

$$S(x) \cong \frac{1}{2} + \frac{1}{\pi\beta} Cos(\frac{\pi\beta^2}{2}) \quad ; \quad \beta >> 1 \tag{2.80}$$

So,

$$C(-\beta_1) = -C(\beta_1) \tag{2.81}$$

$$S(-\beta_1) = -S(\beta_1) \tag{2.82}$$

Therefore, *S(w)* can be written as

$$S(w) = \sqrt{\frac{\pi}{\alpha'}} \exp(\frac{-jw^2}{2\alpha'}) \left\{ \left[C(\beta_2) + C(\beta_1) \right] + j \left[S(\beta_2) + S(\beta_1) \right] \right\} \tag{2.83}$$

Replacing $\alpha' = 2\pi\alpha$, we have

$$S(w) = \sqrt{\frac{1}{2\alpha}} \exp(\frac{-jw^2}{4\pi\alpha}) \left\{ \left[C(\beta_2) + C(\beta_1) \right] + j \left[S(\beta_2) + S(\beta_1) \right] \right\} \tag{2.84}$$

Figure 2.16 shows a typical plot of amplitude spectrum of LFM waveform [9].

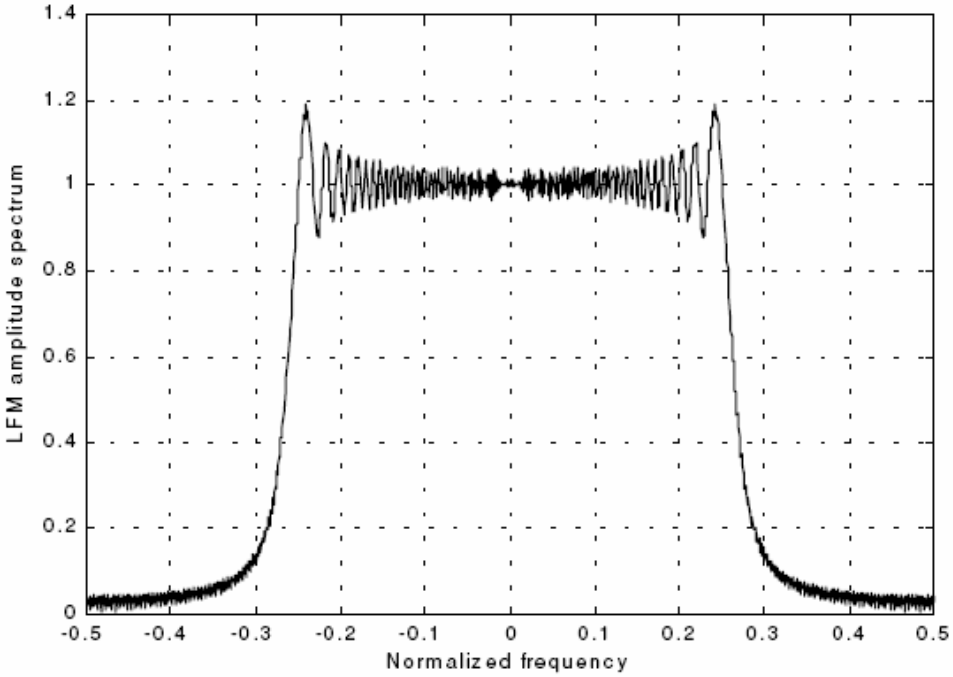

Figure 2.16. Amplitude spectrum of LFM waveform

2.4.3. Signal Flow & Signal Processing

For the up-chirp waveform, the instantaneous frequency of the transmitted signal can be written as

$$f_T(t) = f_0 + \alpha t \tag{2.85}$$

where $\alpha = B/T$. The transmitted signal travels to the target at distance R and returns after a time delay τ where $\tau = 2R/c$.

The instantaneous frequency of the received signal can be written as

$$f_R(t) = f_0 + \alpha (t - \tau) \tag{2.86}$$

The beat frequency can be written as follows:

$$f_b = f_T - f_R = \alpha \tau = \frac{B}{T}\frac{2R}{c} \tag{2.87}$$

So, the range to the target is

$$R = \frac{c T f_b}{2B} \tag{2.88}$$

The main task for finding the range is estimating the beat frequency, or frequencies if multiple targets are present, and distinguishing different beat frequencies that are close to each other. Classical methods employ Fourier Transform to find the beat frequencies. In section three, high resolution methods for estimating the beat frequency will be presented and they will be implemented and tested using synthetic FMCW radar returns and their performances will be compared in chapter four.

3. SPECTRAL ESTIMATION METHODS

Spectral estimation can be defined as estimating the distribution of total power over frequency bins of a finite-length record of a second-order stationary random process, i.e. finding the density of power in narrow spectral bands. Spectral estimation methods find application in many diverse fields such as speech processing, electromagnetics, communications, economics, medicine, meteorology, astronomy, radar and sonar systems.

There are two approaches in spectral analysis: non-parametric and parametric methods. Non-parametric methods makes no assumption on data and uses basic definitions of Power Spectral Density (PSD) while parametric methods postulate some models for the data and find the parameters in the model. Parametric methods outperform the non-parametric methods if data satisfies the assumed model, i.e. model postulated on data is appropriate, otherwise, non-parametric methods provide better spectral estimates than parametric methods. In cases where a priori knowledge about the signal is available, it may be better to use parametric methods to obtain better spectral estimates even when it is not easy or feasible to obtain large data set.

This chapter will cover both the parametric and non-parametric methods and explain their advantages and disadvantages. Then, the methods explained in this chapter will be implemented and tested using synthetic stepped-frequency and FMCW radar returns in chapter four and experimental stepped-frequency radar data in chapter five.

This chapter is organized as follows: section 3.1 covers the basic concepts that will be frequently used in following sections, non-parametric methods are explained section 3.2, section 3.3 covers parametric methods for rational spectra and parametric methods for line spectra are explained in section 3.4.

This chapter is an improved summary of the first four chapters of [14]. Many proofs are added and the topics are associated with BOD and TWOD. Detailed information about the topics in this chapter can be obtained from [14].

3.1. Introduction

3.1.1. Energy Spectral Density

Let $\{x(n); n=0,\pm 1,\pm 2,...\}$ denote a *deterministic* discrete time data sequence which is obtained by sampling a continuous time signal. Assume $x(n)$ is a finite energy signal, i.e.,

$$\sum_{n=-\infty}^{\infty} |x(n)|^2 < \infty \tag{3.1}$$

Discrete Time Fourier Transform (DTFT) of $\{x(n)\}$ is defined as

$$X(w) = \sum_{n=-\infty}^{\infty} x(n) e^{-jwn} \tag{3.2}$$

and the corresponding Inverse Discrete Time Fourier Transform (IDFT) is

$$x(n) = \frac{1}{2\pi} \int_{-\pi}^{\pi} X(w) e^{jwn}\, dw \tag{3.3}$$

Energy Spectral Density, *S(w),* which represents the distribution of energy of the deterministic discrete time data sequence over frequencies is defined as follows

$$S(w) = \sum_{k=-\infty}^{\infty} \rho(k) e^{-jwk} \tag{3.4}$$

where $\rho(k)$ is *autocorrelation* of the finite energy sequence $x(n)$ which is defined by

$$\rho(k) = \sum_{n=-\infty}^{\infty} x(n) x^*(n-k) \tag{3.5}$$

Note that Fourier Transform is exists only for finite energy signals.

3.1.2. Power Spectral Density

Let the discrete time signal $\{x(n); n=0,\pm 1,\pm 2,...\}$ denote a sequence of *random variables* with zero mean, i.e.

$$E\{x(n)\}=0 \tag{3.6}$$

where $E\{\bullet\}$ denotes the expectation operator (which finds the average of samples in $x(n)$).

The *autocovariance sequence* (ACS) of $x(n)$ is defined as

$$r(k) = E\{x(n)x^*(n-k)\} \tag{3.7}$$

where * denotes the complex conjugate operator. Equation (3.6) and (3.7) imply that $x(n)$ is a *White Sense Stationary* (WSS) sequence.

ACS has the following useful properties :

$$r(k)=r^*(-k) \tag{3.8}$$

and

$$r(0)\geq |r(k)| \qquad \forall k \tag{3.9}$$

Let

$$\boldsymbol{X}_m = [x(n-1) \quad x(n-2) \quad \cdots \quad x(n-m)] \tag{3.10}$$

The *covariance matrix* of $x(n)$ is defined as

$$\boldsymbol{R}_m = E\{\boldsymbol{X}_m^H \boldsymbol{X}_m\} \tag{3.11}$$

$$= E\left\{ \begin{bmatrix} x^*(n-1) \\ x^*(n-2) \\ \vdots \\ x^*(n-m) \end{bmatrix} [x(n-1) \quad x(n-2) \quad \ldots \quad x(n-m)] \right\} \tag{3.12}$$

$$\Rightarrow \boldsymbol{R_m} = \begin{bmatrix} r(0) & r^*(1) & r^*(2) & \cdots & r^*(m-1) \\ r(1) & r(0) & & & r^*(m-2) \\ r(2) & \vdots & \ddots & & \vdots \\ \vdots & \vdots & & \ddots & r^*(1) \\ r(m-1) & r(m-2) & \cdots & r(1) & r(0) \end{bmatrix} \tag{3.13}$$

where $(.)^H$ denotes the hermitian (complex conjugate transpose) operator.

3.1.3. First definition of Power Spectral Density

Power Spectral Density (PSD) is defined as the DTFT of the covariance sequence:

$$\phi(w) = \sum_{k=-\infty}^{\infty} r(k) e^{jwk} \tag{3.14}$$

which is similar to the ESD definition for the deterministic discrete time sequence. Also, from the inverse transform, we have,

$$r(k) = \frac{1}{2\pi} \int_{-\pi}^{\pi} \phi(w) e^{jwk} dw \tag{3.15}$$

Note that $E\left\{ \left| x(n) \right|^2 \right\} = r(0) = \frac{1}{2\pi} \int_{-\pi}^{\pi} \phi(w) dw$. Since $\phi(w)d(w)/2\pi$ is the infinitesimal power in the $(w - dw/2, w + dw/2)$ band and the total power in the signal can be calculated by integrating these infinitesimal contributions over $(-\pi, \pi)$, $\phi(w)$ given by (3.14) can be named as power spectral density.

3.1.4. Second definition of Power Spectral Density

The second definition of the PSD is given by

$$\phi(w) = \lim_{N \to \infty} E\left\{ \frac{1}{N} \left| \sum_{n=1}^{N} x(n) e^{-jwn} \right|^2 \right\} \tag{3.16}$$

This definition is equivalent to first one under the assumption

$$\lim_{N\to\infty} \frac{1}{N} \sum_{k=-N}^{N} |k||r(k)| = 0 \tag{3.17}$$

which means $\{r(k)\}$ decays sufficiently fast.

3.2. Non-Parametric Methods

Two common nonparametric spectral estimators are correlogram and periodogram which are derived directly from the first and second definition of PSD. Periodogram and correlogram can provide high resolution spectral estimate if the data length is sufficiently large. It is observed that the variance of these estimators is high and does not decrease as the data length increases, which make these estimators poor spectral estimators. Blackman-Tukey, Barlett, and Welch are some popular spectral estimators that will be explained in this chapter which has lower variance at the cost of reduced resolution.

3.2.1. Periodogram

Periodogram relies on the second definition of the PSD. Dropping the expectation and truncating the infinite sum in the second definition of the PSD for $\{x(n); n=1,2,...,N\}$ where $\{x(1)\cdots x(N)\}$ are the samples of a discrete time WSS random process, periodogram spectral estimate is defined as follows:

$$\hat{\phi}_P(w) = \frac{1}{N}\left|\sum_{n=1}^{N} x(n)e^{-jwn}\right|^2 \tag{3.18}$$

3.2.2. Correlogram

Correlogram relies on the first definition of the PSD. For $\{x(n); n=1, ..., N\}$ where $\{x(1)\cdots x(N)\}$ are the samples of a discrete time WSS random process, correlogram is defined as

$$\hat{\phi}_C(w) = \sum_{k=-(N-1)}^{N-1} \hat{r}(k) e^{-jwk} \tag{3.19}$$

where $\hat{r}(k)$ denotes the estimate of the autocovariance sequence. $\hat{r}(k)$ can be obtained in two standard ways:

3.2.2.1. Unbiased ACS Estimator.

$$\hat{r}^U(k) = \frac{1}{N-k} \sum_{n=k+1}^{N} x(n) x^*(n-k) \qquad for \quad 0 \le k \le N-1 \tag{3.20}$$

$\hat{r}^U(k)$ is called as unbiased ACS estimator since $E\{\hat{r}^U(k)\} = r(k)$, i.e.,

$$E\{\hat{r}^U(k)\} = \frac{1}{N-k} \sum_{n=k+1}^{N} E\{x(n) x^*(n-k)\} = \frac{1}{N-k} \sum_{n=k+1}^{N} r(k) = r(k)$$

3.2.2.2. Biased ACS Estimator.

$$\hat{r}^b(k) = \frac{1}{N} \sum_{n=k+1}^{N} x(n) x^*(n-k) \qquad for \quad 0 \le k \le N-1 \tag{3.21}$$

$\hat{r}^b(k)$ is called as biased ACS estimator since $E\{\hat{r}^b(k)\} \neq r(k)$, i.e.,

$$E\{\hat{r}^b(k)\} = \frac{1}{N} \sum_{n=k+1}^{N} E\{x(n) x^*(n-k)\} = \frac{1}{N} \sum_{n=k+1}^{N} r(k) = \frac{N-k}{N} r(k)$$

Sample covariances with negative lags are obtained via the property of the autocovariance function

$$\hat{r}(-k) = \hat{r}^*(k) \qquad for \quad k = 0,1,\cdots N-1 \tag{3.22}$$

Let $\hat{\phi}_C^U(w)$ denote the correlogram estimate when unbiased ACS estimate is used in (3.19).

An interesting property which is worth to note is that

$$\hat{\phi}_P(w) = \hat{\phi}_C^b(w) \tag{3.23}$$

i.e., periodogram spectral estimate coincides with correlogram spectral estimate if biased ACS estimate is used in (3.19).

In order to prove the above claim consider an Linear Time Invariant (LTI) system with a transfer function

$$h(n) = \frac{1}{\sqrt{N}} x(n) \tag{3.24}$$

where $\{x(1), x(2), \cdots x(N)\}$ are the realizations of a random process for which we would like to find the spectral estimate $\hat{\phi}_X(w)$.

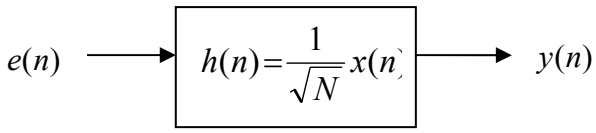

$e(n)$ is chosen as white discrete time random process with unit variance, i.e, $r_e(k) = \delta_{k,0}$ and $\phi_e(w) = 1$, $\forall w$, where,

$$\delta_{k,0} = \begin{cases} 0, & k = 0 \\ 1, & elsewhere \end{cases} \tag{3.25}$$

So, we have,

$$y(n) = h(n) * x(n)$$

$$\Rightarrow \phi_y(w) = \phi_e(w) \left|H(w)\right|^2 = \left|H(w)\right|^2$$

where

$$H(w) = \sum h(n) e^{-jwn}$$

$$\Rightarrow \left|H(w)\right|^2 = \frac{1}{N}\left|\sum x(n) e^{-jwn}\right|^2 = \hat{\phi}_P(w)$$

$$\Rightarrow \phi_y(w) = \hat{\phi}_P(w) \tag{3.26}$$

Calculating the ACS of the output $y(n)$ for $k>0$

$$r_y(k) = E\left\{y(n)\, y^*(n-k)\right\} = \frac{1}{N}\sum_{l=1}^{l=N}\sum_{m=1}^{m=N} h(l)\,h^*(m)\,E\left\{e(n-l)\; e^*(n-k-m)\right\}.$$

Since $e(n)$ is white, i.e.,

$$E\left\{e(n-l)e^*(n-k-m)\right\} = \delta(k+m-l)$$

where

$$\delta(k+m-l) = \begin{cases} 1, & m = l-k \\ 0, & otherwise \end{cases}$$

we have,

$$\begin{aligned} r_y(k) &= \frac{1}{N}\sum_{l=1}^{l=N}\sum_{m=1}^{m=N} h(l)\,h^*(m)\;\delta(k+m-l) \\ &= \frac{1}{N}\sum_{l=k+1}^{N} h(l)\,h^*(l-k) \\ &= \frac{1}{N}\sum_{l=k+1}^{N} x(l)\,x^*(l-k) \\ &= \begin{cases} \hat{r}^b(k) \;\; (biased\;\; ACS\;\; estimator\;) & for \quad k = 0,1,2,\cdots N-1 \\ 0 & for \;\; k \geq N \end{cases} \end{aligned}$$

$$\Rightarrow \phi_y(w) = \phi_C^b(w)$$

$$\Rightarrow \hat{\phi}_P(w) \;=\; \hat{\phi}_C^b(w)$$

3.2.3. Properties of Periodogram

This section covers the analysis of the statistical properties of periodogram and shows that the periodogram is a poor PSD estimator. Since the bias and variance are two important measures to characterize the quality of an estimator, we will derive expressions for the bias of periodogram in section 3.2.3.1 and variance of peridogram in section 3.2.3.2.

3.2.3.1. Bias Analysis of Periodogram

Standard bias ACS estimate given by the expression

$$\hat{r}^b(k) = \frac{1}{N}\sum_{n=k+1}^{N} x(n)\,x^*(n-k) \qquad for \quad 0 \le k \le N-1 \tag{3.27}$$

will be used in the following derivations. Note that the negative lags will be calculated using the following property of covariance function given by (3.8)

$$\hat{r}(-k) = \hat{r}^*(k)\ , \qquad k = 0,...,N-1$$

So, the periodogram estimate is given by (using the previous proof)

$$\hat{\phi}_P(w) = \sum_{k=-(N-1)}^{N-1} \hat{r}^b(k)\,e^{-jwk} \tag{3.28}$$

Therefore, we have,

$$E\{\phi_P(w)\} = \sum_{k=-(N-1)}^{N-1} E\{\hat{r}^b(k)\}e^{-jwk}\ . \tag{3.29}$$

For the positive lags, i.e., for $k \ge 0$, we have

$$\begin{aligned} E\{\hat{r}^b(k)\} &= \frac{1}{N}\sum_{n=k+1}^{N} E\{x(n)\,x^*(n-k)\} \\ &= \frac{1}{N}\sum_{n=k+1}^{N} r(k) \\ &= \frac{N-k}{N} r(k) \\ &= (1-\frac{k}{N}) r(k) \end{aligned} \tag{3.30}$$

For the negative lags, i.e., for $k < 0$, we have

$$E\{\hat{r}^b(k)\} = E\{(\hat{r}^{b^*}(-k)\} \tag{3.31}$$

Replacing $k' = -k$, we have

$$E\{\hat{r}^b(k)\} = E\{(\hat{r}^{b^*}(k')\} \tag{3.32}$$

$$
\begin{aligned}
E\{\hat{r}^b(k)\} &= E\left\{ \frac{1}{N} \sum_{n=k'+1}^{N} \left(x(n)\, x^*(n-k') \right)^* \right\} \\
&= \frac{1}{N} \sum_{n=k'+1}^{N} E\left\{ x^*(n)\; x(n-k') \right\} \\
&= \frac{1}{N} \sum_{n=k+1}^{N} R(-k') \\
&= \frac{N-k'}{N} R(-k') \\
&= \left(\frac{N+k}{N}\right) R(k) \\
&= \left(1+\frac{k}{N}\right) R(k)
\end{aligned} \tag{3.33}
$$

Combining (3.30) and (3.33), we have,

$$
E\left\{\hat{r}^b(k)\right\} = \left(1-\frac{|k|}{N}\right) r(k)\,, \qquad -(N-1) \le k \le (N-1) \tag{3.34}
$$

Combining (3.29) and (3.34), we have,

$$
E\left\{\phi_P(w)\right\} = \sum_{k=-(N-1)}^{N-1} \left(1-\frac{|k|}{N}\right) r(k)\, e^{-jwk} \tag{3.35}
$$

Define

$$
w_B(k) = \begin{cases} 1-\dfrac{|k|}{N}\,, & -(N-1) \le k \le (N-1) \\ 0, & \textit{otherwise} \end{cases} \tag{3.36}
$$

where $w_B(k)$ is called as the Bartlett window and it is shown in figure 3.1.

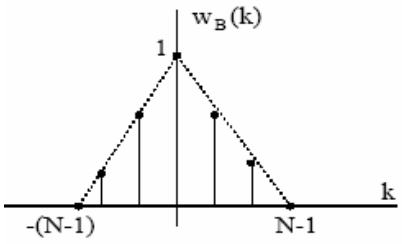

Figure 3.1. Bartlett window

Inserting (3.36) in (3.34), we get,

$$\Rightarrow \; E\left\{\hat{r}^b(k)\right\} = w_B(k)\,r(k) \tag{3.37}$$

So, (3.35) can be rewritten as

$$E\left\{\phi_P(w)\right\} = \sum_{k=-\infty}^{+\infty}\left[w_B(k)\,r(k)\right]e^{-jwk} \tag{3.38}$$

$$= DTFT\left\{\, w_B(k)\,r(k)\,\right\} \tag{3.39}$$

$$= \frac{1}{2\pi}\,W(w) * \phi(w) \tag{3.40}$$

where

$$W(w) = \frac{1}{N}\left[\frac{\sin(\frac{wN}{2})}{\sin(\frac{w}{2})}\right]^2 \tag{3.41}$$

and is called as Fejer Kernel and it is shown in figure 3.2.

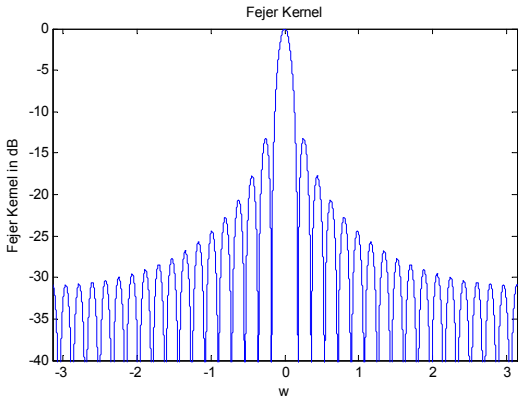

Figure 3.2. Normalized Fejer Kernel for N=35

It can be shown that 3-dB width of the main lobe of $W_B(w)$ is approximately $2\pi / N$ in radians and *1/N* in hertz. Note that $W_B(w)$ has a large main lobe, especially for small values of *N,* which will cause estimated spectrum to be smoothed (which is called *smearing*). Two tones separated in frequency by less than *1/N* will yield a broad peak

instead of two separate peaks. So, *1/N* is the resolution limit of the periodogram. Our goal in the next sections will be finding some spectrum estimators which would provide better spectral resolution than periodogram with the same number of data.

3.2.3.2. Variance Analysis of Periodogram

Asymptotic variance of the periodogram PSD estimate will be derived to show that the poor statistical accuracy of periodogram. For the derivations in this section, first some basic concepts will be explained and then the variance of periodogram will be derived.

If $\{e(n)\}$ is a complex white noise sequence, it satisfies

$$E\,[\,e(n)e^{*}(m)\,] = \sigma^2\delta_{n,m} \tag{3.42}$$

$$E\big[e(n)\,e(m)\big] = 0 \tag{3.43}$$

where σ^2 is the variance of *e(n)*.

Equation (3.42) can be rewritten as,

$$\begin{aligned} &E\big\{[\mathrm{Re}(e(n)) + j\,\mathrm{Im}(e(n))][\mathrm{Re}\,(e(m)) - j\,\mathrm{Im}(e(m))]\big\} \\ &\quad = E\{[\,\mathrm{Re}(e(n))\,\mathrm{Re}(e(m)) + \mathrm{Im}(e(n))\;\mathrm{Im}(e(m))\,] \\ &\qquad + j[\,\mathrm{Im}(e(m))\,\mathrm{Re}(e(n)) + \mathrm{Re}(e(m))\;\mathrm{Im}(e(n))\,]\} \\ &\quad = \sigma^2\delta_{n,m} \end{aligned} \tag{3.44}$$

So, we have,

$$E[\mathrm{Re}(e(n))\,\mathrm{Re}(e(m)) + \mathrm{Im}(e(n))\,\mathrm{Im}(e(m))] = \sigma^2\delta_{n,m} \tag{3.45}$$

$$E[\mathrm{Im}(e(n))\,\mathrm{Re}(e(m)) + \mathrm{Im}(e(m))\,\mathrm{Re}(e(n))] = 0 \tag{3.46}$$

Equation (3.43) can be rewritten as,

$$\begin{aligned} E[e(n)e(m)] &= E\{[\mathrm{Re}(e(n)) + j\,\mathrm{Im}(e(n))][\mathrm{Re}(e(m)) + j\,\mathrm{Im}(e(n))]\} \\ &= E[\mathrm{Re}(e(n))\,\mathrm{Re}(e(m)) - \mathrm{Im}(e(n))\,\mathrm{Im}(e(m))] \\ &\quad + j\,E[\mathrm{Re}(e(m))\,\mathrm{Im}(e(n)) + \mathrm{Re}(e(n))\,\mathrm{Im}(e(m))] \\ &= 0 \end{aligned} \tag{3.47}$$

So, we have,

$$E[\mathrm{Re}(e(n))\mathrm{Re}(e(m)) - \mathrm{Im}(e(n))\mathrm{Im}(e(m))] = 0 \tag{3.48}$$

$$E[\mathrm{Re}(e(n))\mathrm{Im}(e(m)) + \mathrm{Re}(e(m))\mathrm{Im}(e(n))] = 0 \tag{3.49}$$

Combining (3.45) and (3.48), we have,

$$E[\mathrm{Re}(e(n))\mathrm{Re}(e(m))] = \frac{\sigma^2}{2}\delta_{n,m} \tag{3.50}$$

$$E[\mathrm{Im}(e(n))\mathrm{Im}(e(m))] = \frac{\sigma^2}{2}\delta_{n,m} \tag{3.51}$$

Combining (3.45) and (3.48), we have,

$$E[\mathrm{Re}(e(n))\mathrm{Im}(e(m))] = 0 \tag{3.52}$$

$$E[\mathrm{Re}(e(m))\mathrm{Im}(e(n))] = 0 \tag{3.53}$$

Asymptotic variance of periodogram estimate in the case of Gaussian complex white noise is given as

$$\lim_{N\to\infty} E\left\{\left[\hat{\phi}_x^p(w_1) - \phi_x(w_1)\right]\left[\hat{\phi}_x^p(w_2) - \phi_x(w_2)\right]\right\} = \begin{cases} \phi_x^2(w_1), & w_1 = w_2 \\ 0, & w_1 \neq w_2 \end{cases} \tag{3.54}$$

We begin proof by expanding the expression on the left hand side of equation (3.54)

$$\begin{aligned} &\lim_{N\to\infty} E\left\{[\hat{\phi}_x^p(w_1) - \phi_x(w_1)]\,[\hat{\phi}_x^p(w_2) - \phi_x(w_2)]\right\} \\ &= \lim_{N\to\infty} E\left\{\hat{\phi}_x^p(w_1)\hat{\phi}_x^p(w_2)\right\} + \phi_x(w_1)\phi_x(w_2) \\ &\quad - \phi_x(w_1)\lim_{N\to\infty} E\hat{\phi}_x^p(w_2) \\ &\quad - \phi_x(w_2)\lim_{N\to\infty} E\hat{\phi}_x^p(w_1) \end{aligned} \tag{3.55}$$

Note that

$$\phi_x(w_1)\lim_{N\to\infty} E\hat{\phi}_x^p(w_2) \;\to\; \phi_x(w_2) \tag{3.56}$$

$$\phi_x(w_2)\lim_{N\to\infty} E\hat{\phi}_x^p(w_1) \;\to\; \phi_x(w_1) \tag{3.57}$$

So, we have,

$$\begin{aligned}\lim_{N\to\infty}\ E\left\{[\hat{\phi}_x^p(w_1)-\phi_x(w_1)]\,[\hat{\phi}_x^p(w_2)-\phi_x(w_2)]\right\}&\\ =\lim_{N\to\infty}E\left[\hat{\phi}_x^p(w_1)\hat{\phi}_x^p(w_2)\right]-\phi_x(w_2)\phi_x(w_1)&\\ =\begin{cases}\phi_x^2(w_1), & w_1=w_2\\ 0, & w_1\neq w_2\end{cases}&\end{aligned} \tag{3.58}$$

Hence, in order to prove (3.54) we need to show

$$\lim_{N\to\infty}\ E\left[\hat{\phi}_x^p(w_1)\phi_x^p(w_2)\right]=\begin{cases}2\phi_x^2(w_1) & ,\ w_1=w_2\\ \phi_x(w_1)\phi_x(w_2) & ,\ w_1\neq w_2\end{cases} \tag{3.59}$$

Since

$$\begin{aligned}\hat{\phi}_x^p(w)&=\frac{1}{N}\left|\sum_1^N x(n)e^{-jwn}\right|^2\\ &=\frac{1}{N}\sum_{n=1}^N\sum_{m=1}^N x(n)x^*(m)e^{-jw(n-m)}\end{aligned} \tag{3.60}$$

we have

$$E\left[\hat{\phi}_x^p(w_1)\hat{\phi}_x^p(w_2)\right]=\frac{1}{N^2}\sum_{n=1}^N\sum_{m=1}^N\sum_{k=1}^N\sum_{l=1}^N E\left[x(n)x^*(m)x(k)x^*(l)\right]e^{-jw_1(n-m)}\,e^{-jw_2(k-l)} \tag{3.61}$$

Using the property given for the jointly Gaussian complex random variables

$$\begin{aligned}E[\boldsymbol{ABCD}]\ =\ &E[\boldsymbol{AB}]\ E[\boldsymbol{CD}]+E[\boldsymbol{AC}]E[\boldsymbol{BD}]+E[\boldsymbol{AD}]E[\boldsymbol{BC}]\\ &-2\ E[\boldsymbol{A}]\ E[\boldsymbol{B}]\ E[\boldsymbol{C}]\ E[\boldsymbol{D}]\end{aligned} \tag{3.62}$$

the expression in the summation in equation (3.61) can be written as

$$\begin{aligned}E\left[(x(n)x^*(m)\ x(k)x^*(l)\right]\ =\ &E\left[x(n)x^*(m)\right]E\left[x(k)x^*(l)\right]\\ &+E\left[x(n)x(k)\right]\left\{E\left[x(m)x(l)\right]\right\}^*\\ &+E\left[x(n)\ x^*(l)\right]E\left[x^*(m)x(k)\right]\\ &-2E[x(n)]E[x(k)]\ E[x^*(m)]\ E[x^*(l)]\end{aligned} \tag{3.63}$$

Using (3.42) and (3.43), we have

$$E\left[(x(n)x^*(m)\;x(k)x^*(l)\right] = \sigma^4\,\delta_{n,m}\,\delta_{k,l} + \sigma^4\,\delta_{n,l}\,\delta_{k,m} \tag{3.64}$$

Using (3.64), equation (3.61) can be written as

$$E\left[\hat{\phi}_x^p(w_1)\,\hat{\phi}_x^p(w_2)\right] = \left(\sum_{n,k} e^{-jw_1(n-m)}\Big|_{n=m}\, e^{-jw_2(k-l)}\right)\frac{\sigma^4}{N^2} + \frac{\sigma^4}{N^2}\sum_{n,k} e^{-jw_1(n-m)}\, e^{-jw_2(k-n)} \tag{3.65}$$

$$= \frac{\sigma^4}{N^2}N^2 + \frac{\sigma^4}{N^2}\sum_n\sum_k (e^{-j(w_1-w_2)n})\;(e^{j(w_1-w_2)k}) \tag{3.66}$$

$$= \sigma^4 + \frac{\sigma^4}{N^2}\left|\sum_{n=1}^{N} e^{-j(w_1-w_2)n}\right|^2 \tag{3.67}$$

$$= \sigma^4 + \frac{\sigma^4}{N^2}\left|\frac{\sin(\frac{(w_1-w_2)N}{2})}{\sin(\frac{(w_1-w_2)}{2})}\right|^2 \tag{3.68}$$

Since

$$\lim_{N\to\infty}\frac{\sin\alpha x}{\sin x} = \alpha \tag{3.69}$$

we have

$$\lim_{N\to\infty}\left|\frac{\sin(\frac{(w_1-w_2)N}{2})}{\sin(\frac{(w_1-w_2)}{2})}\right| = \begin{cases} N\;, & w_1 = w_2 \\ \le \text{constant} \end{cases} \tag{3.70}$$

So, equation (3.68) can be written as

$$\lim_{N\to\infty}\;E\left[\hat{\phi}_x^p(w_1)\,\hat{\phi}_x^p(w_2)\right] = \begin{cases} \lim_{N\to\infty}\;\sigma^4 + \dfrac{\sigma^4}{N^2}N^2 \;, & w_1 = w_2 \\ \lim_{N\to\infty}\;\sigma^4 + \dfrac{\sigma^4\,\text{constant}}{\mathrm{N}^2} \;, & w_1 \ne w_2 \end{cases} \tag{3.71}$$

$$= \begin{cases} 2\sigma^4\;, & w_1 = w_2 \\ \sigma^4\;, & w_1 \ne w_2 \end{cases} \tag{3.72}$$

Equation (3.72) is the proof of (3.59), hence the proof for the asymptotic variance of periodogram estimate is complete.

The expression given for the asymptotic variance of periodogram estimate means that even when N goes to infinity, variance does not die off and this is the main problem of periodogram spectral estimator. Several refined periodogram-based and window-based non-parametric spectral estimators have been developed to overcome the high statistical variability of the periodogram and they are presented in the following sections.

3.2.4. Blackman-Tukey Method

The poor statistical quality of the peridogram can be explained as arising from the poor accuracy of $\hat{r}(k)$ in $\hat{\phi}_C(w)$ for extreme lags and the large number of covariance estimation errors that are cumulatively summed up in $\hat{\phi}_C(w)$. Both of the effects can be reduced by truncating the sum in the definition of $\hat{\phi}_C(w)$. Following this idea leads to the Blackman-Tukey spectral estimator is, which is given by,

$$\hat{\phi}_{BT}(w) = \sum_{k=-(M-1)}^{M-1} w(k)\hat{r}(k)e^{-jwk} \tag{3.73}$$

where $\{w(k)\}$ is an even function, i.e., $w(k) = w(-k)$, $w(0) = 1, w(k) = 0$ for $|k| > M$, and $w(k)$ decays decays smoothly to zero with *k,* and $M<N$. Since $w(k)$ weights the sample ACS, it is called as the lag window.

Writing the Blackman-Tukey spectral estimator as a DTFT, we get,

$$\hat{\phi}_{BT}(w) = \sum_{k=-\infty}^{\infty} [\, w(k)\hat{r}(k)\,]e^{-jwk} \tag{3.74}$$

Since the DTFT of the product of two sequences is equal to the convolution of their respective DTFTs,

$$\hat{\phi}_{BT}(w) = \hat{\phi}_P(w) * W(w) = \frac{1}{2\pi}\int_{-\pi}^{\pi} \hat{\phi}_P(\beta)\, W(w-\beta)\, d\beta \tag{3.75}$$

So, high statistical variability of the periodogram is eliminated by windowing the sample ACS by an appropriate window. However, smoothing the spectral estimate by windowing decreases the resolution. The smaller the *M*, the narrower the $\{w(k)\}$, the wider the $W(w)$, the smaller the variance and the lower the resolution. The results established by the analysis of $\hat{\phi}_{BT}(w)$ show that the resolution of Blackman-Tukey spectral estimator is on the order of $1/M$, whereas it variance is on the order of M/N. As can be seen, there is trade-off between resolution and variance and this should be considered while choosing the window length.

Common Window Examples :

The expressions for the common windows can be seen in the table 3.1. These windows satisfy $w(k) = w(-k)$, $w(0) = 1$, and $w(k) = 0$ for $|k| > M$.

Table 3.1. Expressions of common windows

Window Name	**Defining expression**
Rectangular	$w(k)=1$
Bartlett	$w(k)=\frac{M-\|k\|}{M}$
Hamming	$w(k)=0.54+0.46\,Cos(\frac{\pi k}{M-1})$
Hanning	$w(k)=0.5+0.5\,Cos(\frac{\pi k}{M})$
Blackman	$w(k)=0.42+0.5\,Cos(\frac{\pi k}{M-1})+0.08\,Cos(\frac{2\pi k}{M-1})$
Blackman-Harris	$w(k) = 0.35875-0.48829\,Cos(\frac{2\pi k}{M-1}) +0.14128\,Cos(\frac{4\pi k}{M-1})-0.01168\,Cos(\frac{6\pi k}{M-1})$
Flat-top	$w(k) = 1-1.93\,Cos(\frac{2\pi k}{M})+1.29\,Cos(\frac{4\pi k}{M}) -0.388\,Cos(\frac{6\pi k}{M})+0.322\,Cos(\frac{8\pi k}{M})$

Parzen	$w(k)=\begin{cases} 1-6\left[\frac{k}{M/2}\right]^2\left[1-\frac{\lvert k\rvert}{M/2}\right] & for\ \ 0\le\lvert k\rvert\le\frac{M}{4} \\ 2\left[1-\frac{\lvert k\rvert}{M/2}\right]^3 & for\ \ \frac{M}{4}\le\lvert k\rvert\le\frac{M}{2} \end{cases}$
Bohman	$w(k)=\left[1-\frac{k-\frac{M}{2}}{\frac{M}{2}}\right]Cos\left[\pi\frac{k-\frac{M}{2}}{\frac{M}{2}}\right]+\frac{1}{\pi}Sin\left[\pi\frac{k-\frac{M}{2}}{\frac{M}{2}}\right]$
Tukey	$w(k)=\begin{cases} 1, & 0\le\lvert k\rvert\le\frac{M}{2}(1+\alpha) \\ 0.5\left[1+Cos\left(\pi\frac{k-\frac{M}{2}(1+\alpha)}{M(1-\alpha)}\right)\right], & \frac{M}{2}(1+\alpha)\le\lvert k\rvert\le M \end{cases}$ for some α, where $0\le\alpha\le1$ and α denotes the ratio of taper.
Bartlett-Hanning	$w(k)=0.62-0.48\left\lvert\frac{k}{M-1}-0.5\right\rvert+0.38Cos\left[2\pi\left(\frac{k}{M-1}-0.5\right)\right]$

The following figures shows the time domain and frequency domain responses of the windows listed in table 3.1.

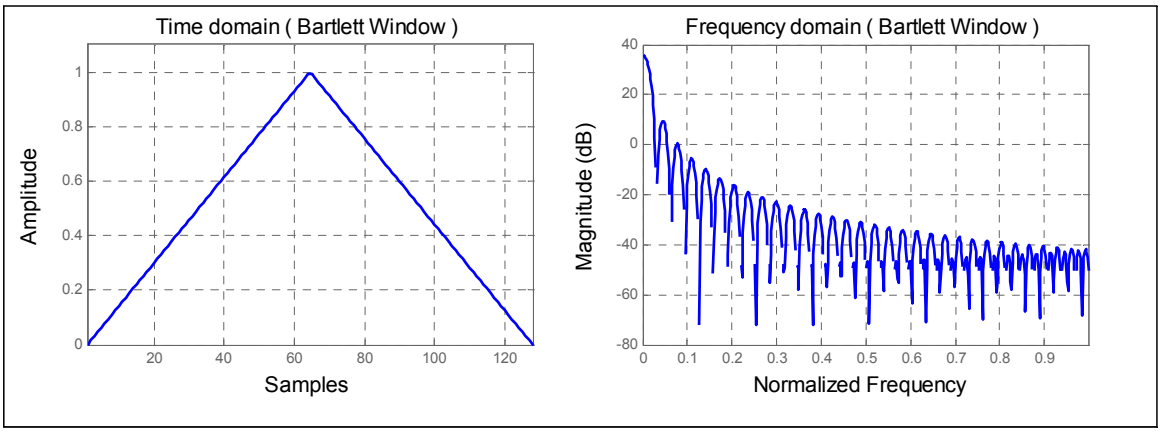

Figure 3.3. Time and frequency domain response of Bartlett window

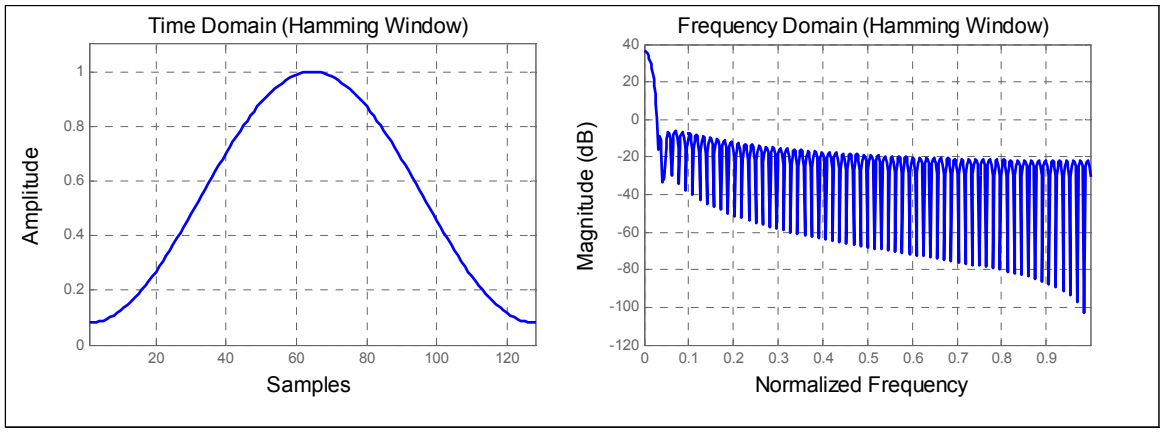

Figure 3.4. Time and frequency domain response of Hamming Window

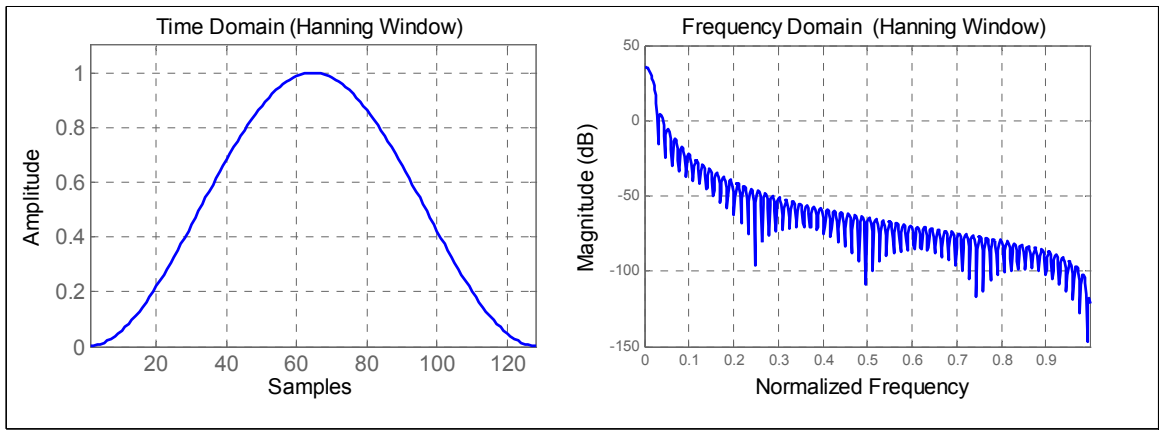

Figure 3.5. Time and frequency domain response of Hanning Window

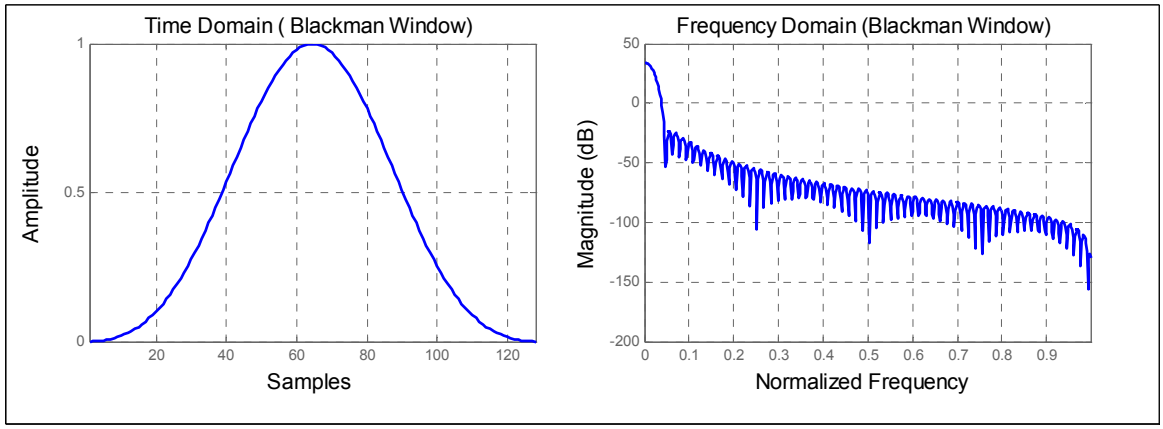

Figure 3.6. Time and frequency domain response of Blackman Window

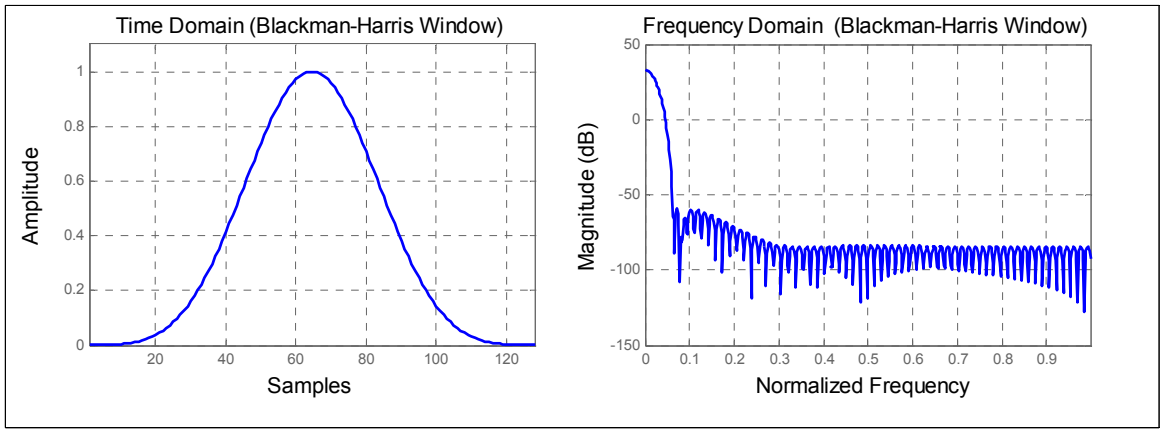

Figure 3.7. Time and frequency domain response of Blackman-Harris Window

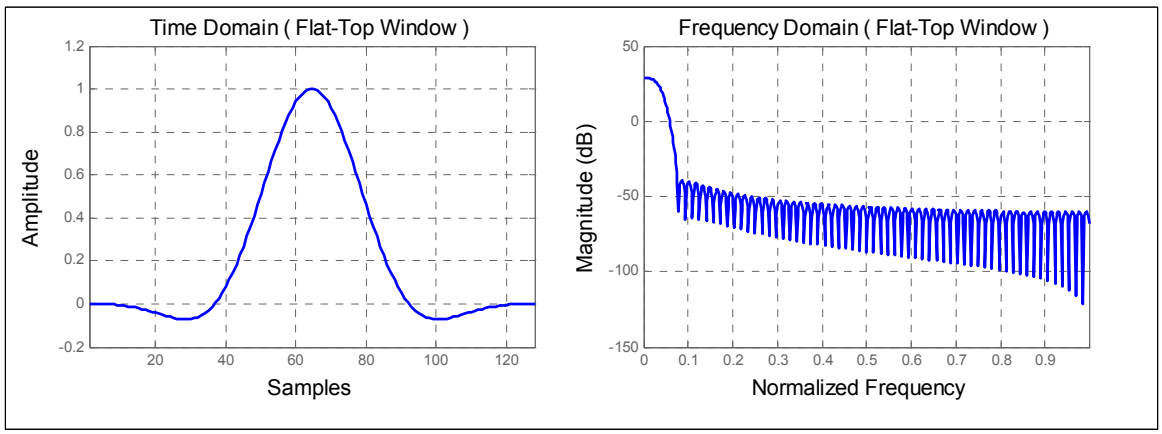

Figure 3.8. Time and frequency domain response of Flat-top Window

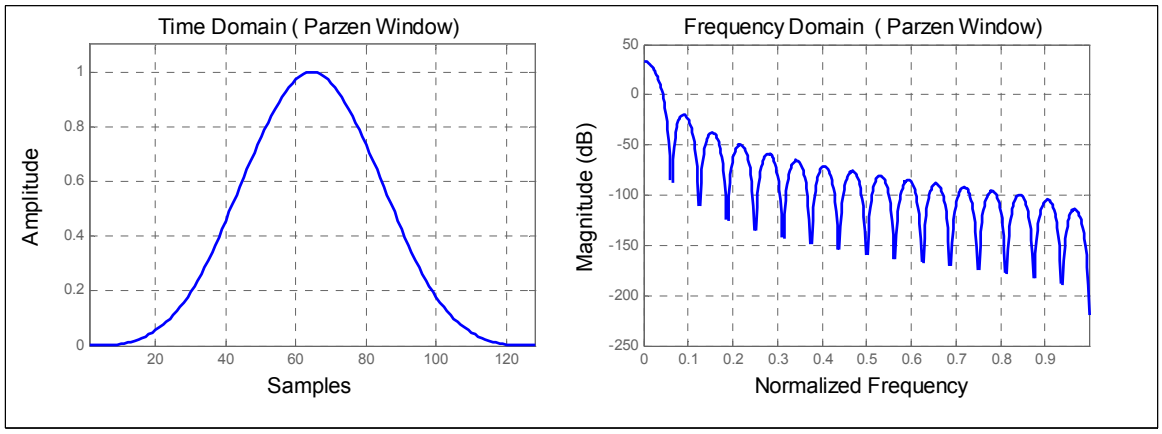

Figure 3.9. Time and frequency domain response of Parzen Window

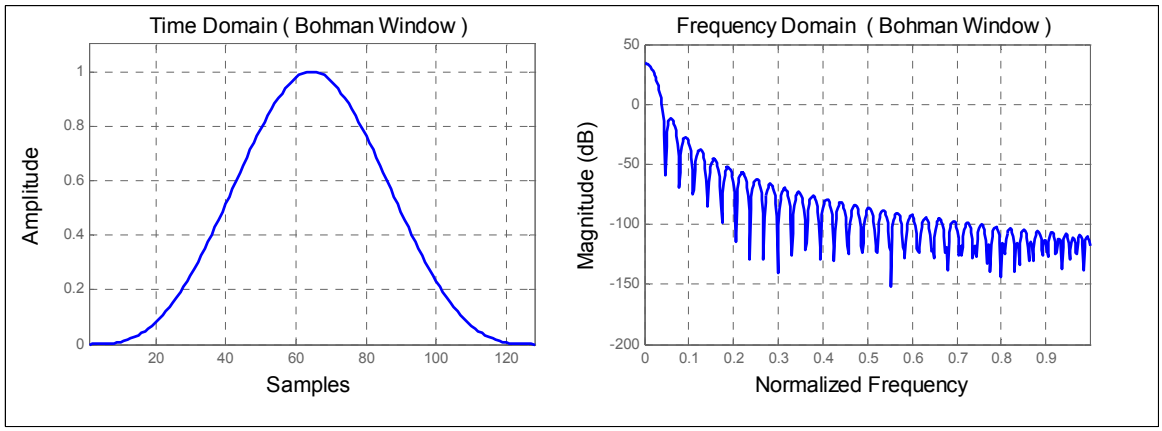

Figure 3.10. Time and frequency domain response of Bohman Window

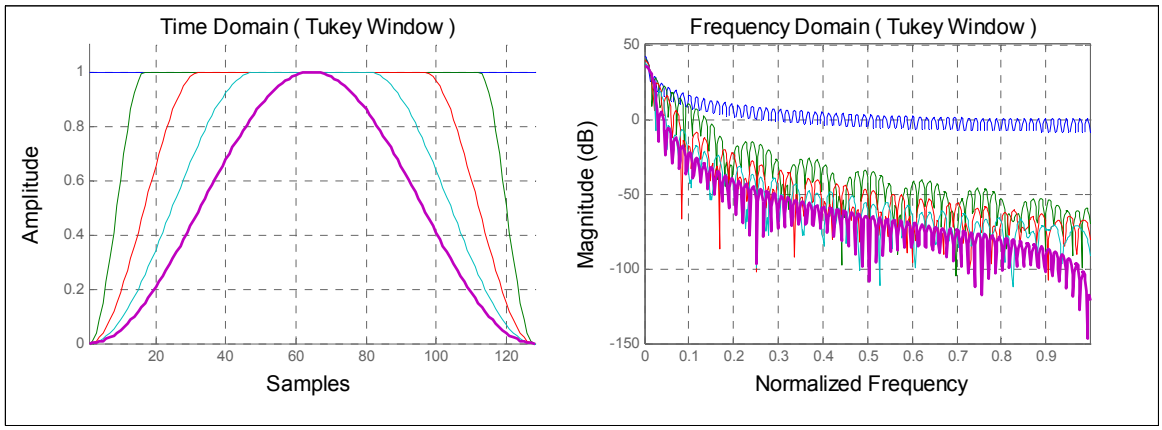

Figure 3.11. Time and frequency domain response of Tukey Windows for $\alpha = 0, 0.25, 0.5, 0.75$ and 1

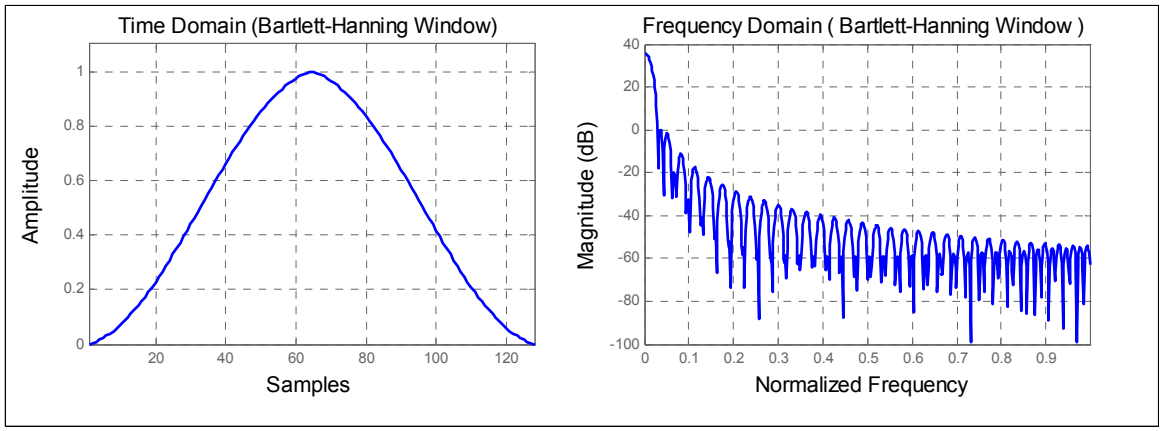

Figure 3.12. Time and frequency domain response of Bartlett-Hanning Window

3.2.5. Bartlett Method

The idea of the Bartlett method is to reduce the variance of the periodogram by splitting up the N observations into $L = N/M$ groups, each group with length M, and then average the periodograms obtained from each group.

Divide $\{x_1.....x_N\}$ into L non-overlapping groups as

$$\underbrace{\overbrace{(x_1.....x_M)}^{\text{Group 1}}}_{x_1(n)}\underbrace{\overbrace{(x_{M+1}.....x_{2M})}^{\text{Group 2}}}_{x_2(n)}.....\underbrace{\overbrace{(x_{N-M+1}.....x_N)}^{\text{Group } L}}_{x_L(n)}.$$

$$\hat{\phi}_1^p(w) \qquad \hat{\phi}_2^p(w) \qquad \hat{\phi}_L^p(w)$$

Bartlett Method can be summarized as follows: First, we define each group as

$$\begin{aligned} x_i(n) &= x[(i-1)M + n] \\ 1 &\le i \le L \\ 1 &\le n \le M \\ N &= LM \end{aligned} \tag{3.76}$$

Then, the periodogram estimate of each group is defined as

$$\hat{\phi}_i^p(w) = \frac{1}{M}\left|\sum_{n=1}^{M}(x_i(n))e^{-jwn}\right|^2 \tag{3.77}$$

Bartlett Method computes the spectral estimate by

$$\hat{\phi}_B(w) = \frac{1}{L}\sum_{i=1}^{L}\hat{\phi}_i^p(w) \tag{3.78}$$

Bartlett method reduces the variance by a factor L. However, since the Bartlett method uses data segments of length M, the resolution is on the order of $1/M$, where it was originally $1/N$, thus leading a reduction in the resolution by a factor L. So, the same

trade-off in Blackman-Tukey method between resolution and variance exists also in Bartlett method.

It may be interesting to relate the Bartlett method to the Blackman-Tukey method. Remembering the periodogram definition, the periodogram estimate of each group is defined as

$$\hat{\phi}_i^p(w) = \sum_{k=-(M-1)}^{M-1} (\hat{r}_i^b(k))\, e^{-jwk} \tag{3.79}$$

where $\hat{r}_i^b(k)$ is the biased ACS estimate of each group and calculated as follows:

$$k \geq 0 \Rightarrow \hat{r}_i^b(k) = \frac{1}{M} \sum_{k=0}^{M-1} x_i(n) x_i^*(n-k) \tag{3.80}$$

$$k \leq 0 \Rightarrow \hat{r}_i^b(k) = [\hat{r}_i^b(-k)]^* \tag{3.81}$$

The Bartlett spectral estimate can be written as

$$\hat{\phi}_B(w) = \frac{1}{L} \sum_{i=1}^{L} \hat{\phi}_i^p(w) \tag{3.82}$$

$$= \frac{1}{L} \sum_{i=1}^{L} \sum_{k=-(M-1)}^{M-1} \hat{r}_i^b(k) e^{-jwk} \tag{3.83}$$

$$= \sum_{k=-(M-1)}^{M-1} \underbrace{\frac{1}{L} \sum_{i=1}^{L} \hat{r}_i^b(k)}_{\tilde{r}_B(k)}\, e^{-jwk} \tag{3.84}$$

So, the Bartlet spectral estimate is given as

$$\hat{\phi}_B(w) = \sum_{k=-(M-1)}^{M-1} \tilde{r}_B(k) e^{-jwk} \tag{3.85}$$

From equations (3.73) and (3.85), we see that Bartlett spectral estimate looks like Blackman-Tukey spectral estimate with rectangular window.

Note that, Bartlett method uses fewer samples to form the ACS estimate, so, the variance of the Bartlett spectral estimate is higher than that of Blackman-Tukey method.

3.2.6. Welch Method

Welch method is similar Bartlett method with the following differences: Blocks are allowed to overlap and each block is windowed prior to computation of periodogram.

Welch method can be summarized as follows: First, we define the overlapping groups as

$$x_j(n) = x[(j-1)K + n], \qquad 1 \le n \le M \quad ,1 \le j \le S \tag{3.86}$$

Let $\upsilon(n)$ denote the window coefficients. Then, the windowed periodogram corresponding to $x_j(n)$ is given as

$$\hat{\phi}_j(w) = \frac{1}{MP}\left|\sum (\upsilon(n))\ (x_j(n))e^{-jwn}\right|^2 \tag{3.87}$$

where P denotes the window power,i.e.,

$$P \overset{\Delta}{=} \frac{1}{M}\left|\sum (\upsilon(n))^2\right| \tag{3.88}$$

Welch method computes the spectral estimate by averaging the windowed periodograms, i.e.,

$$\hat{\phi}_w(w) = \frac{1}{S}\sum_{j=1}^{S}\hat{\phi}_j(w) \tag{3.89}$$

Note that *(j-1)K* in (3.86) is the starting point of the j^{th} group. If *K=M,* groups do not overlap, and we get a similar grouping used in Bartlett method. The recommended value for *K* in the Welch method is $K = M/2$ in which *50%* overlap is obtained.

Note that the overlapping the blocks increases the number of periodograms to be averaged and, hence, decreases the variance. Windowing provides control over the resolution/variance properties of the PSD estimate and decreases the correlation between the blocks, which leads to decraese in the variance.

It may be interesting to relate the Bartlett method to the Blackman-Tukey method.

$$\hat{\phi}_w(w) = \frac{1}{S}\sum_{j=1}^{S}\hat{\phi}_j(w) \tag{3.90}$$

$$= \frac{1}{M\,P\,S}\sum_{j=1}^{S}\sum_{n=1}^{M}\sum_{m=1}^{M} \upsilon(n)\,\upsilon^*(m)\,x_j(n)\,x_j^*(m)\,e^{-jwn}\,e^{jwm} \tag{3.91}$$

$$= \frac{1}{M\,P}\sum_{n=1}^{M}\sum_{m=1}^{M}(\upsilon(n))\,(\upsilon^*(m))\underbrace{\left[\frac{1}{S}\sum_{j=1}^{S}(x_j(n))\,(x_j^*(m))\right]}_{\tilde{r}_x(n-m)}e^{-jw(n-m)} \tag{3.92}$$

$$= \sum_{n=1}^{M}\sum_{m=1-(m-n)}^{m+(n-1)}\upsilon(n)\,\upsilon^*(m)\,\tilde{r}_x(n-m)\,e^{-jw(n-m)} \tag{3.93}$$

Let $k = n - m$

$$= \frac{1}{M\,P}\sum_{n=1}^{N}\sum_{k=-(m-1)}^{M-1}\upsilon(n)\,\upsilon^*(n-k)\,\tilde{r}_x(k)\,e^{-jwk} \tag{3.94}$$

So, the Welch spectral estimate can be written as

$$\hat{\phi}_w(w) = \sum_{k=-(M-1)}^{M-1}\left[\frac{1}{M\,P}\sum_{k=0}^{M-1}\upsilon(n)\,\upsilon^*(n-k)\right]\tilde{r}_x((k))\,e^{-jwk} \tag{3.95}$$

As can be seen from equations (3.73) and (3.95), we see that Welch spectral estimator is an approximate of Blackman-Tukey spectral estimator.

3.3. Parametric Methods for Rational Spectra

3.3.1. Introduction

The difference between the non-parametric methods explained in section 3.2 and the parametric methods that will be explained in this section is that non-parametric methods impose no assumption on the signal whereas the parametric methods postulate a model for the data estimates the parameters in the assumed model. It has been shown that, in cases where a priori knowledge about the signal is available, parametric methods achieve better spectral estimates than non-parametric methods do.

Non-parametric methods are good spectral estimators if the data size, N, is sufficiently large. However, if the data size is small they can not provide high resolution spectral estimates. So, the question that will be answered in this and next section is how can we obtain a good estimate of spectrum if N is not large enough? Persimony principle states that better estimates can be obtained with fewer samples by using appropriate data models. So, the goal is finding good models for the signal. The procedure for the parametric methods can be summarized as follows :

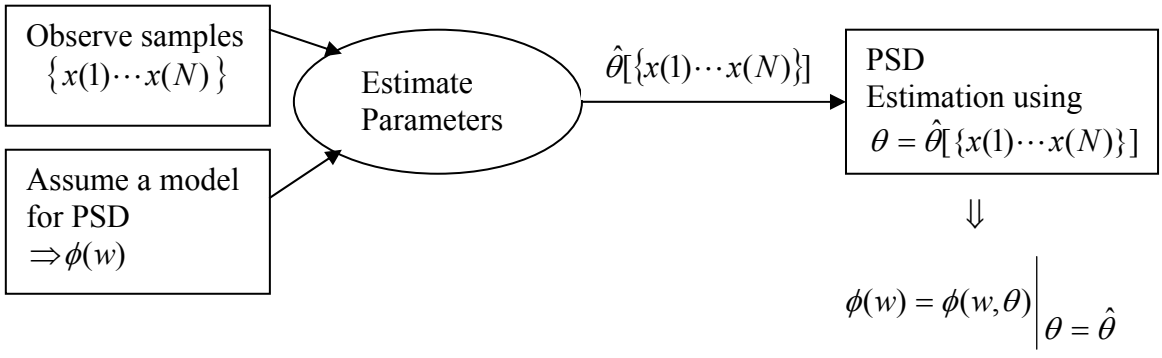

Figure 3.13. Procedure for parametric methods

Only the class of *continuous spectra* will be considered in this section. *Discrete spectra* will be considered in section 3.4.

Let $f(x)$ be a continuous function on the interval $[a,b]$. Weierstrass Approximation Theorem asserts that for any $\varepsilon>0$, there exists a polynomial

$$P_m(x) = c_0 + c_1 x + c_2 x^2 + \cdots + c_m x^m \tag{3.96}$$

for which

$$\left| f(x) - P_m(x) \right| < \varepsilon \qquad \forall x \in [a,b] \tag{3.97}$$

Weierstrass Approximation Theorem implicitly asserts that any PSD can be approximated by a rational PSD which is of the form

$$\varphi(w) = \frac{\sum_{k=-q}^{q} \alpha_k e^{-jwk}}{\sum_{k=-p}^{p} \beta_k e^{-jwk}} \tag{3.98}$$

where

$$\alpha_{-k} = \alpha_k^* \tag{3.99}$$

$$\beta_{-k} = \beta_k^* \tag{3.100}$$

Since $\phi(w)\geq 0$, the expression above can be factored as

$$\phi(w) = \left| \frac{B(w)}{A(w)} \right|^2 \sigma^2 \tag{3.101}$$

where

$$A(w) = 1 + a_1 e^{-jw} + \cdots + a_p e^{-jpw} \tag{3.102}$$

$$B(w) = 1 + b_1 e^{-jw} + \cdots + b_q e^{-jqw} \tag{3.103}$$

Then, the rational PSD can be considered as filtering the white noise with zero mean and variance σ^2 by a filter whose transfer function is $B(w)/A(w)$. Therefore, the problem of estimating the PSD turns out to be estimating $h(n)$.

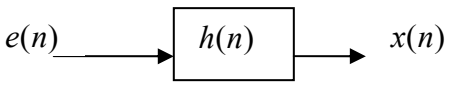

where

$$H(w) = DTFT\{h(n)\} = \frac{B(w)}{A(w)} \tag{3.104}$$

$$\Rightarrow \phi_x(w) = \left|H(w)\right|^2 \phi_e(w) \tag{3.105}$$

and

$$\phi_e(w) = \sigma^2 \quad , \quad \forall w \tag{3.106}$$

Consider the difference equation of the form:

$$x(n) + \sum_{k=1}^{p} a_k\, x(n-k) = \sum_{l=0}^{q} b_l\, e(n-l) \tag{3.107}$$

where $\{e(n)\}$ is white with

$$r_e(k) = \sigma_e^2\, \delta_k \tag{3.108}$$

Applying Z transform to both sides

$$X(z) + X(z)\sum_{k=1}^{p} a_k\, z^{-k} = E(z)\sum_{l=0}^{q} b_l\, z^{-l} \tag{3.109}$$

where

$$X(z) = \sum x(n) z^{-n} \tag{3.110}$$

$$E(z) = \sum e(n) z^{-n} \tag{3.111}$$

$$X(z) = \frac{\sum_{l=0}^{q} b_l\, z^{-l}}{\sum_{k=0}^{p} a_k\, z^{-k}} E(z) = \frac{B(z)}{A(z)} E(z) \ , \qquad (\ a_o = 1) \tag{3.112}$$

$$\Rightarrow \quad X(z)\,A(z) = E(z)\,B(z) \tag{3.113}$$

A signal satisfying $X(z)\,A(z) = E(z)\,B(z)$ is called *autoregressive moving average* signal with order (p,q), i.e., $ARMA(p,q)$. If $A(z) = 1$, i.e., $p = 0$, then *x(n)* is called *moving average* signal with order *q , i.e., MA(q)* ; x(n) is called *autoregressive* signal if *q = 0* with order *p*, i.e., *AR(p)*.

Then, we will investigate the covariance structure of *ARMA(p,q)* process. Consider the difference equation of the form:

$$x(n)+\sum_{i=1}^{p} a_i\, x(n-i) = \sum_{j=0}^{q} b_j\, e(n-j) \qquad (b_0=1) \tag{3.114}$$

where $\{e(n)\}$ is white with $R_e(k) = \sigma_e^2\, \delta_k$.

Multiplying both side of equation (3.114) by $x^*(n-k)$ and taking expectation yields

$$E\{x^*(n-k)[x(n)+\sum_{i=1}^{p} a_i\, x(n-i)]\} = E\{x^*(n-k)\,[\sum_{j=0}^{q} b_j\, e(n-j)\,]\}$$

$$E\{\,x^*(n-k)\,x(n)\}+\sum_{i=1}^{p} a_i\; E\{x(n-i)\;x^*(n-k)\} = \sum_{j=0}^{q} b_j\, E\{e(n-j)\,x^*(n-k)\}$$

$$r(k)+\sum_{i=1}^{p} a_i\; r(k-i) = \sum_{j=0}^{q} b_j\, E\{e(n-j)\,x^*(n-k)\}$$

Remembering

$$x(n) = \sum_{m=0}^{\infty} h(m)\,e(n-m)$$

$$E\{e(n-j)\,x^*(n-k)\} = \sum_{m=0}^{\infty} h^*(m)\; E\{e(n-j)\,e^*(n-k-m)\,\}$$

$$= \sum_{m=0}^{\infty} h^*(m)\;\sigma_e^2\,\delta_{j,k+m} \quad \text{,assume } h_0=1 \text{ and } h(n)=0 \text{ for } n<0$$

$$= \sigma_e^2\, h^*(j-k)$$

$$\Rightarrow\; r(k) + \sum_{i=1}^{p} a_i\; r(k-i) = \sigma_e^2 \sum_{j=0}^{q} b_j\, h^*(j-k) \tag{3.115}$$

$$h^*(j-k)=0 \qquad \text{for } j<k \text{ and } 0\le j\le q$$

$$\Rightarrow h^*(j-k)=0 \quad \forall j \quad if\ \ k>q \tag{3.116}$$

Combining (3.115) and (3.116), we get,

$$\Rightarrow\; r(k) + \sum_{i=1}^{p} a_i\; r(k-i) = 0 \qquad for\ k>q \tag{3.117}$$

3.3.2. Autoregressive Signals

When the B-polynomial in equation (3.101) is equal to unity for all frequencies, we come up with a special class of ARMA signals. AR model is used to model spectra with narrow peaks by placing zeros of the A-polynomial in (3.101) close to the unit circle. So, AR signals are also called as all-pole signals.

Rewriting the difference equation in (3.114) for AR signals yields

$$x(n)+\sum_{k=1}^{p} a_k\, x(n-k) = e(n) \tag{3.118}$$

$$x(n) = e(n) - \sum_{k=1}^{p} a_k\, x(n-k) \tag{3.119}$$

$$x(n) = e(n) - a_1\, x(n-1) - a_2\, x(n-2) - \ \ldots\ - a_p\, x(n-p) \tag{3.120}$$

Equation (3.120) means that it is possible to obtain *x(n)* from the past samples of *x(n)*, that is why AR model is also called autoregressive model.

Two methods, Yule-Walker (YW) method and Least-Squares (LS) method, will be explained in detail for autoregressive spectral estimation.

3.3.2.1. Yule – Walker Method. From the covariance structure of *ARMA(p,q)* process, we have

$$r(k) + \sum_{i=1}^{p} a_i\, r(k-i) = \sigma_e^2 \sum_{j=0}^{q} b_j\, h^*(j-k)$$

For AR(p) process and for $k = 0$, we have

$$\Rightarrow\ r(0) + \sum_{i=1}^{p} a_i\, r(-i) = \sigma_e^2 \sum_{j=0}^{0} b_j\, h^*(j) = \sigma_e^2 \tag{3.121}$$

Also, we know that

$$r(k) + \sum_{i=1}^{p} a_i\, r(k-i) = 0 \qquad for\ k > q \tag{3.122}$$

Combining (3.121) and (3.122) and writing for $k=0,1,2,\cdots p$ in matrix notation yields

$$\begin{bmatrix} r(0) & r(-1) & \cdots & r(-p) \\ r(1) & r(0) & & r(-p+1) \\ \vdots & & \ddots & r(-1) \\ r(p) & \dots & r(1) & r(0) \end{bmatrix} \begin{bmatrix} 1 \\ a_1 \\ \vdots \\ a_p \end{bmatrix} = \begin{bmatrix} \sigma_e^2 \\ 0 \\ \vdots \\ 0 \end{bmatrix} \tag{3.123}$$

These equations are called the Yule-Walker or Normal equations. Let

$$\boldsymbol{A}_{p+1} = \begin{bmatrix} r(0) & r(-1) & \cdots & r(-p) \\ r(1) & r(0) & & r(-p+1) \\ \vdots & & \ddots & \vdots \\ r(p) & \dots & r(1) & r(0) \end{bmatrix}, \qquad \boldsymbol{a} = \begin{bmatrix} a_1 \\ a_2 \\ \vdots \\ a_p \end{bmatrix} \tag{3.124}$$

and

$$\boldsymbol{A}_p = \begin{bmatrix} r(0) & r(-1) & \cdots & r(-p+1) \\ r(1) & r(0) & & \vdots \\ \vdots & & \ddots & r(-1) \\ r(p-1) & \cdots & r(1) & r(0) \end{bmatrix} = \begin{bmatrix} r^*(0) & r^*(1) & \cdots & r^*(p-1) \\ r(1) & r(0) & & \vdots \\ \vdots & & \ddots & r^*(1) \\ r(p-1) & \cdots & r(1) & r(0) \end{bmatrix} \tag{3.125}$$

Note that the $\boldsymbol{A}_p$ matrix is Hermitian ($\boldsymbol{A}_p = \boldsymbol{A}_p^H$) and Toeplitz.

An important property of $\boldsymbol{A}_p$ matrix that will be useful is that it is positive semi-definite (p.s.d.) for all p. In order to prove this property, first, note that if the matrix $\boldsymbol{A}_p$ is p.s.d., then, $\boldsymbol{x}^H \boldsymbol{A}_p \boldsymbol{x} > 0 \quad \forall \boldsymbol{x} \in \Omega^p, \ \boldsymbol{x} \neq 0$ where Ω^p denotes the complex field with dimension p.

Define

$$\bar{\boldsymbol{x}}_n = \begin{bmatrix} x^*(n-1) \\ x^*(n-2) \\ \\ x^*(n-p) \end{bmatrix} \qquad \text{and} \quad \boldsymbol{B}_p = \bar{\boldsymbol{x}}_n \, \bar{\boldsymbol{x}}_n^H \qquad (3.126)$$

$$\Rightarrow \boldsymbol{B}_p(i,j) = x^*(n-i)x(n-j)$$

$$\Rightarrow E\{\boldsymbol{B}_p(i,j)\} = E\{x^*(n-i)x(n-j)\} = r(i-j) = r^*(j-i)$$

$$\Rightarrow E\{\boldsymbol{B}_p\} = \boldsymbol{A}_p$$

Multiplying A_p matrix with y^H from left and with y from right yields

$$\begin{aligned} \boldsymbol{y}^{\boldsymbol{H}} \boldsymbol{A}_p \, \boldsymbol{y} &= \boldsymbol{y}^H E\{\boldsymbol{B}_p\} \, \boldsymbol{y} \\ &= \boldsymbol{y}^H E\{\bar{\boldsymbol{x}}_n \, \bar{\boldsymbol{x}}_n^H\} \, \boldsymbol{y} \\ &= E\{(\boldsymbol{y}^H \bar{\boldsymbol{x}}_n)(\bar{\boldsymbol{x}}_n^H \, \boldsymbol{y})\} \\ &= E\{\left| \bar{\boldsymbol{x}}_n \, \boldsymbol{y} \right|^2\} \geq 0 \end{aligned} \qquad (3.127)$$

Equation (3.127) is valid for any $\boldsymbol{y} \in \Omega^p$, if $\boldsymbol{y} \neq 0$. Hence the proof.

The important result is that, for AR signals, $\boldsymbol{A_p}$ (autocovariance) matrix is positive semi-definite, i.e., $\boldsymbol{A}_p \geq 0$.

Another important fact will be useful is that if a matrix is positive definite then it is non-singular. This property can be shown by proof by contradiction.

Suppose there exists $\mathbf{x} \neq 0$ where $\mathbf{A}\mathbf{x} = 0 \Rightarrow \mathbf{x}^H \mathbf{A}\, \mathbf{x} = 0$. However, we know that $\mathbf{x}^H \mathbf{A}\, \mathbf{x} > 0$. This is a contradiction and the proof is complete.

Next we will consider how to solve Yule-Walker equations. First solve for $\boldsymbol{a} = \begin{bmatrix} a_1 \\ a_2 \\ \vdots \\ a_p \end{bmatrix}$. Omitting the first row of (3.123), we obtain,

$$\begin{bmatrix} r(1) \\ r(2) \\ \\ r(p) \end{bmatrix} + \begin{bmatrix} r(0) & r(-1) & \cdots & r(-p+1) \\ r(1) & r(0) & & r(-p+2) \\ \vdots & & \ddots & \vdots \\ r(p-1) & r(p-2) & \cdots & r(0) \end{bmatrix} \begin{bmatrix} a_1 \\ a_2 \\ \vdots \\ a_p \end{bmatrix} = \begin{bmatrix} 0 \\ 0 \\ \vdots \\ 0 \end{bmatrix} \tag{3.128}$$

$$\Leftrightarrow \quad \boldsymbol{y}_p + \boldsymbol{A}_p \boldsymbol{a} = 0 \tag{3.129}$$

If $\boldsymbol{A}_p$ is invertable,

$$\boldsymbol{a} = -\boldsymbol{A}_p^{-1} \boldsymbol{y}_p \tag{3.130}$$

Note that $\hat{\boldsymbol{A}}_p$ is not invertable for any $\{\hat{r}(k);\ k = 0,1,2,\cdots,p\}$.

An important property to ensure the invertibility of the $\hat{\boldsymbol{A}}_p$ matrix is that if $\{\hat{r}(k);\ k = 0,1,2,\cdots p\}$ are found via biased ACS estimator, then,

$$\boldsymbol{A}_p = \begin{bmatrix} \hat{r}(0) & \hat{r}(-1) & \cdots & \hat{r}(-p+1) \\ \hat{r}(1) & \hat{r}(0) & & \vdots \\ \vdots & & \ddots & \hat{r}(-1) \\ \hat{r}(p-1) & \cdots & \hat{r}(1) & \hat{r}(0) \end{bmatrix} = \begin{bmatrix} \hat{r}(0) & \hat{r}^*(1) & \cdots & \hat{r}^*(p-1) \\ \hat{r}(1) & \hat{r}(0) & & \vdots \\ \vdots & & \ddots & \hat{r}^*(1) \\ \hat{r}(p-1) & \cdots & \hat{r}(1) & \hat{r}(0) \end{bmatrix} \tag{3.131}$$

matrix is positive definite for any p and the solution is unique.

In order to prove this claim, remember the biased ACS estimator given by

$$\hat{r}^b(k) = \frac{1}{N} \sum_{n=k+1}^{N} x(n) x^*(n-k) \ , \qquad 0 \le k \le N-1$$

where negative lags for the ACS estimate are computed via the property

$$\hat{r}(-k) = \hat{r}^{\,*}(k) \ , \qquad k = 0,1,...,N-1$$

Define

$$\boldsymbol{X} = \begin{bmatrix} x(1) & 0 & 0 & 0 & \cdots & 0 \\ x(2) & x(1) & 0 & 0 & \dots & 0 \\ x(3) & x(2) & x(1) & 0 & \cdots & 0 \\ \vdots & \vdots & \vdots & \vdots & \vdots & \vdots \\ x(p-1) & x(p-2) & x(p-3) & x(p-4) & \cdots & 0 \\ x(p) & x(p-1) & x(p-2) & x(p-3) & \cdots & x(1) \\ x(p+1) & x(p) & x(p-1) & x(p-2) & \cdots & x(2) \\ \vdots & \vdots & & & \cdots & \vdots \\ x(N) & x(N-1) & & & \cdots & \vdots \\ 0 & x(N) & & & \cdots & \vdots \\ \vdots & \vdots & & & \cdots & x(N-1) \\ 0 & & & & \cdots & x(N) \end{bmatrix} \begin{matrix} \left.\begin{matrix} \\ \\ \\ \\ \end{matrix}\right\} (p-1) \text{ rows} \\ \left.\begin{matrix} \\ \\ \\ \\ \\ \\ \\ \\ \end{matrix}\right\} N \text{ rows} \end{matrix} \tag{3.132}$$

Notice that

$$N\,\boldsymbol{A}_{\boldsymbol{p}}^{H} = \boldsymbol{X}^{H}\boldsymbol{X} \tag{3.133}$$

and the columns of $\boldsymbol{X}$ are arranged as

$$\boldsymbol{X}(i,:) = \begin{bmatrix} 0 \\ 0 \\ \vdots \\ 0 \\ x(1) \\ x(2) \\ \vdots \\ x(N) \\ 0 \\ 0 \\ \vdots \\ 0 \end{bmatrix} \begin{matrix} \left.\begin{matrix} \\ \\ \\ \\ \end{matrix}\right\} (i-1)\,\text{rows} \\ \left.\begin{matrix} \\ \\ \\ \\ \end{matrix}\right\} N\,\text{rows} \\ \left.\begin{matrix} \\ \\ \\ \\ \end{matrix}\right\} (p-i)\,\text{rows} \end{matrix} \tag{3.134}$$

Note that

$$\frac{1}{N}\left\langle \boldsymbol{X}^*(i,:)\,\boldsymbol{X}(j,:)\right\rangle = \begin{cases} \dfrac{1}{N}\sum |x(n)|^2 & i=j \\ \dfrac{1}{N}\displaystyle\sum_{n=1}^{N-(i-j)} x^*(n)x(n+i-j) \;=\; \sum_{n=(i-j)+1}^{N} x(n)x^*(n-(i-j)) & \\ \qquad\qquad = \hat{r}(i-j) & i>j \\ \left(\dfrac{1}{N}\displaystyle\sum_{n=(j-i)+1}^{N} x(n)\,x^*(n-(j-i))\right) = \hat{r}(j-i) & i<j \end{cases} \tag{3.135}$$

Also, notice that

$$rank(\boldsymbol{X}) = p \quad if \quad \{x(1),..., x(N)\} \neq 0$$

and

$$\boldsymbol{X}^H\boldsymbol{X} \text{ is positive definite.}$$

So, the *null space* of $\mathbf{X}$ and $\boldsymbol{X}^H\boldsymbol{X}$ is empty, i.e.,

$$N(\boldsymbol{X}) = N(\boldsymbol{X}^H\boldsymbol{X}) = \{0\}$$

So,

$$\boldsymbol{X}^H\boldsymbol{X} \text{ is invertable}$$

Hence,

$$\hat{\boldsymbol{A}}_{\boldsymbol{p}} \text{ is invertable.}$$

Yule-Walker method can be summarized as follows: First, find the biased ACS estimate, $\{\hat{r}(k);\, k=0,1,2,\cdots p\}$. Then, solve for $\hat{\boldsymbol{a}} = -\hat{\boldsymbol{A}}_{\boldsymbol{p}}^{-1}\,\hat{\boldsymbol{y}}_{\boldsymbol{p}}$. Then compute the noise power as

$$\sigma_e^2 = \hat{r}(0) + \sum_{i=1}^{p} \hat{\boldsymbol{a}}_{\boldsymbol{i}}\,\hat{\boldsymbol{r}}^*_{\boldsymbol{i}}$$

Finally, the spectral estimate is computed via

$$\phi(w) = \frac{\sigma_e^2}{\left|\hat{A}(w)\right|^2}$$

3.3.2.2. Least – Squares Method. If *x(n)* is an autoregressive process of order *p*, then we have

$$x(n)+\sum_{k=1}^{p} a_k\, x(n-k) = e(n)$$

Interpreting *e(n)* as the prediction error, the problem of estimating the AR coefficients turns out to be a simple minimization problem where the cost function is

$$C(x) = \sum_{n=N_1}^{N_2} \left| e(n) \right|^2 = \sum_{n=N_1}^{N_2} \left| x(n) + \sum_{k=1}^{p} a_k\, x(n-k) \right|^2 \tag{3.136}$$

$$= \left\| \begin{bmatrix} x(N_1) \\ x(N_1+1) \\ \\ x(N_2) \end{bmatrix} + \begin{bmatrix} x(N_1-1) & \cdots & x(N_1-p) \\ x(N_1) & \cdots & x(N_1-p+1) \\ \vdots & \ddots & \vdots \\ x(N_2-1) & \cdots & x(N_2-p) \end{bmatrix} \begin{bmatrix} a_1 \\ a_2 \\ \vdots \\ a_p \end{bmatrix} \right\|^2 \tag{3.137}$$

$$= \left\| \boldsymbol{x} + \boldsymbol{X}\boldsymbol{a} \right\|^2 \tag{3.138}$$

The vector that minimizes $C(x)$ is

$$\hat{\boldsymbol{a}}_{\boldsymbol{LS}} = -(\boldsymbol{X}^*\boldsymbol{X})^{-1}(\boldsymbol{X}\boldsymbol{x}) \tag{3.139}$$

where, for $N_1 = 1$, $N_2 = N + p$, and

$$\boldsymbol{x} = \begin{bmatrix} x(1) \\ x(2) \\ \vdots \\ x(p) \\ x(p+1) \\ x(p+2) \\ \vdots \\ x(N) \\ 0 \\ 0 \\ \vdots \\ 0 \end{bmatrix} \begin{matrix} \left.\begin{matrix} \\ \\ \\ \\ \end{matrix}\right\} p \\ \left.\begin{matrix} \\ \\ \\ \\ \end{matrix}\right\} N-p-1 \\ \left.\begin{matrix} \\ \\ \\ \\ \end{matrix}\right\} p \end{matrix} \qquad \boldsymbol{X} = \begin{bmatrix} 0 & 0 & \cdots & 0 \\ x(1) & 0 & & \\ \vdots & \ddots & \ddots & \vdots \\ x(p-1) & x(p-2) & \cdots & 0 \\ x(p) & x(p-1) & \cdots & x(1) \\ x(p+1) & & & x(2) \\ \vdots & & & \vdots \\ x(N-1) & X(N-2) & \cdots & x(N-p) \\ X(N) & x(N-1) & \cdots & X(N-p+1) \\ 0 & X(N) & \cdots & x(N-p+2) \\ \vdots & \ddots & \ddots & \\ 0 & 0 & 0 & x(N) \end{bmatrix} \begin{matrix} \left.\begin{matrix} \\ \\ \\ \\ \end{matrix}\right\} p \\ \left.\begin{matrix} \\ \\ \\ \\ \end{matrix}\right\} N-p-1 \\ \left.\begin{matrix} \\ \\ \\ \\ \end{matrix}\right\} p \end{matrix} \tag{3.140}$$

There are some common choices for N_1 and N_2. The methods will be given briefly and the details will be skipped.

Autocorrelation method assumes that data prior to *x(1)* and *x(N)* are to be zero and $N_1=1$ and $N_2=N+p$.

Covariance LS method assumes that $N_1=p+1$ and $N_2=N$. Only the data that is explicitly available is used, no assumption about data outside the observed data segment. This choice removes the first and last *p* rows from $\boldsymbol{X}$ and $\boldsymbol{x}$.

Pre-windowing method assumes that $x(n)=0$ for $n<0$ and use data up to x(*N*), so, $N_1=1$ and $N_2=N$.

Post-window method begins with $N_1=p+1$ and assumes that data after *N* are equal to zero.

Although LS Method is more accurate than YW method, it may be unstable whereas Yule-Walker method has been guaranteed to be stable for medium or small *N*. For large *N*, the difference between Yule-Walker and LS autoregressive coefficient estimates are quiet small.

3.3.3. Moving Average Signals

There is a limited interest in MA signals since MA model is appropriate to model spectrum which has sharp nulls and broad peaks which is rarely encountered in engineering and MA parameter estimation is a nonlinear parameter estimation problem. Since MA model will not be an useful tool for our application where we will observe narrow peaks, MA model will not be explained.

3.3.4. ARMA Signals

Neither AR (all-pole) nor MA(all-zero) model can model the spectra with sharp peaks and deep nulls. ARMA (pole-zero) model is an useful tool to model such spectra. Although there exists no reliable and statistically accurate algorithms, modified Yule-Walker and two-stage least squares are the mostly used ARMA spectral estimators.

3.3.4.1. Modified Yule-Walker Method. This method is a two stage procedure where in the first stage, AR coefficients are obtained using equation (3.117) and in the second stage MA coefficients are computed using the AR coefficients computed in the first stage and ACS estimates.

Our goal in the first stage is to estimate the AR coefficients. A procedure similar to the solution YW equations will be followed in this stage.

From equation (3.117), we have

$$r(k) + \sum_{i=1}^{p} a_i \, r(k-i) = 0 \qquad for\ k > q$$

Rewriting (3.117) in matrix form for $k = q+1, q+2, \cdots, q+M$ gives

$$\begin{bmatrix} r(q+1) & r(q) & \cdots & r(q-p+1) \\ r(q+2) & r(q+1) & \cdots & r(q-p+2) \\ \vdots & \vdots & \ddots & \vdots \\ r(q+M) & r(p+M-1) & \cdots & r(q-p+M) \end{bmatrix} \begin{bmatrix} 1 \\ a_1 \\ \vdots \\ a_p \end{bmatrix} = \begin{bmatrix} 0 \\ 0 \\ \vdots \\ 0 \end{bmatrix} \tag{3.141}$$

Rewriting (3.141) yields

$$\begin{bmatrix} r(q) & r(q-1) & \cdots & r(q-p+1) \\ r(q+1) & r(q) & \cdots & r(q-p+2) \\ \vdots & \vdots & \ddots & \vdots \\ r(q+M-1) & r(p+M-2) & \cdots & r(q-p+M) \end{bmatrix} \begin{bmatrix} a_1 \\ a_2 \\ \vdots \\ a_p \end{bmatrix} = - \begin{bmatrix} r(q+1) \\ r(q+2) \\ \vdots \\ r(q+M) \end{bmatrix} \tag{3.142}$$

These equations are called *Modified Yule Walker equations* if *M=p* and *over-determined modified Yule Walker equations* if *M>p*. Replacing *{r(k)}'s* by the estimates yields

$$\begin{bmatrix} \hat{r}(q) & \hat{r}(q-1) & \cdots & \hat{r}(q-p+1) \\ \hat{r}(q+1) & \hat{r}(q) & \cdots & \hat{r}(q-p+2) \\ \vdots & \vdots & \ddots & \vdots \\ \hat{r}(q+M-1) & \hat{r}(p+M-2) & \cdots & \hat{r}(q-p+M) \end{bmatrix} \begin{bmatrix} a_1 \\ a_2 \\ \vdots \\ a_p \end{bmatrix} = - \begin{bmatrix} \hat{r}(q+1) \\ \hat{r}(q+2) \\ \vdots \\ \hat{r}(q+M) \end{bmatrix} \tag{3.143}$$

This system of *p* equations with *p* unknowns can be solved via

$$\min_{(a_1 \cdots a_p)} \left\| \begin{bmatrix} \hat{r}(q) & \hat{r}(q-1) & \cdots & \hat{r}(q-p+1) \\ \hat{r}(q+1) & \hat{r}(q) & \cdots & \hat{r}(q-p+2) \\ \vdots & \vdots & \ddots & \vdots \\ \hat{r}(q+M-1) & \hat{r}(p+M-2) & \cdots & \hat{r}(q-p+M) \end{bmatrix} \begin{bmatrix} a_1 \\ a_2 \\ \vdots \\ a_p \end{bmatrix} + \begin{bmatrix} \hat{r}(q+1) \\ \hat{r}(q+2) \\ \vdots \\ \hat{r}(q+M) \end{bmatrix} \right\| \tag{3.144}$$

$$\min_{(a_1 \cdots a_p)} \left\| \hat{\boldsymbol{R}} \boldsymbol{a} + \hat{\boldsymbol{r}} \right\| \tag{3.145}$$

where the last equation can be solved via least squares method, i.e.,

$$\hat{\boldsymbol{a}}_{\boldsymbol{LS}} = -(\hat{\boldsymbol{R}}^* \hat{\boldsymbol{R}})^{-1} (\hat{\boldsymbol{R}}^* \hat{\boldsymbol{r}}) \tag{3.146}$$

It has been shown that the statistical accuracy of the AR coefficient estimates are good if the condition number of the matrix $\hat{\boldsymbol{R}}$ in (3.144) is small. So, *M* should be selected so as to make $\hat{\boldsymbol{R}}$ matrix reasonably well conditioned. In the case of narrowband signals, for slowly decaying covariance sequences, the columns of the $\hat{\boldsymbol{R}}$ matrix are nearly linearly dependent. Hence, the condition number $\hat{\boldsymbol{R}}$ is quite high, so, in such a case, *M* should be increased in order to lower the condition number to a reasonable level.

Our goal in the second stage is to estimate the MA coefficients. The AR coefficients computed in the first stage will be used in this stage.

From the ARMA model, we have,

$$x(n) = \frac{B(z)}{A(z)} e(n) \quad \Leftrightarrow x(n)\, A(z) = e(n)\; B(z)$$

and for the MA signal, ($A(w)=1$) , we have,

$$\phi(w) = \left|\frac{B(w)}{A(w)}\right|^2 \sigma^2 = \left|B(w)\right|^2 \sigma^2 = \sum_{k=-q}^{q} \beta_k\, e^{-jwk} \tag{3.147}$$

where

$$\beta_k = E\{[B(z)e(n)][B(z)e(n-k)]^*\} \tag{3.148}$$

$$= E\{[A(z)x(n)][A(z)x(n-k)]^*\} \tag{3.149}$$

$$= \sum_{j=0}^{p}\sum_{i=0}^{p} a_j\, a_i^*\, E\{x(n-j)\, x^*(n-k-i)\} \tag{3.150}$$

$$= \sum_{j=0}^{p}\sum_{i=0}^{p} a_j\, a_i^*\, r(k+i-j) \quad , \quad k = 0, ..., q \tag{3.151}$$

Replacing theoretical AR and ACS values with estimates yields

$$\hat{\beta}_k = \sum_{j=0}^{p}\sum_{i=0}^{p} \hat{a}_j\, \hat{a}^*_i\, \hat{r}(k+i-j)\,, \qquad k = 0,...,q \tag{3.152}$$

where

$$\hat{\beta}_k = \hat{\beta}^*_{-k} \quad , \qquad k = -1,...,-q \tag{3.153}$$

So, the ARMA spectrum estimate is

$$\hat{\phi}(w) = \frac{\sum_{k=-q}^{q} \hat{\beta}_k\, e^{-jwk}}{\left|\hat{A}(w)\right|^2} \tag{3.154}$$

Note that the numerator in (3.154) is not guaranteed to be positive for all *w* values, so this approach may lead to negative ARMA spectral estimates.

3.3.4.2. Two-Stage Least-Squares Method. Recall the *ARMA(p,q)* model given in (3.107)

$$x(n) + \sum_{i=1}^{p} a_i\, x(n-i) = \sum_{j=0}^{q} b_j\, e(n-j) \qquad (a_0 = b_0 = 1)$$

Our goal is to find the $\{a_k\}_{k=1}^{p}$ and $\{b_k\}_{k=1}^{q}$, hence the PSD. In the first stage, we assume that we are given *e(n)* and solve for AR and MA coefficients and in the second stage we find a reliable estimate of *e(n)*.

Rewriting (3.107) in matrix notation yields

$$x(n) + [\, x(n-1),...,x(n-p) \mid -e(n-1),...,-e(n-q)\,] \begin{bmatrix} a_1 \\ \vdots \\ a_p \\ b_1 \\ \vdots \\ b_q \end{bmatrix} = e(n) \tag{3.155}$$

Rewriting (3.155) for $n = L+1,...,N$ for some $L > \max(p,q)$ gives

$$\boldsymbol{z} + \boldsymbol{Z}\boldsymbol{\theta} = \boldsymbol{e} \tag{3.156}$$

where

$$Z = \left[\begin{array}{cccc|cccc} x(L) & x(L-1) & \cdots & x(L-p+1) & -e(L) & -e(L) & \cdots & -e(L) \\ x(L+1) & x(L) & \cdots & x(L-p+2) & -e(L+1) & -e(L) & \cdots & -e(L) \\ x(L+2) & x(L+1) & \cdots & x(L-p+3) & -e(L+2) & -e(L) & \cdots & -e(L) \\ \vdots & \vdots & & & \vdots & \vdots & & \vdots \\ \vdots & \vdots & & & \vdots & \vdots & & \vdots \\ x(N-1) & x(N-2) & & x(N-p) & -e(L) & -e(L) & \cdots & -e(L) \end{array}\right] \tag{3.157}$$

$$\boldsymbol{z} = \begin{bmatrix} x(L+1) \\ x(L+2) \\ x(L+3) \\ \vdots \\ \vdots \\ x(N) \end{bmatrix}, \qquad \boldsymbol{e} = \begin{bmatrix} e(L+1) \\ e(L+2) \\ e(L+3) \\ \vdots \\ \vdots \\ e(N) \end{bmatrix}, \qquad \boldsymbol{\theta} = \begin{bmatrix} a_1 \\ \vdots \\ a_p \\ b_1 \\ \vdots \\ b_q \end{bmatrix} \tag{3.158}$$

Assuming we know $\{e(n)\}$, (3.156) can be solved as

$$\hat{\boldsymbol{\theta}}_{\boldsymbol{LS}} = -(\boldsymbol{Z}^{*}\boldsymbol{Z})^{-1}(\boldsymbol{Z}^{*}\boldsymbol{z}) \tag{3.159}$$

However, $\{e(n)\}$ are not known. They will be estimated as follows:

Recall the *ARMA(p,q)* model

$$X(z) = \frac{B(z)}{A(z)}E(z)$$

where

$$A(z)=\sum_{i=0}^{p} a_i z^{-i} \quad \text{and} \quad B(z)=\sum_{i=0}^{q} b_i z^{-i}$$

So, we have,

$$E(z) = \frac{A(z)}{B(z)}X(z)=C(z)X(z) \quad \Leftrightarrow \quad e(n)=C(z)x(n)$$

Assuming the ARMA model is minimum phase, *C(z)* can be written as

$$C(z) = 1 + \alpha_1 z^{-1} + \alpha_2 z^{-2} + ... \tag{3.160}$$

where $\{\alpha_k\}$ can be obtained using YW or LS method from AR models. However, AR models can be solved via YW or LS only for finite orders, so we need to truncate the order to some constant *K*. Solving the truncated AR model via YW or LS method gives the *e(n)* which can be used in the first stage two estimate the AR and MA coefficients.

The spectral estimate is guaranteed to be positive for all frequencies, by construction. Because of the truncation of the AR model, the two-stage LS estimate is biased. The bias can be decrased by choosing *K* sufficiently large; however, *K* should not be too large with respect to *N*, otherwise, the accuracy of the $\hat{\boldsymbol{\theta}}$ will decrease.

3.4. Parametric Methods for Line Spectra

3.4.1. Introduction

Parametric (model-based) methods considered in this section are primarily used for estimation of the parameters of sinusoidal signals observed in an additive white noise. Eigen analysis is used for partitioning the eigenvectors and eigenvalues, of the covariance matrix of a noisy signal, into two subspaces: noise and signal subspace. This decomposition forms the basis of the methods considered in this section.

In radar applications, we frequently encounter nearly sinusoidal components. So, a method that can model the spectra with sinusoids in noise will be valuable.

Let,

$$y(n)=x(n)+e(n) \quad , \qquad n=0,1,...,N \tag{3.161}$$

and let *x(n)* be the noise-free complex valued sinusoidal signal, i.e.,

$$x(n)=\sum_{k=1}^{p} x_k(n)=\sum_{k=1}^{p}\alpha_k e^{j(w_k n+\varphi_k)} \tag{3.162}$$

where p is the number of sinusoidal signals and $\{\alpha_k\},\{w_k\},\{\varphi_k\}$ are the amplitudes, angular frequencies and phases, respectively.

We make the following assumptions for the data model in (3.162)

1) $\alpha_k>0$; $w_k\in[-\pi,\pi]$. Otherwise, model ambiguity may come up since

$$\alpha_k \exp[j(w_k n+\varphi_k)]=-\alpha_k \exp[j(w_k n+\varphi_k+\pi)]$$

2) $\varphi_k's$ are independent random variables with uniform distribution between $-\pi \; and \; \pi$.

3) $\{e(n)\}$ is complex-valued circular white noise with power σ^2, i.e.,

$$E\{e(n)e(m)\}=0$$
$$E\{e(n)e^{*}(m)\}=\delta_{n,m}\sigma^2, \qquad \forall n,m$$

3.4.1.1. Covariance Function & PSD. Our goal is to find expressions for $r_y(k)$ and $\phi_y(w)$ for the signal model

$$y(n)=x(n)+e(n) \quad \text{where} \quad x(n)=\sum_{k=1}^{p} x_k(n)=\sum_{k=1}^{p}\alpha_k\, e^{j(w_k n+\varphi_k)}$$

Several useful corollaries and their proofs will be given before proceeding with the details of the line spectral methods. First one and the mostly used corollary is given as follows:

$$E\{e^{j\varphi_k}\, e^{-j\varphi_l}\}=\delta_{k,l} \tag{3.163}$$

Following equations describe the proof of this claim.

$$if\ k=l,\quad E\{e^{j\varphi_k}\, e^{-j\varphi_l}\}=1 \tag{3.164}$$

$$if\ k\neq l,\quad E\{e^{j\varphi_k}\, e^{-j\varphi_l}\}=E\{e^{j\varphi_k}\}E\{e^{-j\varphi_l}\} \tag{3.165}$$

where

$$E\{e^{j\varphi_k}\}=\int_{-\pi}^{\pi} e^{ju}\,\frac{1}{2\pi}\,du=\frac{1}{2\pi}\frac{1}{j}\,e^{ju}\Big|_{-\pi}^{\pi}=\frac{1}{2\pi j}(e^{j\pi}-e^{-j\pi})=\frac{1}{2\pi j}2j\,Sin(\pi)=0$$

$$\Rightarrow E\{e^{j\varphi_k}\, e^{-j\varphi_l}\}=\delta_{k,l}$$

Another corollary that will often be used is given as follows:

$$E\{x_p(n)\,x_r^*(n-k)\}=\alpha_p^2\, e^{jw_p k}\,\delta_{p,r} \tag{3.166}$$

The proof of this claim is shown by directly replacing the expressions of the signals, i.e.,

$$\begin{aligned}
E\{x_p(n)\,x_r^*(n-k)\} &= E\{\alpha_p\, e^{j(w_p n+\varphi_p)}\,\alpha_r\, e^{-j(w_r(n-k)+\varphi_r)}\}\\
&= \alpha_p\,\alpha_r\, e^{jw_p n}\, e^{jw_p(n-k)}\, E\{e^{j\varphi_p}\, e^{-j\varphi_r}\}\\
&= \alpha_p^2\, e^{jw_p n}\, e^{jw_p(n-k)}\,\delta_{p,r} \quad (if\ p=r)\\
&= \alpha_p^2\, e^{jw_p k}\,\delta_{p,r}
\end{aligned}$$

Finally, the expression of ACS of the noisy signal is given as

$$r_y(k)=E\{y(n)\,y^*(n-k)\}=\sum_{s=1}^{p}\alpha_s^2\exp(j\,w_s k)\;+\;\sigma_e^2\,\delta_{k,0} \tag{3.167}$$

Notice that the proof of this claim uses the second corollary.

$$r_y(k) = E\{y(n)\, y^*(n-k)\}$$

$$= E\{[\,(\sum_{s=1}^{p} x_s(n)) + e(n)]\,[(\sum_{r=1}^{p} x_r{}^*(n-k)) + e^*(n-k)]\}$$

$$= \sum_{s=1}^{p}\sum_{r=1}^{p} E\{x_s(n)\, x_r{}^*(n-k)\} + \sum_{s=1}^{p} E\{x_s(n)\; e^*(n-k)\;\}$$

$$+ \sum_{r=1}^{p} E\{x_r{}^*(n-k)\, e(n)\} \;+\; E\{e(n)e(n-k)\}$$

Since $E\{e(n)\} = 0$ and $e(n)$ is indepedent of $x(n)$

$$r_y(k) = \sum_{s=1}^{p}\sum_{r=1}^{p} E\{x_s(n)\, x_r{}^*(n-k)\} + 0 + 0 + \delta_{k,0}\,\sigma_e^2$$

Using (3.166), we get,

$$r_y(k) = \sum_{s=1}^{p}\sum_{r=1}^{p} \alpha_s^2 \exp(j\, w_s k)\,\delta_{s,r} \;+ \delta_{k,0}\,\sigma_e^2$$

$$r_y(k) = \sum_{s=1}^{p} \alpha_s^2 \exp(j\, w_s k) + \delta_{k,0}\,\sigma_e^2$$

From the definition of PSD,

$$\phi_y(w) = DTFT\,\{r_y(k)\}$$

$$= DTFT\,\{\sum_{s=1}^{p} \alpha_s^2 \exp(j\, w_s k) + \delta_{k,0}\,\sigma_e^2\,\}$$

$$= 2\pi \sum_{s=1}^{p} \alpha_s^2\, \delta(w - w_s) + \sigma_e^2 \qquad (3.168)$$

The PSD in (3.168) is depicted in figure 3.14. Noise floor is equal to noise power σ_e^2 and the magnitude of the impulses is $2\pi\alpha_k^2$ *where* $k = 1,..., p$. Because of its appearance, the PSD in (3.168) is called a *discrete* or *line spectra*.

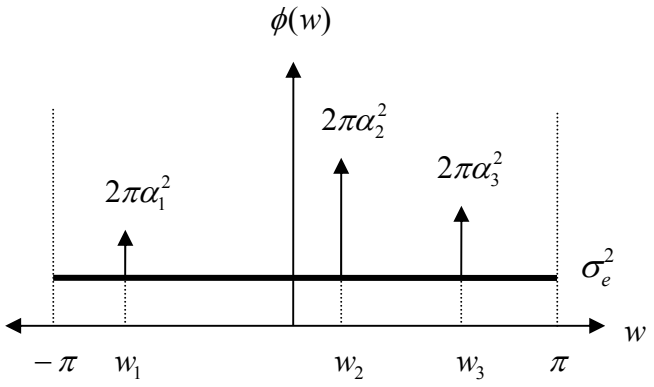

Figure 3.14. PSD of complex sinusoidal signals in noise

Our goal is to estimate the parameters $\{w_k\}, \{\alpha_k\}, \{\varphi_k\}, \sigma_e^2$ in the signal model. It should be noted that the parameter that should be primarily concentrated on is the frequencies of the sinusoids since the estimation of other parameters knowing frequencies is a simple linear regression problem, i.e.,

Define

$$\beta_k = \alpha_k e^{j\varphi_k} \tag{3.169}$$

Therefore, (3.161) can be rewritten as

$$y(n) = \sum_{k=1}^{p} \beta_k e^{jw_k n} + e(n) \ , \qquad n = 0,1,..., N \tag{3.170}$$

Rewriting (3.170) in matrix notation yields

$$\begin{bmatrix} y(1) \\ y(2) \\ \vdots \\ y(N) \end{bmatrix} = \begin{bmatrix} e^{jw_1} & e^{jw_2} & \cdots & e^{jw_p} \\ e^{j2w_1} & e^{j2w_2} & \cdots & e^{j2w_p} \\ \vdots & \vdots & \ddots & \vdots \\ e^{jNw_1} & e^{jNw_2} & \cdots & e^{jNw_p} \end{bmatrix} \begin{bmatrix} \beta_1 \\ \beta_2 \\ \vdots \\ \beta_p \end{bmatrix} + \begin{bmatrix} e(1) \\ e(2) \\ \vdots \\ e(N) \end{bmatrix} \quad \Leftrightarrow \quad \boldsymbol{y} = \boldsymbol{A}\boldsymbol{\beta} + \boldsymbol{e} \tag{3.171}$$

Note that if β_k is known, $\alpha_k\,(>0)$ and φ_k can be readily found by

$$\alpha_k = \text{mag}(\beta_k) \tag{3.172}$$

$$\varphi_k = \arg(\beta_k) \tag{3.173}$$

Solving the minimization problem

$$\min_{(\beta_1,\beta_2\cdots\beta_p)} \left\| \begin{bmatrix} y(1) \\ y(2) \\ \vdots \\ y(N) \end{bmatrix} - \begin{bmatrix} e^{jw_1} & e^{jw_2} & \cdots & e^{jw_p} \\ e^{j2w_1} & e^{j2w_2} & \cdots & e^{j2wp} \\ \vdots & \vdots & \ddots & \vdots \\ e^{jNw_1} & e^{jNw_2} & \cdots & e^{jNw_p} \end{bmatrix} \begin{bmatrix} \beta_1 \\ \beta_2 \\ \vdots \\ \beta_p \end{bmatrix} \right\| \tag{3.174}$$

by LS metod gives

$$\hat{\boldsymbol{\beta}}_{\boldsymbol{LS}} = (\boldsymbol{A}^* \boldsymbol{A})^{-1} \boldsymbol{A}^* \boldsymbol{y} \tag{3.175}$$

3.4.1.2. Models of Sinusoidal Signals in Noise. Frequency estimation methods represented in this section rely on two different models for the noisy sinusoidal signal *y(n)*.

The first model, ARMA model, is a very special form. All its poles and zeros are located on the unit circle. Also, its AR and MA parts are identical. For the noisy sinusoidal signal model in (3.161), the ARMA model is given as

$$A(z)\, y(n) = A(z)\, e(n) \tag{3.176}$$

where

$$A(z) = \prod_{k=1}^{p} (1 - e^{jw_k} z^{-1}) \tag{3.177}$$

The second equality follows from the fact that

$$A(z)\, x(n) = 0 \tag{3.178}$$

Since

$$(1 - e^{jw_k} z^{-1})\, x_k(n) = 0 \tag{3.179}$$

Hence, $(1-e^{jw_k}z^{-1})$ is an annihilating filter for the k^{th} component of *x(n)*. $A(z)x(n)=0$ follows from the fact that any filter that has zeros at frequencies $\{w_k\}$ is an annihilating filter for *x(n)* and the PSD of *x(n)* has p spectral lines located at $\{w_k\}_{k=1}^{p}$.

The second method is the covariance model. In order to explain the model, define the $a(w)$ vector and $\boldsymbol{A}$ matrix as

$$a(w)=[1\ e^{-jw}\ \ e^{-j2w}\ \ ....\ \ e^{-j(m-1)w}]^T \qquad (m\,x\,1) \tag{3.180}$$

$$\boldsymbol{A} = [a(w_1)\ \ a(w_2)\ ...\ \ a(w_p)] \qquad (m\,x\,p) \tag{3.181}$$

The Vandermonde matrix $\boldsymbol{A}$ has the following rank property :

$$rank(\boldsymbol{A})=p \qquad \text{if } m\geq p \text{ and } w_i\neq w_j \text{ for } i\neq j \tag{3.182}$$

This claim can be easily proved by contradiction. It is sufficient to show that first p rows are linearly independent, or, A is non-singular, i.e., it is invertable. Suppose $\boldsymbol{A}$ is not non-singular, i.e., there exists some $\boldsymbol{\beta}\in\Omega^m$, where Ω^m represents *m*- dimensional field, such that,

$$\boldsymbol{\beta}\,\boldsymbol{A}=0 \qquad \text{and } \boldsymbol{\beta}\neq 0 \tag{3.183}$$

where

$$\boldsymbol{\beta}=[\beta_0\ \ \beta_1\ \ \beta_2\ ...\ \ \beta_{p-1}] \tag{3.184}$$

Define

$$z_i=e^{jw_i}\ ,\quad i=0,1,...,p-1 \tag{3.185}$$

So, the multiplication of β with any column of A can be written as

$$P_\beta(z_i)=\beta_0+\beta_1 z_i+.....+\beta_{n-1}z_i^{p-1}=0 \tag{3.186}$$

Note that the polynomial $P_\beta(z_i)$ has p distinct non-zero roots. However, $P_\beta(z_i)$ is a polynomial of order *(p-1)* and it can have at most *(p-1)* non-zero roots. So, this is a contradiction, and hence the proof.

Define

$$\tilde{y}(n) = \begin{bmatrix} y(n) \\ y(n-1) \\ \vdots \\ y(n-m+1) \end{bmatrix} = \boldsymbol{A}\tilde{x}(n) + \tilde{e}(n) \tag{3.187}$$

where

$$\tilde{x}(n) = [\, x_1(n) \;\; x_2(n) \;\; x_p(n)]^T \tag{3.188}$$

$$\tilde{e}(n) = [\, e(n) \;\; e(n-1) \;\; e(n-m+1)]^T \tag{3.189}$$

The covariance matrix of $\tilde{y}(n)$ can be computed as

$$\boldsymbol{R} = E\{\tilde{y}(n)\, \tilde{y}^*(n)\} \tag{3.190}$$

$$= E\{[\boldsymbol{A}\tilde{x}(n) + \tilde{e}(n)][\boldsymbol{A}\tilde{x}(n) + \tilde{e}(n)]^*\} \tag{3.191}$$

$$= E\{[\boldsymbol{A}\tilde{x}(n) + \tilde{e}(n)][\, \tilde{x}^*(n)\boldsymbol{A}^* + \tilde{e}^*(n)]\} \tag{3.192}$$

$$= E\{\, [\boldsymbol{A}\underbrace{\tilde{x}(n)\, \tilde{x}^*(n)}_{P}\boldsymbol{A}^* + \boldsymbol{A}\underbrace{\tilde{x}(n)\tilde{e}^*(n)}_{0} + \underbrace{\tilde{e}(n)\, \tilde{x}^*(n)}_{0}\boldsymbol{A}^* + \underbrace{\tilde{e}(n)\tilde{e}^*(n)}_{\sigma^2 I}\} \tag{3.193}$$

$$= \boldsymbol{A}\boldsymbol{P}\boldsymbol{A}^* + \sigma^2\boldsymbol{I} \tag{3.194}$$

where

$$\boldsymbol{P} = \begin{bmatrix} \alpha_1^2 & & 0 \\ & \ddots & \\ 0 & & \alpha_p^2 \end{bmatrix} \tag{3.195}$$

As will be shown in the following sections, the eigenstructure of $\boldsymbol{R}$ contains complete information on the frequencies $\{w_k\}$.

3.4.2. Higher Order Yule Walker Method

Higher Order Yule-Walker method is derived from the ARMA model of sinusoidal signal. If the polynomial *A(z)* in ARMA model is multiplied by $\overline{A}(z)$ with degree *L-p* , then the higher order ARMA model for the sinusoidal data is given by

$$y(n)+b_1\,y(n-1)+\ldots+b_L\,y(n-L)=e(n)+b_1\,e(n-1)+\ldots+b_L\,e(n-L) \tag{3.196}$$

$$\Rightarrow B(z)y(n)=B(z)e(n) \tag{3.197}$$

where

$$B(z)=1+\sum_{k=1}^{L} b_k\,z^{-k}=A(z)\,\overline{A}(z) \tag{3.198}$$

Rewriting (3.196) in matrix notation yields

$$\begin{bmatrix} y(n) & y(n-1) & \ldots & y(n-L)\end{bmatrix}\begin{bmatrix}1\\ \boldsymbol{b}\end{bmatrix}=e(n)+\ldots.+b_L\,e(n-L) \tag{3.199}$$

Multiplying (3.199) with $\begin{bmatrix} y^*(n-L-1) & \ldots & y^*(n-L-m)\end{bmatrix}^T$ and taking the expectation leads to

$$\boldsymbol{\Gamma}^*\begin{bmatrix}1\\ \boldsymbol{b}\end{bmatrix}=0 \tag{3.200}$$

where

$$\boldsymbol{\Gamma}=E\left\{\begin{bmatrix} y(n-L-1)\\ \vdots\\ y(n-L-m)\end{bmatrix}\begin{bmatrix} y^*(n) & \cdots & y(n-L)\end{bmatrix}\right\} \tag{3.201}$$

Equation (3.200) can also be written as

$$\begin{bmatrix} r(L) & \cdots & r(1) \\ \vdots & \ddots & \vdots \\ r(L+m-1) & \cdots & r(m) \end{bmatrix} \boldsymbol{b} = -\begin{bmatrix} r(L+1) \\ \vdots \\ r(L+m) \end{bmatrix} \tag{3.202}$$

The equation (3.202) is similar to the Yule-Walker system of equations encountered in AR signals, so, this set of equations associated with the noisy sinusoidal signal model is said to form a HOYW system.

Replacing the theoretical covariances by the the sample covariances yields

$$\begin{bmatrix} \hat{r}(L) & \cdots & \hat{r}(1) \\ \vdots & \ddots & \vdots \\ \hat{r}(L+m-1) & \cdots & \hat{r}(m) \end{bmatrix} \hat{\boldsymbol{b}} \cong -\begin{bmatrix} \hat{r}(L+1) \\ \vdots \\ \hat{r}(L+m) \end{bmatrix} \tag{3.203}$$

Define Ψ as the *mxL* covariance matrix in HOYW system and similarly $\hat{\boldsymbol{\Psi}}$ as the approximate covariance matrix in (3.203), i.e.,

$$\boldsymbol{\Psi} = \begin{bmatrix} r(L) & \cdots & r(1) \\ \vdots & \ddots & \vdots \\ r(L+m-1) & \cdots & r(m) \end{bmatrix} \tag{3.204}$$

and

$$\hat{\boldsymbol{\Psi}} = \begin{bmatrix} \hat{r}(L) & \cdots & \hat{r}(1) \\ \vdots & \ddots & \vdots \\ \hat{r}(L+m-1) & \cdots & \hat{r}(m) \end{bmatrix} \tag{3.205}$$

It can be shown that

$$rank(\boldsymbol{\Psi}) = p \qquad \text{for } L, m \geq p \tag{3.206}$$

On the other hand, the matrix $\hat{\boldsymbol{\Psi}}$ has full rank (almost surely)

$$rank(\hat{\boldsymbol{\Psi}}) = \min(m, L) \tag{3.207}$$

owing to the random errors in $\{\hat{r}(k)\}$. Hence, the linear system (3.203) is expected to be ill-conditioned. So, any LS method that estimates the $\hat{\boldsymbol{b}}$ directly form (3.203) has very poor accuracy. A priori rank information can be used to overcome this difficulty.

Let

$$\hat{\boldsymbol{\Psi}} = \boldsymbol{U}\,\boldsymbol{\Sigma}\,\boldsymbol{V}^{*} = [\underbrace{\boldsymbol{U}_1}_{p}\ \underbrace{\boldsymbol{U}_2}_{m-p}]\begin{bmatrix}\boldsymbol{\Sigma}_1 & 0\\ 0 & \boldsymbol{\Sigma}_2\end{bmatrix}\begin{bmatrix}\boldsymbol{V}_1^{*}\\ \boldsymbol{V}_2^{*}\end{bmatrix}\begin{matrix}\}\,p\\ \}\,L-p\end{matrix} \tag{3.208}$$

denote the Singular Value Decomposition (SVD) of $\hat{\boldsymbol{\Psi}}$. In (3.208), $\boldsymbol{U}$ is an *m x m* unitary matrix, $\boldsymbol{V}$ is an *LxL* unitary matrix and $\boldsymbol{\Sigma}$ is and *mxL* diagonal matrix.

Since $\hat{\boldsymbol{\Psi}}$ is close to a rank-*p* matrix, $\boldsymbol{\Sigma}_2$ should be close to zero. Hence, the best (in the Frobenius-norm sense) rank-*p* approximation of $\hat{\boldsymbol{\Psi}}$ is given by

$$\hat{\boldsymbol{\Psi}}_p = \boldsymbol{U}_1\,\boldsymbol{\Sigma}_1\,\boldsymbol{V}_1 \tag{3.209}$$

So, the rank-truncated HOYW system of equations is

$$\hat{\boldsymbol{\Psi}}_p\,\hat{\boldsymbol{b}} \cong -\begin{bmatrix}\hat{r}(L+1)\\ \vdots\\ \hat{r}(L+m)\end{bmatrix} \tag{3.210}$$

The pseudoinverse of $\hat{\boldsymbol{\Psi}}_p$ is given as

$$\hat{\boldsymbol{\Psi}}_p^{+} = \boldsymbol{V}_1\,\boldsymbol{\Sigma}_1^{-1}\,\boldsymbol{U}_1^{*} \tag{3.211}$$

So, the Least Squares solution for the $\hat{\boldsymbol{b}}$ is

$$\hat{\boldsymbol{b}} = -\,\boldsymbol{V}_1\,\boldsymbol{\Sigma}_1^{-1}\,\boldsymbol{U}_1^{*}\begin{bmatrix}\hat{r}(L+1)\\ \vdots\\ \hat{r}(L+m)\end{bmatrix} \tag{3.212}$$

Note that the accuracy in the frequency estimates increases as L and M increases and $\hat{\boldsymbol{\Psi}}_p = \hat{\boldsymbol{\Psi}}$ for $L = p$ or $m = p$.

Then, form the polynomial,

$$B(z) = 1 + \sum_{k=1}^{L} \hat{b}_k \, z^{-k} \tag{3.213}$$

Frequency estimates can be obtained as the angular positions of the p roots of $B(z)$ that are nearest to the unit circle.

3.4.3. MUSIC

MUltiple SIgnal Classification (MUSIC) method is derived from the covariance model, $\boldsymbol{R} = \boldsymbol{A}\,\boldsymbol{P}\,\boldsymbol{A}^* + \sigma^2 \boldsymbol{I}$, with $m>p$. The covariance matrix of the noisy signal can be written as the sum of the covariance matrices of signal and noise as

$$\begin{aligned} \boldsymbol{R} &= \boldsymbol{A}\,\boldsymbol{P}\,\boldsymbol{A}^* + \sigma^2 \boldsymbol{I} \\ &= \boldsymbol{R}_X + \boldsymbol{R}_n \end{aligned} \tag{3.214}$$

Let $\lambda_1 \geq \lambda_2 \geq .... \geq \lambda_m$ denote the eigenvalues of $\boldsymbol{R}$, arranged in non-decreasing order, and let $\{\boldsymbol{s}_1, ..., \boldsymbol{s}_p\}$ be the orthogonal eigenvectors associated with $\{\lambda_1, ..., \lambda_p\}$ and $\{\boldsymbol{g}_1, ..., \boldsymbol{g}_{m-p}\}$ denote the orthogonal eigenvectors associated with $\{\lambda_{p+1}, ..., \lambda_m\}$. Since

$$rank(\boldsymbol{A}\,\boldsymbol{P}\,\boldsymbol{A}^*) = p \tag{3.215}$$

$\boldsymbol{A}\,\boldsymbol{P}\,\boldsymbol{A}^*$ has p strictly positive eigenvalues, and the remaining (m-p) eigenvalues all being equal to zero, $\lambda_{p+1} = ... = \lambda_m = 0$. Now, consider the eigenvalue decomposition of the $p \times p$ covariance matrix $\boldsymbol{R}_X$ where

$$\boldsymbol{R}_X = \sum_{k=1}^{p} \lambda_k \boldsymbol{s}_k \boldsymbol{s}_k^H \tag{3.216}$$

Since the covariance matrix of the noisy signal is sum of the covariance matrices of signal and noise, the covariance matrix of the noisy signal can be expressed as

$$\boldsymbol{R} = \sum_{k=1}^{p} (\lambda_k + \sigma^2) \boldsymbol{s}_k \boldsymbol{s}_k^H + \sigma^2 \sum_{k=p+1}^{m} \boldsymbol{g}_k \boldsymbol{g}_k^H \tag{3.217}$$

Using equation (3.217), the eigenvectors and the eigenvalues of the covariance matrix of the noisy signal can be partitioned into two disjoint subsets.

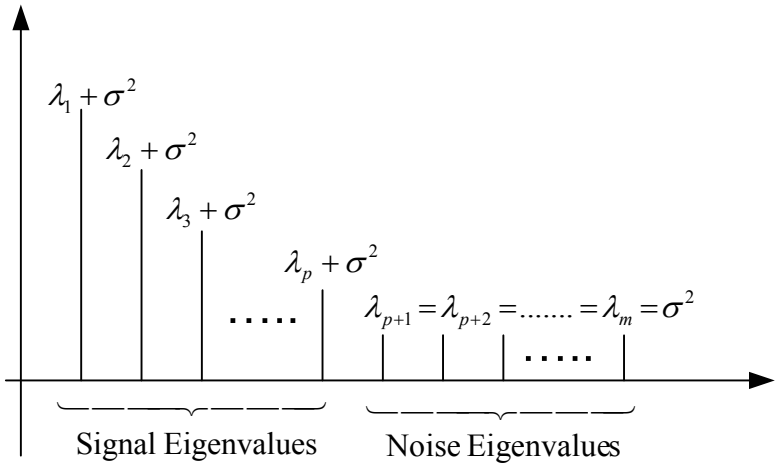

Figure 3.15. Decomposition of the eigenvalues of a noisy signal into signal and noise eigenvalues

The set of eigenvectors $\{\boldsymbol{s}_1, ..., \boldsymbol{s}_p\}$ associated with the *p* largest eigenvalues span the *signal subspace* and the eigenvectors $\{\boldsymbol{g}_1, ..., \boldsymbol{g}_{m-p}\}$ associated with the remaining *(m-p)* eigenvalues span the *noise subspace.*

Let

$$\boldsymbol{S} = [\boldsymbol{s}_1 \boldsymbol{s}_2 ... \boldsymbol{s}_p] \quad (m \times p) \tag{3.218}$$

and

$$\boldsymbol{G} = [\boldsymbol{g}_1 \boldsymbol{g}_2 ... \boldsymbol{g}_{m-p}] \quad (m \times (m-p)) \tag{3.219}$$

Note that

$$\boldsymbol{R}\,\boldsymbol{G} = \boldsymbol{G}\begin{bmatrix} \lambda_{p+1} & & 0 \\ & \ddots & \\ 0 & & \lambda_m \end{bmatrix} = \sigma^2 \boldsymbol{G} = \boldsymbol{A}\boldsymbol{P}\boldsymbol{A}^*\boldsymbol{G} + \sigma^2\,\boldsymbol{G} \tag{3.220}$$

where the last equality implies that $\boldsymbol{A}\boldsymbol{P}\boldsymbol{A}^*\boldsymbol{G} = 0$. Since the $\boldsymbol{A}\boldsymbol{P}$ is full rank,

$$\boldsymbol{A}^*\boldsymbol{G} = 0 \tag{3.221}$$

which means that the columns $\{\boldsymbol{g}_k\}$ of $\boldsymbol{G}$ belong to the *null space* of $\boldsymbol{A}^*$, i.e.,

$$\boldsymbol{g}_k \in N(\boldsymbol{A}^*) \tag{3.222}$$

Since the *rank(A)=p,* the dimension of null space of $\boldsymbol{A}^*$ is *(m-p)* which is also the dimension of *range space* of $\boldsymbol{G}$. From this observation and the fact that $\boldsymbol{A}^*\boldsymbol{G} = 0$, it follows that

$$R(\boldsymbol{G}) = N(\boldsymbol{A}^*) \tag{3.223}$$

which means that the the columns $\{\boldsymbol{g}_k\}$ of $\mathbf{G}$ span both $R(\boldsymbol{G})$ and $N(\boldsymbol{A}^*)$. Since $\boldsymbol{S}$ and $\boldsymbol{G}$ are orthogonal, by definition,

$$\boldsymbol{S}^*\boldsymbol{G} = 0 \tag{3.224}$$

So, we also have $R(\boldsymbol{G}) = N(\boldsymbol{S}^*)$; hence, $N(\boldsymbol{S}^*) = N(\boldsymbol{A}^*)$. Since *R(A)* and *R(S)* are orthogonal complements to $N(\boldsymbol{S}^*)$ and $N(\boldsymbol{A}^*)$, we get,

$$R(\boldsymbol{S}) = R(\boldsymbol{A}) \tag{3.225}$$

The subspaces $R(\boldsymbol{S})$ and $R(\boldsymbol{G})$ are called the *signal subspace* and *noise subspace*, respectively.

From the result $\boldsymbol{A}^*\boldsymbol{G}=0$, it can be concluded that the frequency values $\{w_k\}_{k=1}^{p}$ are the only solutions of the equation

$$a^*(w)\boldsymbol{G}\boldsymbol{G}^*a(w)=0 \qquad \forall\ m>p \tag{3.226}$$

MUSIC algorithm can be summarized as follows: First, compute the sample covariance matrix estimate by

$$\hat{R}=\frac{1}{N}\sum_{n=m}^{N}\tilde{y}(n)\tilde{y}^*(n) \tag{3.227}$$

and the find its eigendecomposition. Let $\hat{\boldsymbol{S}}$ and $\hat{\boldsymbol{G}}$ denote the matrices, constructed from the the eigenvectors $\{\hat{\boldsymbol{s}}_1,\ldots,\hat{\boldsymbol{s}}_p\}$ and $\{\hat{\boldsymbol{g}}_1,\ldots,\hat{\boldsymbol{g}}_{m-p}\}$ of $\hat{\boldsymbol{R}}$, defined similarly to $\boldsymbol{S}$ and $\boldsymbol{G}$. Then, frequency estimates can be determined as the locations of the p highest peaks of the function

$$\frac{1}{a^*(w)\hat{\boldsymbol{G}}\hat{\boldsymbol{G}}^*a(w)}, \quad w\in[-\pi,\pi] \tag{3.228}$$

It can be shown that the accuracy of the MUSIC frequency estimates increases with increasing m. However, the computational complexity also increases with m. If computational complexity is not a problem, m may be chosen as large as possible, but not to close to N, in order to allow a reliable estimation of $\hat{\boldsymbol{R}}$. However, if m takes large values, spurious frequency estimates may occur. Several modified MUSIC methods have been developed to overcome this problem but they will not be explained in this study.

3.4.4. Root-MUSIC

Root-MUSIC method facilitates the same ideas with MUSIC and differs only in the second step of the MUSIC algoritm. The main advantage of Root-MUSIC over MUSIC is its lower computational complexity.

Root-MUSIC algorithm can be summarized as follows: First compute the sample covariance matrix estimate by

$$\hat{R}=\frac{1}{N}\sum_{n=m}^{N}\tilde{y}(n)\tilde{y}^{*}(n) \tag{3.229}$$

and the find its eigendecomposition. Let $\hat{\boldsymbol{S}}$ and $\hat{\boldsymbol{G}}$ denote the matrices, constructed from the the eigenvectors $\{\hat{\boldsymbol{s}}_1,\ldots,\hat{\boldsymbol{s}}_p\}$ and $\{\hat{\boldsymbol{g}}_1,\ldots,\hat{\boldsymbol{g}}_{m-p}\}$ of $\hat{\boldsymbol{R}}$, defined similarly to $\boldsymbol{S}$ and $\boldsymbol{G}$. Then, frequency estimates can be determined as the the angular positions of the p roots of the equation

$$a^{T}(z^{-1})\hat{\boldsymbol{G}}\hat{\boldsymbol{G}}^{*}a(z)=0 \tag{3.230}$$

which are located nearest to the unit circle.

3.4.5. Min-Norm Method

Minimum norm method uses only one vector from the range space of $\hat{G}$ to achieve some computational saving without sacrificing too much accuracy.

Let

$$\begin{bmatrix}1\\ \hat{\boldsymbol{g}}\end{bmatrix} \tag{3.231}$$

be the vector in $R(\hat{G})$ with the minimum Euclidean norm.

Spectral Min-Norm method finds the frequency estimates as the locations of the p highest peaks in the pseudospectrum

$$\frac{1}{\left|a^*(w)\begin{bmatrix}1\\ \hat{\boldsymbol{g}}\end{bmatrix}\right|^2} \tag{3.232}$$

Root Min-Norm method estimates the frequencies can be as the angular positions of the p roots of the polynomial

$$\boldsymbol{a}^{\boldsymbol{T}}(z^{-1})\begin{bmatrix}1\\ \hat{\boldsymbol{g}}\end{bmatrix} \tag{3.233}$$

that are closest to the unit circle.

The procedure of finding the vector $\begin{bmatrix}1 & \hat{\boldsymbol{g}}\end{bmatrix}^T$ is described as follows:

Partition the matrix $\hat{\boldsymbol{S}}$ as

$$\hat{\boldsymbol{S}} = \begin{bmatrix}\boldsymbol{\alpha}^*\\ \overline{\boldsymbol{S}}\end{bmatrix}\begin{matrix}\}1\\ \}m-1\end{matrix} \tag{3.234}$$

Since $\begin{bmatrix}1 & \hat{\boldsymbol{g}}\end{bmatrix}^T \in R(\hat{\boldsymbol{G}})$, it must satisfy

$$\hat{\boldsymbol{S}}^*\begin{bmatrix}1\\ \hat{\boldsymbol{g}}\end{bmatrix} = 0 \tag{3.235}$$

which can be rewritten as

$$\overline{\boldsymbol{S}}^*\,\hat{\boldsymbol{g}} = -\boldsymbol{\alpha} \tag{3.236}$$

The minimum-norm solution to (3.236) is

$$\hat{\boldsymbol{g}} = -\overline{\boldsymbol{S}}(\overline{\boldsymbol{S}}^{*}\overline{\boldsymbol{S}})^{-1}\boldsymbol{\alpha} \tag{3.237}$$

assuming that the inverse exists. Note that

$$\boldsymbol{I} = \hat{\boldsymbol{S}}^{*}\hat{\boldsymbol{S}} = \overline{\boldsymbol{S}}^{*}\overline{\boldsymbol{S}} + \boldsymbol{\alpha}\boldsymbol{\alpha}^{*} \tag{3.238}$$

and also that one eigenvalue of $\boldsymbol{I} - \boldsymbol{\alpha}\boldsymbol{\alpha}^{*}$ is equal to $1 - \|\boldsymbol{\alpha}\|^{2}$ and the remaining *(p-1)* eigenvalues of $\boldsymbol{I} - \boldsymbol{\alpha}\boldsymbol{\alpha}^{*}$ are equal to one. Hence, the inverse in equation (3.237) exists if and only if

$$\|\boldsymbol{\alpha}\|^{2} \neq 1 \tag{3.239}$$

If this condition is not satisfied, there will be no vector of the form $\begin{bmatrix}1 & \hat{\boldsymbol{g}}\end{bmatrix}^{T}$ in $R(\hat{\boldsymbol{G}})$.

Under the condition $\|\boldsymbol{\alpha}\|^{2} \neq 1$, since

$$\boldsymbol{I} = \overline{\boldsymbol{S}}^{*}\overline{\boldsymbol{S}} + \boldsymbol{\alpha}\boldsymbol{\alpha}^{*} \tag{3.240}$$

$$\Rightarrow \overline{\boldsymbol{S}}^{*}\overline{\boldsymbol{S}} = \boldsymbol{I} - \boldsymbol{\alpha}\boldsymbol{\alpha}^{*} \tag{3.241}$$

$$\Rightarrow (\overline{\boldsymbol{S}}^{*}\overline{\boldsymbol{S}})^{-1} = (\boldsymbol{I} - \boldsymbol{\alpha}\boldsymbol{\alpha}^{*})^{-1} \tag{3.242}$$

$$\Rightarrow (\overline{\boldsymbol{S}}^{*}\overline{\boldsymbol{S}})^{-1}\boldsymbol{\alpha} = (\boldsymbol{I} - \boldsymbol{\alpha}\boldsymbol{\alpha}^{*})^{-1}\boldsymbol{\alpha} \tag{3.243}$$

$$\Rightarrow (\overline{\boldsymbol{S}}^{*}\overline{\boldsymbol{S}})^{-1}\boldsymbol{\alpha} = \frac{\boldsymbol{\alpha}}{(1 - \|\boldsymbol{\alpha}\|^{2})} \tag{3.244}$$

Using (3.244) and (3.237), $\hat{g}$ can be computed by

$$\hat{\boldsymbol{g}} = -\overline{\boldsymbol{S}}\frac{\boldsymbol{\alpha}}{(1 - \|\boldsymbol{\alpha}\|^{2})} \tag{3.245}$$

which expresses $\hat{\boldsymbol{g}}$ as a function of elements of $\hat{\boldsymbol{S}}$.

Min-Norm method achieves the MUSIC's performance at a reduced computational cost. Moreover, there is empirical evidence that the use of minimum-norm vector in $R(\hat{\boldsymbol{G}})$ in the form of $\begin{bmatrix}1 & \hat{\boldsymbol{g}}\end{bmatrix}^T$ decreases the risk of spurious frequency estimates, as compared to MUSIC.

3.4.6. ESPRIT

In the covariance model, *a(w)* vector and *A* matrix was given as

$$a(w)=[1\ e^{-jw}\ e^{-j2w}\ ....\ e^{-j(m-1)w}]^T \quad (m\,x1) \tag{3.246}$$

$$\boldsymbol{A} = [a(w_1)\ a(w_2)\ ...\ a(w_p)] \quad (m\,x\,p) \tag{3.247}$$

Define

$$\boldsymbol{A_1}=[\,\boldsymbol{I_{m-1}}\ 0\,]\boldsymbol{A} \quad (m-1)xp \quad \text{, } i.e.\text{, first } (\mathrm{m}-1) \text{ rows of } \boldsymbol{A} \tag{3.248}$$

$$\boldsymbol{A_2}=[\,0\ \boldsymbol{I_{m-1}}\,]\boldsymbol{A} \quad (m-1)xp \quad \text{, } i.e.\text{, last } (\mathrm{m}-1) \text{ rows of } \boldsymbol{A} \tag{3.249}$$

where $\boldsymbol{I_{m-1}}$ is the identity matrix of dimension $(m-1)x(m-1)$ and the matrices $[\,\boldsymbol{I_{m-1}}\ 0\,]$ and $[\,0\ \boldsymbol{I_{m-1}}\,]$ are of dimension $(m-1)x\,m$. It can be verified that

$$\boldsymbol{A_2} = \boldsymbol{A_1}\,\boldsymbol{D} \tag{3.250}$$

where

$$\boldsymbol{D}=\begin{bmatrix} e^{-jw_1} & & 0 \\ & \ddots & \\ 0 & & e^{-jw_p} \end{bmatrix} \tag{3.251}$$

is a unitary matrix, so the transformation in (3.250) is a *rotation.* ESPRIT (Estimation of Signal Parameters via Rotational Invariance Techniques) relies on the rotational transformation.

Let

$$\lambda_1 \geq \lambda_2 \geq .... \geq \lambda_p > \lambda_{p+1} = \lambda_{p+1} = ... = \lambda_m = \sigma^2 \tag{3.252}$$

denote the eigenvalues of $\boldsymbol{R}$ and $\{ \boldsymbol{s_1}, \boldsymbol{s_2}, ..., \boldsymbol{s_p} \}$ denote the corresponding signal eigenvectors.

Define

$$\boldsymbol{S} = [\, \boldsymbol{s_1}\, \boldsymbol{s_2}\, \ldots\, \boldsymbol{s_p}\,] \quad (m\, x\, p) \tag{3.253}$$

and

$$\boldsymbol{\Lambda} = \begin{bmatrix} \lambda_1 & & 0 \\ & \ddots & \\ 0 & & \lambda_p \end{bmatrix} \tag{3.254}$$

So, we have,

$$\boldsymbol{R}\,\boldsymbol{S} = \boldsymbol{S}\,\boldsymbol{\Lambda} \tag{3.255}$$

Rewriting (3.255) yields

$$\boldsymbol{RS} = (\boldsymbol{APA}^* + \sigma^2 \boldsymbol{I})\,\boldsymbol{S}$$

$$\boldsymbol{RS} = \boldsymbol{APA}^*\boldsymbol{S} + \sigma^2 \boldsymbol{I}\,\boldsymbol{S}$$

$$\boldsymbol{APA}^*\boldsymbol{S} + \sigma^2 \boldsymbol{I}\,\boldsymbol{S} = \boldsymbol{S}\,\boldsymbol{\Lambda}$$

$$\boldsymbol{APA}^*\boldsymbol{S} = \boldsymbol{S}\,(\boldsymbol{\Lambda} - \sigma^2 \boldsymbol{I})$$

$$\boldsymbol{APA}^*\boldsymbol{S} = \boldsymbol{S}\,\overline{\boldsymbol{\Lambda}}$$

$$\boldsymbol{S} = (\boldsymbol{APA}^*\boldsymbol{S})\,\overline{\boldsymbol{\Lambda}}^{-1}$$

$$\boldsymbol{S} = \boldsymbol{A}(\,\boldsymbol{PA}^*\boldsymbol{S}\,\overline{\boldsymbol{\Lambda}}^{-1}\,) \tag{3.256}$$

where

$$\overline{\boldsymbol{\Lambda}} = \begin{bmatrix} \lambda_1 - \sigma^2 & & 0 \\ & \ddots & \\ 0 & & \lambda_p - \sigma^2 \end{bmatrix} \tag{3.257}$$

Similarly, define

$$\boldsymbol{S}_1 = [\boldsymbol{I}_{m-1}\ 0]\boldsymbol{S} \tag{3.258}$$

$$\boldsymbol{S}_2 = [0\ \boldsymbol{I}_{m-1}]\boldsymbol{S} \tag{3.259}$$

From (3.256), we have

$$\boldsymbol{S} = \boldsymbol{A}\boldsymbol{C} \tag{3.260}$$

where

$$\boldsymbol{C} = \boldsymbol{P}\boldsymbol{A}^{*}\boldsymbol{S}\,\overline{\boldsymbol{\Lambda}}^{-1} \tag{3.261}$$

Note that $\boldsymbol{S}$ and $\boldsymbol{A}$ have full column rank, hence, $\boldsymbol{C}$ must be non-singular. Similar to (3.250), we can conclude that

$$\boldsymbol{S}_2 = \boldsymbol{A}_2\boldsymbol{C} \tag{3.262}$$

$$= (\boldsymbol{A}_1\boldsymbol{D})\boldsymbol{C} \tag{3.263}$$

$$= \boldsymbol{S}_1\boldsymbol{C}^{-1}\boldsymbol{D}\boldsymbol{C} \tag{3.264}$$

$$= \boldsymbol{S}_1\boldsymbol{\varphi} \tag{3.265}$$

where

$$\boldsymbol{\varphi} = \boldsymbol{C}^{-1}\boldsymbol{D}\boldsymbol{C} \tag{3.266}$$

As proven in the covariance model, the Vandermonde matrix *A* has full rank which implies that the matrices $\boldsymbol{A}_1$ and $\boldsymbol{A}_2$ have full column rank. Also note that $\boldsymbol{S}_1$ and $\boldsymbol{S}_2$ also have full column rank. So, the matrix $\boldsymbol{\varphi}$ is given uniquely by the equation

$$\boldsymbol{\varphi} = (\boldsymbol{S}_1^{*}\boldsymbol{S}_1)^{-1}\boldsymbol{S}_1^{*}\boldsymbol{S}_2 \tag{3.267}$$

which expresses $\boldsymbol{\varphi}$ as a function of some quantities that can be estimated from the available samples.

The matrices $\boldsymbol{\varphi}$ and $\boldsymbol{D}$, where $\boldsymbol{\varphi} = \boldsymbol{C}^{-1}\boldsymbol{D}\boldsymbol{C}$ and $\boldsymbol{C}$ is any nonsingular matrix, have the same eigenvalues. ($\boldsymbol{\varphi}$ is said to be related to $\boldsymbol{D}$ by a similarity transformation.)

The proof of the previous claim can easily be shown considering the equation

$$\left|\boldsymbol{\varphi}-\lambda\boldsymbol{I}\right| = \left|\boldsymbol{C}^{-1}(\boldsymbol{D}-\lambda\boldsymbol{I})\boldsymbol{C}\right| = \left|\boldsymbol{C}^{-1}\right\|\boldsymbol{D}-\lambda\boldsymbol{I}\|\ \boldsymbol{C}\left| = 0\right.$$

which is is equivalent to

$$\left|\boldsymbol{D}-\lambda\boldsymbol{I}\right| = 0$$

which implies that $\boldsymbol{\varphi}$ and $\boldsymbol{D}$ have same eigenvalues.

ESPRIT uses the previous claim to find the frequency estimates. Since $\boldsymbol{D}$ is given as $\boldsymbol{D} = diag\{\exp(-jw_1)...\exp(-jw_p)\}$, finding the eigenvalues of $\boldsymbol{\varphi}$ (which are also the eigenvalues of $\boldsymbol{D}$) will give us the frequency estimates, i.e., frequency estimates $\{w_k\}_{k=1}^{p}$ can be obtained as $-\arg(v_k)$ where $\{v_k\}_{k=1}^{p}$ are the eigenvalues of the matrix $\boldsymbol{\varphi}$.

The two ways of obtaining $\boldsymbol{\varphi}$ by solving the linear system of equations

$$\boldsymbol{S_1}\,\boldsymbol{\varphi} = \boldsymbol{S_2} \tag{3.268}$$

are Least Squares(LS) and Total Least Squares(TLS) methods and computing the frequency estimates using LS and TLS are explained in the following subsections.

3.4.6.1. LS ESPRIT Solution. Algorithm of the solution of the ESPRIT method by Least Squares method can be summarized as follows :

i. Compute the sample covariance matrix

$$\hat{R} = \frac{1}{N}\sum_{n=m}^{N}\ \tilde{y}(n)\,\tilde{y}^{*}(n) \tag{3.269}$$

ii. Compute the eigendecomposition of $\hat{\boldsymbol{R}}$

iii. Estimate the number of sinusoids in the noisy signal (find $\hat{p}$).

iv. Construct the $\hat{\boldsymbol{S}}$ matrix from the eigenvectors and obtain the $\hat{\boldsymbol{S}}_1$ and $\hat{\boldsymbol{S}}_2$ matrices

v. Solve the linear system of equations

$$\hat{\boldsymbol{S}}_1 \hat{\boldsymbol{\varphi}} = \hat{\boldsymbol{S}}_2 \tag{3.270}$$

by LS method, i.e., compute $\hat{\boldsymbol{\varphi}}$ by

$$\hat{\boldsymbol{\varphi}} = (\hat{\boldsymbol{S}}_1^* \hat{\boldsymbol{S}}_1)^{-1} \hat{\boldsymbol{S}}_1^* \hat{\boldsymbol{S}}_2 \tag{3.271}$$

vi. Compute the eigendecomposition of $\hat{\boldsymbol{\varphi}}$.

vii. Compute the frequency estimates as

$$w_k = -\arg(v_k) \quad , \quad k = 1,2,..., \hat{p} \, , \tag{3.272}$$

where $\{v_k\}_{k=1}^{\hat{p}}$ are the eigenvalues of $\hat{\boldsymbol{\varphi}}$.

3.4.6.2. TLS ESPRIT Solution. Algorithm of the solution of the ESPRIT method by Total Least Squares method can be summarized as follows :

i. Compute the sample covariance matrix using (3.269).

ii. Compute the eigendecomposition of $\hat{\boldsymbol{R}}$

iii. Estimate the number of sinusoids in the noisy signal (find $\hat{p}$).

iv. Construct the $\hat{\boldsymbol{S}}$ matrix from the eigenvectors and obtain the $\hat{\boldsymbol{S}}_1$ and $\hat{\boldsymbol{S}}_2$ matrices.

v. Compute the eigendecomposition

$$\begin{bmatrix} \hat{\boldsymbol{S}}_1^* \\ \hat{\boldsymbol{S}}_2^* \end{bmatrix} [\, \hat{\boldsymbol{S}}_1 \,\big|\, \hat{\boldsymbol{S}}_2 \,] = \boldsymbol{E}\, \boldsymbol{\Lambda}^0\, \boldsymbol{E}^* \tag{3.273}$$

vi. Partition the $\boldsymbol{E}$ matrix into $\hat{p}\, x\, \hat{p}$ submatrices as

$$\boldsymbol{E} = \begin{bmatrix} \boldsymbol{E}_{11} & \boldsymbol{E}_{12} \\ \boldsymbol{E}_{21} & \boldsymbol{E}_{22} \end{bmatrix} \tag{3.274}$$

vii. Compute the eigenvalues of the matrix $\boldsymbol{\Psi}$, where

$$\boldsymbol{\Psi} = -\boldsymbol{E}_{12}\,\boldsymbol{E}_{22}^{-1} \tag{3.275}$$

viii. Compute the frequency estimates as

$$w_k = -\arg(\gamma_k) \quad , k = 1,2,..., \hat{p} \tag{3.276}$$

where $\{\gamma_k\}_{k=1}^{\hat{p}}$ are the eigenvalues of $\boldsymbol{\Psi}$.

It has been empirically observed that TLS-ESPRIT solution can achieve better finite-sample accuracy than LS-ESPRIT.

ESPRIT has a similar statistical accuracy to that of HOYW, MUSIC, Root-MUSIC and Min-Norm. However, in most cases, ESPRIT can provide more accurate frequency estimates than these methods can and it has no problem with spurious frequency estimates. Moreover, ESPRIT has lower computational complexity. All these considerations make the ESPRIT as the first choice in any frequency estimation application.

3.4.7. Smoothing Process

The previously described methods derive their frequency estimates utilizing the eigenstructure of the sample covariance matrix. In radar applications, since the reflection coefficients of the targets have constant values and do not change from measurement to measurement, the signals are coherent. Since the eigenanalysis-based methods do not work properly when the signals are coherent, a decorrelation process is required to eliminate problems encountered with coherent signals.

Consider the application of the eigenanalysis-based methods for finding the high range resolution profile of the stepped frequency radar. As shown in figure 3.16, the received signal is divided *L* overlapping *subarrays* each of with length *M*. Note that using smoothing techniques decreases the effective bandwith from $(f_{N-1} - f_0)$ to $(f_{M-1} - f_0)$

which, in turn decreases the resolution. In spite of this disadvantage, eigenanalysis-based methods employing smoothing process can achieve much better performance than conventional FFT techniques.

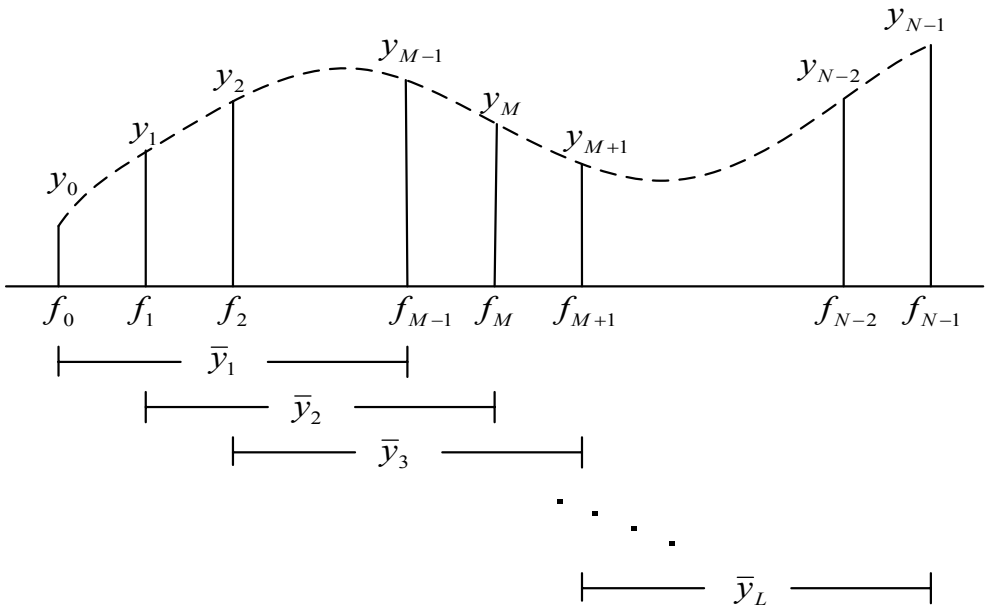

Figure 3.16. Subarray Arrangement

The vector $\bar{y}_k$ representing the k^{th} subarray, where $k = 1,2,...,L$, can be written as

$$\bar{\boldsymbol{y}}_{\boldsymbol{k}} = \boldsymbol{A}\,\boldsymbol{D}^{(k-1)}\boldsymbol{x} + \boldsymbol{e}_{\boldsymbol{k}} \tag{3.277}$$

where $\boldsymbol{e}_{\boldsymbol{k}}$ denotes the vector of additive white gaussian noise at the k^{th} subarray and, and D denotes the $p \times p$ diagonal matrix expressed as

$$\boldsymbol{D} = \{\exp(-j2\pi\Delta f\,\tau_1), \exp(-j2\pi\Delta f\,\tau_2) \;\; , \ldots , \exp(-j2\pi\Delta f\,\tau_p)\} \tag{3.278}$$

where Δf is the sampling frequency separation and τ is the two way time delay.

The covariance matrix of the k^{th} subarray is given by

$$\boldsymbol{R}_k = \bar{\boldsymbol{y}}_k \, \bar{\boldsymbol{y}}_k^* \tag{3.279}$$

$$= (\boldsymbol{A}\,\boldsymbol{D}^{(k-1)}\boldsymbol{x})\,(\boldsymbol{A}\,\boldsymbol{D}^{(k-1)}\boldsymbol{x}) \tag{3.280}$$

$$= \boldsymbol{A}\,\boldsymbol{D}^{(k-1)}\boldsymbol{x}\,\boldsymbol{x}^*(\boldsymbol{D}^{(k-1)})^*\,\boldsymbol{A} + \sigma^2\boldsymbol{I} \tag{3.281}$$

3.4.7.1. Spatial Smoothing Process (SSP). This method uses the $\boldsymbol{R}_{SSP}$ as the covariance matrix where $\boldsymbol{R}_{SSP}$ is the sample mean of the subarray covariance matrices [15], i.e.,

$$\boldsymbol{R}_{SSP} = \frac{1}{L}\sum_{k=1}^{L} \boldsymbol{R}_k \tag{3.282}$$

3.4.7.2. Modified Spatial Smoothing Process (MSSP). This method uses the uses $\boldsymbol{R}_{MSSP}$ as the covariance matrix [16], where,

$$\boldsymbol{R}_{MSSP} = \frac{1}{2L}\sum_{k=1}^{L} (\,\boldsymbol{R}_k + \boldsymbol{J}\,\boldsymbol{R}_k^*\,\boldsymbol{J}\,) \tag{3.283}$$

and

$$\boldsymbol{J} = \begin{bmatrix} 0 & & 1 \\ & \iddots & \\ 1 & & 0 \end{bmatrix} \tag{3.284}$$

is the so called reversal matrix.

It should be noted that, in both techniques, there exists a trade-off when choosing L and M. If M is increased, effective bandwidth and resolution increases but decorrelation performance decreases. If L is increased, decorrelation performance increases but effective bandwidth and resolution decreases. Therefore, M and L should be chosen depending on the application. Both of these techniques will be implemented in chapter four and five and their performance will be compared.

3.4.8. Model Order Estimation

One of the key steps in the parametric methods is the accurate and consistent estimation of the number of signals, the so called model order. In radar applications, our goal is to estimate the number of high energy scattering centers. Among the model order estimation methods in the literature, Akaike information criterion (AIC) [17] and minimum description length (MDL) [18] are the frequently used methods. Since it has been shown that MDL outperforms AIC, especially for noisy signals [18], MDL will be used as model order estimation tool in this study.

3.4.8.1. Minimum Description Length Principle. Due to the random errors in the covariance matrix estimate, $\hat{\boldsymbol{R}}$, its eigenvalues will be perturbed and from their true values and the true multiplicity of the minimum eigenvalue may not be evident. MDL is a popular approach for model order estimation. It determines the underlying eigenvalue multiplicity to determine number of signals. The estimate of number of signals $\hat{p}$ is given by the value of k for which the following MDL function is minimized :

$$MDL(k) = (P-k)N \log\left\{ \frac{\frac{1}{P-k}\sum_{i=1}^{P-k}\hat{\lambda}_i}{\left(\prod_{i=1}^{P-k}\hat{\lambda}_i\right)^{1/P-k}} \right\} + \frac{k}{2}(2P-k+1) \tag{3.285}$$

where P is the upper bound for the model order, N is the number of observations, $\hat{\lambda}_i$ are the eigenvaues of covariance matrix. The estimated model order is computed via

$$\hat{p} = \arg \min_{k\in\{0,1,\ldots,P-1\}} MDL(k) \tag{3.286}$$

4. RESOLVING CAPABILITY of SUPER-RESOLUTION METHODS : SIMULATION STUDY

4.1. Introduction

It was noted that HRR provides the ability of resolving closely spaced targets in range, improves the range accuracy, reduces the amount of clutter within the range cell, reduces multi-path, and aids in target recognition and classification. HRR is very helpful in detection of targets with low radar cross sections embedded in high clutter. It increases signal-to-clutter ratio which, in turn, makes targets with low RCS visible. Therefore, it is crucial to enhance the range resolution. However, in practice, the frequency bandwidth of a radar is limited by several factors, and the range profiles obtained by IFFT often result in a limited range resolution.

This chapter investigates the resolving capability of super-resolution spectral estimation methods explained in chapter three using synthetic radar returns of stepped-frequency and linear frequency modulated continuous wave radars explained in chapter two. First, signal models for returns form targets for the stepped-frequency and linear frequency modulated continuous wave radars are given. Secondly, super-resolution spectral estimation methods explained in detail in chapter three are implemented on synthetic signals. Finally, the results are compared. In this chapter, "super-resolving capability" is used as the super-resolution spectral estimation methods' ability to find the target ranges and distinguish the two closely separated targets.

4.2. Stepped-Frequency Radar Signal Model

As explained in detail in section 2.3.3., the frequency of the n^{th} pulse of the stepped-frequency radar is given as

$$f_n = f_0 + n\Delta f, \qquad n = 0,1,...N-1 \tag{4.1}$$

where $f_0 = f_{COHO} + f_{STALO}$. So, the transmitted signal can be expressed as

$$\begin{aligned} s_T(t) &= A_1 Cos(2\pi f_n t) \\ &= A_1 Cos[2\pi (f_{COHO} + f_{STALO} + n\Delta f) t] \end{aligned} \tag{4.2}$$

Assuming a point scatterer at range *R,* the received signal after a two-way time delay of $2R/c$ is given as

$$s_R(t) = A_n Cos[2\pi f_n (t - 2R/c)] \tag{4.3}$$

After down-conversion, quadrature demodulation and low-pass filtering, in-phase and quadrature signals at the output of phase detector are given as (see section 2.3.3. for details)

$$I(n) = A_n Cos[2\pi (f_0 + n\Delta f)(2R/c)] \tag{4.4}$$

$$Q(n) = A_n Sin[-2\pi (f_0 + n\Delta f)(2R/c)] \tag{4.5}$$

where

$$n = 0,1,...,N-1 \tag{4.6}$$

and *N* represents the total number of steps in the stepped-frequency waveform, and A_n depends on frequency, RCS of target, antenna gain and range attenuation. For the sake of simplicity, A_n will be assumed to be independent of frequency and *A* will be used instead of A_n. Therefore, the received signal from a point scatterer at range *R* in complex notation is

$$s_R(n) = A \exp\left\{-2\pi (f_0 + n\Delta f)\left(\frac{2R}{c}\right)\right\} \tag{4.7}$$

Now, assume *d* targets located at ranges $R_1, R_2, ... R_d$. So, the total received signal can be expressed as

$$s_R(n) = \sum_{k=1}^{d} A_k \exp\left\{ -2\pi (f_0 + n\Delta f)\left(\frac{2R_k}{c}\right)\right\} \tag{4.8}$$

and the in-phase and quadrature voltages at the output of phase detector are given as

$$I(n) = \sum_{k=1}^{d} A_k \; Cos[2\pi \; (f_0 + n\Delta f) \; (2R_k / c) \;] \tag{4.9}$$

$$Q(n) = \sum_{k=1}^{d} A_k \; Sin \; [-2\pi \; (f_0 + n\Delta f) \; (2R_k / c) \;] \tag{4.10}$$

for $n = 0,1,...,N-1$.

Equations (4.9) and (4.10) are used to generate the synthetic signals representing stepped-frequency radar returns from d targets located at ranges $R_1, R_2, ... R_d$.

Super-resolution spectral estimation methods are normally used to estimate the power spectral density from the time-domain observations, i.e, they are transformations from time-domain to frequency-domain. However, in stepped-frequency radar application, they will be used to estimate range profile from frequency-domain data, i.e., they will be used as a transformation from frequency-domain to spatial-domain.

The aim of this chapter is to show that high resolution spectral estimators explained in chapter three can achieve better down-range resolution than IFFT. In order to compare the performance of high resolution spectral estimators and IFFT, synthetic stepped-frequency radar returns from several targets will be generated using (4.9) and (4.10), white Gaussian distributed noise will be added to returnsignal to obtain different SNR ratio, and the noisy return signals will be processed by all the spectral estimation methods.

4.3. Comparison of IFFT and Super-Resolution Spectral Estimators for Stepped-Frequency Radar

For the following simulations, the parameters of the stepped-frequency waveform and the signal processing algorithms will be given in the tables for each case. Except the parameters given in the tables, f_0 will be set to 1 GHz although it has any importance since we have assumed that the magnitude of the scatterers are independent of frequency.

4.3.1. Yule-Walker Method vs. IFFT

Table 4.1. Parameters for simulation shown in figure 4.1

N	Δf	ΔR	Target Ranges (R_k) & RCSs (A_k)						SNR
256	10 MHz	5.86 cm	2 m 100	3 m 100	5 m 100	6 m 100	7 m 100	11 m 100	50

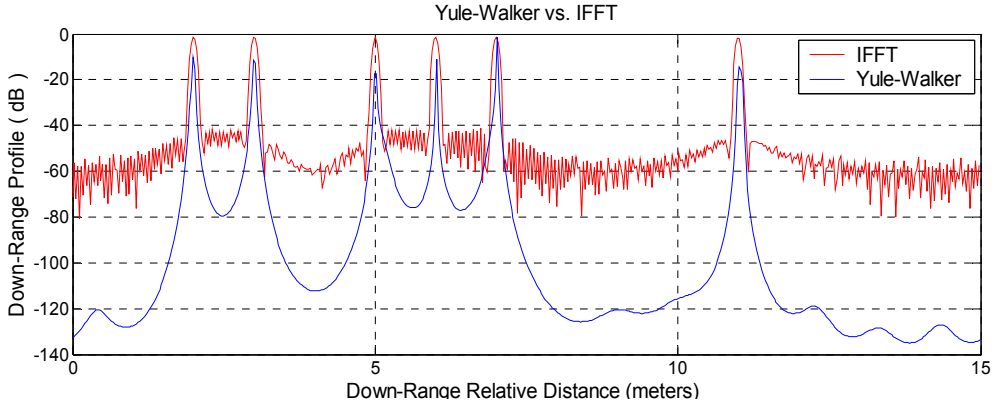

Figure 4.1. Comparison of Yule-Walker method and IFFT

Figure 4.1 show that Yule-Walker method provides narrower peaks at the target locations than IFFT. Also note that Yule-Walker range profile has higher signal-to-clutter ratio (SCR) than IFFT range profile.

Table 4.2. Parameters for simulation shown in figure 4.2

N	Δf	ΔR	Target Ranges (R_k) & RCSs (A_k)						SNR
256	10 MHz	5.86 cm	2 m 100	3 m 100	5 m 100	6 m 100	7 m 100	11 m 100	10

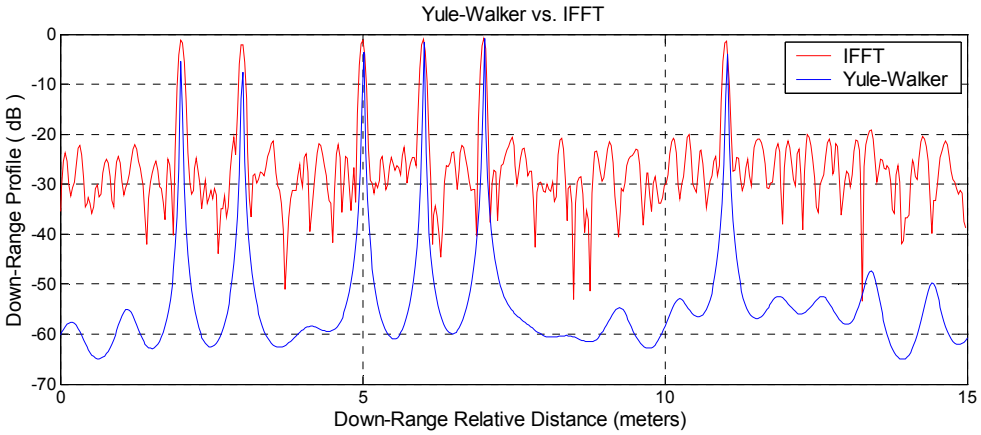

Figure 4.2. Comparison of Yule-Walker method and IFFT

Figure 4.2 shows that Yule-Walker method provides much sharper peaks at the target locations even in the low SNR case than IFFT and its range profile has higher SCR than range profile obtained via IFFT.

Table 4.3. Parameters for simulation shown in figure 4.3

N	Δf	ΔR	Target Ranges (R_k) & RCSs (A_k)					SNR
128	10 MHz	11.72 cm	2 m 100	2.2 m 100	2.4 m 100	6 m 100	10 m 100	40

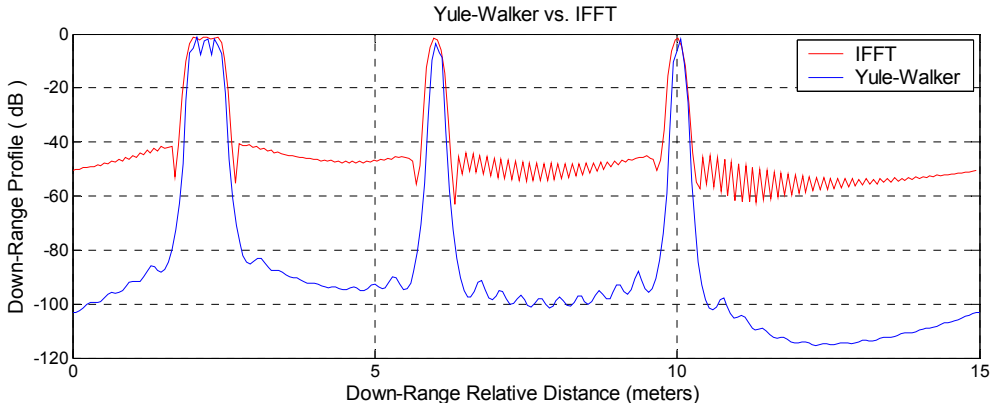

Figure 4.3. Comparison of Yule-Walker method and IFFT

Figure 4.3 illustrates that Yule-Walker method can resolve closely separated targets, however, IFFT can not. Yule-Walker range profile has three separate peaks at 2, 2.2, and 2.4 meters and three closely spaced targets can be distinguished but IFFT range profile has one broad peak, thus, it can not resolve the three closely spaced targets. Note that the range resolution obtained via the IFFT is 11.72 cm and the distance between the closely spaced

targets is 20 cm, however, because of the smearing problem of periodogram explained in section 3.2.3.1, IFFT could not resolve the targets with separation higher than its resolution.

Table 4.4. Parameters for simulation shown in figure 4.4

N	Δf	ΔR	Target Ranges (R_k) & RCSs (A_k)					SNR
128	10 MHz	11.72 cm	2 m 100	2.2 m 100	2.4 m 100	6 m 100	10 m 100	10

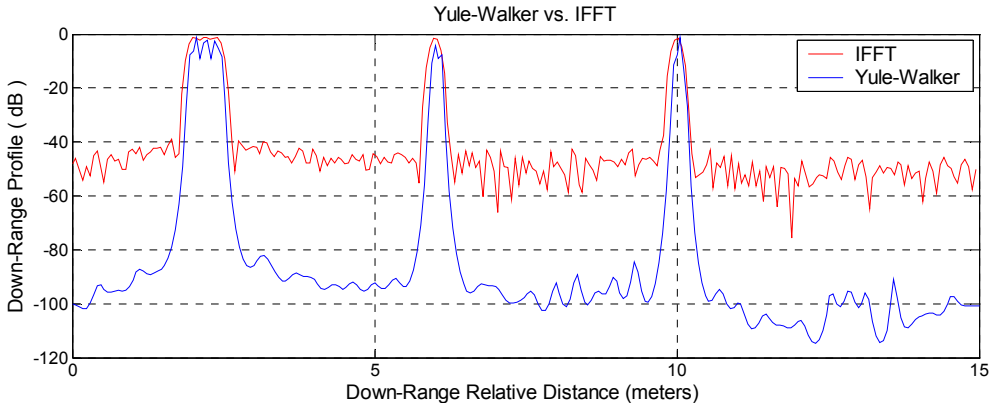

Figure 4.4. Comparison of Yule-Walker method and IFFT

Yule-Walker method outperforms the IFFT in terms of range resolution and accuracy even in low SNR case as shown in figure 4.4. Yule-Walker can resolve closely spaced targets even low SNR case.

4.3.2. Least Squares Method vs. IFFT

Table 4.5. Parameters for simulation shown in figure 4.5

N	Δf	ΔR	Target Ranges (R_k) & RCSs (A_k)						SNR
256	10 MHz	5.86 cm	2 m 100	3 m 100	5 m 100	6 m 100	7 m 100	11 m 100	50

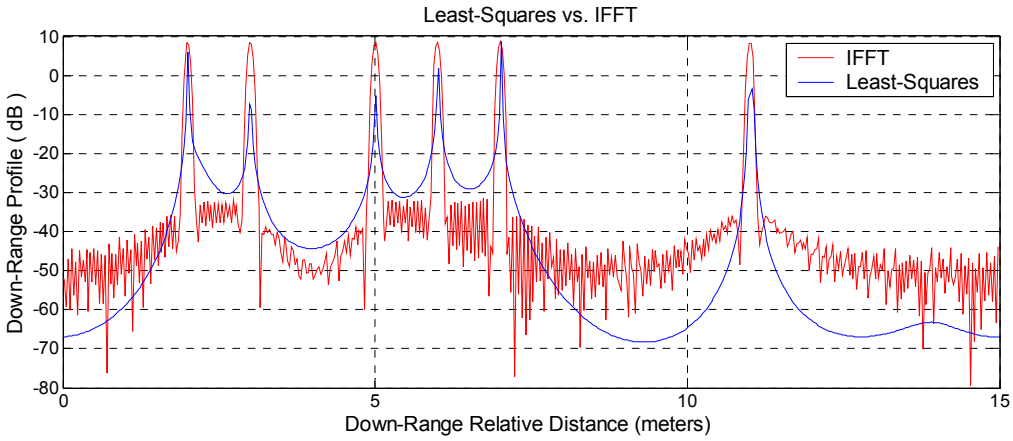

Figure 4.5. Comparison of least-squares method and IFFT

Table 4.6. Parameters for simulation shown in figure 4.6

N	Δf	ΔR	Target Ranges (R_k) & RCSs (A_k)						SNR
128	10 MHz	11.72 cm	2 m 100	3 m 100	5 m 100	6 m 100	7 m 100	11 m 100	10

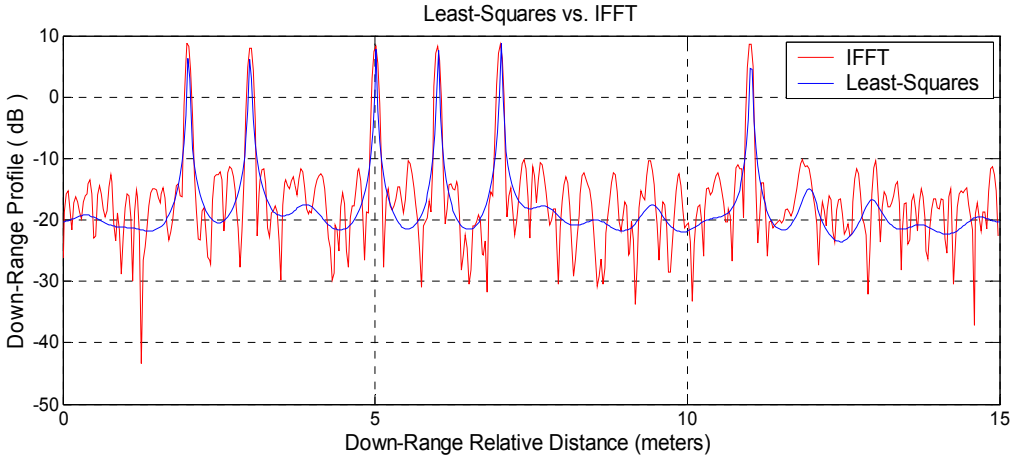

Figure 4.6. Comparison of least-squares method and IFFT

Figures 4.5 and 4.6, LS method provides sharper peaks at the target locations even in low SNR case. Also, note that range profile obtained from the LS method has lower variance, which improves the image quality when it is used in radar imaging.

Table 4.7. Parameters for simulation shown in figure 4.7

N	Δf	ΔR	Target Ranges (R_k) & RCSs (A_k)					SNR
128	10 MHz	11.72 cm	2 m 100	2.2 m 100	2.4 m 100	6 m 100	10 m 100	50

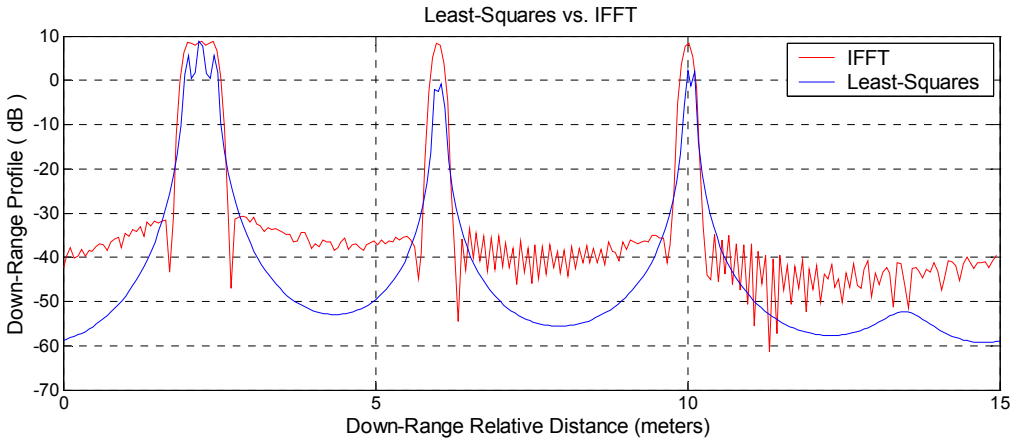

Figure 4.7. Comparison of least-squares method and IFFT

Table 4.8. Parameters for simulation shown in figure 4.8

N	Δf	ΔR	Target Ranges (R_k) & RCSs (A_k)					SNR
128	10 MHz	11.72 cm	2 m 100	2.2 m 100	2.4 m 100	6 m 100	10 m 100	20

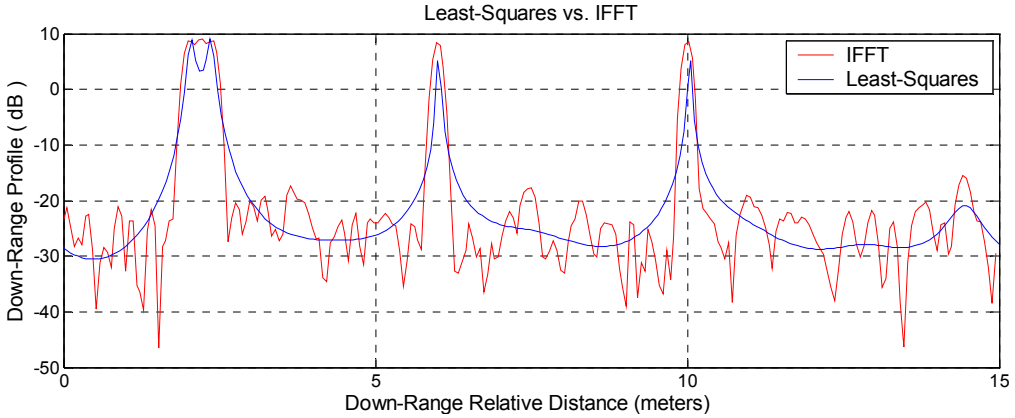

Figure 4.8. Comparison of least-squares method and IFFT

Figures 4.7 and 4.8 shows the performance of LS method to resolve closely separated targets both in high and low SNR case. When the SNR is high, LS can resolve three closely separated targets whereas IFFT can not. When the SNR is lower, LS can resolve two of the three targets.

Figures in this section show that LS method achieves better range resolution than IFFT. LS range profile has low variance, and it higher SCR and these advantages can be utilized in radar imaging, target identification and classification.

The previous sections showed that AR modeling is a good model to find the range profile of stepped-frequency radar. Same simulations have been carried out for ARMA model using modified Yule-Walker and two-stage least-squares methods explained in section 3.3.4.1 and 3.3.4.2, respectively, however, they did not provide stable and reliable range profiles. It has been observed that the choice of over-determination, M, in modified Yule-Walker method and the choice of AR model order truncation, K, in two-stage least-squares method and the choice of AR and MA model orders in both methods greatly affect the estimated range profile. Actually, this is not an unexpected situation since the ARMA model that is used to model spectra with narrow peaks and deep nulls is not appropriate for the stepped-frequency radar return signals where we only have narrow peaks. So, the simulation results of the modified Yule-Walker and two-stage least-squares methods will not be presented.

Sections 4.3.1 and 4.3.2 have provided the comparison of IFFT with parametric methods for rational spectra that are explained in section 3.3. Following sections present the results of the implementation of parametric methods for line spectra explained in section 3.4 and the comparison of each method with IFFT is presented.

4.3.3. Higher-Order Yule-Walker Method vs. IFFT

Table 4.9. Parameters for simulation shown in figure 4.9

N	Δf	M	L	ΔR	Target Ranges (R_k) & RCSs (A_k)						SNR
128	10 MHz	50	50	11.72 cm	0.5 m 100	1.5 m 100	2.8 m 100	4.5 m 100	5.7 m 100	7.2 m 100	50

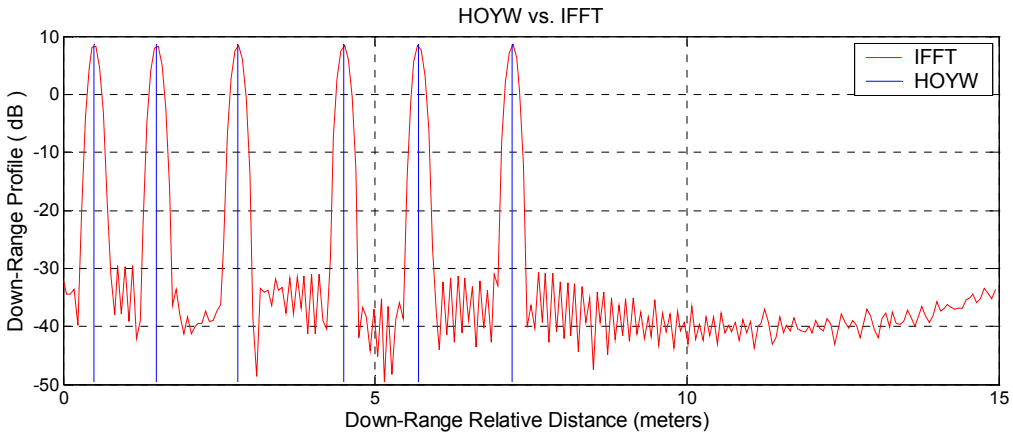

Figure 4.9. Comparison of HOYW method and IFFT

Table 4.10. Estimated HOYW ranges (in meters) in simulation shown in figure 4.9

0.4962	1.4999	2.8028	4.5017	5.7003	7.1989

Table 4.11. Parameters for simulation shown in figure 4.10

N	Δf	M	L	ΔR	Target Ranges (R_k) & RCSs (A_k)						SNR
128	10 MHz	50	50	11.72 cm	0.5 m 100	1.5 m 100	2.8 m 100	4.5 m 100	5.7 m 100	7.2 m 100	1

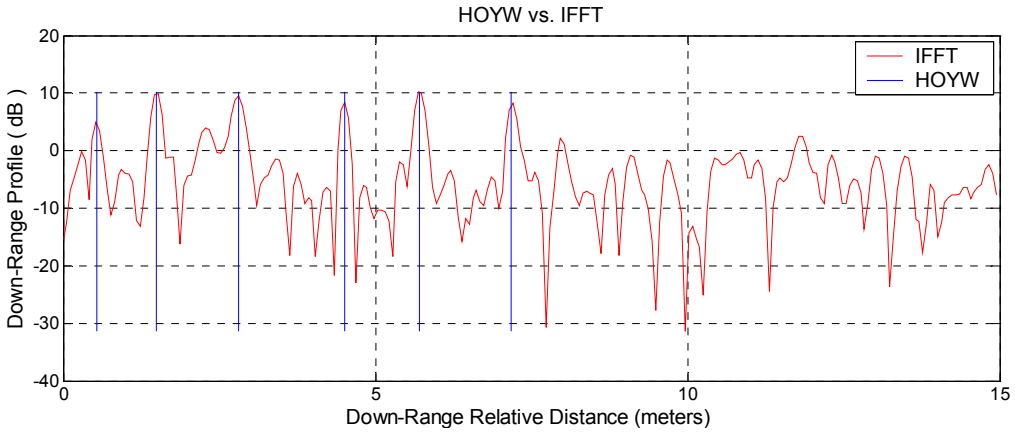

Figure 4.10. Comparison of HOYW method and IFFT

Table 4.12. Estimated HOYW ranges (in meters) in simulation shown in figure 4.10

0.5324	1.4972	2.8146	4.5059	5.7041	7.1776

Figures 4.9 and 4.10 illustrates that HOYW method can detect the ranges of the targets very accurately even in the very low SNR case.

Table 4.13. Parameters for simulation shown in figure 4.11

N	Δf	M	L	ΔR	Target Ranges (R_k) & RCSs (A_k)						SNR
128	10 MHz	**50**	**50**	11.72 cm	1.4 m 100	1.45 100	1.5 m 100	4 m 100	4.1 m 100	4.2 m 100	**50**

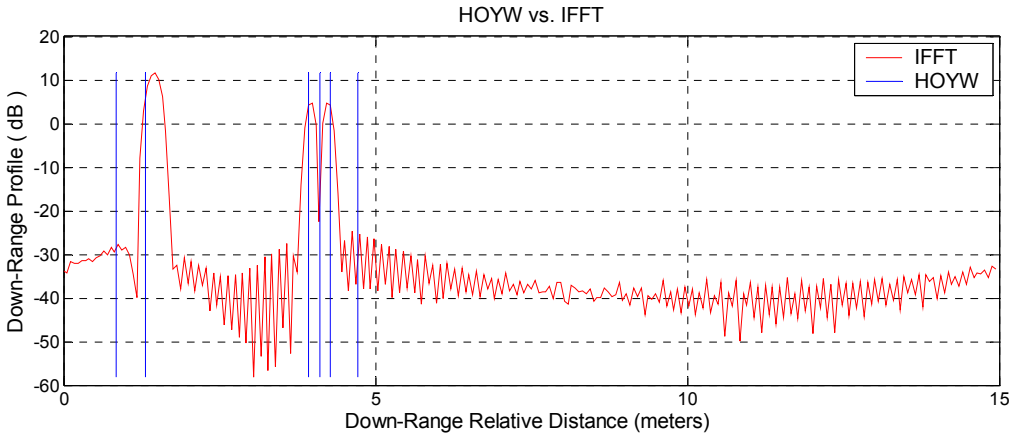

Figure 4.11. Comparison of HOYW method and IFFT

Table 4.14. Estimated HOYW ranges (in meters) in simulation shown in figure 4.11

1.3125	0.8401	4.7251	3.9303	4.1046	4.2724

Table 4.15. Parameters for simulation shown in figure 4.12

N	Δf	M	L	ΔR	Target Ranges (R_k) & RCSs (A_k)						SNR
128	10 MHz	**50**	**50**	11.72 cm	1.4 m 100	1.45 100	1.5 m 100	4 m 100	4.1 m 100	4.2 m 100	**20**

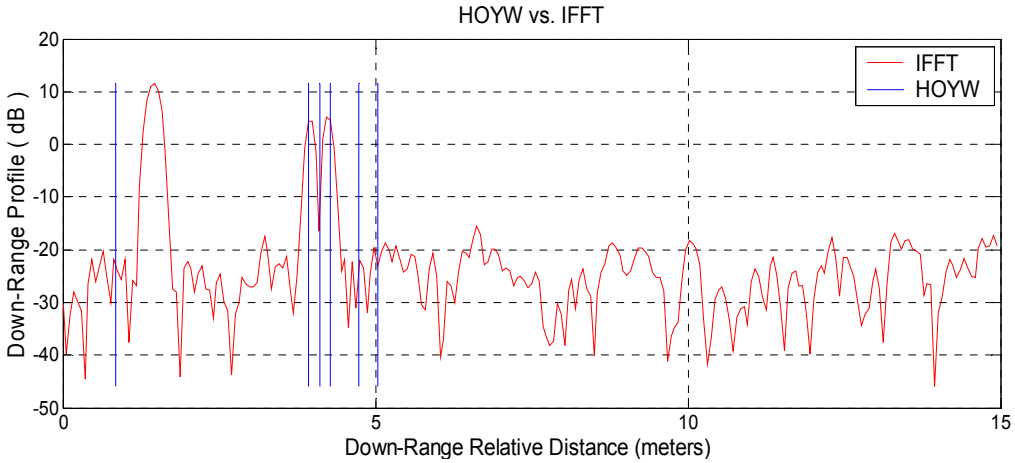

Figure 4.12. Comparison of HOYW method and IFFT

Table 4.16. Estimated HOYW ranges (in meters) in simulation shown in figure 4.12

0.8420	4.7272	5.0403	3.9296	4.1117	4.2746

Figures 4.11 and 4.12 show that, for the chosen M and L values, HOYW method may result in false alarms. Following figures show the effect of choice of M and L in the performance of HOYW method. Note that HOYW can resolve the last three closely spaced targets that can not be resolved by IFFT.

Table 4.17. Parameters for simulation shown in figure 4.13

N	Δf	M	L	ΔR	Target Ranges (R_k) & RCSs (A_k)						SNR
128	10 MHz	**40**	**40**	11.72 cm	1.4 m 100	1.45 100	1.5 m 100	4 m 100	4.1 m 100	4.2 m 100	**50**

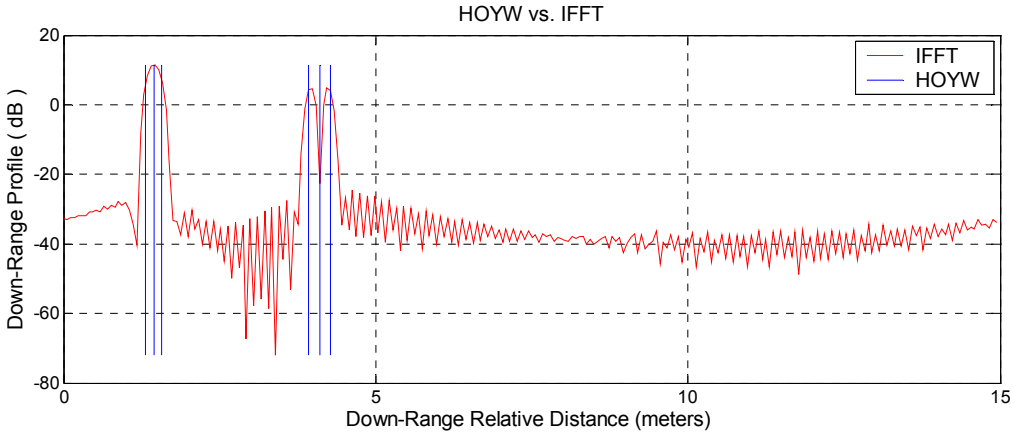

Figure 4.13. Comparison of HOYW method and IFFT

Table 4.18. Estimated HOYW ranges (in meters) in simulation shown in figure 4.13

1.3181	1.4480	1.5788	3.9296	4.0993	4.2704

Table 4.19. Parameters for simulation shown in figure 4.14

N	Δf	M	L	ΔR	Target Ranges (R_k) & RCSs (A_k)						SNR
128	10 MHz	**40**	**40**	11.72 cm	1.4 m 100	1.45 100	1.5 m 100	4 m 100	4.1 m 100	4.2 m 100	**20**

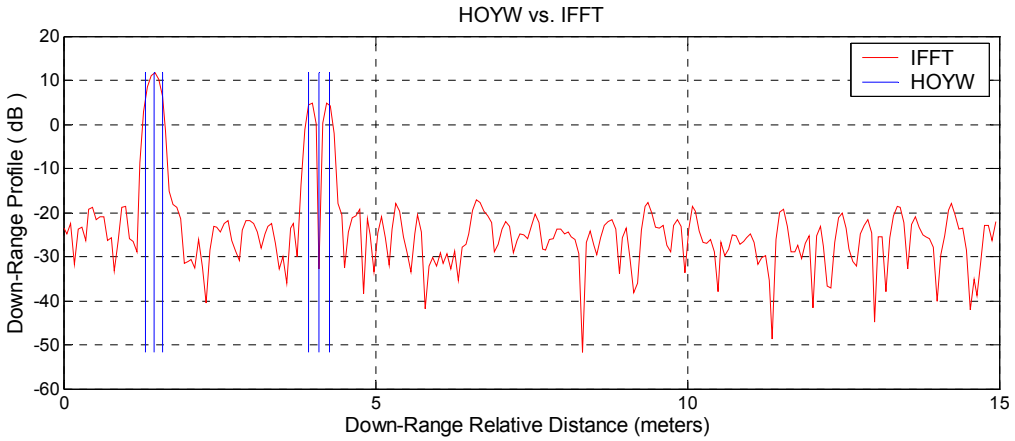

Figure 4.14. Comparison of HOYW method and IFFT

Table 4.20. Estimated HOYW ranges (in meters) in simulation shown in figure 4.14

1.3195	1.4525	1.5831	3.9321	4.0983	4.2680

Figures 4.13 and 4.14 show that when M and L are chosen as 40, and keeping the radar parameters and targets' ranges and RCS values same, HOYW can resolve all the targets and estimates the target ranges even in low SNR case. This illustrates the sensitivity of HOYW method to the choice of M and L.

Table 4.21. Parameters for simulation shown in figure 4.15

N	Δf	M	L	ΔR	Target Ranges (R_k) & RCSs (A_k)						SNR
128	10 MHz	**50**	**50**	11.72 cm	1.4 m 1000	1.45 **1**	1.5 m 1000	4 m 1000	4.1 m 1	4.2 m 1	**50**

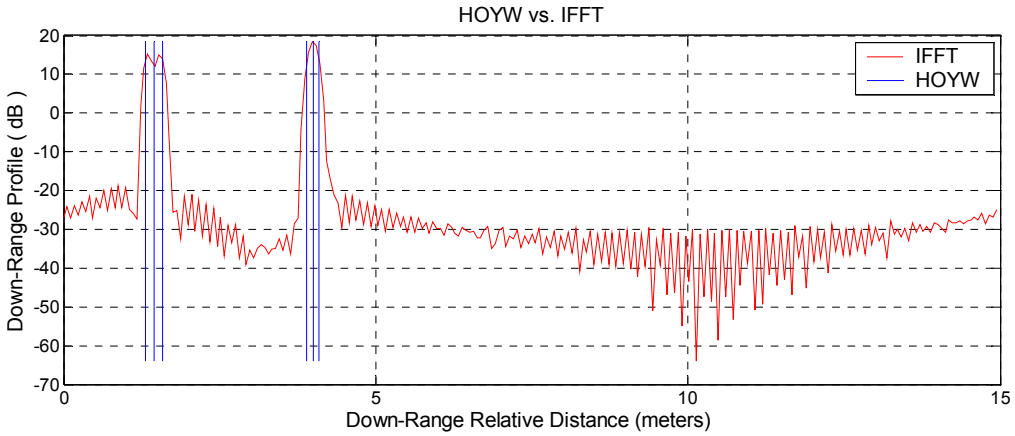

Figure 4.15. Comparison of HOYW method and IFFT

Table 4.22. Estimated HOYW ranges (in meters) in simulation shown in figure 4.15

1.3195	1.4424	1.5795	3.8882	3.9935	4.0988

Table 4.23. Parameters for simulation shown in figure 4.16

N	Δf	M	L	ΔR	Target Ranges (R_k) & RCSs (A_k)						SNR
128	10 MHz	**50**	**50**	11.72 cm	1.4 m 1000	1.45 **100**	1.5 m 1000	4 m 1000	4.1 m 1	4.2 m 1	**50**

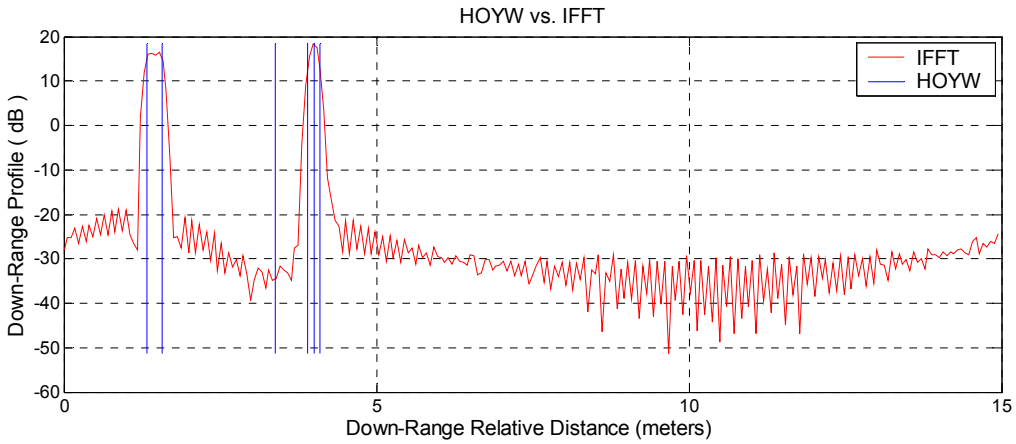

Figure 4.16. Comparison of HOYW method and IFFT

Table 4.24. Estimated HOYW ranges (in meters) in simulation shown in figure 4.16

1.3266	3.3817	1.4424	3.8926	3.9975	4.1008

In figures 4.15 and 4.16, only the RCS value of the second targets is changed. Although the second target is expected to be detected when it has higher RCS value, the simulations yield the opposite result. It can be concluded that HOYW method is very sensitive not only to M and L values but also to the target locations and RCS values. Note that using 40 as M and L values provided correct range estimates. On the other hand, also note that HOYW can resolve the last three targets whereas IFFT can not, i.e., HOYW method provides better range resolution than IFFT. So, a combined technique that uses HOYW method together with IFFT can achieve better range resolution and lower false alarms.

4.3.4. Root-MUSIC vs. IFFT

Table 4.25. Parameters for simulation shown in figure 4.17

N	Δf	M	MSSP	ΔR	Target Ranges (R_k) & RCSs (A_k)						SNR
128	10 MHz	**20**	**NO**	11.72 cm	0.5 m 100	1.5 m 100	2.8 m 100	4.5 m 100	5.7 m 100	7.2 m 100	**50**

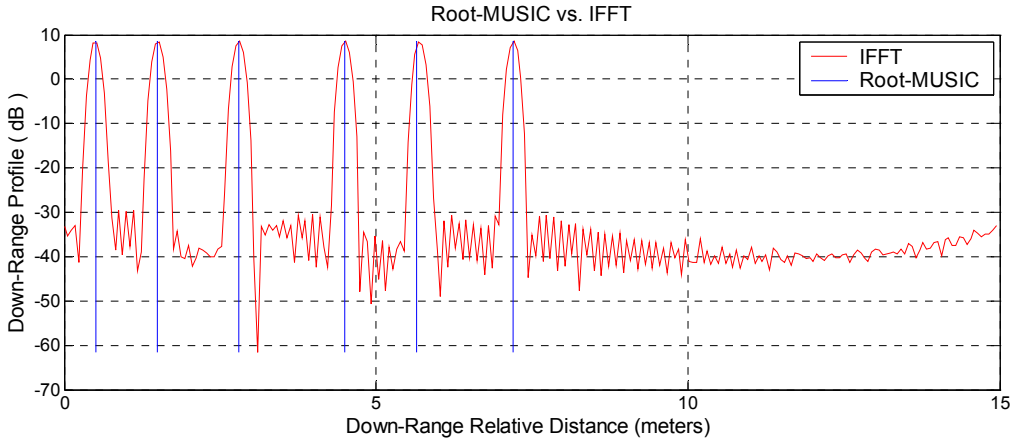

Figure 4.17. Comparison of Root-MUSIC method and IFFT

Table 4.26. Estimated Root-MUSIC ranges (in meters) in simulation shown in figure 4.17

0.5053	1.4975	2.8012	4.4982	5.6564	7.1974

Table 4.27. Parameters for simulation shown in figure 4.18

N	Δf	M	MSSP	ΔR	Target Ranges (R_k) & RCSs (A_k)						SNR
128	10 MHz	**20**	**NO**	11.72 cm	0.5 m 100	1.5 m 100	2.8 m 100	4.5 m 100	5.7 m 100	7.2 m 100	**7**

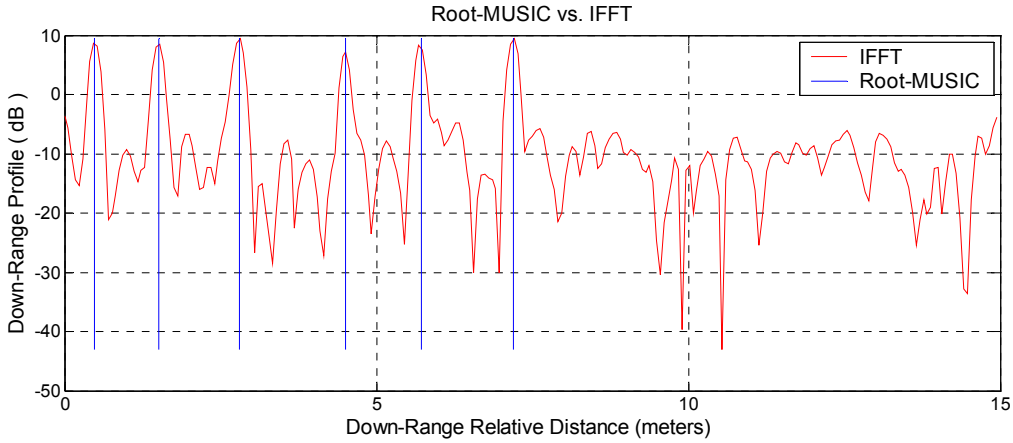

Figure 4.18. Comparison of Root-MUSIC method and IFFT

Table 4.28. Estimated Root-MUSIC ranges (in meters) in simulation shown in figure 4.18

0.4799	1.5046	2.7977	4.4865	5.7152	7.1857

Figures 4.17 and 4.18 shows that Root-MUSIC method can detect the ranges of the targets very accurately even in the very low SNR case.

Table 4.29. Parameters for simulation shown in figure 4.19

N	Δf	M	MSSP	ΔR	Target Ranges (R_k) & RCSs (A_k)						SNR
128	10 MHz	**20**	**NO**	11.72 cm	1.4 m 100	1.45 100	1.5 m 100	4 m 100	4.1 m 100	4.2 m 100	**50**

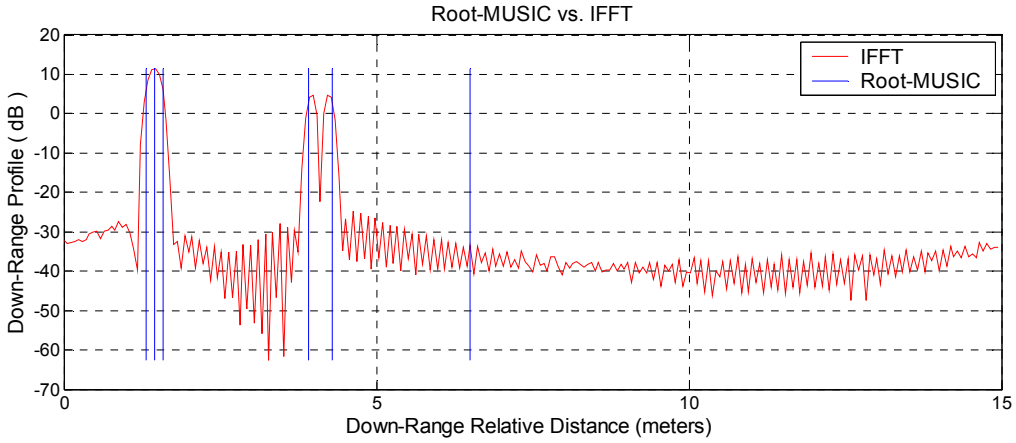

Figure 4.19. Comparison of Root-MUSIC method and IFFT

Table 4.30. Estimated Root-MUSIC ranges (in meters) in simulation shown in figure 4.19

1.3136	1.4499	1.5866	3.9199	6.4950	4.2876

Table 4.31. Parameters for simulation shown in figure 4.20

N	Δf	M	MSSP	ΔR	Target Ranges (R_k) & RCSs (A_k)						SNR
128	10 MHz	**20**	**YES**	11.72 cm	1.4 m 100	1.45 100	1.5 m 100	4 m 100	4.1 m 100	4.2 m 100	**50**

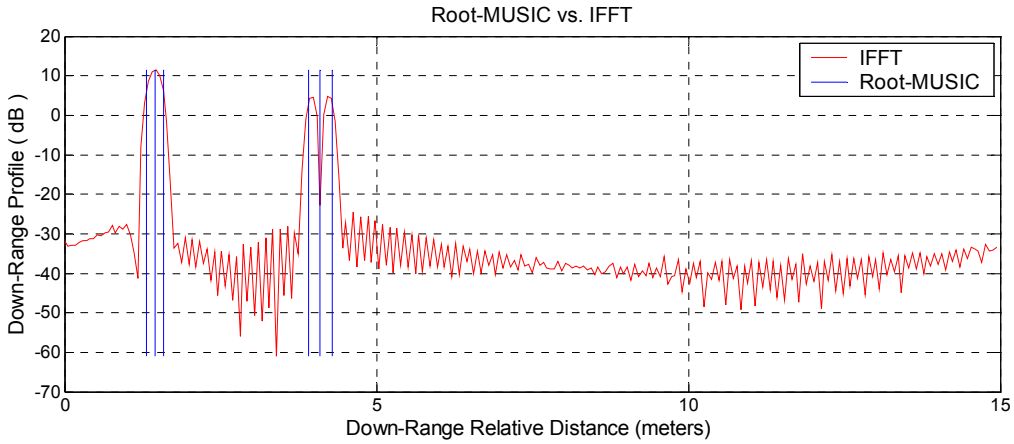

Figure 4.20. Comparison of Root-MUSIC method and IFFT

Table 4.32. Estimated Root-MUSIC ranges (in meters) in simulation shown in figure 4.20

1.3105	1.4486	1.5865	3.9151	4.1023	4.2866

As can be seen from figures 4.19 and 4.20, using modified spatial smoothing technique improves the accuracy of range estimates. Note that Root-MUSIC method achieves much better range resolution than IFFT. Also note that Root-MUSIC can resolve very closely spaced targets where the distance between the targets are less than the range resolution of the IFFT.

Table 4.33. Parameters for simulation shown in figure 4.21

N	Δf	M	MSSP	ΔR	Target Ranges (R_k) & RCSs (A_k)						SNR
128	10 MHz	**20**	**NO**	11.72 cm	1.4 m 1000	1.45 1	1.5 m 1000	4 m 1000	4.1 m 1	4.2 m 1	**50**

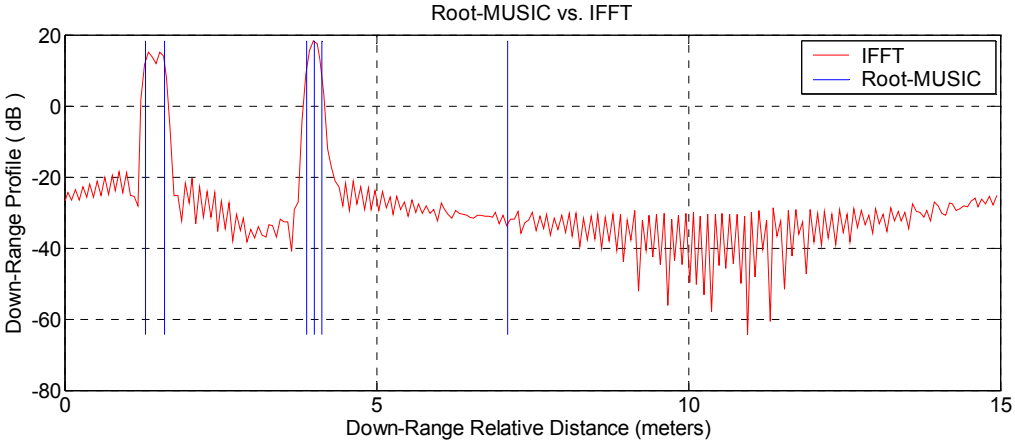

Figure 4.21. Comparison of Root-MUSIC method and IFFT

Table 4.34. Estimated Root-MUSIC ranges (in meters) in simulation shown in figure 4.21

1.2931	7.1122	1.6018	3.8801	3.9992	4.1202

Table 4.35. Parameters for simulation shown in figure 4.22

N	Δf	M	MSSP	ΔR	Target Ranges (R_k) & RCSs (A_k)						SNR
128	10 MHz	**20**	**YES**	11.72 cm	1.4 m 1000	1.45 1	1.5 m 1000	4 m 1000	4.1 m 1	4.2 m 1	**50**

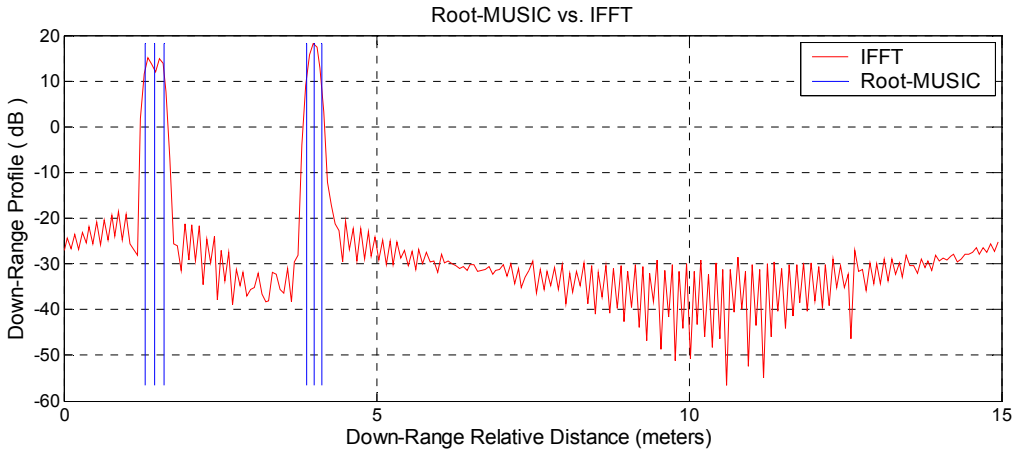

Figure 4.22. Comparison of Root-MUSIC method and IFFT

Table 4.36. Estimated Root-MUSIC ranges (in meters) in simulation shown in figure 4.22

1.2962	1.4515	1.6071	3.8866	4.0041	4.1257

Figures 4.21 and 4.22 show that MSSP technique improves the accuracy of Root-MUSIC range estimates and decreases the number of false alarms. Note that in all cases, Root-MUSIC achieves much better range-resolution than IFFT. It has been observed that a method that combines Root-MUSIC and IFFT can increase the range resolution and decrease the false alarms.

4.3.5. Minimum-Norm Method vs. IFFT

Table 4.37. Parameters for simulation shown in figure 4.23

N	Δf	M	ΔR	Target Ranges (R_k) & RCSs (A_k)						SNR
128	10 MHz	50	11.72 cm	0.5 m 100	1.5 m 100	2.8 m 100	4.5 m 100	5.7 m 100	7.2 m 100	50

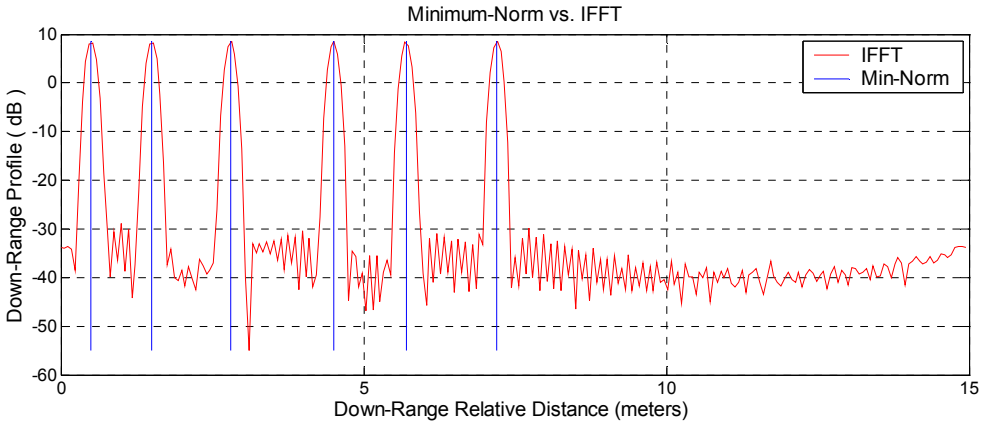

Figure 4.23. Comparison of Min-Norm method and IFFT

Table 4.38. Estimated Min-Norm ranges (in meters) in simulation shown in figure 4.23

0.5011	1.5001	2.7984	4.5023	5.6992	7.1986

Table 4.39. Parameters for simulation shown in figure 4.24

N	Δf	M	ΔR	Target Ranges (R_k) & RCSs (A_k)						SNR
128	10 MHz	50	11.72 cm	0.5 m 100	1.5 m 100	2.8 m 100	4.5 m 100	5.7 m 100	7.2 m 100	1

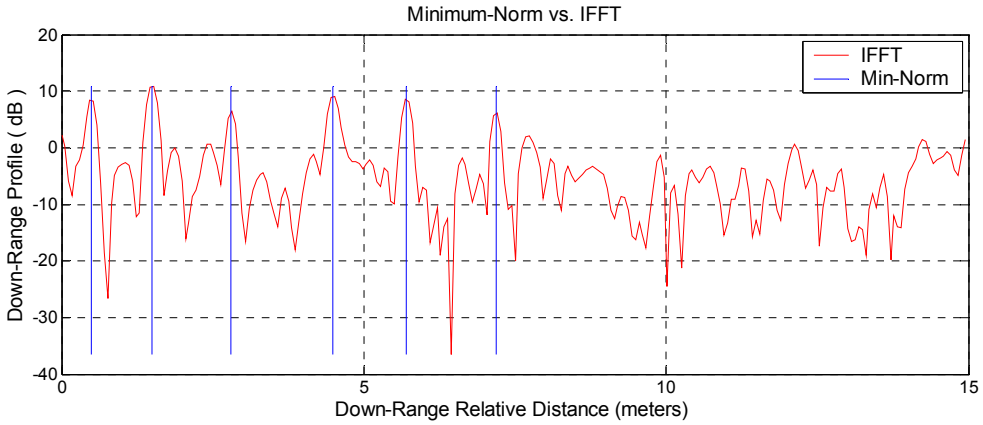

Figure 4.24. Comparison of Min-Norm method and IFFT

Table 4.40. Estimated Min-Norm ranges (in meters) in simulation shown in figure 4.24

0.4990	1.4897	2.7680	4.4663	5.7009	7.1941

Figures 4.23 and 4.24 illustrates that Minimum-Norm method can find the ranges of the targets very accurately even in the very low SNR case.

Table 4.41. Parameters for simulation shown in figure 4.25

N	Δf	M	ΔR	Target Ranges (R_k) & RCSs (A_k)						SNR
128	10 MHz	50	11.72 cm	1.4 m 100	1.45 100	1.5 m 100	4 m 100	4.1 m 100	4.2 m 100	50

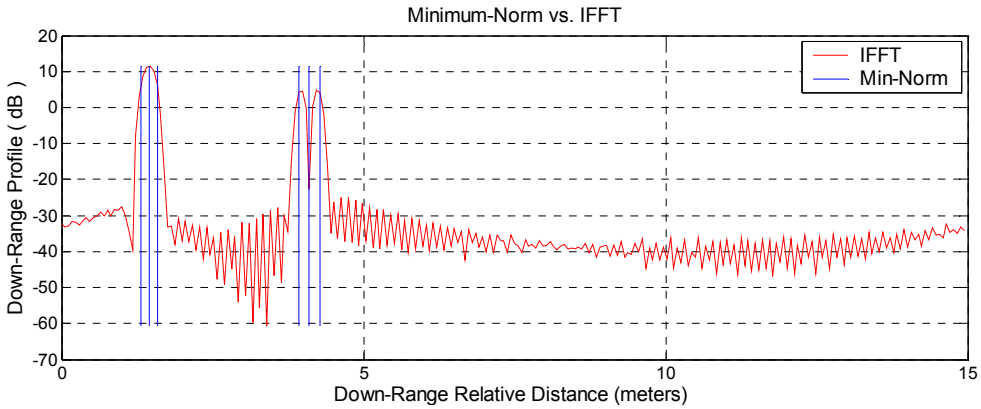

Figure 4.25. Comparison of Min-Norm method and IFFT

Table 4.42. Estimated Min-Norm ranges (in meters) in simulation shown in figure 4.25

1.3190	1.4585	1.5956	3.9300	4.1026	4.2714

Table 4.43. Parameters for simulation shown in figure 4.26

N	Δf	M	ΔR	Target Ranges (R_k) & RCSs (A_k)						SNR
128	10 MHz	50	11.72 cm	1.4 m 100	1.45 100	1.5 m 100	4 m 100	4.1 m 100	4.2 m 100	20

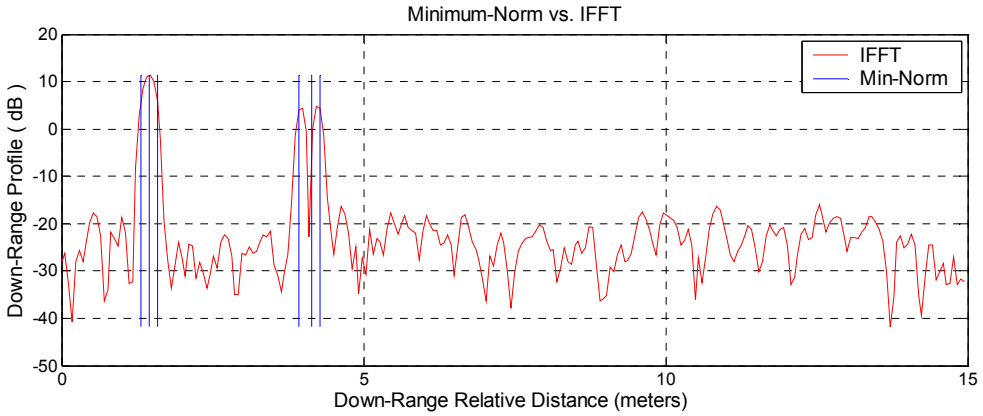

Figure 4.26. Comparison of Min-Norm method and IFFT

Table 4.44. Estimated Min-Norm ranges (in meters) in simulation shown in figure 4.26

1.3145	1.4511	1.5854	3.9352	4.1381	4.2756

From figures 4.25 and 4.26, it can be concluded that Minimum-Norm can detect the closely separated targets accurately even in low SNR case. Note that IFFT results have one broad peak for the first three very closely separated targets and two peaks for the second closely separated three targets whereas Minimum-Norm can resolve all the closely separated targets very accurately even in low SNR case.

Table 4.45. Parameters for simulation shown in figure 4.27

N	Δf	M	ΔR	Target Ranges (R_k) & RCSs (A_k)						SNR
128	10 MHz	50	11.72 cm	1.4 m 1000	1.45 1	1.5 m 1000	4 m 1000	4.1 m 1	4.2 m 1	50

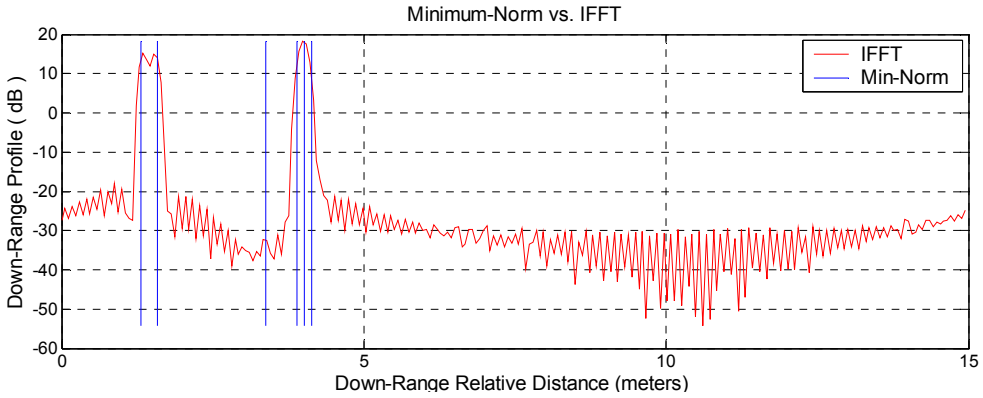

Figure 4.27. Comparison of Min-Norm method and IFFT

Table 4.46. Estimated Min-Norm ranges (in meters) in simulation shown in figure 4.27

1.3093	3.3798	1.5928	3.8890	4.0095	4.1298

Table 4.47. Parameters for simulation shown in figure 4.28

N	Δf	M	ΔR	Target Ranges (R_k) & RCSs (A_k)						SNR
128	10 MHz	50	11.72 cm	1.4 m 1000	1.45 1	1.5 m 1000	4 m 1000	4.1 m 1	4.2 m 1	20

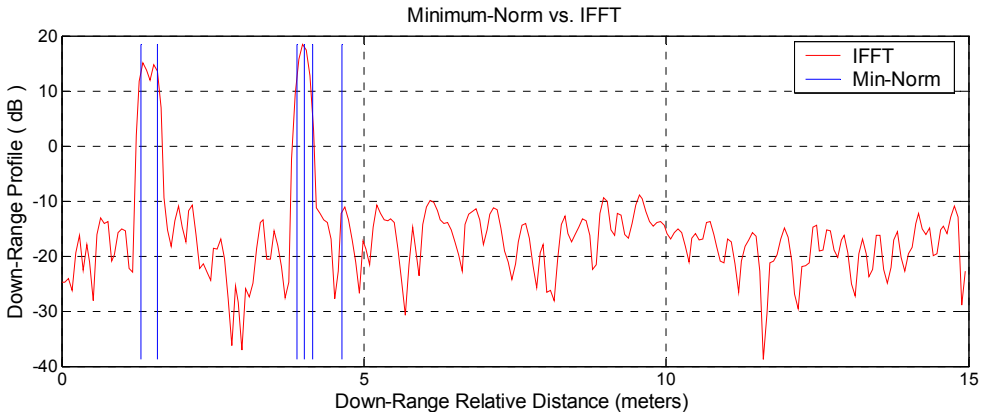

Figure 4.28. Comparison of Min-Norm method and IFFT

Table 4.48. Estimated Min-Norm ranges (in meters) in simulation shown in figure 4.28

1.3103	4.6356	1.5900	3.9002	4.0205	4.1465

As can be seen from the figures 4.27 and 4.28, Minimum-Norm method can detect the closely separated targets which have very different RCS values accurately even in low SNR case. However, note that Minimum-Norm method gives wrong estimate for the second target in both SNR values. It can be concluded that the range resolution of Minimum-Norm method is better than IFFT but when the targets that have very different RCS values are very close to each other, Minimum-Norm method may give false alarms. In order to reduce false alarms, IFFT and Minimum norm method can be used together.

In the next case, modified spatial smoothing processing technique will be implemented to reduce the false alarms for the same radar and target parameters.

Table 4.49. Parameters for simulation shown in figure 4.29

N	Δf	M	ΔR	Target Ranges (R_k) & RCSs (A_k)						SNR
128	10 MHz	50	11.72 cm	1.4 m 1000	1.45 1	1.5 m 1000	4 m 1000	4.1 m 1	4.2 m 1	50

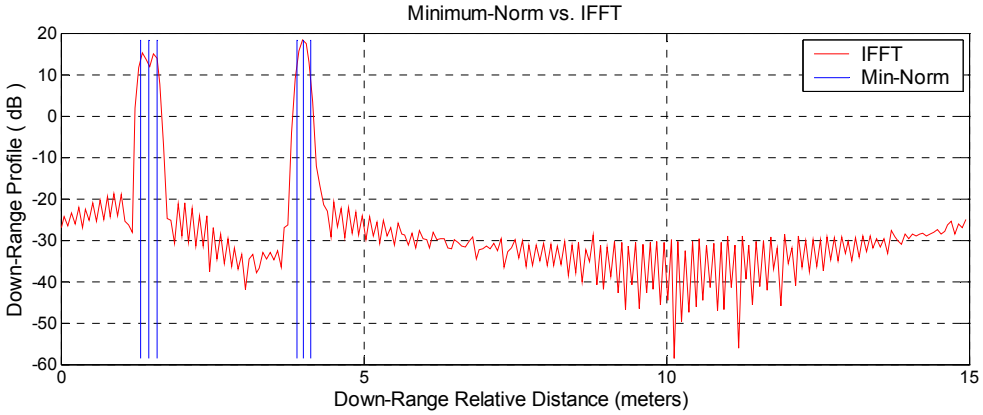

Figure 4.29. Comparison of Min-Norm method and IFFT

Table 4.50. Estimated Min-Norm ranges (in meters) in simulation shown in figure 4.29

1.3100	1.4503	1.5916	3.8932	4.0110	4.1286

Table 4.51. Parameters for simulation shown in figure 4.30

N	Δf	M	ΔR	Target Ranges (R_k) & RCSs (A_k)						SNR
128	10 MHz	50	11.72 cm	1.4 m 1000	1.45 1	1.5 m 1000	4 m 1000	4.1 m 1	4.2 m 1	20

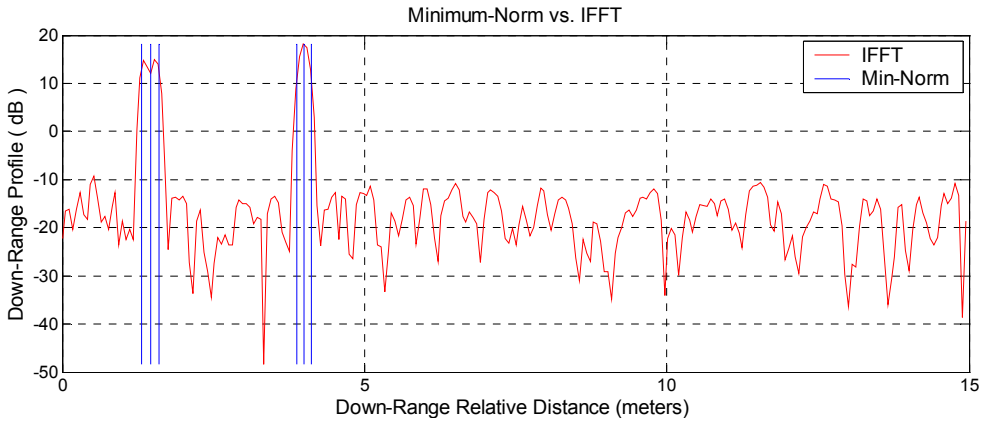

Figure 4.30. Comparison of Min-Norm method and IFFT

Table 4.52. Estimated Min-Norm ranges (in meters) in simulation shown in figure 4.30

1.3183	1.4658	1.5956	3.8837	3.9988	4.1170

As can be seen from figures 4.29 and 4.30, applying modified spatial smoothing processing technique eliminates the false alarms. So, Minimum-Norm method, when implemented together with MSSP, can provide high range resolution and reliable range estimates.

4.3.6. LS-ESPRIT vs. IFFT

Table 4.53. Parameters for simulation shown in figure 4.31

N	Δf	M	ΔR	Target Ranges (R_k) & RCSs (A_k)						SNR
128	10 MHz	50	11.72 cm	0.5 m 100	1.5 m 100	2.8 m 100	4.5 m 100	5.7 m 100	7.2 m 100	50

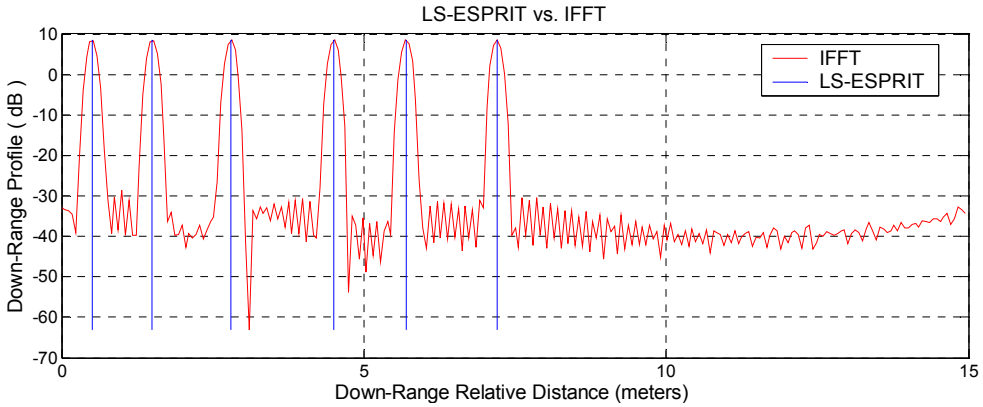

Figure 4.31. Comparison of LS-ESPRIT method and IFFT

Table 4.54. Estimated LS-ESPRIT ranges (in meters) in simulation shown in figure 4.31

0.5023	1.5008	2.7985	4.5021	5.6987	7.1966

Table 4.55. Parameters for simulation shown in figure 4.32

N	Δf	M	ΔR	Target Ranges (R_k) & RCSs (A_k)						SNR
128	10 MHz	50	11.72 cm	0.5 m 100	1.5 m 100	2.8 m 100	4.5 m 100	5.7 m 100	7.2 m 100	1

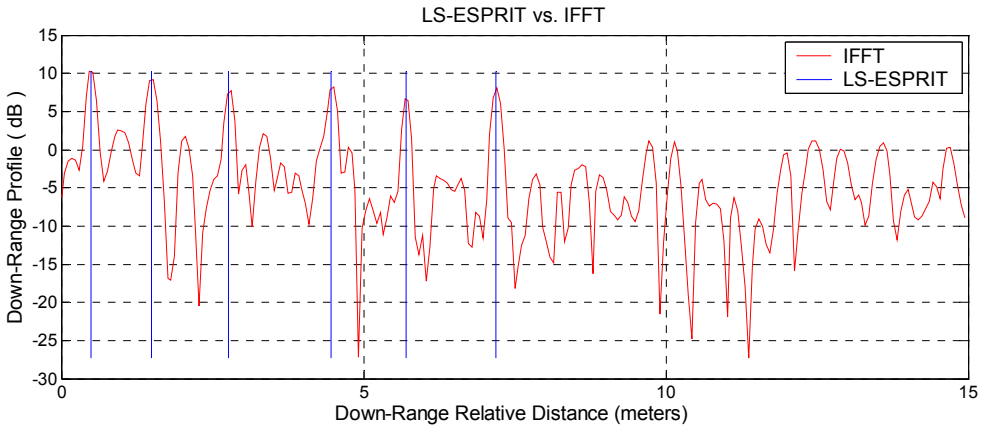

Figure 4.32. Comparison of LS-ESPRIT method and IFFT

Table 4.56. Estimated LS-ESPRIT ranges (in meters) in simulation shown in figure 4.32

0.4990	1.4897	2.7680	4.4663	5.7009	7.1941

Figures 4.31 and 4.32 shows that LS-ESPRIT method provides very accurate range estimates even for very low SNR values.

Table 4.57. Parameters for simulation shown in figure 4.33

N	Δf	M	ΔR	Target Ranges (R_k) & RCSs (A_k)						SNR
128	10 MHz	50	11.72 cm	1.4 m 100	1.45 100	1.5 m 100	4 m 100	4.1 m 100	4.2 m 100	50

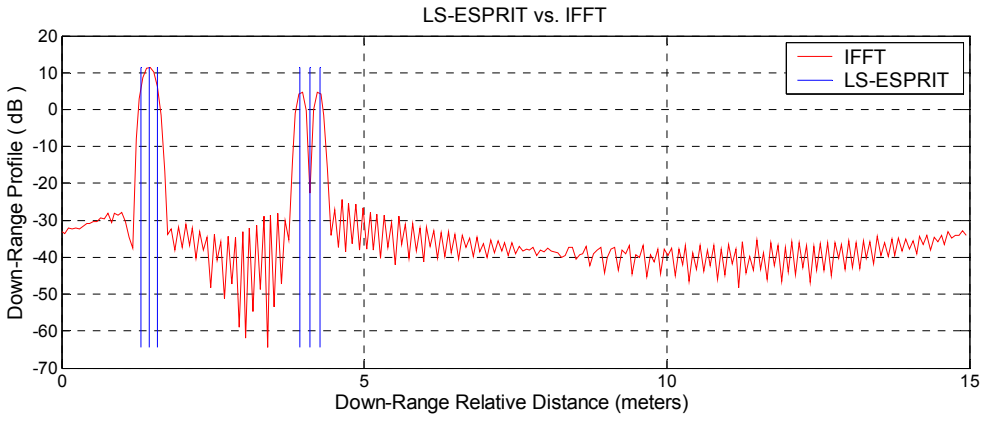

Figure 4.33. Comparison of LS-ESPRIT method and IFFT

Table 4.58. Estimated LS-ESPRIT ranges (in meters) in simulation shown in figure 4.33

1.3177	1.4540	1.5899	3.9347	4.0995	4.2655

Table 4.59. Parameters for simulation shown in figure 4.34

N	Δf	M	ΔR	Target Ranges (R_k) & RCSs (A_k)						SNR
128	10 MHz	50	11.72 cm	1.4 m 100	1.45 100	1.5 m 100	4 m 100	4.1 m 100	4.2 m 100	20

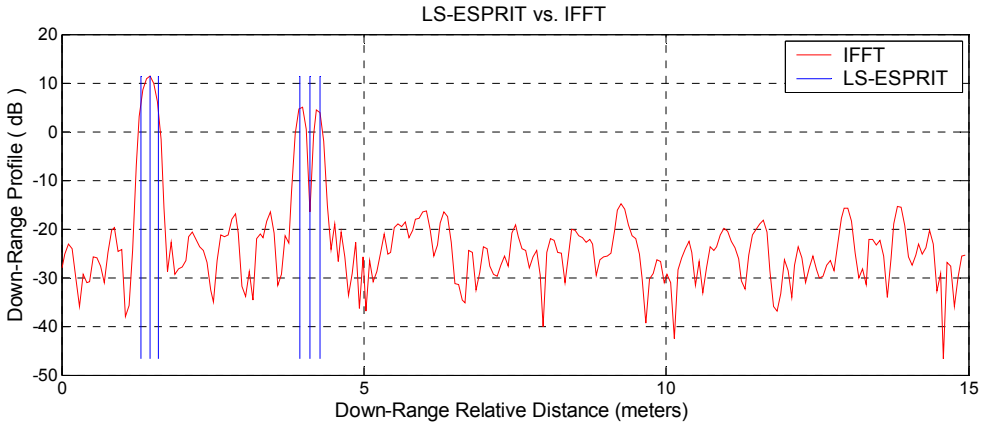

Figure 4.34. Comparison of LS-ESPRIT method and IFFT

Table 4.60. Estimated LS-ESPRIT ranges (in meters) in simulation shown in figure 4.34

1.3192	1.4578	1.5950	3.9327	4.1007	4.2674

From figures 4.33 and 4.34, it can be concluded that TLS-ESPRIT can detect the closely separated targets accurately even in low SNR case. Note that IFFT results have one broad peak for the first three very closely separated targets and two peaks for the second closely separated three targets whereas TLS-ESPRIT can resolve all the closely separated targets very accurately even in low SNR case.

Table 4.61. Parameters for simulation shown in figure 4.35

N	Δf	M	ΔR	Target Ranges (R_k) & RCSs (A_k)						SNR
128	10 MHz	50	11.72 cm	1.4 m 1000	1.45 1	1.5 m 1000	4 m 1000	4.1 m 1	4.2 m 1	50

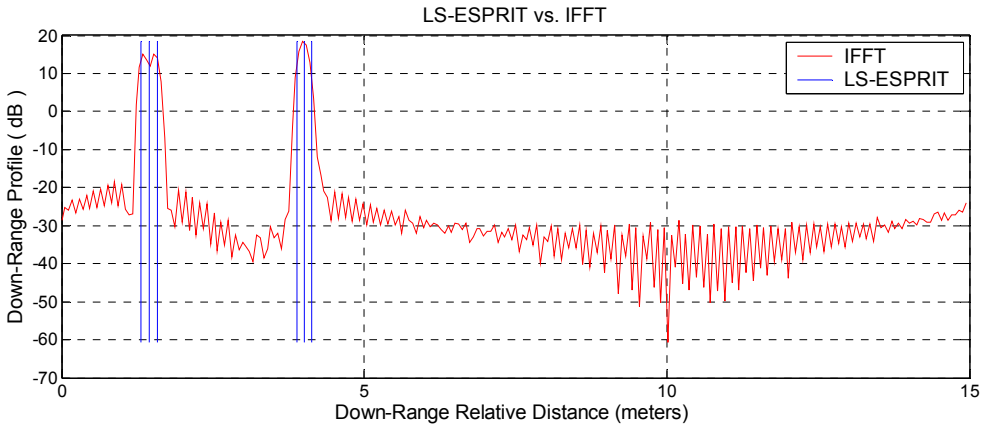

Figure 4.35. Comparison of LS-ESPRIT method and IFFT

Table 4.62. Estimated LS-ESPRIT ranges (in meters) in simulation shown in figure 4.35

1.3085	1.4490	1.5910	3.8895	4.0083	4.1290

Table 4.63. Parameters for simulation shown in figure 4.36

N	Δf	M	ΔR	Target Ranges (R_k) & RCSs (A_k)						SNR
128	10 MHz	50	11.72 cm	1.4 m 1000	1.45 1	1.5 m 1000	4 m 1000	4.1 m 1	4.2 m 1	20

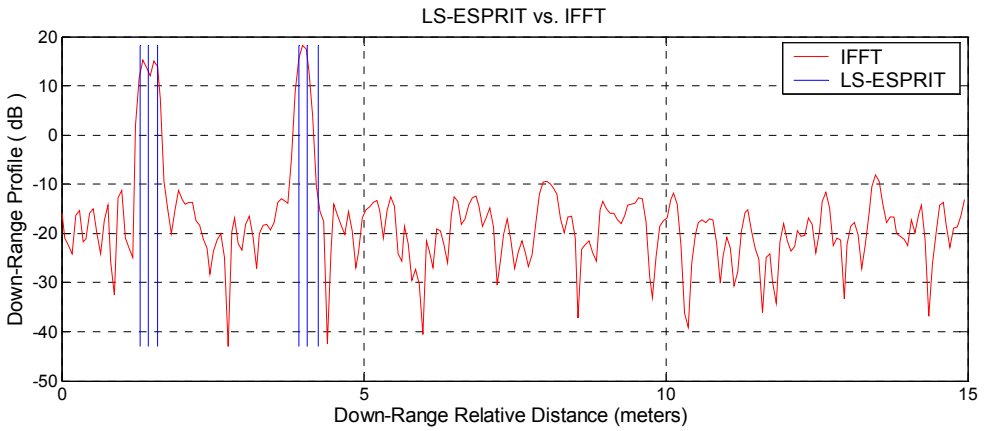

Figure 4.36. Comparison of LS-ESPRIT method and IFFT

Table 4.64. Estimated LS-ESPRIT ranges (in meters) in simulation shown in figure 4.36

1.3066	1.4416	1.5887	3.9334	4.0586	4.2515

From figures 4.35 and 4.36, it can be seen that LS-ESPRIT can detect the closely separated targets which have very different radar cross sections very accurately even in

low SNR case. Note that IFFT results have one broad peak for the last three targets that have RCS values of 1000, 1, and 1 and two peaks for the first three targets that have RCS values of 1000, 1, and 1000. Note that this case is a similar to the scenario where the there is a small hidden object just beneath the wall or a small buried object with small RCS just under the surface. LS-ESPRIT can resolve closely separated targets with very different RCS values, however, because of smearing, IFFT can not resolve them.

4.3.7. TLS-ESPRIT vs. IFFT

Table 4.65. Parameters for simulation shown in figure 4.37

N	Δf	M	ΔR	Target Ranges (R_k) & RCSs (A_k)						SNR
128	10 MHz	50	11.72 cm	0.5 m 100	1.5 m 100	2.8 m 100	4.5 m 100	5.7 m 100	7.2 m 100	50

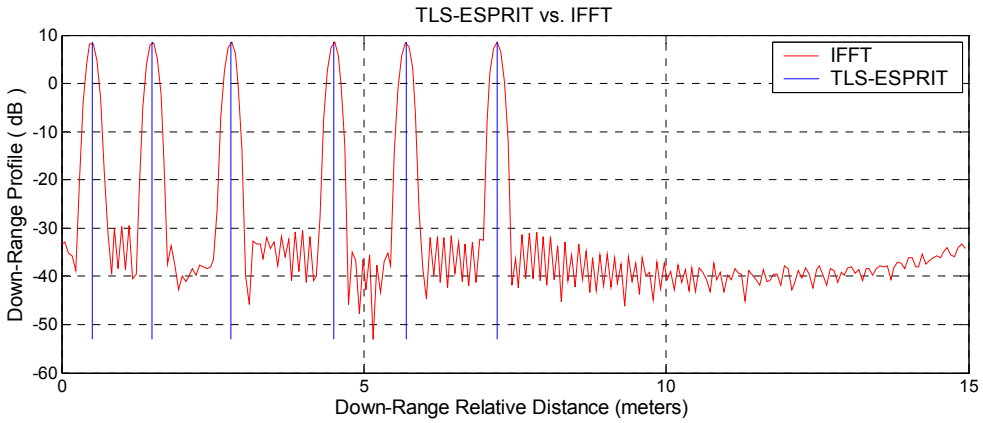

Figure 4.37. Comparison of TLS-ESPRIT method and IFFT

Table 4.66. Estimated TLS-ESPRIT ranges (in meters) in simulation shown in figure 4.37

0.5026	1.5009	2.7985	4.5021	5.6986	7.1966

Table 4.67. Parameters for simulation shown in figure 4.38

N	Δf	M	ΔR	Target Ranges (R_k) & RCSs (A_k)						SNR
128	10 MHz	50	11.72 cm	0.5 m 100	1.5 m 100	2.8 m 100	4.5 m 100	5.7 m 100	7.2 m 100	1

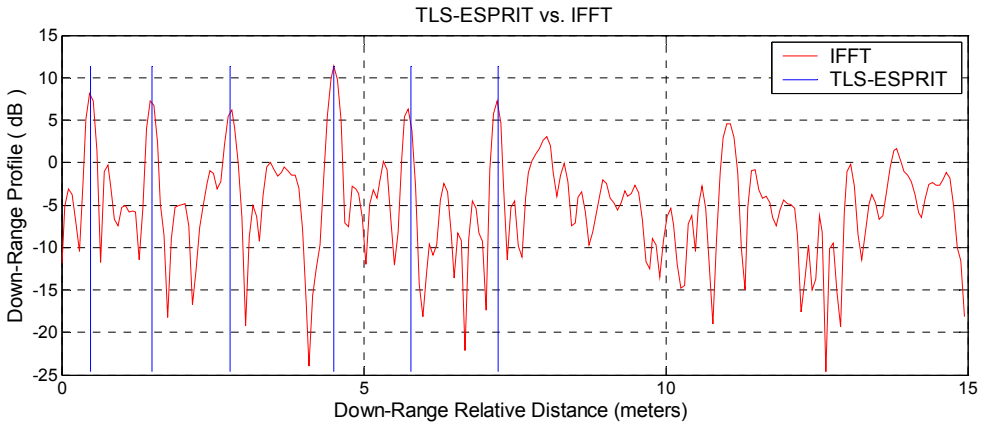

Figure 4.38. Comparison of TLS-ESPRIT method and IFFT

Table 4.68. Estimated TLS-ESPRIT ranges (in meters) in simulation shown in figure 4.38

0.4736	1.5009	2.7954	4.5085	5.7801	7.2303

From figures 4.37 and 4.38, it can be seen that TLS-ESPRIT can detect the ranges of the targets very accurately even in the very low SNR case.

Table 4.69. Parameters for simulation shown in figure 4.39

N	Δf	M	ΔR	Target Ranges (R_k) & RCSs (A_k)						SNR
128	10 MHz	50	11.72 cm	1.4 m 100	1.45 100	1.5 m 100	4 m 100	4.1 m 100	4.2 m 100	50

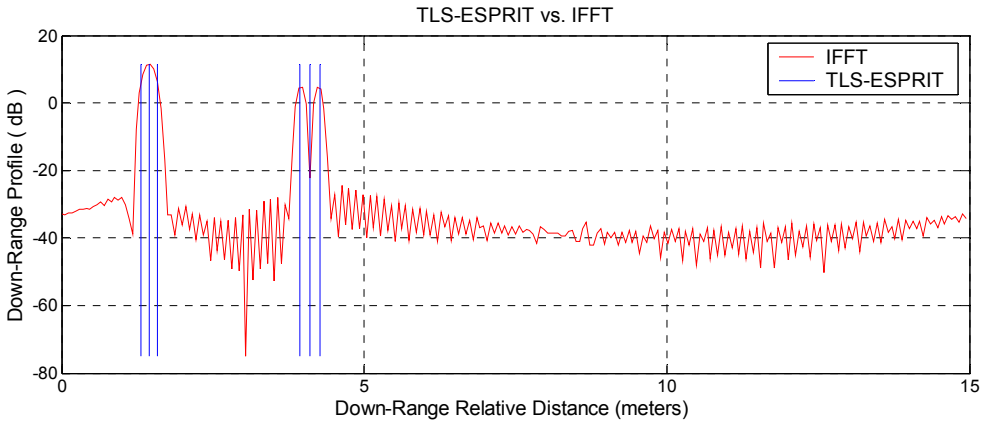

Figure 4.39. Comparison of TLS-ESPRIT method and IFFT

Table 4.70. Estimated TLS-ESPRIT ranges (in meters) in simulation shown in figure 4.39

1.3179	1.4540	1.5897	3.9349	4.1002	4.2657

Table 4.71. Parameters for simulation shown in figure 4.40

$-N$	Δf	M	ΔR	Target Ranges (R_k) & RCSs (A_k)						SNR
128	10 MHz	50	11.72 cm	1.4 m 100	1.45 100	1.5 m 100	4 m 100	4.1 m 100	4.2 m 100	20

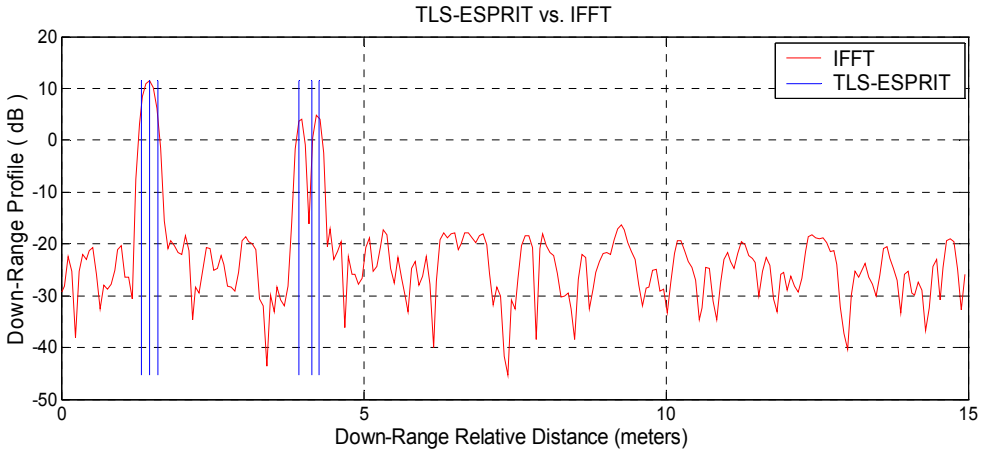

Figure 4.40. Comparison of TLS-ESPRIT method and IFFT

Table 4.72. Estimated TLS-ESPRIT ranges (in meters) in simulation shown in figure 4.40

1.3248	1.4622	1.5960	3.9390	4.1437	4.2628

From figures 4.39 and 4.40, it can be concluded that TLS-ESPRIT can detect the closely separated targets accurately even in low SNR case. Note that IFFT results have one broad peak for the first three very closely separated targets and two peaks for the second closely separated three targets whereas TLS-ESPRIT can resolve all the closely separated targets very accurately even in low SNR case.

Table 4.73. Parameters for simulation shown in figure 4.41

N	Δf	M	ΔR	Target Ranges (R_k) & RCSs (A_k)						SNR
128	10 MHz	50	11.72 cm	1.4 m 1000	1.45 1	1.5 m 1000	4 m 1000	4.1 m 1	4.2 m 1	50

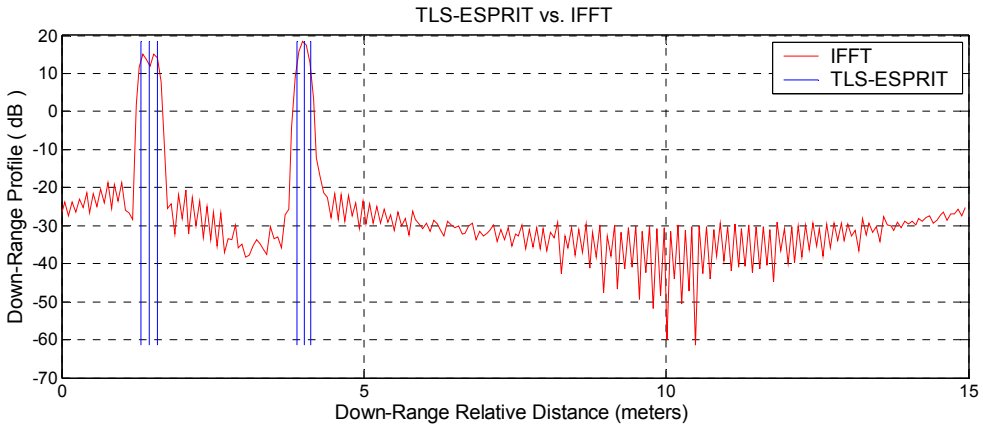

Figure 4.41. Comparison of TLS-ESPRIT method and IFFT

Table 4.74. Estimated TLS-ESPRIT ranges (in meters) in simulation shown in figure 4.41

1.3087	1.4493	1.5910	3.8895	4.0083	4.1290

Table 4.75. Parameters for simulation shown in figure 4.42

N	Δf	M	ΔR	Target Ranges (R_k) & RCSs (A_k)						SNR
128	10 MHz	50	11.72 cm	1.4 m 1000	1.45 1	1.5 m 1000	4 m 1000	4.1 m 1	4.2 m 1	20

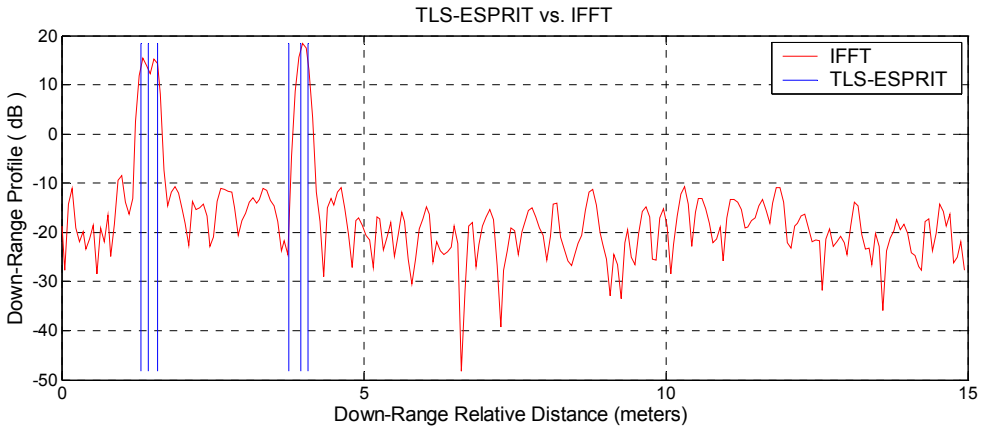

Figure 4.42. Comparison of TLS-ESPRIT method and IFFT

Table 4.76. Estimated TLS-ESPRIT ranges (in meters) in simulation shown in figure 4.42

1.3072	1.4417	1.5877	3.7594	3.9616	4.0818

From figures 4.41 and 4.42, it can be concluded that TLS-ESPRIT can detect the closely separated targets which have very different radar cross sections very accurately

even in low SNR case. Note that IFFT results have one broad peak for the last three targets that have RCS values of 1000, 1, and 1 and two peaks for the first three targets that have RCS values of 1000, 1, and 1000. TLS-ESPRIT can resolve closely separated targets with very different RCS values, however, because of smearing, IFFT can not resolve them.

4.4. Linear Frequency Modulated Continuous Wave Radar Signal Model

As explained in section 2.4.2., the transmitted up-chirp LFM signal can be expressed in complex notation by

$$s_T(t) = rect\,(\frac{t}{T}) \exp[\,j2\pi(f_0 t + \frac{1}{2}\alpha t^2)] \tag{4.11}$$

$$= \exp[\,j2\pi(f_0 t + \frac{1}{2}\alpha t^2)]\ , \quad 0 \le t \le T \tag{4.12}$$

where $\alpha = B/T$ and f_0 is the chirp start frequency. Assuming a point scatterer at range *R*, the received signal can be written as

$$s_R(t) = A\exp\{j2\pi[\,f_0(t-\tau) + \frac{1}{2}\alpha(t-\tau)^2\,]\} \tag{4.13}$$

where *A* depends on target RCS, antenna gain, and range attenuation, and two way time delay τ is given as

$$\tau = \frac{2R}{c} \tag{4.14}$$

As explained in detail in block diagram of FMCW radar, the received signal is mixed with a replica of the transmitted signal and then low-pass filtered. The output of low-pass filter can be written as

$$s_0(t) = A\exp[\,2\pi f_0 \tau + 2\pi\alpha\tau t - \pi\alpha\tau^2] \tag{4.15}$$

Substituting $\tau = 2R/c$ and arranging the terms yield

$$s_0(t) = A \exp\left\{\left(\frac{4\pi B R}{cT}\right)t + \frac{2R}{c}\left(2\pi f_0 - \frac{2\pi BR}{cT}\right)\right\} \tag{4.16}$$

Now, assume *d* targets located at ranges $R_1, R_2, \ldots R_d$. So, the total received signal can be expressed as

$$s_R(t) = \sum_{k=1}^{d} A_k \exp\{j2\pi[f_0(t-\tau_k) + \frac{1}{2}\alpha(t-\tau_k)^2]\} \tag{4.17}$$

Therefore, the total signal at the output of the low-pass filter is

$$s_0(t) = \sum_{k=1}^{d} A_k \exp\left\{\left(\frac{4\pi B R_k}{cT}\right)t + \frac{2R_k}{c}\left(2\pi f_0 - \frac{2\pi BR_k}{cT}\right)\right\} \tag{4.18}$$

This expression will be used to generate the synthetic signals representing FMCW radar returns from *d* targets located at ranges $R_1, R_2, \ldots R_d$.

In section 2.4.3., it was shown that

$$R = \frac{cT f_b}{2B} \tag{4.19}$$

which means that the range is proportional to the beat frequency. Therefore, proper sampling of the low-pass filter output and finding the peaks in the spectrum gives us the target ranges. The methods explained in chapter three will be used to find the spectrum of the output of the low-pass filter, and the ranges, with high resolution.

4.5. Comparison of Periodogram and High-Resolution Spectral Estimators for Linear Frequency Modulated Continuous Wave Radar

For the following simulations, the parameters of the linear frequency modulated continuous radar waveform, target ranges and radar cross sections, and the signal processing methods will be given in the tables for each case.

4.5.1. Yule-Walker Method vs. Periodogram

Table 4.77. Parameters for simulation shown in figure 4.43

N	BW	T	ΔR	Target Ranges (R_k) (meters) & RCSs (A_k)						SNR
600	1.5 GHz	10 mSec	10 cm	2 100	3 100	5 100	7 100	10 100	11 100	50

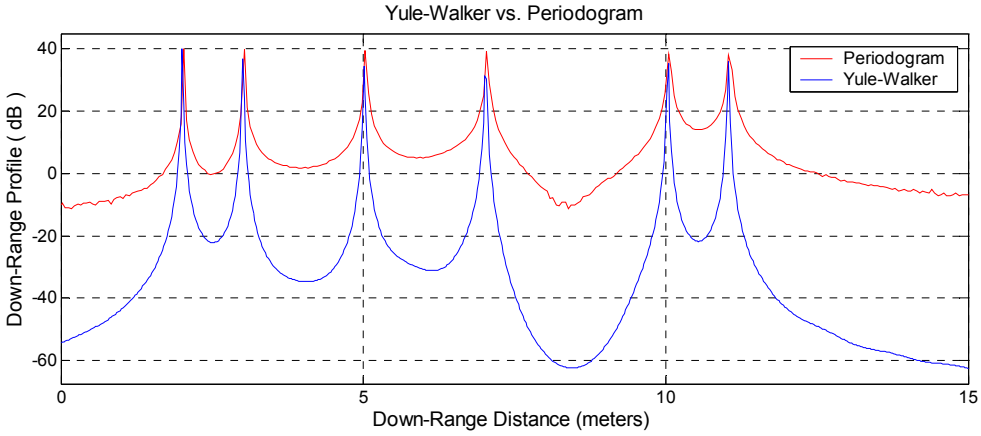

Figure 4.43. Comparison of Yule-Walker method and periodogram

Figure 4.43 shows that Yule-Walker method provides narrower peaks at the target locations. Also note that Yule-Walker range profile has higher signal-to-clutter ratio (SCR) than the range profile obtained via periodogram.

Table 4.78. Parameters for simulation shown in figure 4.44

N	BW	T	ΔR	Target Ranges (R_k) (meters) & RCSs (A_k)						SNR
600	1.5 GHz	10 mSec	10 cm	2 100	3 100	5 100	7 100	10 100	11 100	1

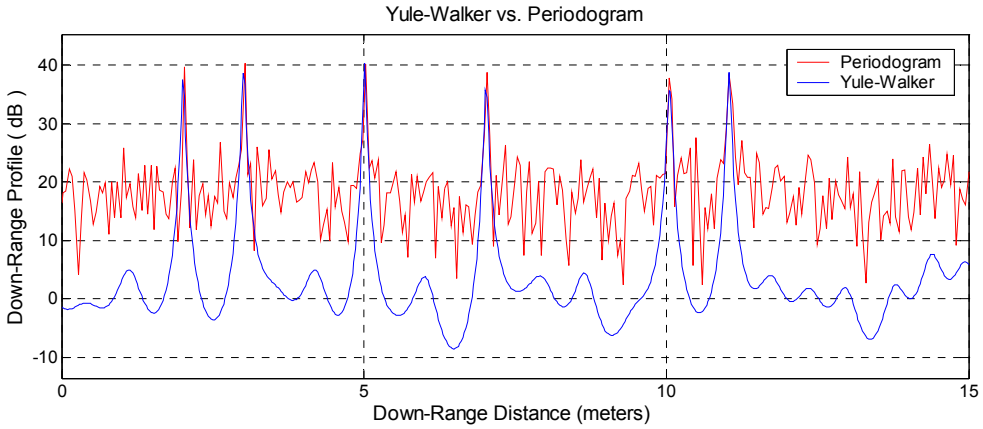

Figure 4.44. Comparison of Yule-Walker method and periodogram

Figure 4.44 shows that Yule-Walker method provides much sharper peaks at the target locations even in the very low SNR case than periodogram and its range profile has higher SCR than range profile obtained via periodogram.

Table 4.79. Parameters for simulation shown in figure 4.45

N	BW	T	ΔR	Target Ranges (R_k) (meters) & RCSs (A_k)						SNR
600	1.5 GHz	10 mSec	10 cm	2 100	2.1 100	7 100	7.2 100	10 100	11 100	50

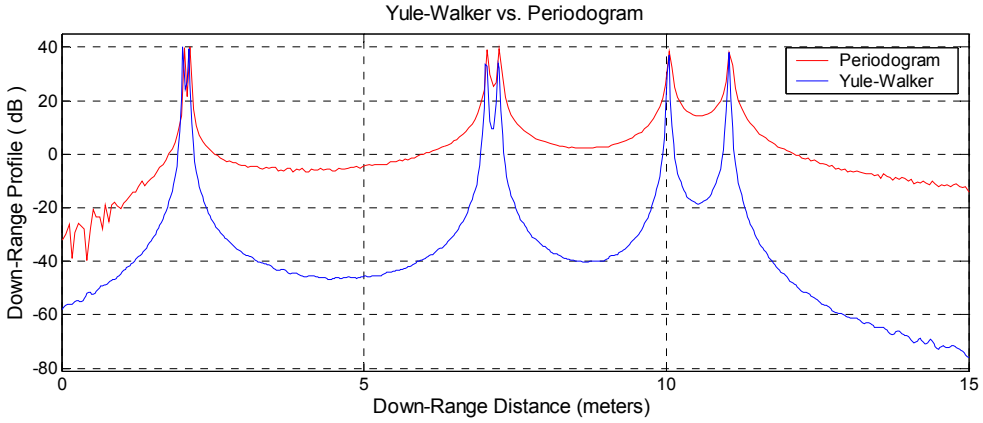

Figure 4.45. Comparison of Yule-Walker method and periodogram

Table 4.80. Parameters for simulation shown in figure 4.46

N	BW	T	ΔR	Target Ranges (R_k) (meters) & RCSs (A_k)						SNR
600	1.5 GHz	10 mSec	10 cm	2 100	2.1 100	7 100	7.2 100	10 100	11 100	1

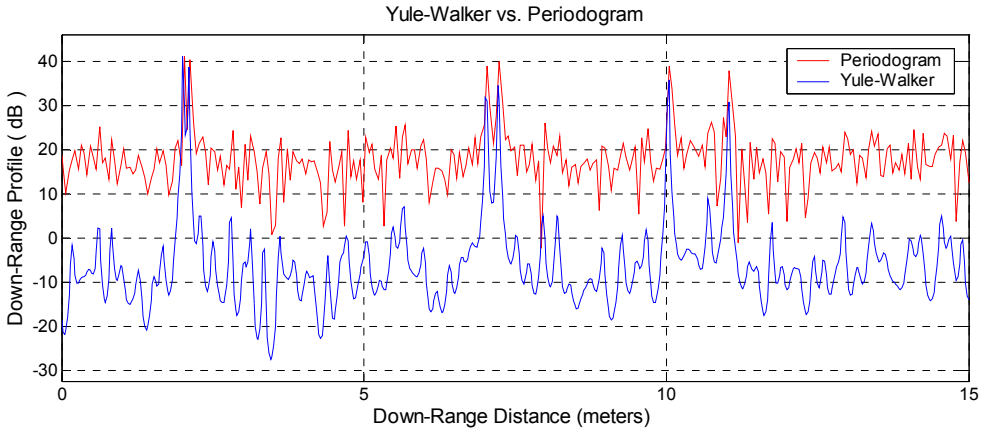

Figure 4.46. Comparison of Yule-Walker method and periodogram

Figures 4.45 and 4.46 show that Yule-Walker method provides much sharper peaks at the target locations even when the SNR is very low and the targets are close to each other and its range profile has higher SCR than range profile obtained via periodogram.

Table 4.81. Parameters for simulation shown in figure 4.47

N	BW	T	ΔR	Target Ranges (R_k) (meters) & RCSs (A_k)						SNR
600	1.5 GHz	10 mSec	10 cm	2 100	2.1 10	7 100	7.2 10	10 100	11 100	50

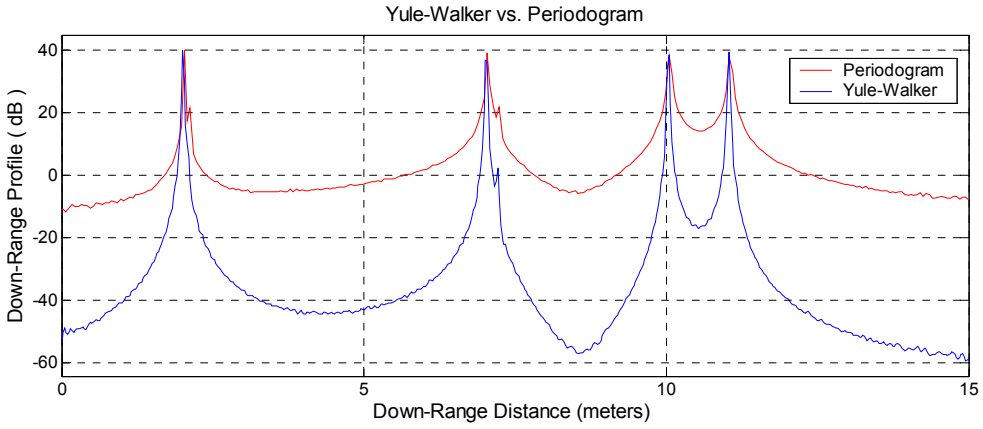

Figure 4.47. Comparison of Yule-Walker method and periodogram

Table 4.82. Parameters for simulation shown in figure 4.48

N	BW	T	ΔR	Target Ranges (R_k) (meters) & RCSs (A_k)						SNR
600	1.5 GHz	10 mSec	10 cm	2 100	2.1 10	7 100	7.2 10	10 100	11 100	5

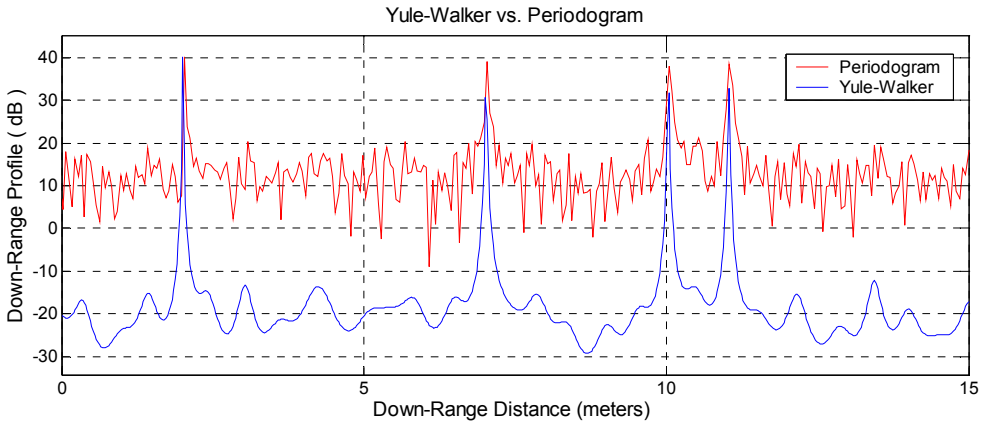

Figure 4.48. Comparison of Yule-Walker method and periodogram

Figures 4.47 and 4.48 show that neither Yule-Walker method nor periodogram can resolve the close targets with very different RCS values. However, note that Yule-Walker method provides much sharper peaks at the target locations even when the SNR is very low and the targets are close to each other and its range profile has higher SCR than range profile obtained via periodogram.

4.5.2. Least-Squares Method vs. Periodogram

Table 4.83. Parameters for simulation shown in figure 4.49

N	BW	T	ΔR	Target Ranges (R_k) (meters) & RCSs (A_k)						SNR
600	1.5 GHz	10 mSec	10 cm	2 100	3 100	5 100	7 100	10 100	11 100	50

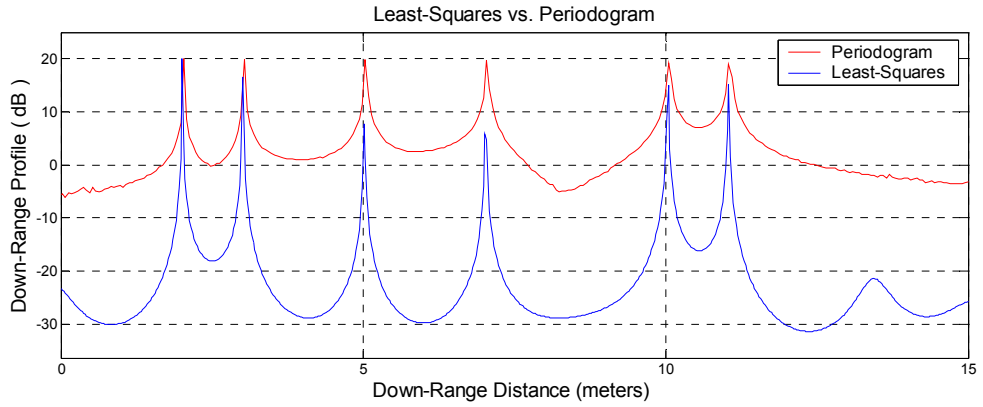

Figure 4.49. Comparison of least-squares method and periodogram

Table 4.84. Parameters for simulation shown in figure 4.50

N	BW	T	ΔR	Target Ranges (R_k) (meters) & RCSs (A_k)						SNR
600	1.5 GHz	10 mSec	10 cm	2 100	3 100	5 100	7 100	10 100	11 100	1

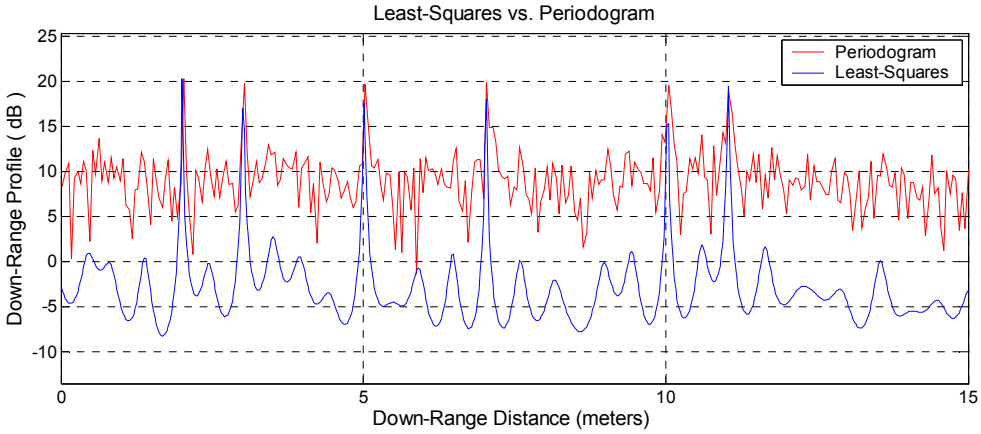

Figure 4.50. Comparison of least-squares method and periodogram

Figures 4.49 and 4.50 show that least-squares method provides much sharper peaks at the target locations even in the very low SNR case than periodogram and its range profile has higher SCR than range profile obtained via periodogram.

Table 4.85. Parameters for simulation shown in figure 4.51

N	BW	T	ΔR	Target Ranges (R_k) (meters) & RCSs (A_k)						SNR
600	1.5 GHz	10 mSec	10 cm	2 100	2.1 100	7 100	7.2 100	10 100	11 100	50

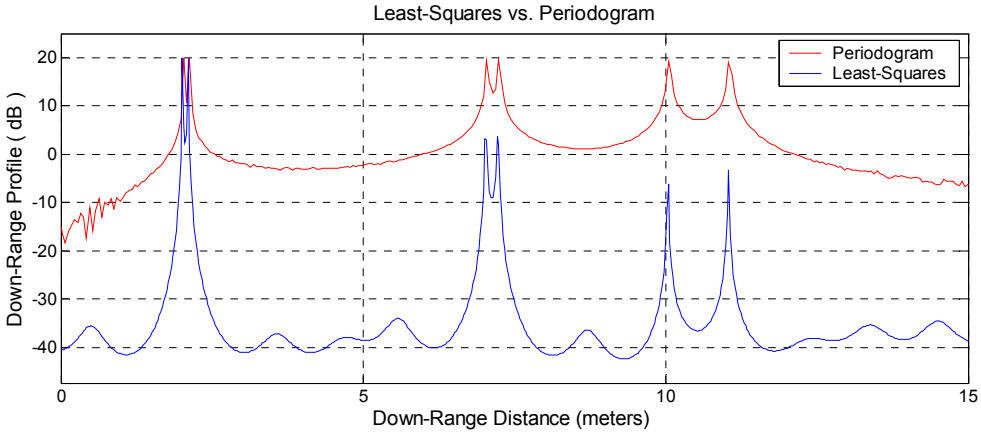

Figure 4.51. Comparison of least-squares method and periodogram

Table 4.86. Parameters for simulation shown in figure 4.52

N	BW	T	ΔR	Target Ranges (R_k) (meters) & RCSs (A_k)						SNR
600	1.5 GHz	10 mSec	10 cm	2 100	2.1 100	7 100	7.2 100	10 100	11 100	5

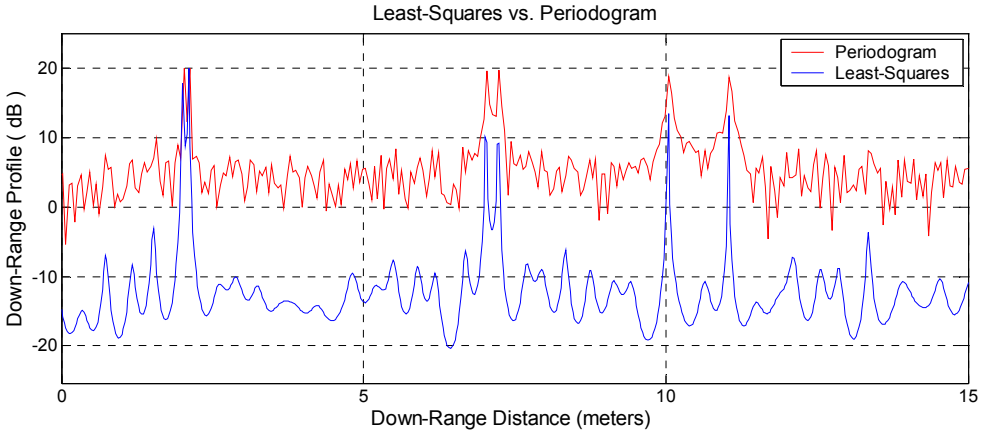

Figure 4.52. Comparison of least-squares method and periodogram

Figures 4.51 and 4.52 show that Yule-Walker method provides much sharper peaks at the target locations even when the SNR is very low and the targets are close to each other and its range profile has higher SCR than range profile obtained via periodogram.

Table 4.87. Parameters for simulation shown in figure 4.53

N	BW	T	ΔR	Target Ranges (R_k) (meters) & RCSs (A_k)						SNR
600	1.5 GHz	10 mSec	10 cm	2 100	2.1 10	7 100	7.2 10	10 100	11 100	50

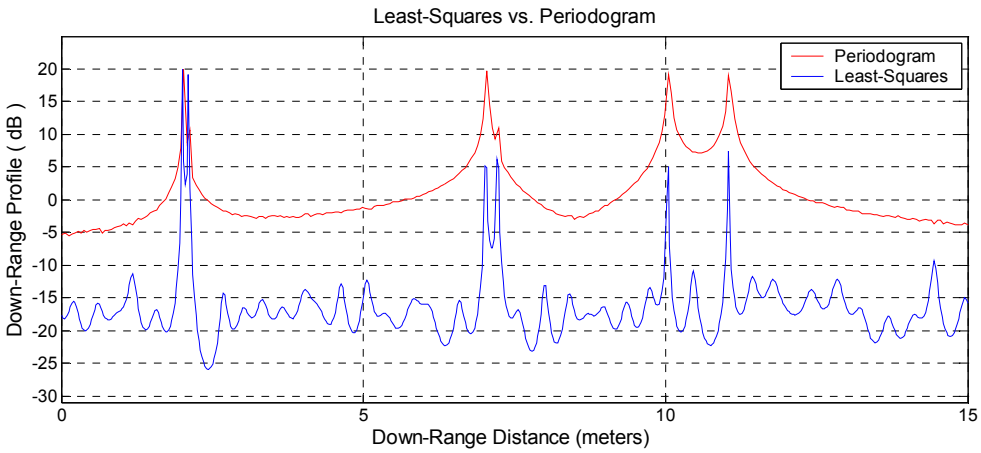

Figure 4.53. Comparison of least-squares method and periodogram

Table 4.88. Parameters for simulation shown in figure 4.54

N	BW	T	ΔR	Target Ranges (R_k) (meters) & RCSs (A_k)						SNR
600	1.5 GHz	10 mSec	10 cm	2 100	2.1 10	7 100	7.2 10	10 100	11 100	15

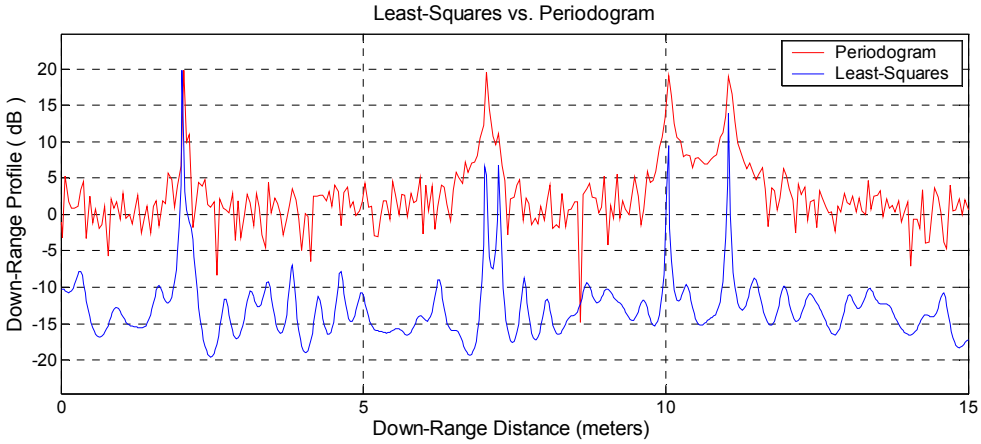

Figure 4.54. Comparison of least-squares method and periodogram

Figures 4.53 and 4.54 show that least-squares method can provide much better range profiles than periodogram. Note that least-squares method can resolve the close targets with very different RCS values and provide much sharper peaks at the target locations even when the SNR is low and the targets are close to each other and its range profile has higher SCR than range profile obtained via periodogram.

4.5.3. Higher-Order Yule-Walker Method vs. Periodogram

Table 4.89. Parameters for simulation shown in figure 4.55

N	BW	T	M	L	ΔR	Target Ranges (R_k) (meters) & RCSs (A_k)						SNR
600	1.5 GHz	10 mSec	50	50	10 cm	2 100	3 100	5 100	7 100	10 100	11 100	50

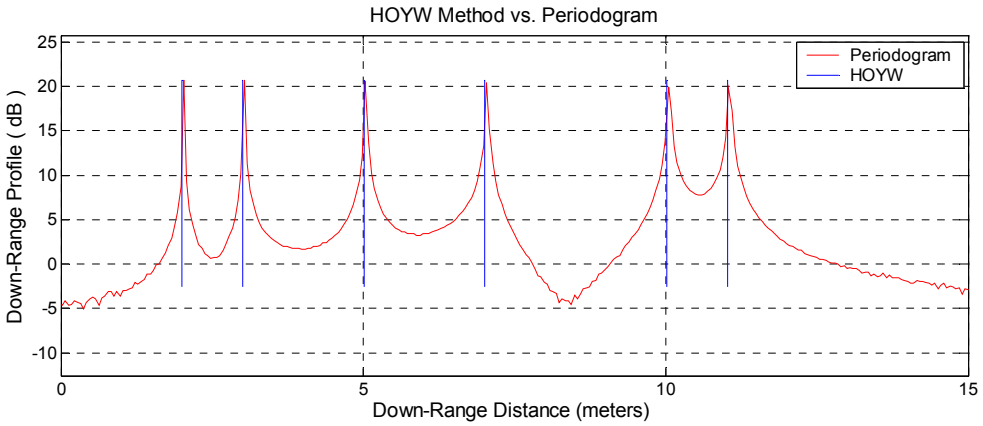

Figure 4.55. Comparison of HOYW method and periodogram

Table 4.90. Estimated HOYW ranges (in meters) in simulation shown in figure 4.55

2.0034	3.0050	5.0084	7.0116	10.0168	11.0183

Table 4.91. Parameters for simulation shown in figure 4.56

N	BW	T	M	L	ΔR	Target Ranges (R_k) (meters) & RCSs (A_k)						SNR
600	1.5 GHz	10 mSec	50	50	10 cm	2 100	3 100	5 100	7 100	10 100	11 100	1

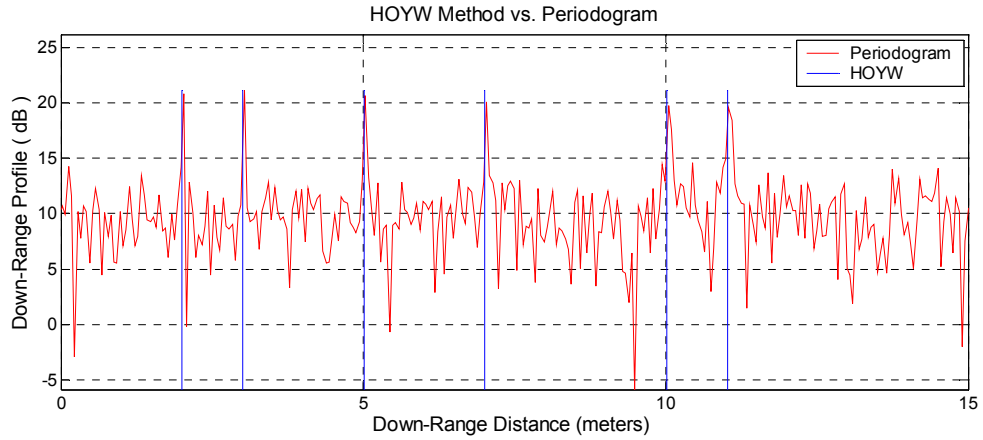

Figure 4.56. Comparison of HOYW method and periodogram

Table 4.92. Estimated HOYW ranges (in meters) in simulation shown in figure 4.56

2.0049	3.0030	5.0065	7.0098	10.0212	11.0230

Figures 4.55 and 4.56 show that HOYW method can find the target ranges very accurately even when the SNR is very low.

Table 4.93. Parameters for simulation shown in figure 4.57

N	BW	T	M	L	ΔR	Target Ranges (R_k) (meters) & RCSs (A_k)						SNR
600	1.5 GHz	10 mSec	50	50	10 cm	2 120	2.1 120	7 120	7.2 120	10 120	11 120	50

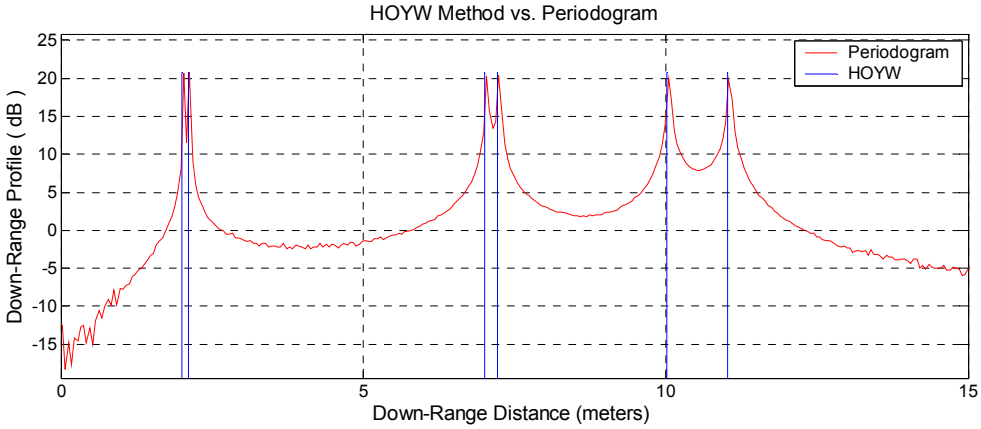

Figure 4.57. Comparison of HOYW method and periodogram

Table 4.94. Estimated HOYW ranges (in meters) in simulation shown in figure 4.57

2.0021	2.1046	7.0115	7.2122	10.0168	11.0182

Table 4.95. Parameters for simulation shown in figure 4.58

N	BW	T	M	L	ΔR	Target Ranges (R_k) (meters) & RCSs (A_k)						SNR
600	1.5 GHz	10 mSec	50	50	10 cm	2 120	2.1 120	7 120	7.2 120	10 120	11 120	1

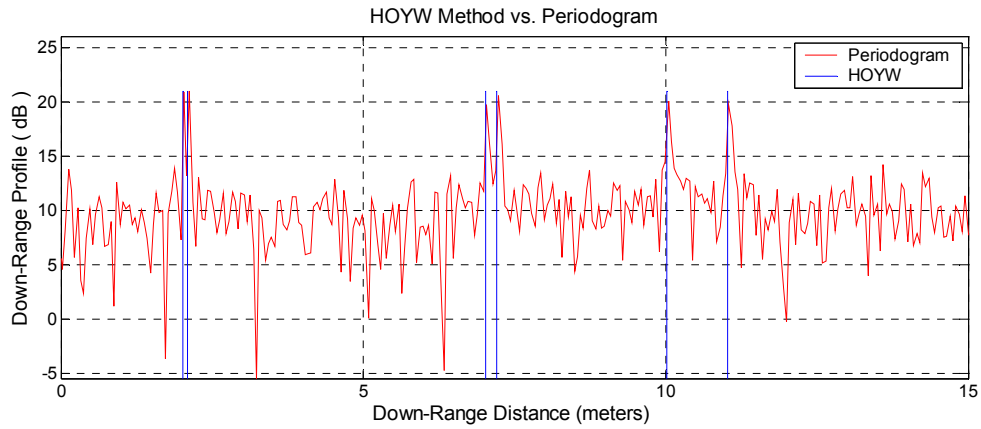

Figure 4.58. Comparison of HOYW method and periodogram

Table 4.96. Estimated HOYW ranges (in meters) in simulation shown in figure 4.58

2.0185	2.0986	7.0142	7.2093	10.0152	11.0186

Figures 4.57 and 4.58 show that HOYW method can find the target ranges very accurately even when the targets are close to each other and the SNR is very low.

Table 4.97. Parameters for simulation shown in figure 4.59

N	BW	T	M	L	ΔR	Target Ranges (R_k) (meters) & RCSs (A_k)						SNR
600	1.5 GHz	10 mSec	50	50	10 cm	2 120	2.001 120	7 120	7.01 120	10 120	10.1 120	50

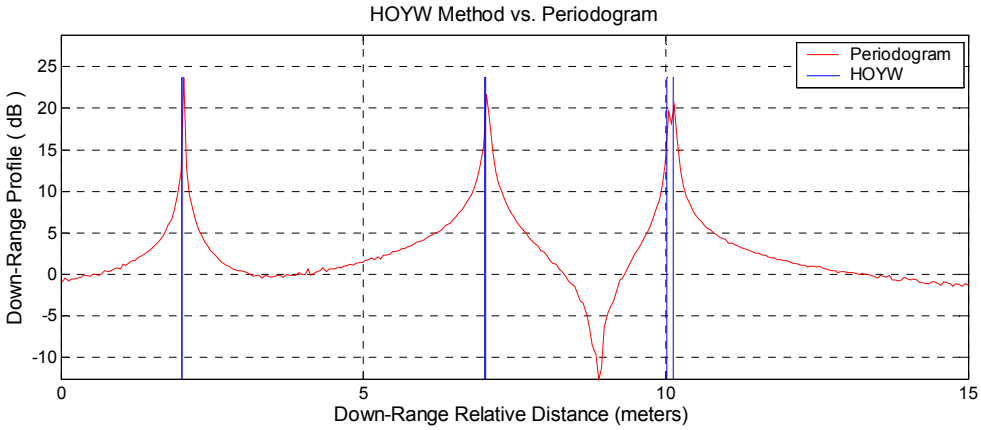

Figure 4.59. Comparison of HOYW method and periodogram

Table 4.98. Estimated HOYW ranges (in meters) in simulation shown in figure 4.59

2.0003	2.0049	7.0046	7.0248	10.0165	10.1172

Table 4.99. Parameters for simulation shown in figure 4.60

N	BW	T	M	L	ΔR	Target Ranges (R_k) (meters) & RCSs (A_k)						SNR
600	1.5 GHz	10 mS	150	150	10 cm	2 120	2.01 120	7 120	7.05 120	10 120	10.1 120	10

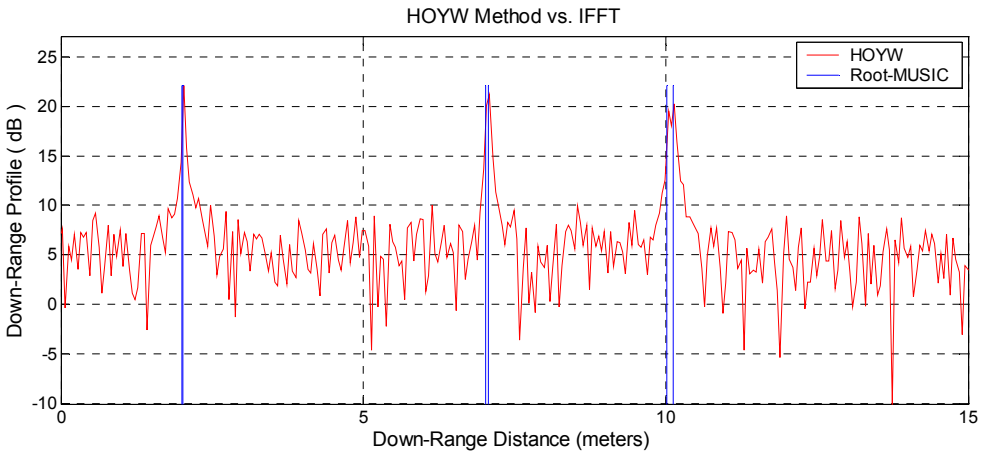

Figure 4.60. Comparison of HOYW method and periodogram

Table 4.100. Estimated HOYW ranges (in meters) in simulation shown in figure 4.60

2.0000	2.0130	7.0166	7.0666	10.0145	10.1183

Figures 4.59 and 4.60 show that HOYW method can provide much better range resolution than periodogram. Note that the range resolution of the periodogram method is 10 cm which means that periodogram method can not distinguish targets that are separated less than 0.1 meter. Tables 4.97 and 4.98 show that HOYW method can resolve targets even when the distance between targets is 0.001 meter where SNR is 50 and tables 4.99 and 4.100 show that HOYW method can resolve targets even when the distance between targets is 0.01 meter where SNR is 10. Also note that the range accuracy of HOYW method is better than periodogram.

Table 4.101. Parameters for simulation shown in figure 4.61

N	BW	T	M	L	ΔR	Target Ranges (R_k) (meters) & RCSs (A_k)						SNR
600	1.5 GHz	10 mS	150	150	10 cm	2 120	2.005 10	7 120	7.01 10	10 120	10.5 10	50

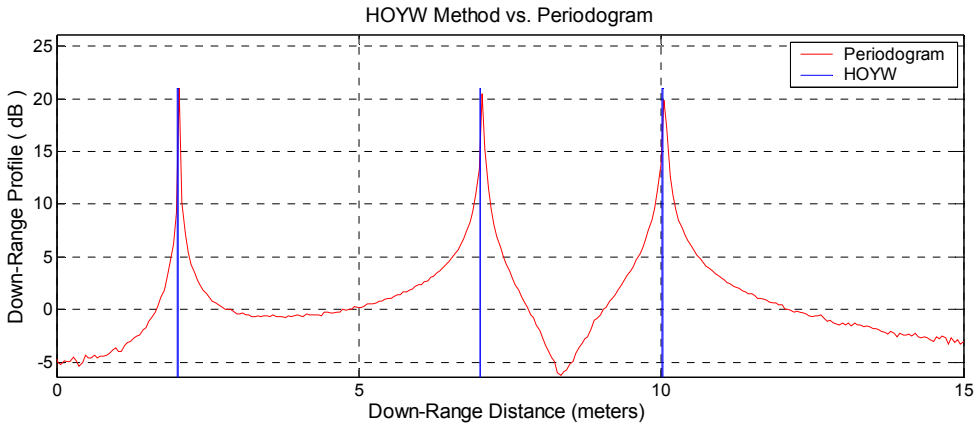

Figure 4.61. Comparison of HOYW method and periodogram

Table 4.102. Estimated HOYW ranges (in meters) in simulation shown in figure 4.61

2.0024	2.0046	7.0099	7.0139	10.0118	10.0325

Table 4.103. Parameters for simulation shown in figure 4.62

N	BW	T	M	L	ΔR	Target Ranges (R_k) (meters) & RCSs (A_k)						SNR
600	1.5 GHz	10 mS	150	150	10 cm	2 120	2.005 10	7 120	7.01 10	10 120	10.5 10	10

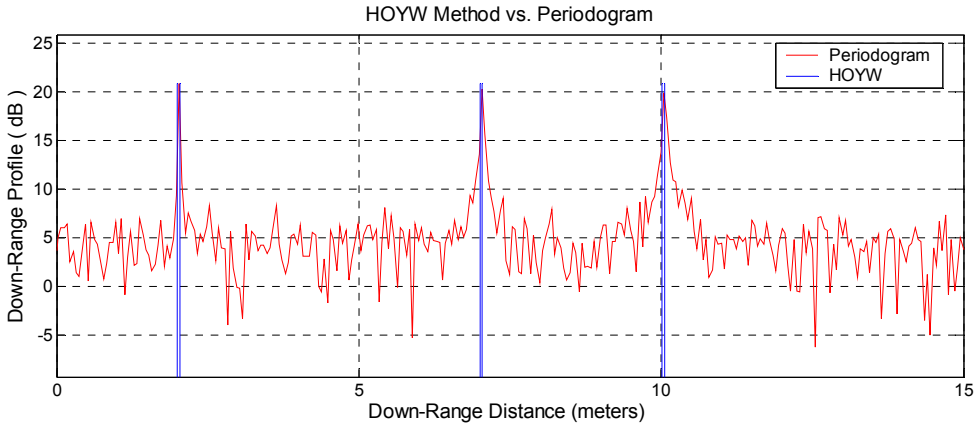

Figure 4.62. Comparison of HOYW method and periodogram

Table 4.104. Estimated HOYW ranges (in meters) in simulation shown in figure 4.62

2.0020	2.0468	7.0050	7.0297	10.0144	10.0597

Figures 4.61 and 4.62 show that HOYW method can provide much better range resolution even when the targets that have very different RCS values are so close.

4.5.4. Root-MUSIC vs. Periodogram

Table 4.105. Parameters for simulation shown in figure 4.63

N	BW	T	M	$MSSP$	ΔR	Target Ranges(R_k)(meters) & RCSs(A_k)						SNR
600	1.5 GHz	10 mS	50	NO	10 cm	2 120	3 120	5 120	7 120	10 120	11 120	50

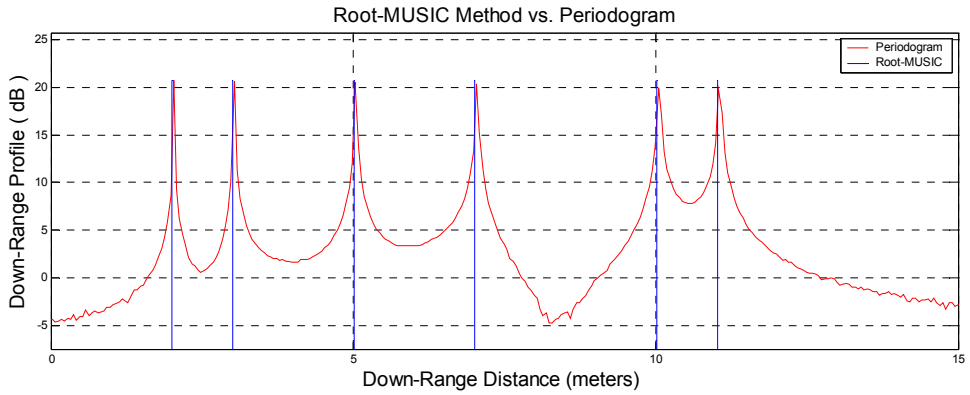

Figure 4.63. Comparison of Root-MUSIC method and periodogram

Table 4.106. Estimated Root-MUSIC ranges (in meters) in simulation shown in figure 4.63

2.0040	3.0050	5.0084	7.0117	10.0167	11.0184

Table 4.107. Parameters for simulation shown in figure 4.64

N	BW	T	M	$MSSP$	ΔR	Target Ranges(R_k)(meters) & RCSs(A_k)						SNR
600	1.5 GHz	10 mS	50	NO	10 cm	2 120	3 120	5 120	7 120	10 120	11 120	7

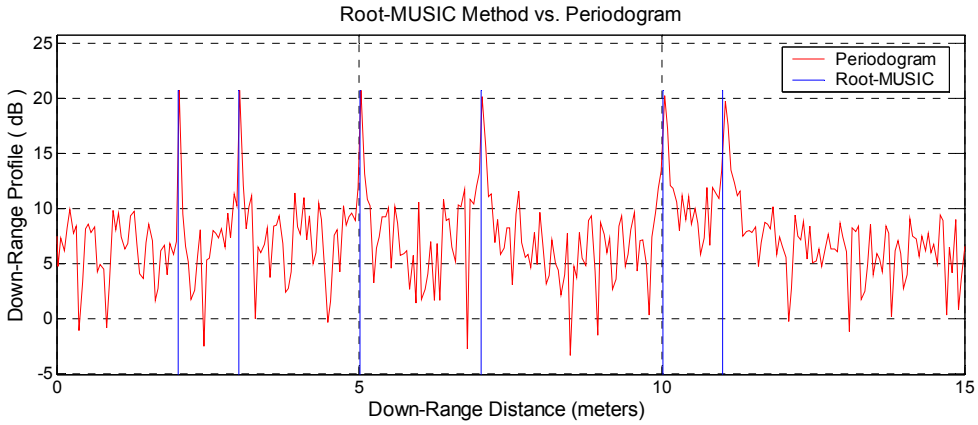

Figure 4.64. Comparison of Root-MUSIC method and periodogram

Table 4.108. Estimated Root-MUSIC ranges (in meters) in simulation shown in figure 4.64

2.0061	3.0063	5.0090	7.0124	10.0173	11.0049

Figures 4.63 and 4.64 show that Root-MUSIC method can find the target ranges very accurately even when the SNR is very low.

Table 4.109. Parameters for simulation shown in figure 4.65

N	BW	T	M	$MSSP$	ΔR	Target Ranges(R_k)(meters) & RCSs(A_k)						SNR
600	1.5 GHz	10 mS	50	NO	10 cm	2 120	2.01 120	7 120	7.05 120	10 120	11 120	50

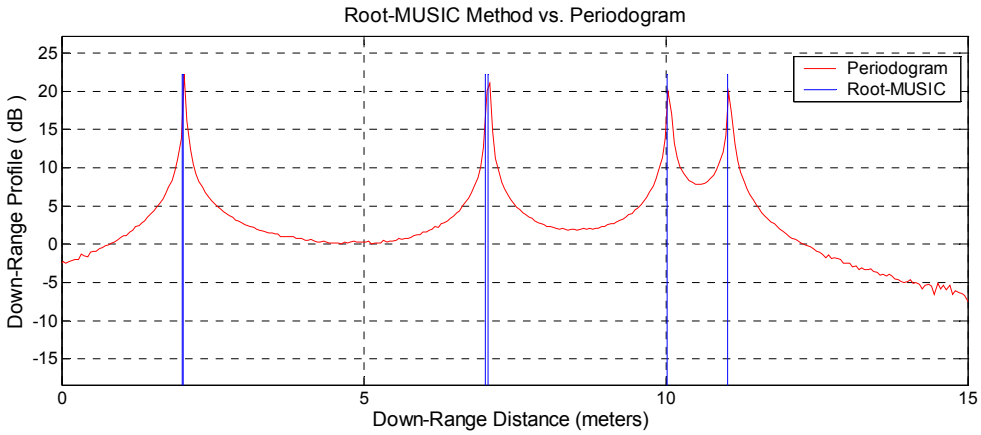

Figure 4.65. Comparison of Root-MUSIC method and periodogram

Table 4.110. Estimated Root-MUSIC ranges (in meters) in simulation shown in figure 4.65

2.0039	2.0119	7.0117	7.0619	10.0167	11.0183

Figures 4.65 shows that Root-MUSIC method can find the target ranges very accurately when SNR is high. Note that Root-MUSIC method can resolve the targets that are separated by 1 cm where the range resolution that can be achieved via periodogram is 10 cm and the periodogram range profile has one broad peak instead of two narrow peaks for the first and second two targets.

Table 4.111. Parameters for simulation shown in figure 4.66

N	BW	T	M	$MSSP$	ΔR	Target Ranges(R_k)(meters) & RCSs(A_k)						SNR
600	1.5 GHz	10 mS	50	NO	10 cm	2 120	2.05 120	7 120	7.1 120	10 120	11 120	10

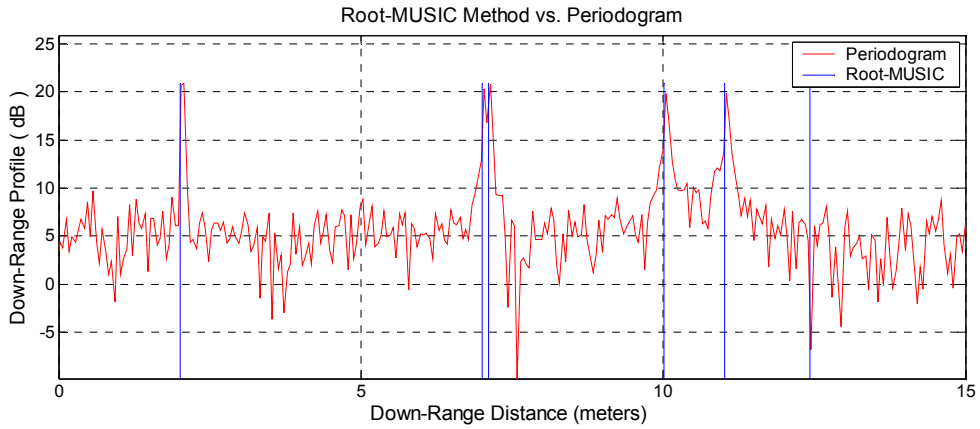

Figure 4.66. Comparison of Root-MUSIC method and periodogram

Table 4.112. Estimated Root-MUSIC ranges (in meters) in simulation shown in figure 4.66

2.0133	12.4266	7.0139	7.1155	10.0157	11.0192

As can be seen from figure 4.66, Root-MUSIC method can yield false alarms when the SNR is low and the targets are too close.

Table 4.113. Parameters for simulation shown in figure 4.67

N	BW	T	M	$MSSP$	ΔR	Target Ranges(R_k)(meters) & RCSs(A_k)						SNR
600	1.5 GHz	10 mS	50	YES	10 cm	2 120	2.05 120	7 120	7.1 120	10 120	11 120	10

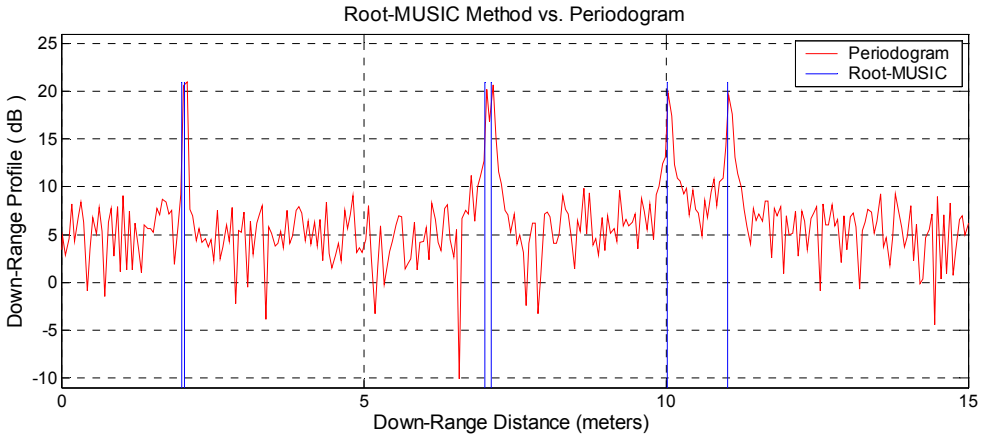

Figure 4.67. Comparison of Root-MUSIC method and periodogram

Table 4.114. Estimated Root-MUSIC ranges (in meters) in simulation shown in figure 4.67

1.9909	2.0451	7.0108	7.1115	10.0176	11.0190

Figure 4.67 and table 4.114 show that the false alarm ratio of the Root-MUSIC method can be decreased using spatial smoothing techniques. Note that Root-MUSIC method implemented together with spatial smoothing techniques can achieve much better range resolution and very accurate range estimates than periodogram even when the SNR is low.

Table 4.115. Parameters for simulation shown in figure 4.68

N	BW	T	M	$MSSP$	ΔR	Target Ranges(R_k)(meters) & RCSs(A_k)						SNR
600	1.5 GHz	10 mS	50	YES	10 cm	2 120	2.05 10	7 120	7.1 10	10 120	11 120	50

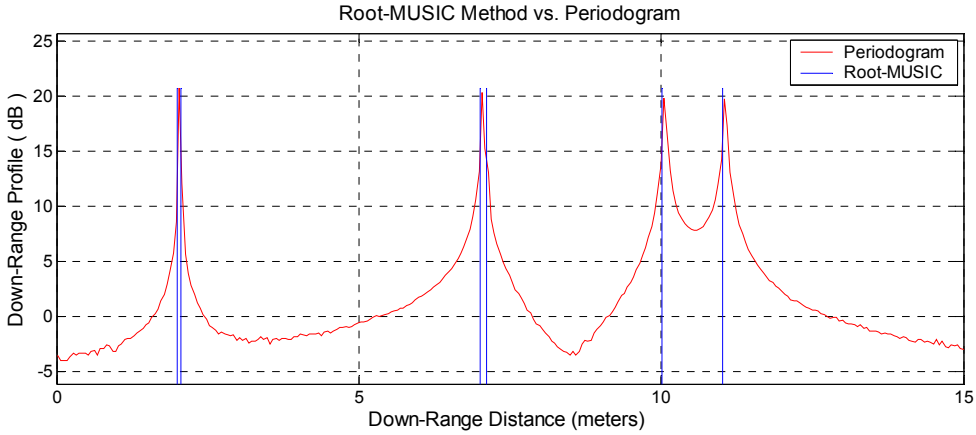

Figure 4.68. Comparison of Root-MUSIC method and periodogram

Table 4.116. Estimated Root-MUSIC ranges (in meters) in simulation shown in figure 4.68

2.0034	2.0544	7.0117	7.1117	10.0167	11.0184

Table 4.117. Parameters for simulation shown in figure 4.68

N	BW	T	M	$MSSP$	ΔR	Target Ranges(R_k)(meters) & RCSs(A_k)						SNR
600	1.5 GHz	10 mS	50	YES	10 cm	2 120	2.05 10	7 120	7.1 10	10 120	11 120	10

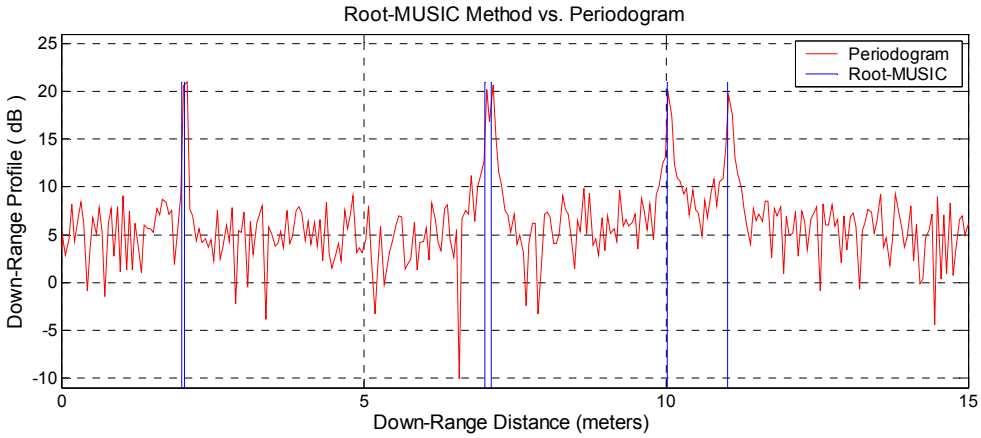

Figure 4.69. Comparison of Root-MUSIC method and periodogram

Table 4.118. Estimated Root-MUSIC ranges (in meters) in simulation shown in figure 4.68

1.9927	2.0763	7.0324	7.1427	10.0138	11.0201

Figures 4.68 and 4.69 show that Root-MUSIC method implemented together with spatial smoothing techniques can resolve targets that are close to each other and have very different RCS values.

4.5.5. Minimum-Norm Method vs. Periodogram

Table 4.119. Parameters for simulation shown in figure 4.70

N	BW	T	M	ΔR	Target Ranges (R_k) (meters) & RCSs (A_k)						SNR
600	1.5 GHz	10 mSec	50	10 cm	2 120	3 120	5 120	7 120	10 120	11 120	50

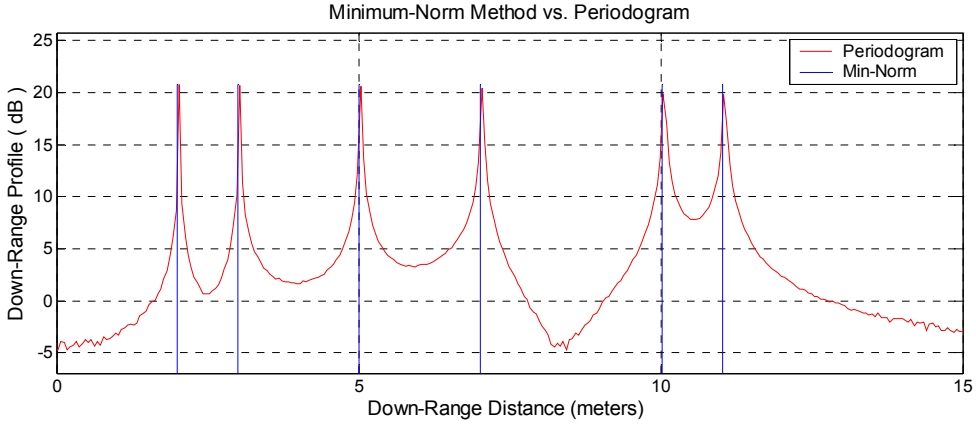

Figure 4.70. Comparison of Minimum-Norm method and periodogram

Table 4.120. Estimated Min-Norm ranges (in meters) in simulation shown in figure 4.70

2.0033	3.0050	5.0084	7.0117	10.0167	11.0184

Table 4.121. Parameters for simulation shown in figure 4.71

N	BW	T	M	ΔR	Target Ranges (R_k) (meters) & RCSs (A_k)						SNR
600	1.5 GHz	10 mSec	50	10 cm	2 120	3 120	5 120	7 120	10 120	11 120	5

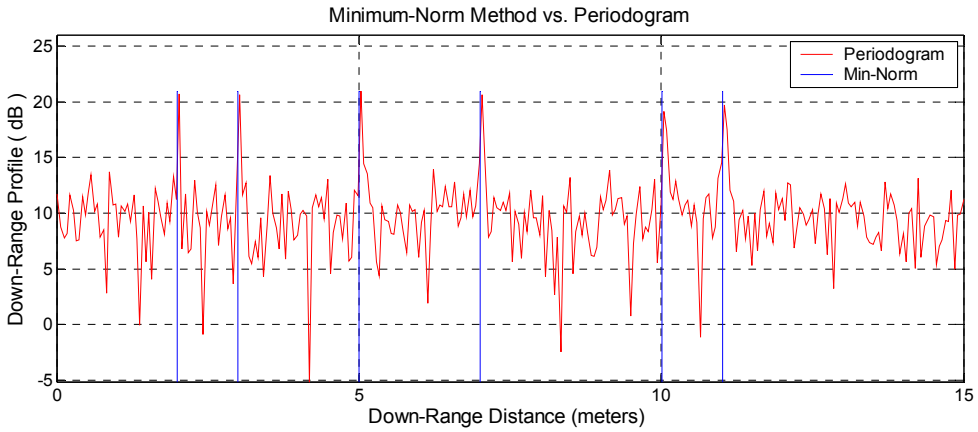

Figure 4.71. Comparison of Minimum-Norm method and periodogram

Table 4.122. Estimated Min-Norm ranges (in meters) in simulation shown in figure 4.71

2.0056	3.0074	5.0094	7.0129	10.0194	11.0167

Figures 4.70 and 4.71 show that Minimum-Norm method can find the target ranges very accurately even when the SNR is very low.

Table 4.123. Parameters for simulation shown in figure 4.72

N	BW	T	M	ΔR	Target Ranges (R_k) (meters) & RCSs (A_k)						SNR
600	1.5 GHz	10 mSec	100	10 cm	2 120	2.005 120	7 120	7.01 120	10 120	10.1 120	50

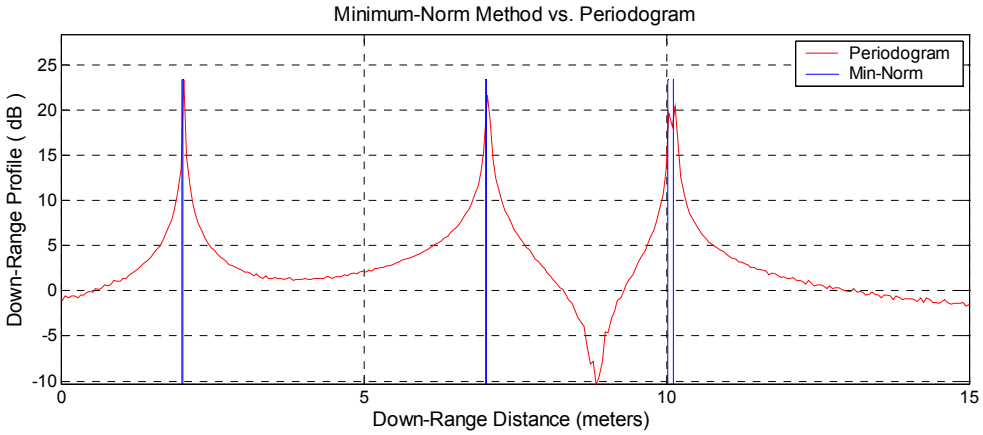

Figure 4.72. Comparison of Minimum-Norm method and periodogram

Table 4.124. Estimated Min-Norm ranges (in meters) in simulation shown in figure 4.72

2.0027	2.0075	7.0115	7.0216	10.0167	10.1168

Figure 4.72 shows that Minimum-Norm method can resolve the targets with 5 mm separation whereas periodogram can barely resolve targets with 10 cm separation. So, it is obvious that Minimum-Norm method provides much better range resolution than periodogram.

Table 4.125. Parameters for simulation shown in figure 4.73

N	BW	T	M	ΔR	Target Ranges (R_k) (meters) & RCSs (A_k)						SNR
600	1.5 GHz	10 mSec	100	10 cm	2 120	2.02 120	7 120	7.03 120	10 120	10.1 120	10

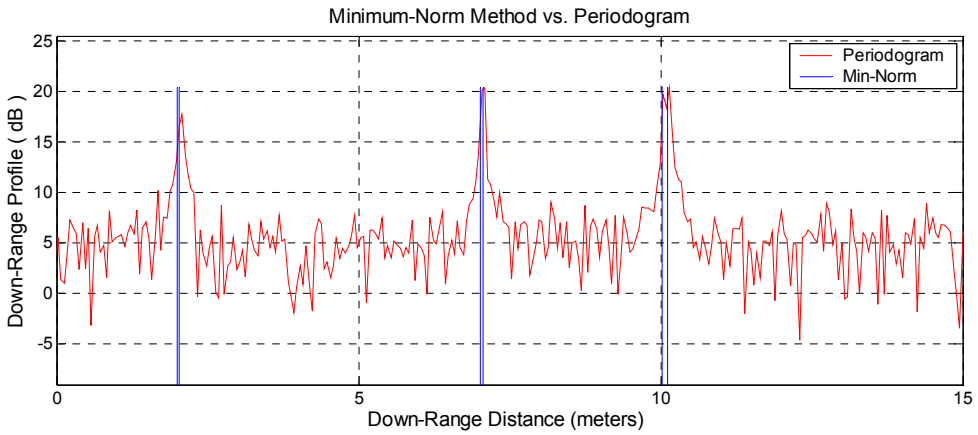

Figure 4.73. Comparison of Minimum-Norm method and periodogram

Table 4.126. Estimated Min-Norm ranges (in meters) in simulation shown in figure 4.73

2.0001	2.0265	7.0168	7.0537	10.0169	10.1160

Figure 4.73 shows that Minimum-Norm method can provide much better range resolution and much more accurate range estimates than periodogram even when the SNR is very low.

Table 4.127. Parameters for simulation shown in figure 4.74

N	BW	T	M	ΔR	Target Ranges (R_k) (meters) & RCSs (A_k)						SNR
600	1.5 GHz	10 mSec	100	10 cm	2 120	2.01 10	7 120	7.02 10	10 120	10.1 10	50

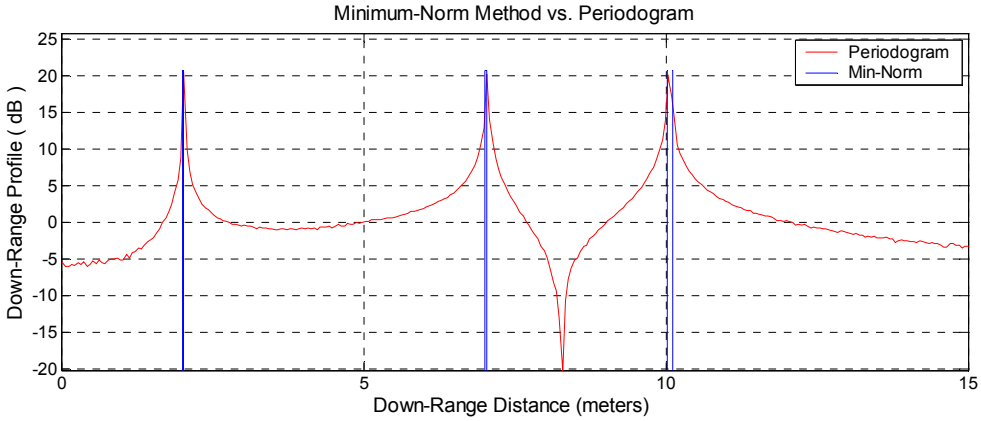

Figure 4.74. Comparison of Minimum-Norm method and periodogram

Table 4.128. Estimated Min-Norm ranges (in meters) in simulation shown in figure 4.74

2.0032	2.0184	7.0116	7.0322	10.0167	10.1168

Table 4.129. Parameters for simulation shown in figure 4.75

N	BW	T	M	ΔR	Target Ranges (R_k) (meters) & RCSs (A_k)						SNR
600	1.5 GHz	10 mSec	100	10 cm	2 120	2.08 10	7 120	7.01 10	10 120	10.5 10	10

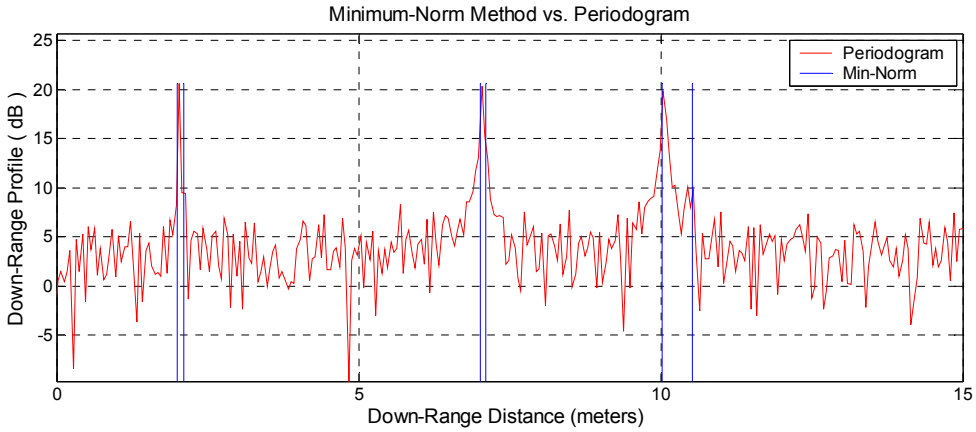

Figure 4.75. Comparison of Minimum-Norm method and periodogram

Table 4.130. Estimated Min-Norm ranges (in meters) in simulation shown in figure 4.75

2.0035	2.0987	7.0116	7.1022	10.0166	10.5241

Figures 4.74 and 4.75 show that Minimum-Norm method can resolve close targets that have very different RCS values. Note that Minimum-Norm method could resolve the first two targets with separation 8 cm whereas periodogram could not resolve the last two targets with separation 50 cm.

4.5.6. LS-ESPRIT vs. Periodogram

Table 4.131. Parameters for simulation shown in figure 4.76

N	BW	T	M	ΔR	Target Ranges (R_k) (meters) & RCSs (A_k)						SNR
600	1.5 GHz	10 mSec	100	10 cm	2 120	3 120	5 120	7 120	10 120	11 120	50

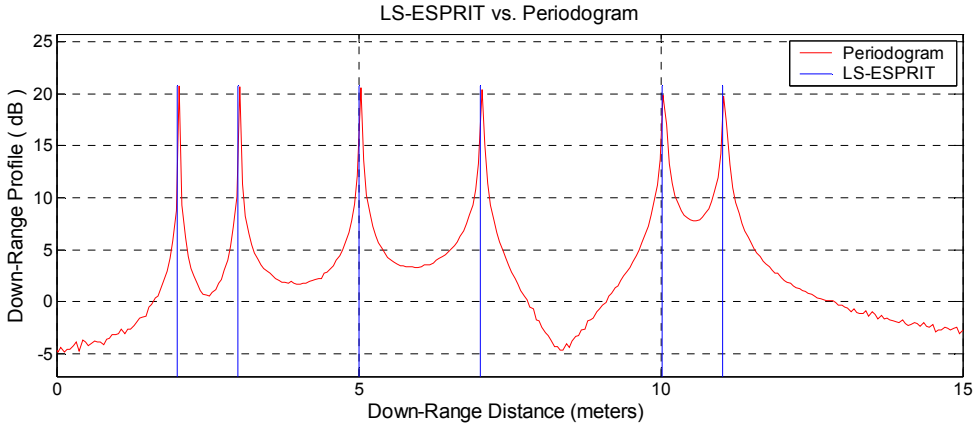

Figure 4.76. Comparison of LS-ESPRIT method and periodogram

Table 4.132. Estimated LS-ESPRIT ranges (in meters) in simulation shown in figure 4.76

2.0033	3.0050	5.0083	7.0117	10.0167	11.0184

Table 4.133. Parameters for simulation shown in figure 4.77

N	BW	T	M	ΔR	Target Ranges (R_k) (meters) & RCSs (A_k)						SNR
600	1.5 GHz	10 mSec	100	10 cm	2 120	3 120	5 120	7 120	10 120	11 120	1

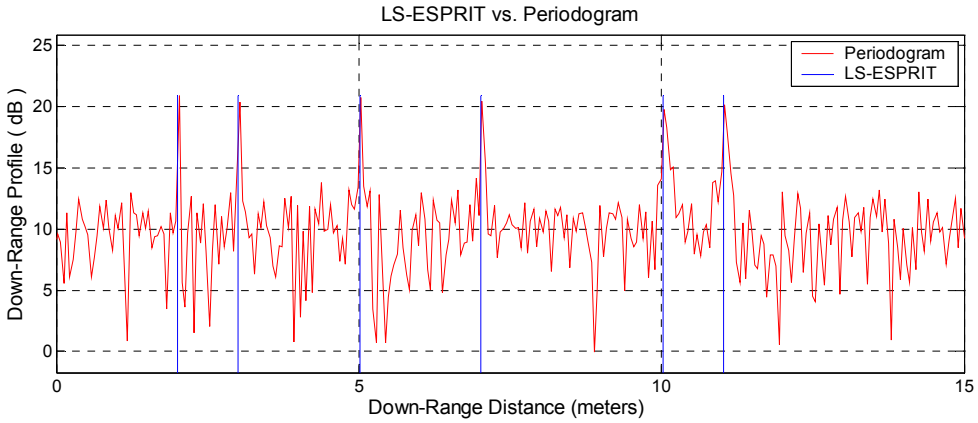

Figure 4.77. Comparison of LS-ESPRIT method and periodogram

Table 4.134. Estimated LS-ESPRIT ranges (in meters) in simulation shown in figure 4.77

2.0033	3.0050	5.0083	7.0117	10.0167	11.0184

Figures 4.76 and 4.77 show that LS-ESPRIT method can find the target ranges very accurately even when the SNR is very low.

Table 4.135. Parameters for simulation shown in figure 4.78

N	BW	T	M	ΔR	Target Ranges (R_k) (meters) & RCSs (A_k)						SNR
600	1.5 GHz	10 mSec	100	10 cm	2 120	2.005 120	7 120	7.01 120	10 120	10.05 120	50

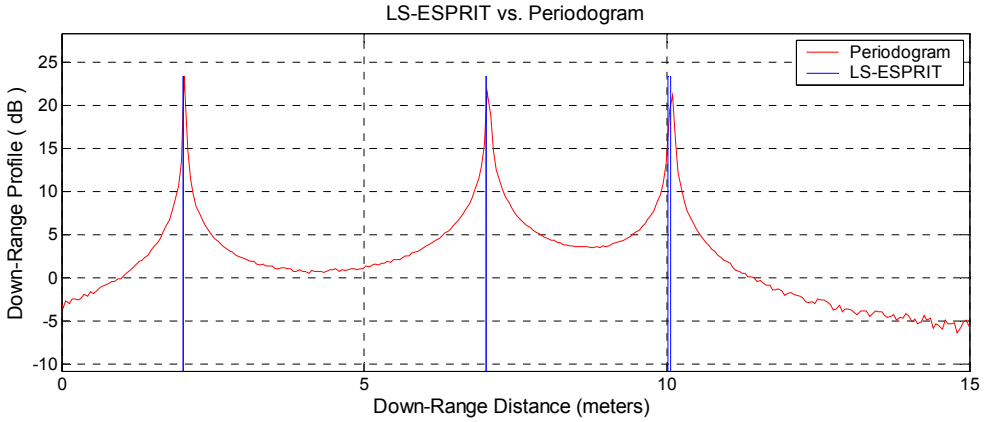

Figure 4.78. Comparison of LS-ESPRIT method and periodogram

Table 4.136. Estimated LS-ESPRIT ranges (in meters) in simulation shown in figure 4.78

2.0047	2.0105	7.0123	7.0204	10.0167	10.0668

Table 4.137. Parameters for simulation shown in figure 4.79

N	BW	T	M	ΔR	Target Ranges (R_k) (meters) & RCSs (A_k)						SNR
600	1.5 GHz	10 mSec	100	10 cm	2 120	2.02 120	7 120	7.05 120	10 120	10.5 120	10

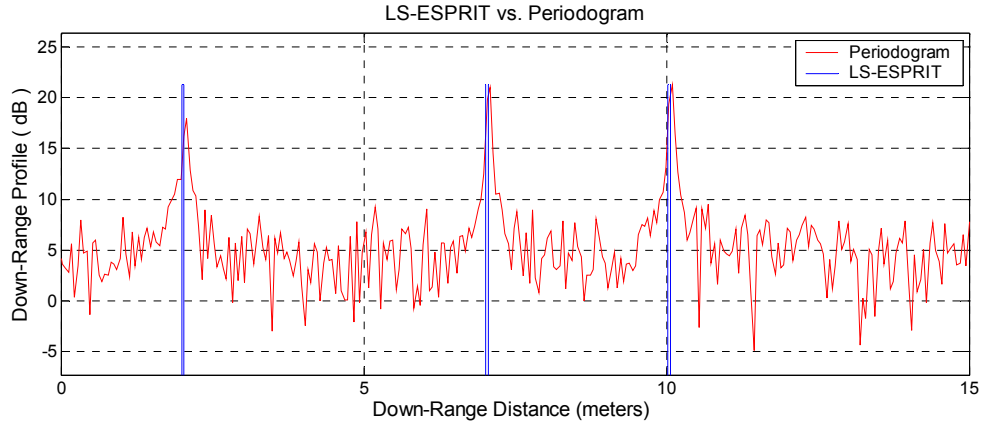

Figure 4.79. Comparison of LS-ESPRIT method and periodogram

Table 4.138. Estimated LS-ESPRIT ranges (in meters) in simulation shown in figure 4.79

1.9998	2.0253	7.0134	7.0608	10.0165	10.0665

Figures 4.78 and 4.79 show that LS-ESPRIT method can find the target ranges very accurately even when the SNR is very low and the targets are very close. Note that periodogram can resolve any close pairs.

Table 4.139. Parameters for simulation shown in figure 4.80

N	BW	T	M	MSSP	ΔR	Target Ranges (R_k) (m) & RCSs (A_k)						SNR
600	1.5 GHz	10 mSec	100	**NO**	10 cm	2 120	2.002 120	7 120	7.01 120	10 120	10.05 120	50

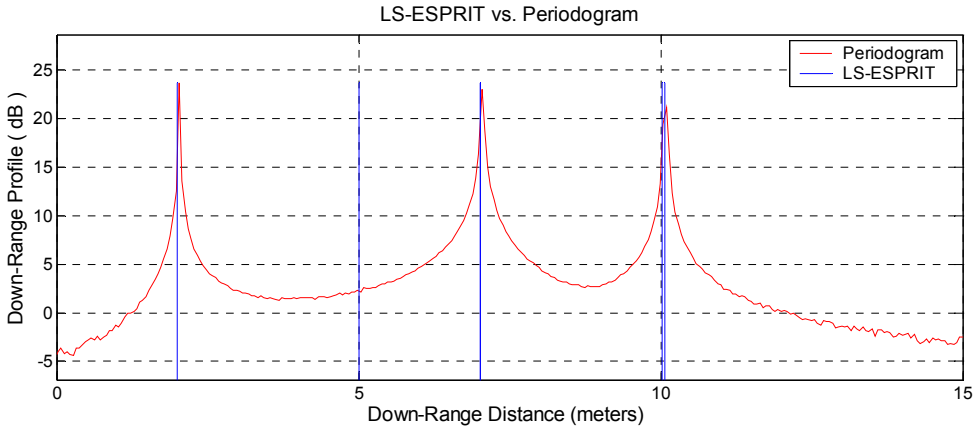

Figure 4.80. Comparison of LS-ESPRIT method and periodogram

Table 4.140. Estimated LS-ESPRIT ranges (in meters) in simulation shown in figure 4.80

2.0033	2.0052	7.0114	7.0156	10.0167	10.0668

Table 4.141. Parameters for simulation shown in figure 4.81

N	BW	T	M	MSSP	ΔR	Target Ranges (R_k) (m) & RCSs (A_k)						SNR
600	1.5 GHz	10 mSec	100	**YES**	10 cm	2 120	2.002 120	7 120	7.01 120	10 120	10.05 120	50

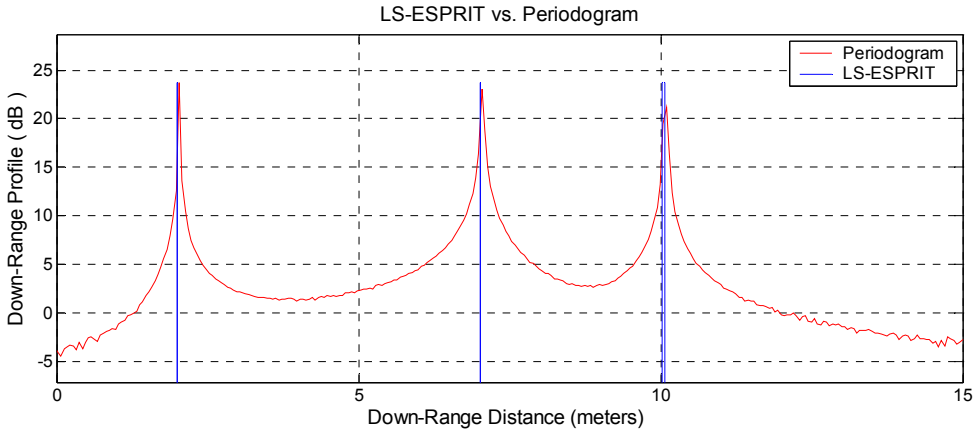

Figure 4.81. Comparison of LS-ESPRIT method and periodogram

Table 4.142. Estimated LS-ESPRIT ranges (in meters) in simulation shown in figure 4.81

2.0033	2.0052	7.0114	7.0156	10.0167	10.0668

Figures 4.80 and 4.81 show that spatial smoothing techniques increases the accuracy of the LS-ESPRIT method. Note that the false alarms are eliminated by modified spatial smoothing processing.

Table 4.143. Parameters for simulation shown in figure 4.82

N	BW	T	M	MSSP	ΔR	Target Ranges (R_k) (m) & RCSs (A_k)						SNR
600	1.5 GHz	10 mSec	100	**YES**	10 cm	2 120	2.01 10	7 120	7.02 10	10 120	10.05 10	50

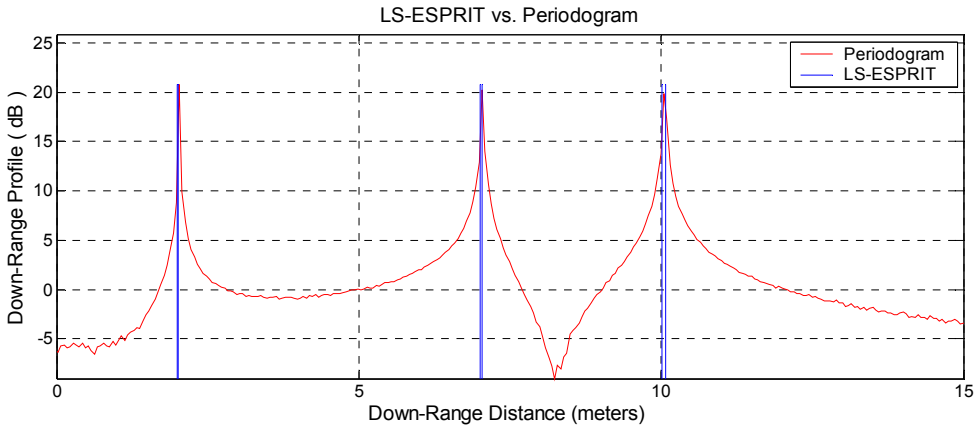

Figure 4.82. Comparison of LS-ESPRIT method and periodogram

Table 4.144. Estimated LS-ESPRIT ranges (in meters) in simulation shown in figure 4.82

2.0033	2.0131	7.0116	7.0325	10.0167	10.0668

Table 4.145. Parameters for simulation shown in figure 4.83

N	BW	T	M	MSSP	ΔR	Target Ranges (R_k) (m) & RCSs (A_k)						SNR
600	1.5 GHz	10 mSec	100	**YES**	10 cm	2 120	2.07 10	7 120	7.08 10	10 120	10.1 10	10

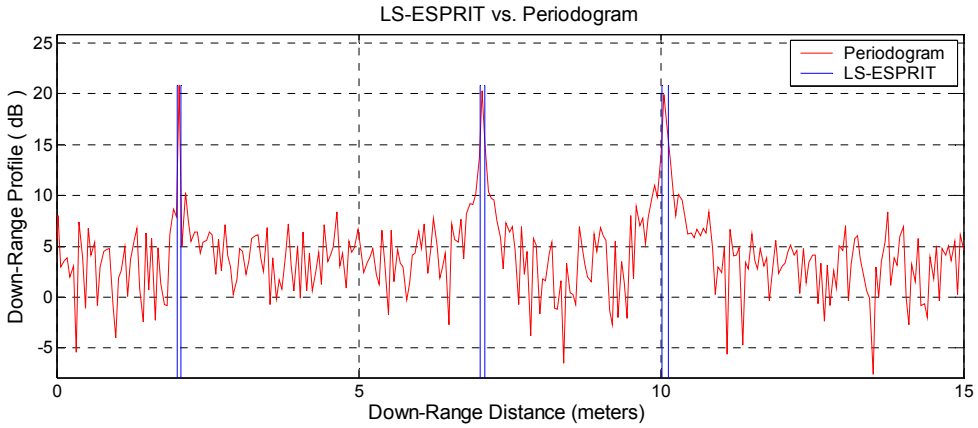

Figure 4.83. Comparison of LS-ESPRIT method and periodogram

Table 4.146. Estimated LS-ESPRIT ranges (in meters) in simulation shown in figure 4.83

2.0031	2.0646	7.0125	7.0866	10.0163	10.1176

Figures 4.82 and 4.83 show that LS-ESPRIT can resolve the close targets with very different RCS values even when the SNR is low.

4.5.7. TLS-ESPRIT vs. Periodogram

Table 4.147. Parameters for simulation shown in figure 4.84

N	BW	T	M	MSSP	ΔR	Target Ranges (R_k) (m) & RCSs (A_k)						SNR
600	1.5 GHz	10 mSec	100	NO	10 cm	2 120	3 120	5 120	7 120	10 120	11 120	50

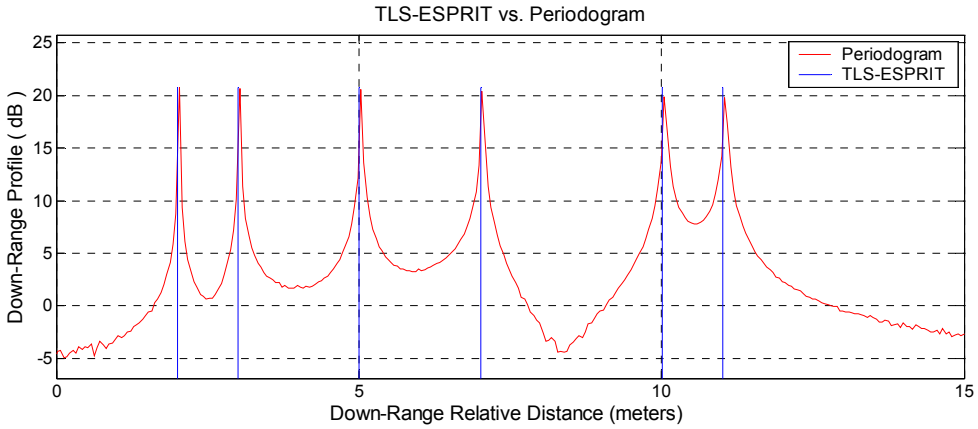

Figure 4.84. Comparison of TLS-ESPRIT method and periodogram

Table 4.148. Estimated TLS-ESPRIT ranges(in meters) in simulation shown in figure 4.84

2.0033	3.0050	5.0084	7.0117	10.0167	11.0184

Table 4.149. Parameters for simulation shown in figure 4.85

N	BW	T	M	MSSP	ΔR	Target Ranges (R_k) (m) & RCSs (A_k)						SNR
600	1.5 GHz	10 mSec	100	NO	10 cm	2 120	3 120	5 120	7 120	10 120	11 120	1

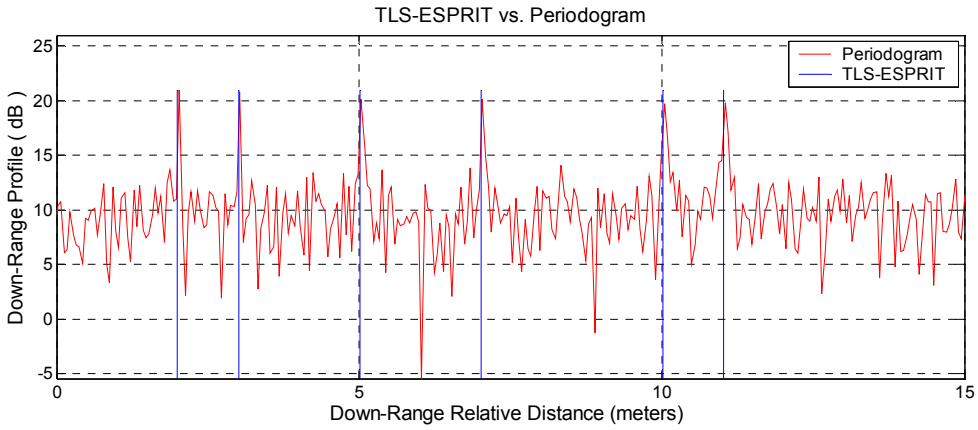

Figure 4.85. Comparison of TLS-ESPRIT method and periodogram

Table 4.150. Estimated TLS-ESPRIT ranges(in meters) in simulation shown in figure 4.85

2.0018	3.0053	5.0120	7.0108	10.0159	11.0174

Figures 4.84 and 4.85 show that TLS-ESPRIT method can find the target ranges very accurately even when the SNR is very low.

Table 4.151. Parameters for simulation shown in figure 4.86

N	BW	T	M	MSSP	ΔR	Target Ranges (R_k) (m) & RCSs (A_k)						SNR
600	1.5 GHz	10 mSec	100	NO	10 cm	2 120	2.003 120	7 120	7.01 120	10 120	10.1 120	50

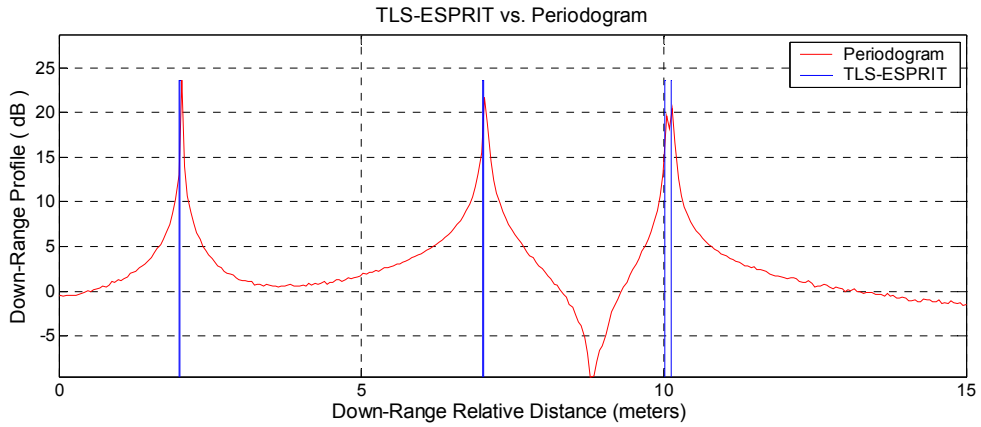

Figure 4.86. Comparison of TLS-ESPRIT method and periodogram

Table 4.152. Estimated TLS-ESPRIT ranges(in meters) in simulation shown in figure 4.86

2.0018	3.0053	5.0120	7.0108	10.0159	11.0174

Table 4.153. Parameters for simulation shown in figure 4.87

N	BW	T	M	MSSP	ΔR	Target Ranges (R_k) (m) & RCSs (A_k)						SNR
600	1.5 GHz	10 mSec	100	NO	10 cm	2 120	2.015 120	7 120	7.02 120	10 120	10.1 120	10

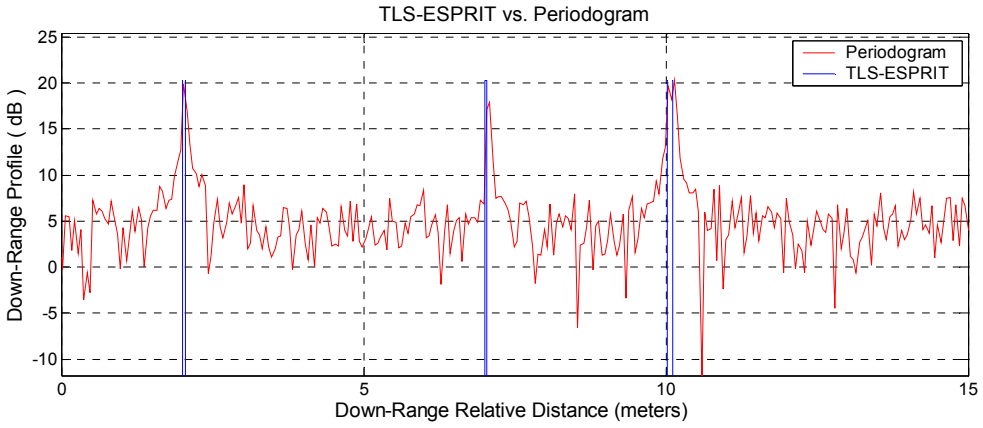

Figure 4.87. Comparison of TLS-ESPRIT method and periodogram

Table 4.154. Estimated TLS-ESPRIT ranges(in meters) in simulation shown in figure 4.87

2.0068	2.0487	7.0063	7.0356	10.0167	10.1168

Figures 4.86 and 4.87 show that TLS-ESPRIT method can find the target ranges very accurately even when the SNR is very low and the targets are so close to each other. Note that in both case TLS-ESPRIT method provides much better range estimates than

periodogram. Also, it is observed that TLS-ESPRIT method can resolve closer targets than LS-ESPRIT method. LS-ESPRIT method could resolve targets with separation 5 mm when SNR is 50 and 2 cm when SNR is 10 whereas TLS-ESPRIT method can resolve targets with separation 3 mm when SNR is 50 and 1.5 cm when SNR is 10.

Table 4.155. Parameters for simulation shown in figure 4.88

N	BW	T	M	MSSP	ΔR	Target Ranges (R_k) (m) & RCSs (A_k)						SNR
600	1.5 GHz	10 mSec	100	NO	10 cm	2 120	2.003 120	7 120	7.01 120	10 120	10.1 120	50

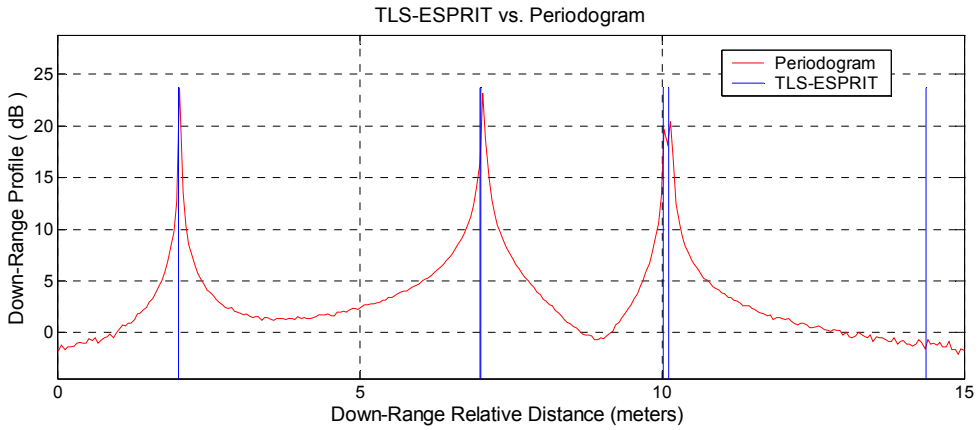

Figure 4.88. Comparison of TLS-ESPRIT method and periodogram

Table 4.156. Estimated TLS-ESPRIT ranges(in meters) in simulation shown in figure 4.88

2.0043	14.3711	6.9950	7.0133	10.0167	10.1169

Table 4.157. Parameters for simulation shown in figure 4.89

N	BW	T	M	MSSP	ΔR	Target Ranges (R_k) (m) & RCSs (A_k)						SNR
600	1.5 GHz	10 mSec	100	YES	10 cm	2 120	2.002 120	7 120	7.003 120	10 120	10.1 120	50

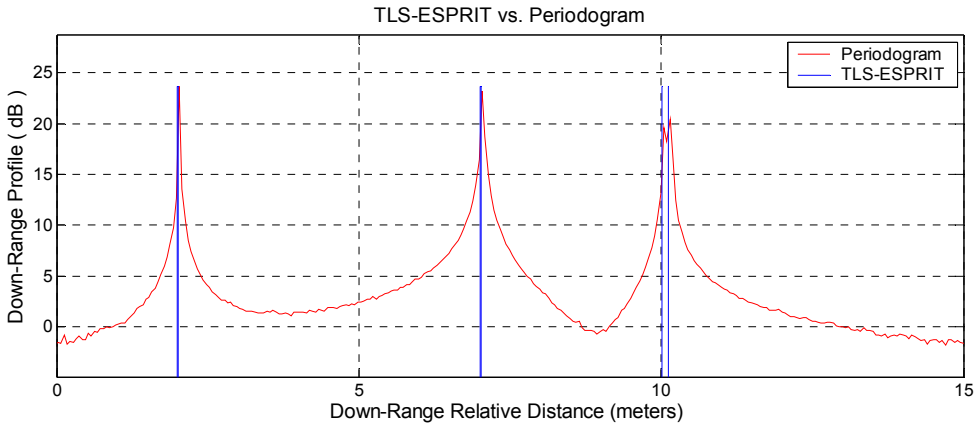

Figure 4.89. Comparison of TLS-ESPRIT method and periodogram

Table 4.158. Estimated TLS-ESPRIT ranges(in meters) in simulation shown in figure 4.89

2.0016	2.0047	7.0118	7.0145	10.0167	10.1169

Figures 4.88 and 4.89 show that spatial smoothing techniques increases the accuracy of the TLS-ESPRIT method. Note that the false alarms are eliminated by modified spatial smoothing processing.

Table 4.159. Parameters for simulation shown in figure 4.90

N	BW	T	M	MSSP	ΔR	Target Ranges (R_k) (m) & RCSs (A_k)						SNR
600	1.5 GHz	10 mSec	100	**YES**	10 cm	2 120	2.005 10	7 120	7.01 10	10 120	10.05 10	50

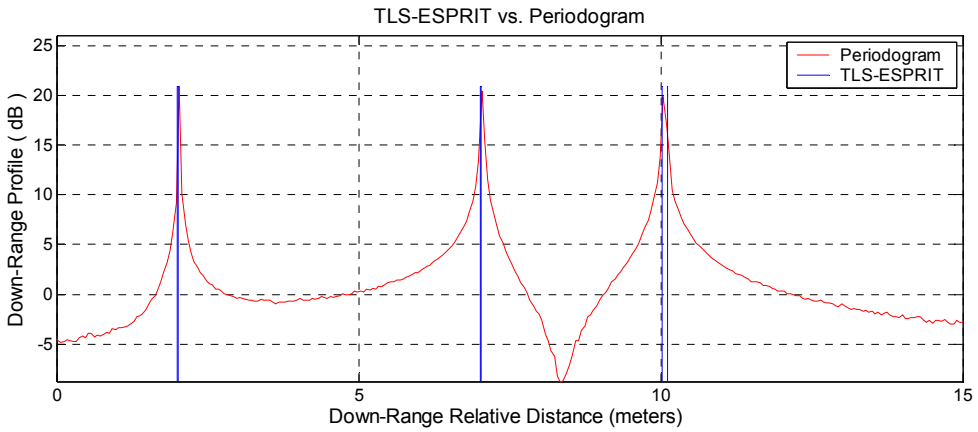

Figure 4.90. Comparison of TLS-ESPRIT method and periodogram

Table 4.160. Estimated TLS-ESPRIT ranges(in meters) in simulation shown in figure 4.90

2.0032	2.0066	7.0117	7.0227	10.0167	10.1168

Table 4.161. Parameters for simulation shown in figure 4.91

N	BW	T	M	MSSP	ΔR	Target Ranges (R_k) (m) & RCSs (A_k)						SNR
600	1.5 GHz	10 mSec	100	**YES**	10 cm	2 120	2.06 10	7 120	7.07 10	10 120	10.05 10	10

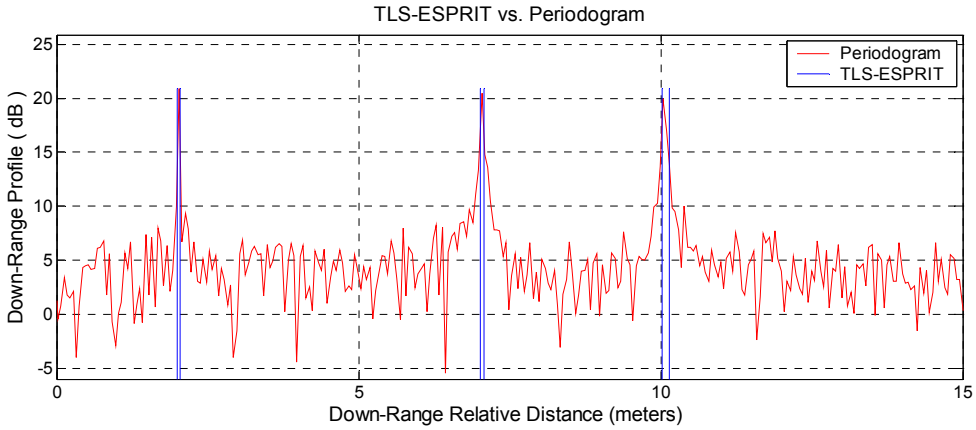

Figure 4.91. Comparison of TLS-ESPRIT method and periodogram

Table 4.162. Estimated TLS-ESPRIT ranges(in meters) in simulation shown in figure 4.91

2.0030	2.0439	7.0119	7.0669	10.0161	10.1463

Figures 4.90 and 4.91 show that TLS-ESPRIT can resolve the close targets with very different RCS values even when the SNR is low. Note that TLS-ESPRIT can resolve closer targets compared with LS-ESPRIT.

5. RESOLVING CAPABILITY of SUPER-RESOLUTION METHODS : EXPERIMENTAL STUDY

This chapter investigates the resolving capability of super-resolution spectral estimation methods explained in chapter three using experimental stepped-frequency radar data for buried and through-the-wall object detection. First, the experimental setup will be explained. Then, the resolving capability of super-resolution spectral estimation methods will be tested using different sets of experimental data.

5.1. Experimental Setup

Field experiments have been performed at the laboratory of National Institute of Electronics and Cryptology using HP-8753 vector network analyzer. This vector network analyzer works as an SFCW radar. Top and front views of the experimental field are shown in figures 5.1 and 5.2, respectively. The wall is realized using a pool filled with ordinary soil.

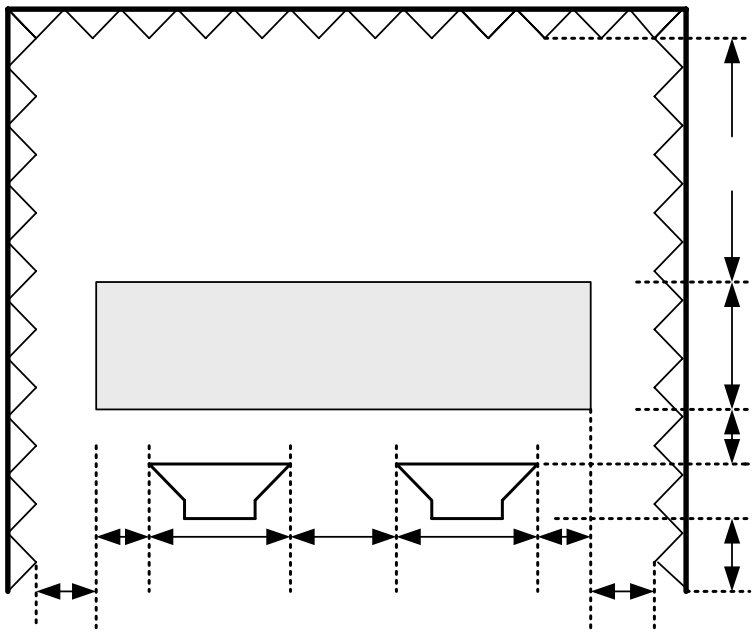

Figure 5.1. Top view of experimental field

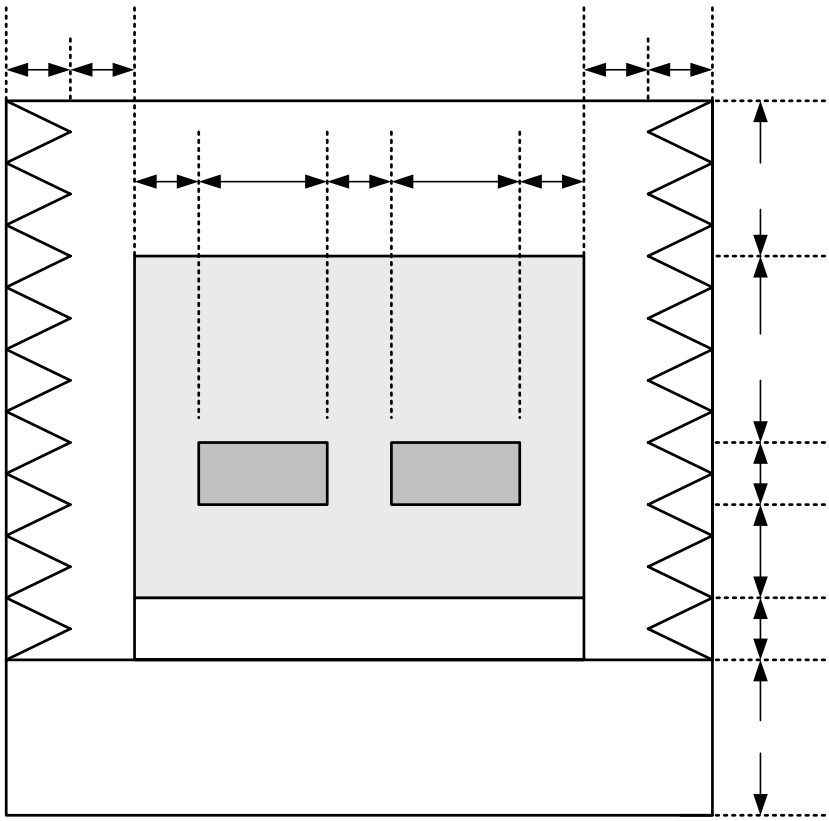

Figure 5.2. Front view of experimental field

Four metallic plates whose dimensions are given in table 5.1 are used as targets.

Table 5.1. Dimensions of the targets

Target	Width (cm)	Length (cm)
M	34	100
A	5	59
B	3	59
C	2	59

Two co-axial cables with length 2 meters are used to connect the network analyzer ports to antennas. The antennas used in the experiments are double ridged waveguide horn antennas which operate in 1-18 GHz frequency band. Two-port calibration was performed at the co-axial cable ends before the tests.

In order to investigate the effect of frequency band of operation and bandwidth of stepped frequency radar waveform on signal processing algorithms, test were performed at different bandwidths and frequencies. Table 5.2 shows the bandwidths used in the tests and corresponding frequency bands.

Table 5.2. Bandwidths and frequency bands used in the experiments

Bandwidth	Frequency Band
500 MHz	1 – 1.5 GHz
750 MHz	1 – 1.75 GHz
1 GHz	1 - 2 GHz
1.5 GHz	1 – 2.5 GHz
2 GHz	1 - 3 GHz
2.5 GHz	1 – 3.5 GHz
3 GHz	1 - 4 GHz

Different number of points which corresponds to the number of steps in the stepped-frequency radar waveform were used to collect data during the tests. HP-8753 network analyzer provides 26, 51, 101, 201, 401, 801, 1601 as options for the number of points. Since increasing the number of steps in the stepped-frequency radar waveform increases the un-ambiguous range if the bandwidth is kept constant and the walls of the test field are covered with absorbers, only 26, 51, 101, and 201 points were used during the tests.

Since stepped-frequency radar uses continuous waveforms, in order to reduce the leakage from transmitter to receiver, bistatic operation was chosen for radar and s_{21} parameter data are collected using network analyzer. In order to automate the data collection process, a simple software was developed in LabWindows/CVI. The software controls the network analyzer and stores the s_{21} data for each bandwidth, target, and target position using HP-IB bus. The graphical user interface(GUI) of the program is shown in figure 5.3. The user can select the s-parameter, number of points and frequency bandwidth (or start and stop frequencies) via the GUI. The “MEASURE” button takes measurement according to selected parameters, “SAVE--DATA” button saves the s-parameter data in a text file and “SAVE--SCREEN” button saves the current screen. The graphs in the GUI shows the in-phase and quadrature data in linear scale and the magnitude of the spectrum in logarithmic scale.

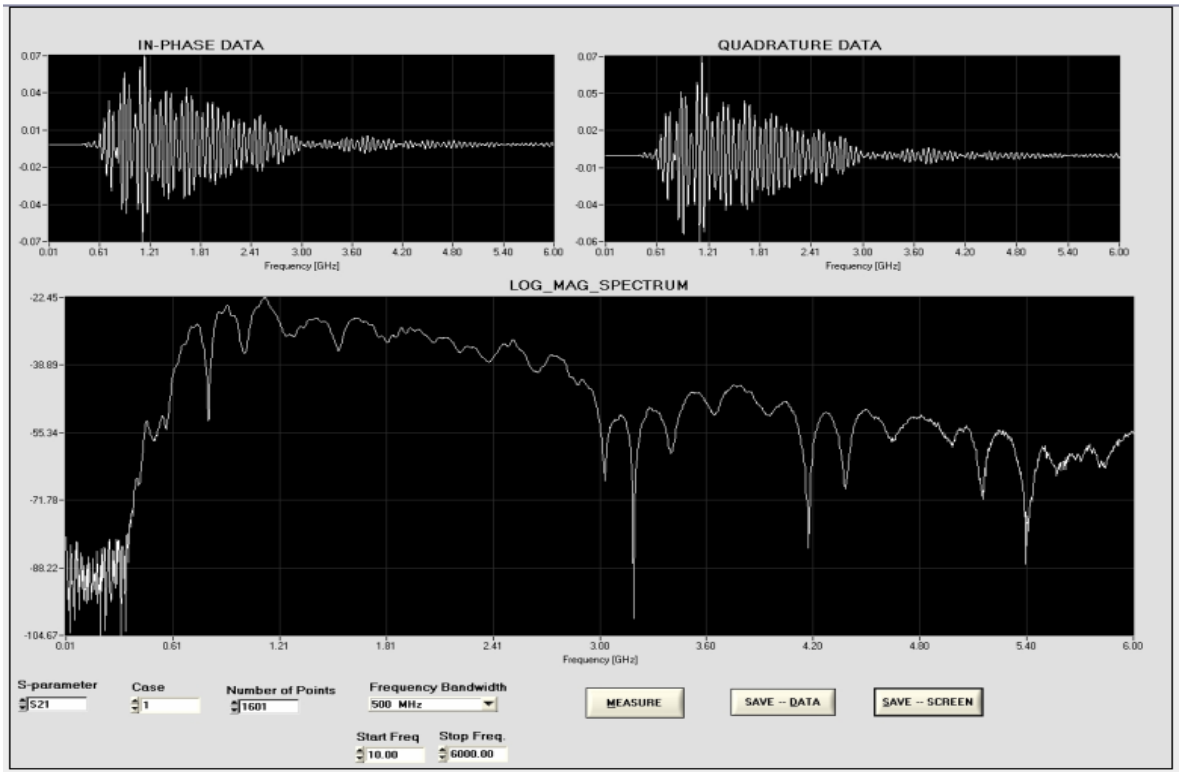

Figure 5.3. GUI of the program used for automated data collection

Frequency band of operation is an important parameter for the stepped frequency radar. It is known that the attenuation constant of the radio frequency signals increases as the frequency increases. We also know that the range resolution of the stepped-frequency radar increases with bandwidth. So, we should find a region in the spectrum where we minimize the attenuation and maximize the bandwidth. As can be seen from figure 5.3, the magnitude of the inphase and quadrature signals decreases drastically after 3 GHz and drops to zero about 4 GHz. Also, since the antennas used in the experiments operates in 1-18 GHz frequency band, the magnitude of the inphase and quadrature signals decreases also below 1 GHz because of antenna. So, the tests are performed in the frequency band of 1-4 GHz. Also, many tests were performed using another network analyzer up to 18 GHz, however, because of the reasons explained above, they did not provide satisfactory results.

5.2. Super-resolution Spectral Estimators for Through-the-Wall Object Detection

In order to investigate the performance of super-resolution spectral estimators for through-the-wall object detection, different sets of experimental data have been taken using network analyzer. Targets and their position are changed during experiments. Tests are numerated according to the targets used in the experiments and their locations. Targets used in each case and their corresponding locations are shown in tables 5.3 and 5.4. Figure 5.4 shows the locations of the targets in the experimental setup.

Table 5.3. Targets and their locations in TWOD experiments

Case	Target	Location
0	-	-
1	M	1
2	M	2
3	M	5
4	A	1
5	A	2
6	A	3
7	A	4
8	A	5
9	B	1
10	B	2
11	B	3
12	B	4
13	B	5
14	C	1
15	C	2
16	C	3
17	C	4
18	C	5

Data collected in cases 1-18 shown in table 5.3 will be used to test the accuracy of super-resolution spectral estimation methods explained in chapter three. In case-0, there is any target in the field and this case corresponds to the background measurement.

Table 5.4. Targets and their locations in TWOD experiments

Case	Target-1	Location-1	Target-2	Location-2
19	M	5	A	1
20	M	5	A	2
21	M	5	A	3
22	M	5	B	1
23	M	5	B	2
24	M	5	B	3
25	A	5	B	1
26	A	5	B	2
27	A	5	B	3
28	A	5	C	1
29	A	5	C	2
30	A	5	C	3

Data collected in cases 19-30 shown in table 5.4 will be used to test the resolving capability of super-resolution spectral estimation methods. In case-19, target-M is at location-5 and target-A is at location-1.

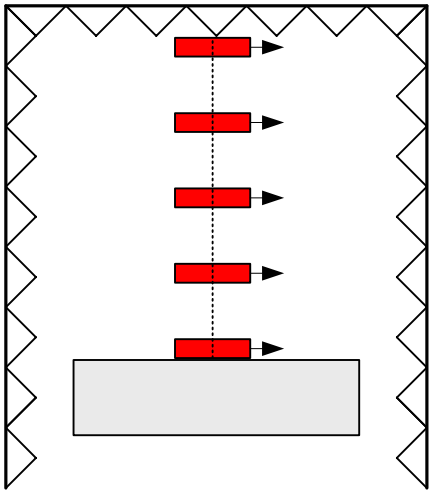

Figure 5.4. Target locations in the TWOD experiments

Following sections will investigate the performance of super-resolution spectral estimators in TWOD application and compare their performance with classically used periodogram method.

5.2.1. Comparison of Yule-Walker Method and Periodogram for TWOD

Several simulations were carried out to investigate the performance of AR modeling using Yule-Walker method for TWOD application. Note that the parameters of the stepped- frequency radar waveform (bandwidth and number of points) and the case numbers are shown in the figures.

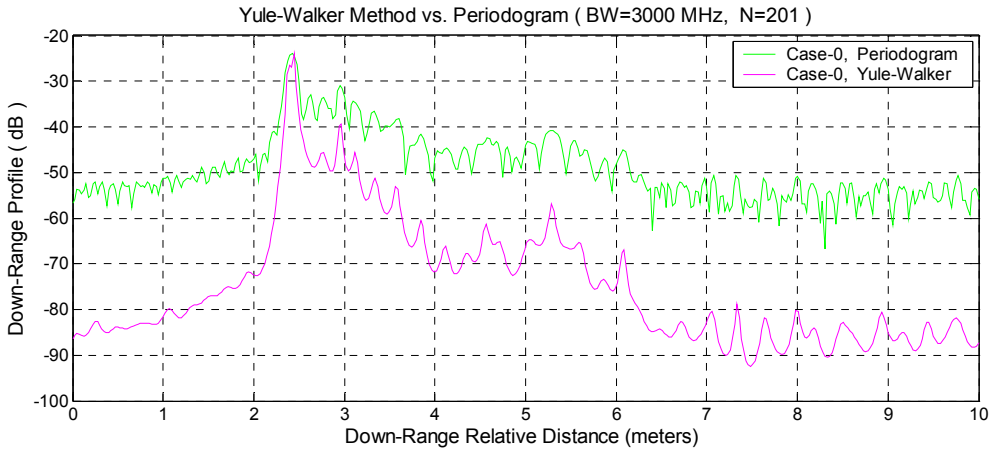

Figure 5.5. Comparison of Yule-Walker method and periodogram for TWOD (Case-0)

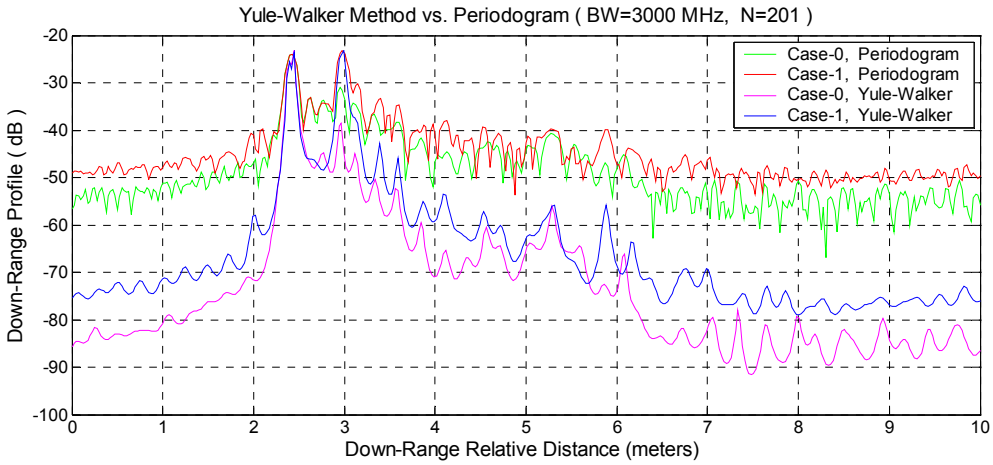

Figure 5.6. Comparison of Yule-Walker method and periodogram for TWOD (Case-1)

Figure 5.6 shows that Yule-Walker method provides narrower peak at the target location. Also note that the Signal-to-Clutter Ratio (SCR) of the Yule-Walker range profile is higher than the SCR of the periodogram range profile.

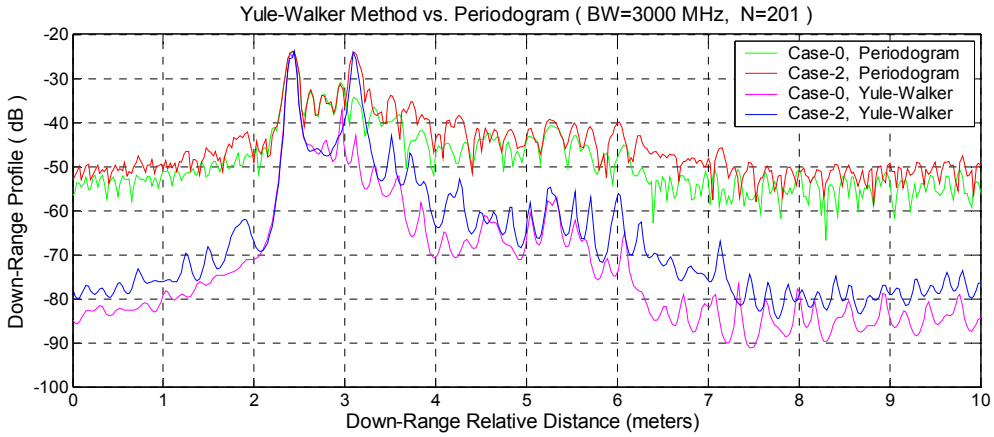

Figure 5.7. Comparison of Yule-Walker method and periodogram for TWOD (Case-2)

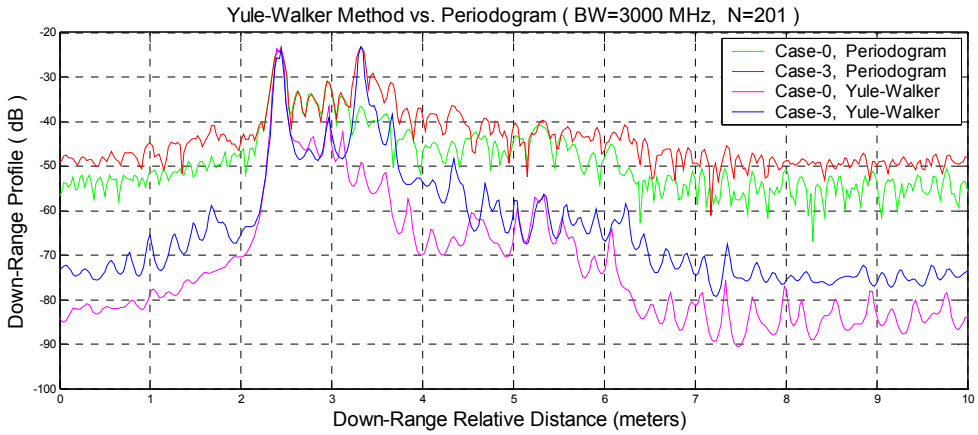

Figure 5.8. Comparison of Yule-Walker method and periodogram for TWOD (Case-3)

Note that both methods find the target location accurately. However, it is obvious that Yule-Walker range profile is better than periodogram range profile.

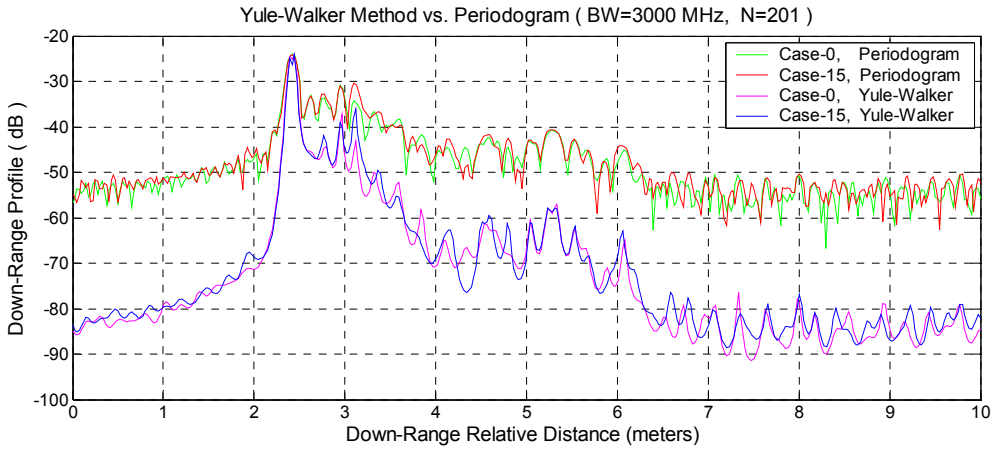

Figure 5.9. Comparison of Yule-Walker method and periodogram for TWOD (Case-15)

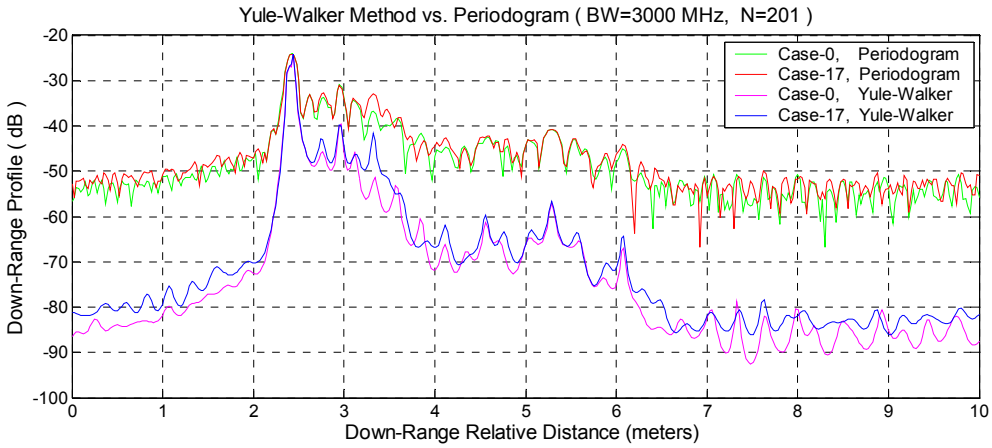

Figure 5.10. Comparison of Yule-Walker method and periodogram for TWOD (Case-17)

Figures 5.9 and 5.10 show that Yule-Walker method provides much better range profiles than periodogram method even when the target has small RCS value. In figure 5.10, Yule-Walker range profile has a small but sharp peak at target location; however, periodogram range profile has several broad peaks around target location and the target is not resolved.

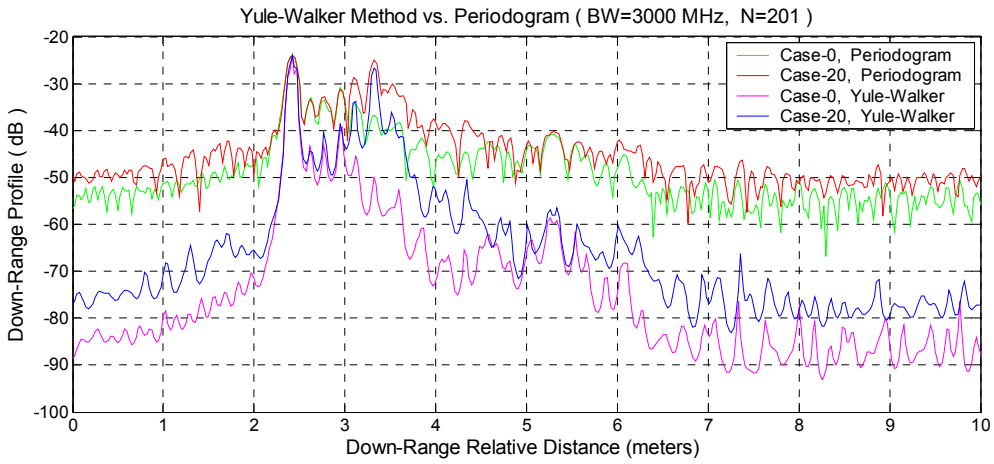

Figure 5.11. Comparison of Yule-Walker method and periodogram for TWOD (Case-20)

In case-20, target-M is in location-5 and target-B is in location-2, and as can be seen from the figure 5.11, Yule-Walker method can resolve them better than periodogram. Note that Yule-Walker method range profile has sharper peaks at target locations. Second highest peak in figure 5.11 corresponds to target-M and the peak on left of it corresponds to the target-B.

5.2.2. Comparison of Least-Squares Method and Periodogram for TWOD

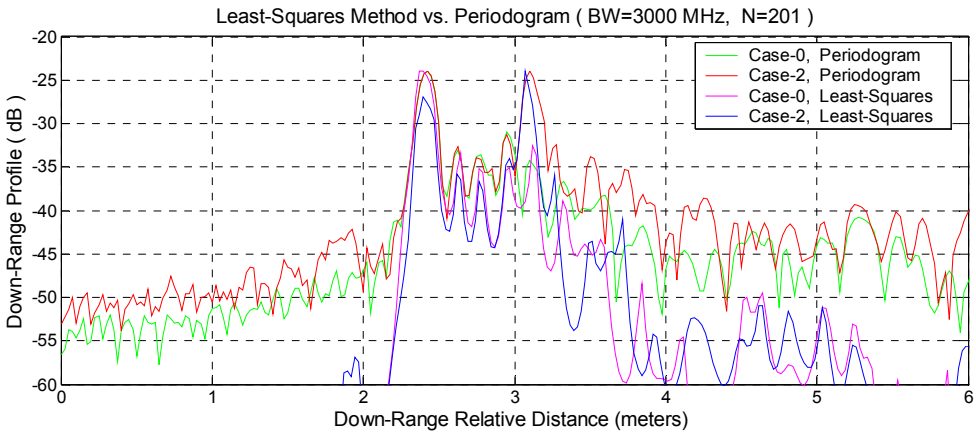

Figure 5.12. Comparison of Least-Squares method and periodogram for TWOD (Case-2)

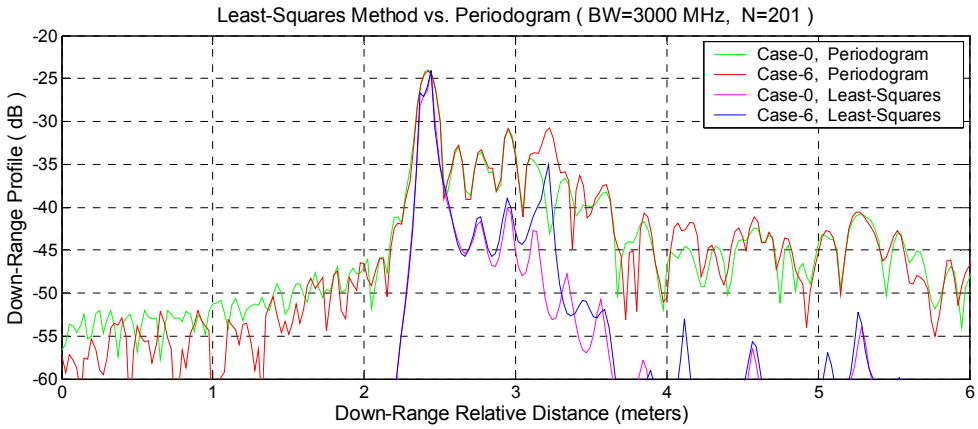

Figure 5.13. Comparison of Least-Squares method and periodogram for TWOD (Case-6)

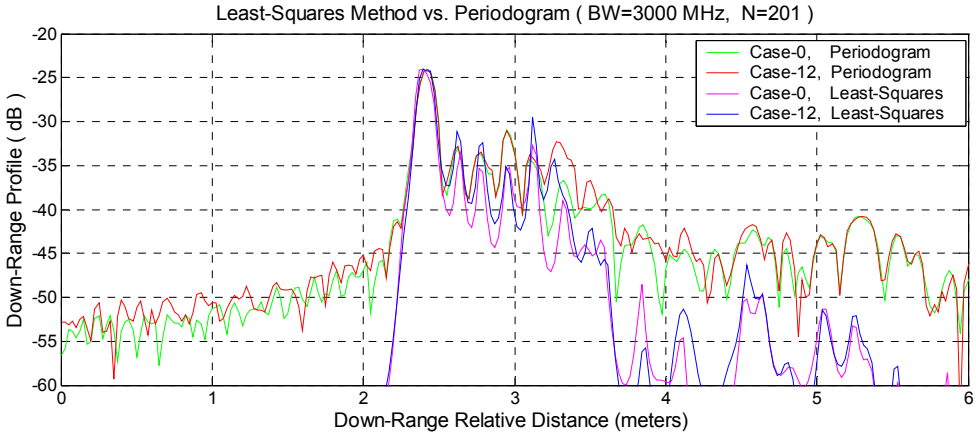

Figure 5.14. Comparison of Least-Squares method and periodogram for TWOD (Case-12)

Figures 5.12-14 show that Least-Squares method provides better range profiles than periodogram method even for the small targets. Note that Least-Squares range profiles have sharper peaks at target locations and higher SCR.

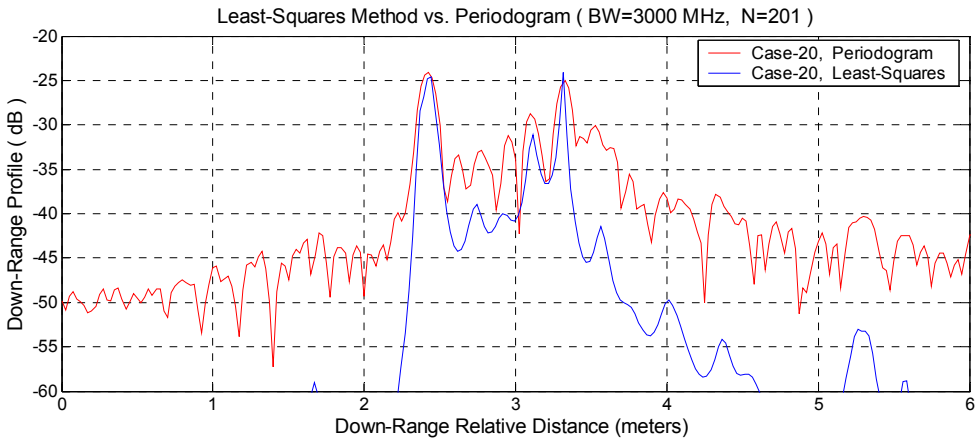

Figure 5.15. Comparison of Least-Squares method and periodogram for TWOD (Case-20)

In case-20, target-M is in location-5 and target-B is in location-2, and as can be seen from figure 5.15, Yule-Walker method can resolve them better than periodogram. Note that Yule-Walker method range profile has sharper peaks at target locations. Second highest peak in figure 5.11 corresponds to target-M and the peak on left of it corresponds to the target-B.

5.2.3. Comparison of Line Spectra Methods and Periodogram for TWOD

This section covers the performance analysis of line spectral estimators explained in detail in section 3.4 in TWOD application. The parameters of the stepped-frequency radar and the target locations are given in the figures. Data collected for the case given in figure is processed using the line spectral estimators and the corresponding range estimates are given in tables below the corresponding figures. In tables, the columns named as “Target-i” represents the range estimates for the i^{th} target and the column named as “Difference” represents the distance between the range estimates of the targets.

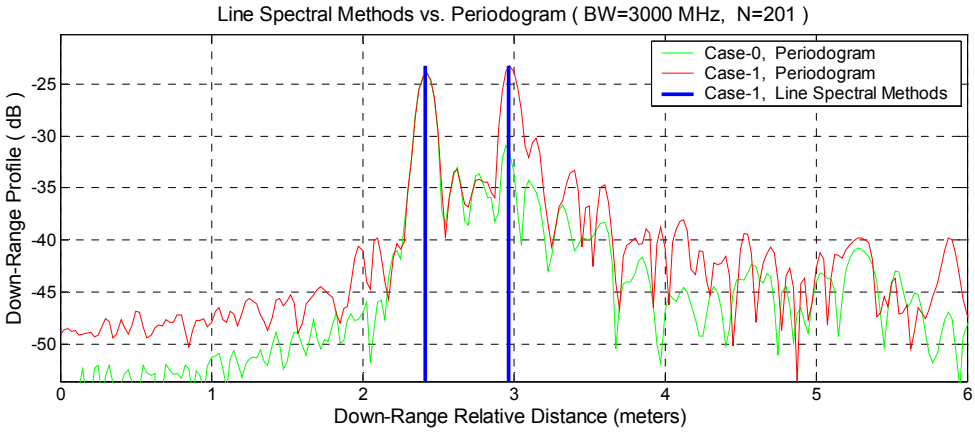

Figure 5.16. Comparison of line spectral estimators and periodogram for TWOD (Case-1)

Table 5.5. Range estimates of line spectral estimators (Case-1)

Case-1	Target-1	Target-2	Difference
HOYW Method	2.4144	2.9659	0.5515
Min-Norm Method	2.4158	2.9669	0.5511
LS-ESPRIT	2.4157	2.9665	**0.5508**
TLS-ESPRIT	2.4157	2.9665	**0.5508**
Root-MUSIC Method	2.4181	2.9705	0.5524

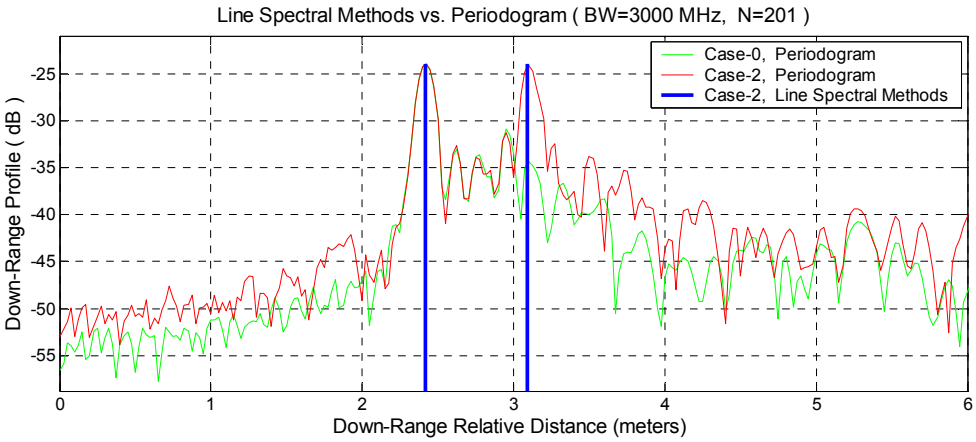

Figure 5.17. Comparison of Line spectral estimators and periodogram for TWOD (Case-2)

Table 5.6. Range estimates of line spectral estimators (Case-2)

Case-2	Target-1	Target-2	Difference	Difference (in case-1)	Displacement
HOYW Method	2.4160	3.0907	0.6747	0.5515	0.1232
Min-Norm Method	2.4151	3.0946	0.6795	0.5511	0.1284
LS-ESPRIT	2.4147	3.0950	0.6803	0.5513	0.1290
TLS-ESPRIT	2.4147	3.0950	0.6803	0.5513	0.1290
Root-MUSIC	2.4162	3.0920	0.6758	0.5524	0.1234

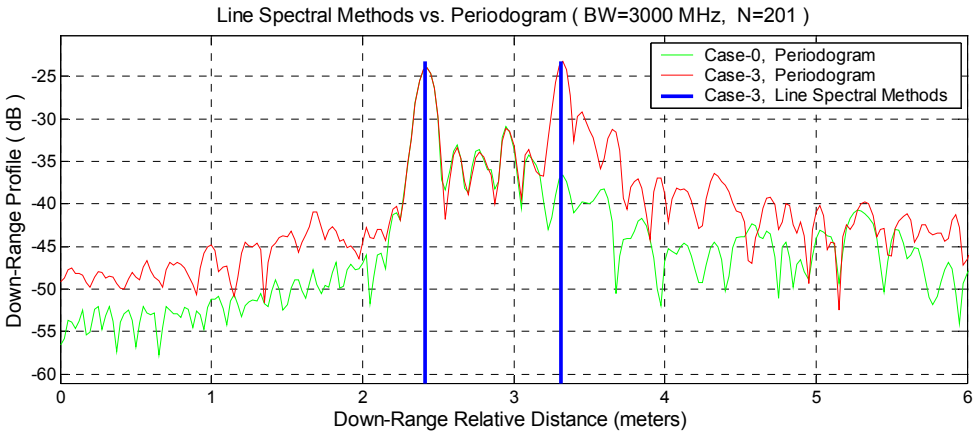

Figure 5.18. Comparison of line spectral estimators and periodogram for TWOD (Case-3)

Table 5.7. Range estimates of line spectral estimators (Case-3)

Case-3	Target-1	Target-2	Difference	Difference (in case-1)	Displacement
HOYW Method	2.4144	3.3123	0.8979	0.5515	0.3464
Min-Norm Method	2.4150	3.3101	0.8951	0.5511	0.3440
LS-ESPRIT	2.4146	3.3105	0.8959	0.5513	0.3446
TLS-ESPRIT	2.4145	3.3105	0.8960	0.5513	0.3447
Root-MUSIC	2.4167	3.3165	0.8998	0.5524	0.3474

Figures 5.16-18 and tables 5.5-7 show that all the line spectral estimators can find the target ranges and they provide very similar range estimates.

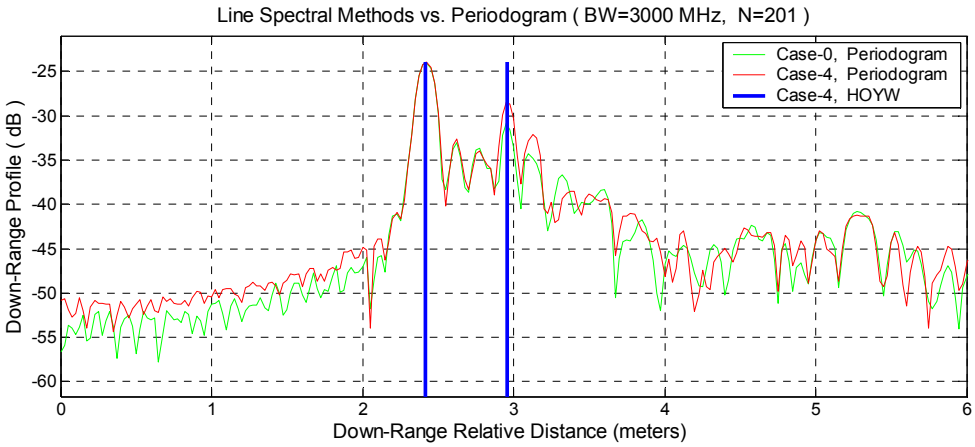

Figure 5.19. Comparison of line spectral estimators and periodogram for TWOD (Case-4)

Table 5.8. Range estimates of line spectral estimators (Case-4)

Case-4	Target-1	Target-2	Difference
HOYW Method	2.4130	2.9508	0.5378
Min-Norm Method	2.4137	2.9276	0.5139
LS-ESPRIT	2.4145	2.9109	**0.4964**
TLS-ESPRIT	2.4145	2.9109	**0.4964**
Root-MUSIC	2.4152	2.9720	0.5568

In case-4, target-A is at location-1. Since the highest peak in the spectrum corresponds to the front side of the wall and the distance between front side of the wall and the location-1, which corresponds to the back side of the wall, is 34 cm, it is obvious that ESPRIT solutions provide the most accurate range estimates.

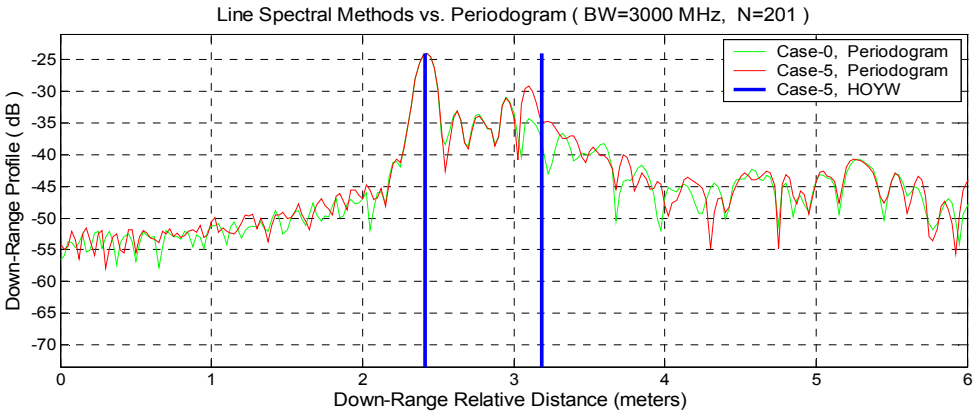

Figure 5.20. Comparison of line spectral estimators and periodogram for TWOD (Case-5)

Table 5.9. Range estimates of line spectral estimators (Case-5)

Case-5	Target-1	Target-2	Difference	Difference (case-4)	Displacement
HOYW Method	2.4170	3.0874	0.6704	0.5378	0.1326
Min-Norm Method	2.4145	3.0724	0.6579	0.5139	0.1440
LS-ESPRIT	2.4141	3.0633	**0.6492**	0.4964	**0.1528**
TLS-ESPRIT	2.4140	3.0634	**0.6494**	0.4964	**0.1530**
Root-MUSIC	2.4157	3.0850	0.6693	0.5568	0.1125

In case-5, the actual difference between the front side of the wall and the location-2 is 50 cm. Table 5.9 shows that ESPRIT solutions provide the most accurate range estimates even for the smaller target. Also note that ESPRIT solutions find the displacement of target-2 between case-4 and case-5, which is 16 cm, very accurately.

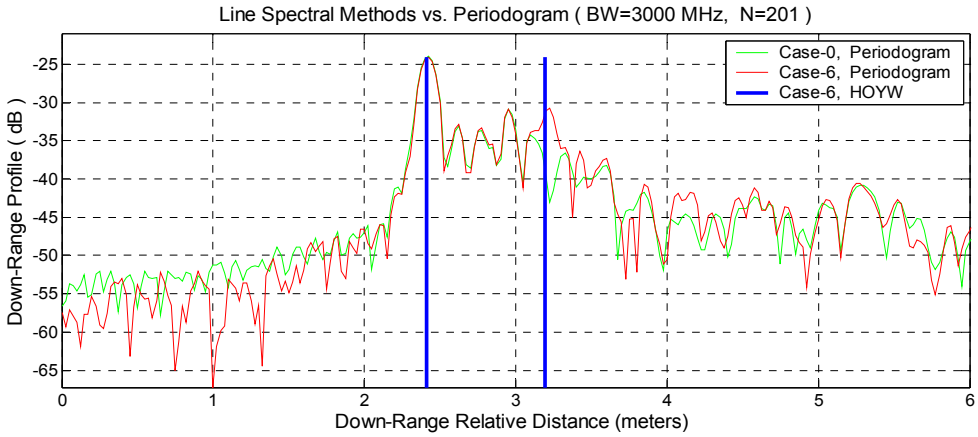

Figure 5.21. Comparison of line spectral estimators and periodogram for TWOD (Case-6)

Table 5.10. Range estimates of line spectral estimators (Case-6)

Case-6	Target-1	Target-2	Difference	Difference (in case-5)	Displacement
HOYW Method	2.4124	3.1915	0.7791	0.6704	0.1087
Min-Norm Method	2.4186	3.1569	0.7383	0.6579	**0.0804**
LS-ESPRIT	2.4190	3.1532	0.7342	0.6492	**0.0850**
TLS-ESPRIT	2.4190	3.1532	0.7342	0.6494	**0.0848**
Root-MUSIC	2.4172	3.1135	0.6963	0.6693	0.0270

Figure 5.21 and table 5.10 shows that all line spectral estimators can find the target ranges whereas it is not possible to determine the number of targets and the positions form the periodogram range profile. We can conclude that line spectral estimators outperform periodogram method even for small targets. Also note that the ESPRIT solutions and Min-Norm method find the displacement of target-2 between case-5 and case-6, which is 8 cm, very accurately.

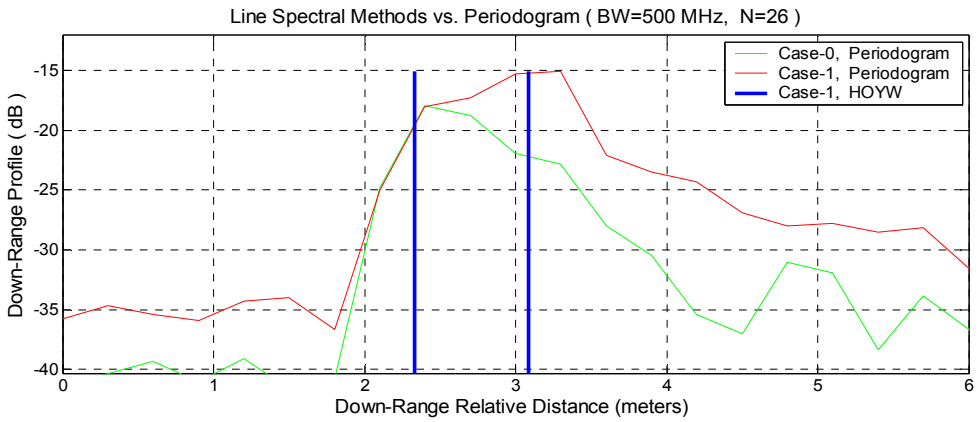

Figure 5.22. Comparison of line spectral estimators and periodogram for TWOD (Case-1)

Table 5.11. Range estimates of line spectral estimators (Case-1)

Case-1 (Small BW,N)	Target-1	Target-2	Difference
HOYW Method	2.3302	3.0878	0.7576
Min-Norm Method	2.5638	3.0674	0.5036
LS-ESPRIT	2.5827	3.0577	**0.4750**
TLS-ESPRIT	2.5826	3.0579	**0.4753**
Root-MUSIC	2.5590	3.1341	0.5751

Figure 5.22 and table 5.11 shows the range profile and range estimates, respectively, for the data with 26 points and 500 MHz stepped-frequency radar bandwidth. It is not possible to determine the number of targets and the target positions from the periodogram range profile.

For 500 MHz stepped-frequency radar bandwidth, periodogram method has 30 cm range resolution which is too high for TWOD application. However, note that even when the number of points and the bandwidth is very small, line spectral estimators can find the target ranges. This means that using line spectral estimators as radar signal processing tool instead of periodogram relaxes the constraints on stepped-frequency radar waveform. First, less number of steps in the stepped-frequency radar waveform will be required to achieve desired range resolution which decreases the operation time and complexity. Secondly, bandwidth of stepped-frequency radar waveform can be decreased which in turn decreases the cost of the system and improves the performance.

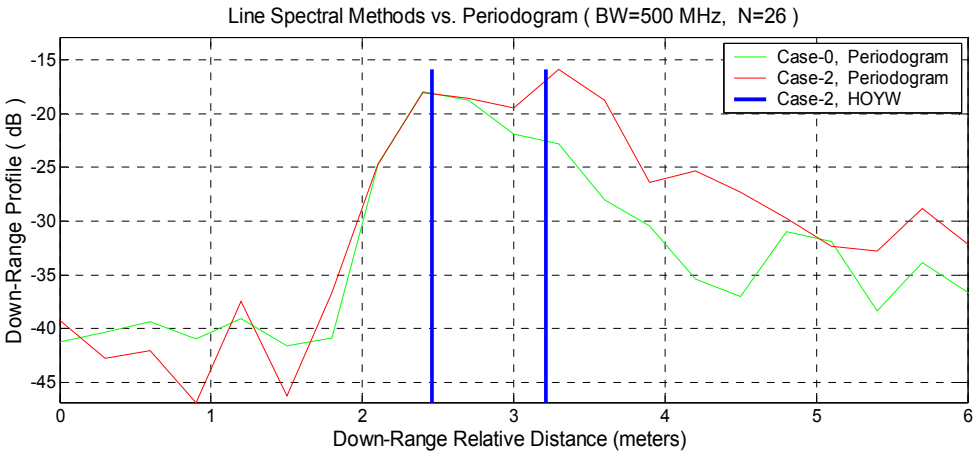

Figure 5.23. Comparison of line spectral estimators and periodogram for TWOD (Case-2)

Table 5.12. Range estimates of line spectral estimators (Case-2)

Case-2 (Small BW,N)	Target-1	Target-2	Difference	Difference (in case-1)	Displacement
HOYW Method	2.3805	3.2335	0.8530	0.7576	0.0954
Min-Norm Method	2.5147	3.1654	0.6507	0.5036	0.1471
LS-ESPRIT	2.5149	3.1618	**0.6469**	0.4750	**0.1719**
TLS-ESPRIT	2.5149	3.1618	**0.6469**	0.4753	**0.1716**
Root-MUSIC	2.4603	3.2468	0.7865	0.5751	0.2114

Figure 5.23 and table 5.12 show that line spectral estimators can find the target ranges even for very small bandwidth and number of points whereas periodogram can provide any information about the targets. Also note that the most accurate estimate of the displacement of target-2 between case-1 and case-2, which is 16 cm, and the distance between target-1 and target-2 in case-2 are provided by ESPRIT solutions.

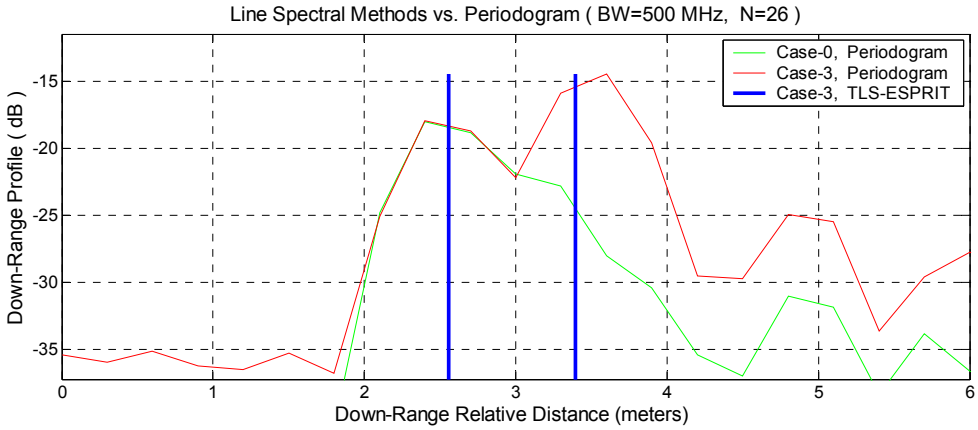

Figure 5.24. Comparison of line spectral estimators and periodogram for TWOD (Case-3)

Table 5.13. Range estimates of line spectral estimators (Case-3)

Case-3 (Small BW,N)	Target-1	Target-2	Difference
HOYW Method	2.4936	3.4029	0.9093
Min-Norm Method	2.5157	3.3909	0.8752
LS-ESPRIT	2.5550	3.3919	**0.8369**
TLS-ESPRIT	2.5546	3.3923	**0.8377**
Root-MUSIC	2.5296	3.4173	0.8877

Table 5.13 shows that the ESPRIT solutions provide the best estimate of the distance between target-1 and target-2 in case 3.

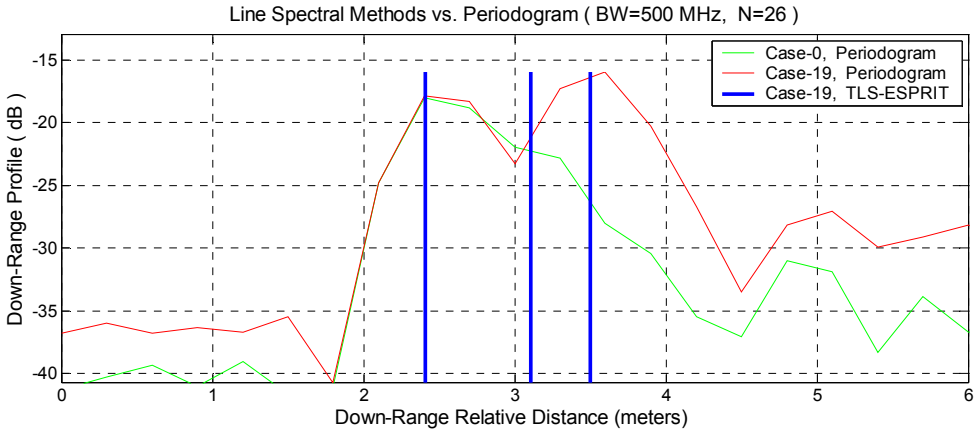

Figure 5.25. Comparison of line spectral estimators and periodogram for TWOD (Case-19)

Table 5.14. Range estimates of line spectral estimators (Case-19)

Case-19 (Small BW,N)	Target-1	Target-2	Target-3	Difference (Betw. 1&2)	Difference (Betw. 1&3)	Difference (Betw. 2&3)
HOYW Method	2.3784	3.1131	3.5176	0.7347	1.1392	**0.4045**
Min-Norm Method	2.3976	3.1135	3.5133	0.7159	1.1157	**0.3998**
LS-ESPRIT	2.4078	3.1049	3.499	0.6971	1.0912	**0.3941**
TLS-ESPRIT	2.4075	3.1048	3.4994	0.6973	1.0919	**0.3946**
Root-MUSIC	2.3975	3.1219	3.523	0.7244	1.1255	**0.4011**

In case-19, target-M is at location-5 and target-A is at location-1. Note that it is not possible to detect the presence of three targets from the periodogram range profile shown in figure 5.25 while line spectral estimators provide consistent range estimates for three targets.

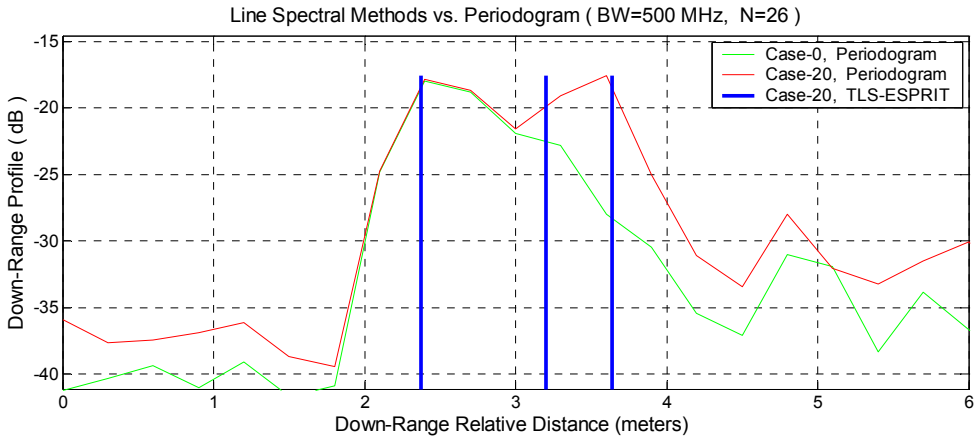

Figure 5.26. Comparison of line spectral estimators and periodogram for TWOD (Case-20)

Table 5.15. Range estimates of line spectral estimators (Case-20)

Case-20 (Small BW, N)	Target-1	Target-2	Target-3	Difference (Betw. 1&2)	Difference (Betw. 1&2 in case 19-small)	Displacement
HOYW Method	2.3529	3.0586	3.4974	0.7057	0.7347	-0.0290
Min-Norm Method	2.3746	3.2087	3.6518	0.8341	0.7159	0.1182
LS-ESPRIT	2.3769	3.2028	3.6407	0.8259	0.6971	0.1288
TLS-ESPRIT	2.3765	3.2017	3.6404	0.8252	0.6973	0.1279
Root-MUSIC	2.3861	3.2793	3.721	0.8932	0.7244	0.1688

It is not possible to detect the presence of three targets also from the periodogram range profile shown in figure 5.26 while line spectral estimators provide consistent range estimates for three target.

So, from figures 5.22-26, we can conclude that line spectral estimators achieve much better range resolution than periodogram even when the number of points and the bandwidth of the stepped-frequency radar waveform are small.

Furthermore, from figures 5.16-26 and tables 5.5-15, we can conclude that ESPRIT provides better range estimates among the line spectral estimators for TWOD application.

5.3. Super-resolution Spectral Estimators for Buried Object Detection

In order to investigate the performance of super-resolution spectral estimators for buried object detection, different sets of experimental data have been taken using network analyzer. Targets and their position are changed during experiments. Tests are numerated according to the targets used in the experiments and their locations. Targets used in each case and their corresponding locations are shown in tables 5.16 and 5.17. Figure 5.27 shows the locations of the targets in the experimental setup.

Table 5.16. Targets and their locations in BOD experiments

Case	Target	Location
1	A	1
2	A	2
3	A	3
4	A	4
5	B	1
6	B	2
7	B	3
8	B	4
9	C	1
10	C	2
11	C	3
12	C	4

Table 5.17. Targets and their locations in BOD experiments

Case	Target-1	Location -1	Target -2	Location -2
13	A	4	A	1
14	A	4	A	2
15	A	4	A	3
16	A	4	B	1
17	A	4	B	2
18	A	4	B	3
19	A	4	C	1
20	A	4	C	2
21	A	4	C	3
22	B	4	B	1
23	B	4	B	2
24	B	4	B	3
25	B	4	C	1
26	B	4	C	2
27	B	4	C	3

Data collected in cases 1-12 shown in table 5.16 will be used to test the accuracy of super-resolution spectral estimation methods explained in chapter three. Similar to through-the-wall experiments, case-0 represents the scenario where there is any target in the field and this case corresponds to the background measurement.

Data collected in cases 13-27 shown in table 5.17 will be used to test the resolving capability of super-resolution spectral estimation methods.

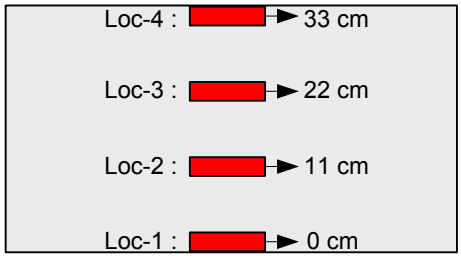

Figure 5.27. Target locations in the BOD experiments

Following sections will investigate the performance of super-resolution spectral estimators in TWOD application and compare their performance with classically used periodogram method.

5.3.1.Comparison of Yule-Walker Method and Periodogram for BOD

Several simulations were carried out to investigate the performance of AR modeling using Yule-Walker method for BOD application. Note that the parameters of the stepped-frequency radar waveform (bandwidth and number of points) and the case numbers are shown in the figures.

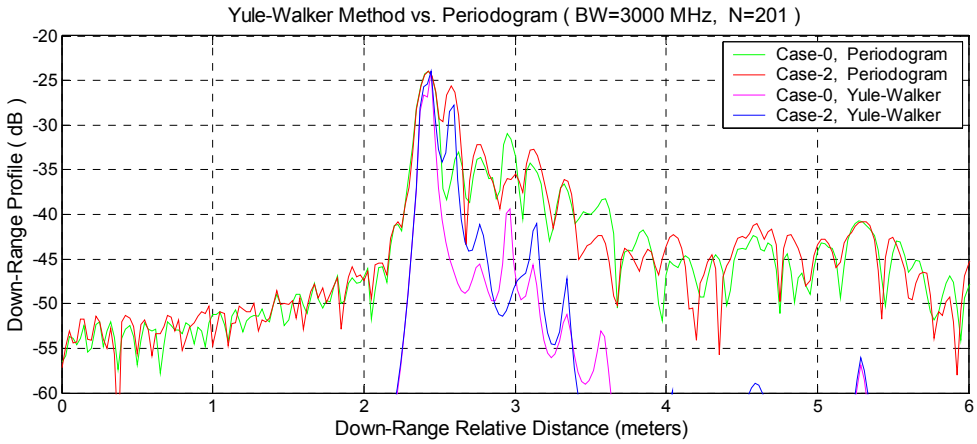

Figure 5.28. Comparison of Yule-Walker method and periodogram for BOD (Case-2)

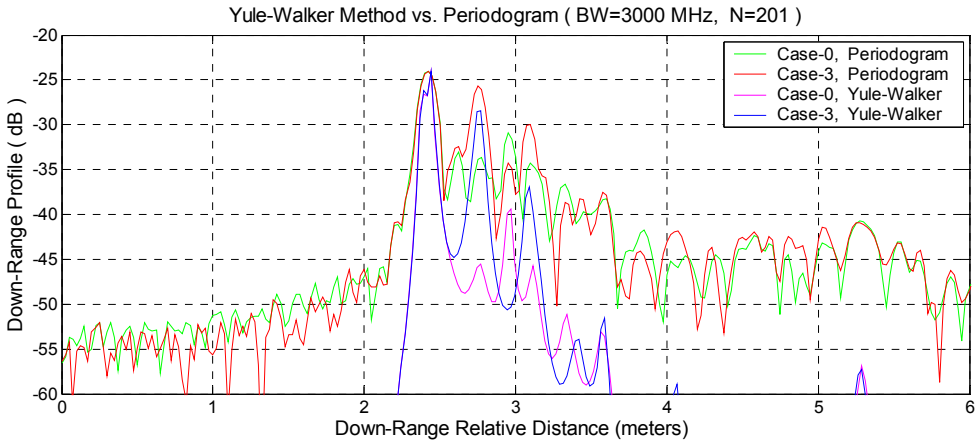

Figure 5.29. Comparison of Yule-Walker method and periodogram for BOD (Case-3)

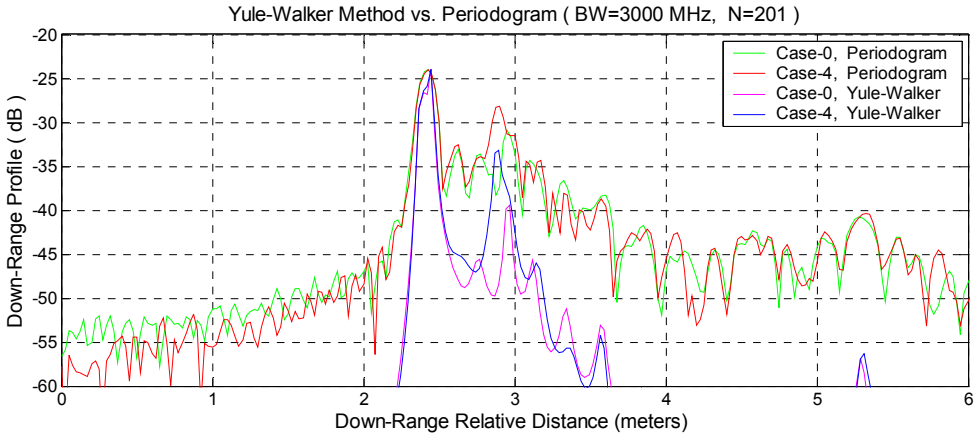

Figure 5.30. Comparison of Yule-Walker method and periodogram for BOD (Case-4)

Figures 5.28-30 show that Yule-Walker method provides narrower peaks at target locations. Also note that the Signal-to-Clutter Ratio (SCR) of the Yule-Walker range profile is higher than the SCR of the periodogram range profile.

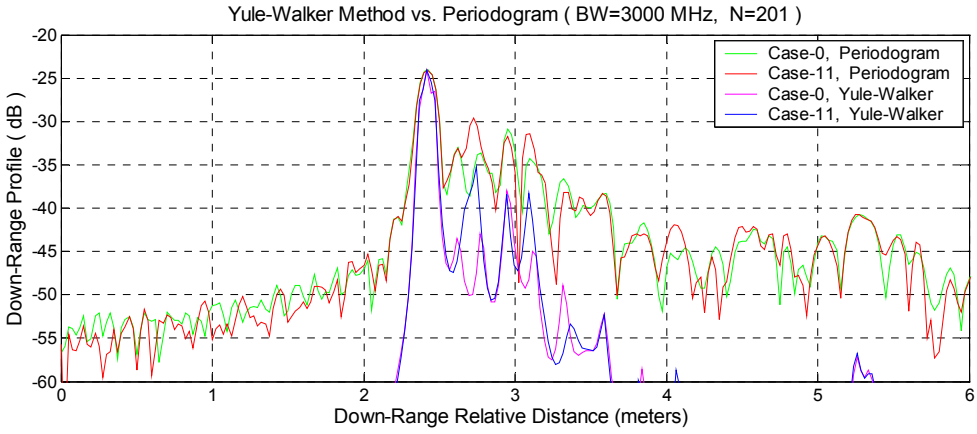

Figure 5.31. Comparison of Yule-Walker method and periodogram for BOD (Case-11)

Figure 5.31 shows that Yule-Walker method provides much better range profile than periodogram method even when the target has small RCS value. Note that range profiles in figures 5.31 and 5.28 have peaks at the same locations with different magnitudes because of the difference in the RCS values of the targets.

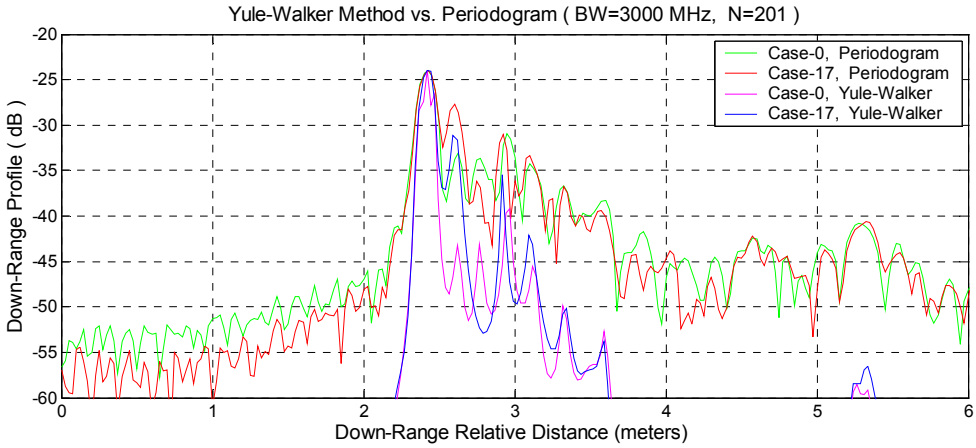

Figure 5.32. Comparison of Yule-Walker method and periodogram for BOD (Case-17)

The locations of the highest three peaks in both range profiles shown in figure 5.32 corresponds to the target positions where the highest peak represents the front side of the wall, the second highest peak represents the target-B and the third highest peak represents the target-A which is beneath the back side of the wall. Note that Yule-Walker method provides sharper peaks at the target locations.

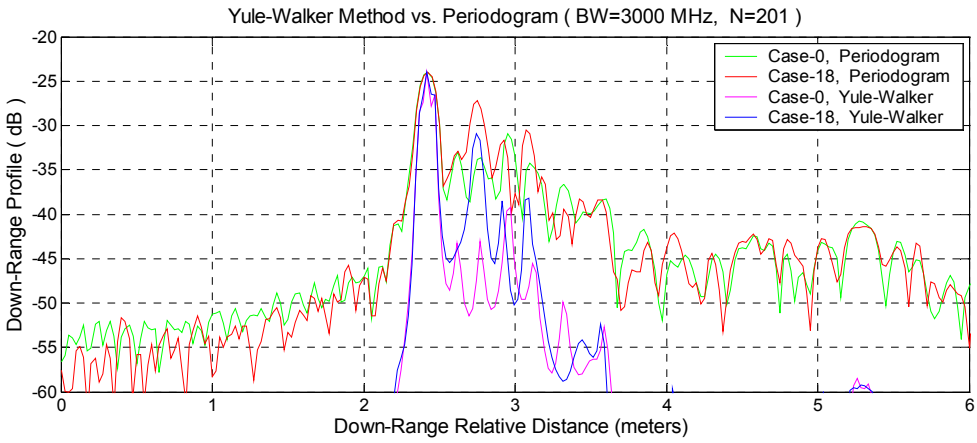

Figure 5.33. Comparison of Yule-Walker method and periodogram for BOD (Case-18)

The difference between case-17 and case-18 is that the location of target-B is changed from location two to three and this is obvious from figures 5.32 and 5.33. It is obvious that Yule-Walker method provides better range profiles than periodogram.

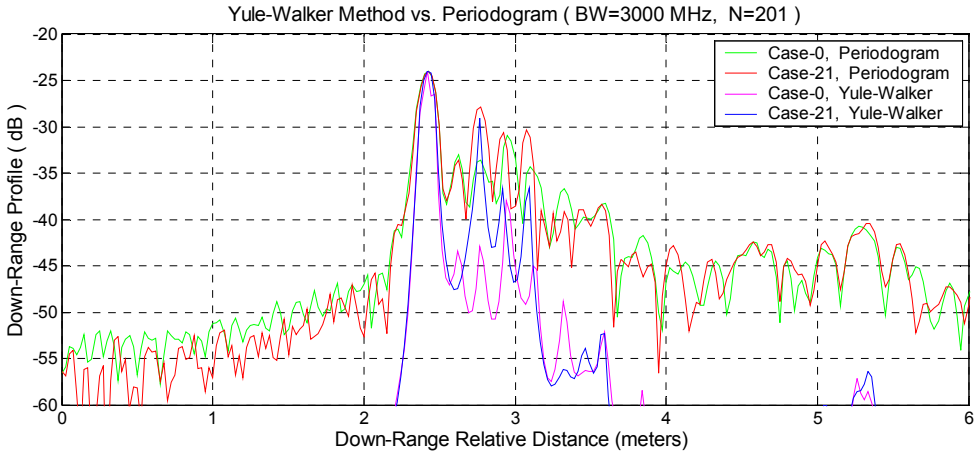

Figure 5.34. Comparison of Yule-Walker method and periodogram for BOD (Case-21)

The difference between case-18 and case-21 is that the target-B in case-18 is changed with target-C which has smaller RCS value and we expect to see smaller peak for target-C. However, it is interesting to note that the peak which represents target-C in figure 5.34 has larger peak value than the peak which represents target-C in figure 5.33. Note that Yule-Walker provides better range profile also for case-21.

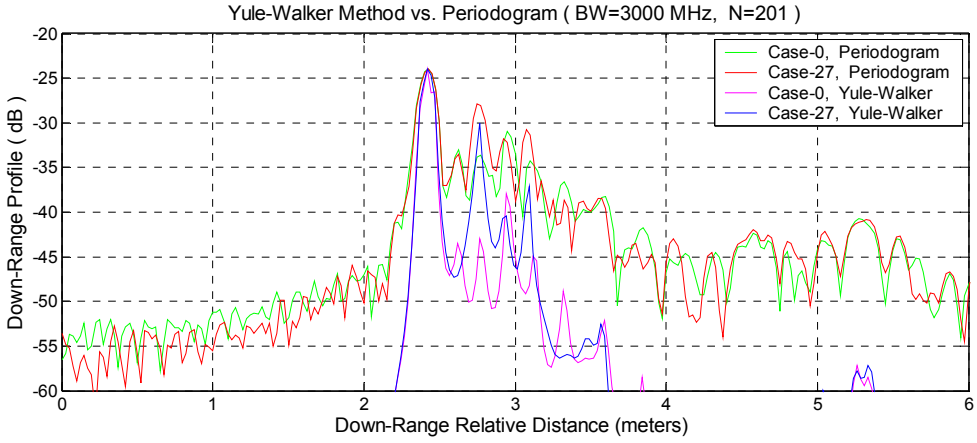

Figure 5.35. Comparison of Yule-Walker method and periodogram for BOD (Case-27)

Figure 5.35 shows that Yule-Walker provides better range profiles even when the close targets have small RCS values.

5.3.2. Comparison of Least-Squares Method and Periodogram for BOD

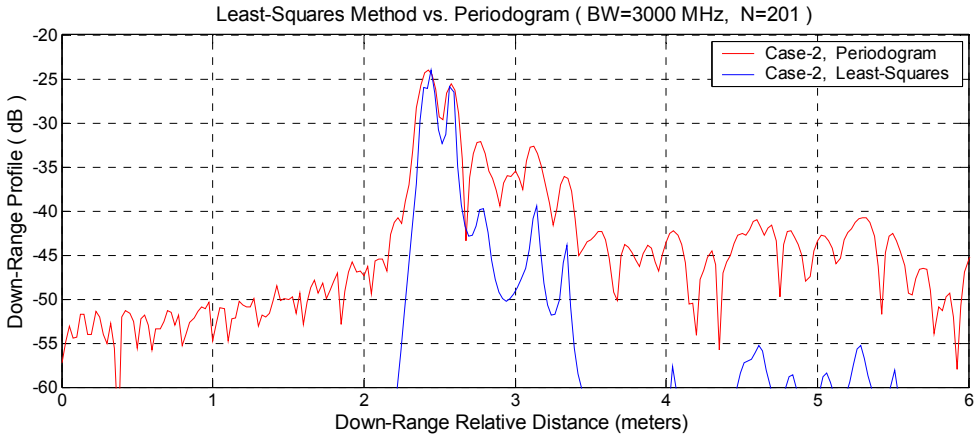

Figure 5.36. Comparison of Least-Squares method and periodogram for BOD (Case-2)

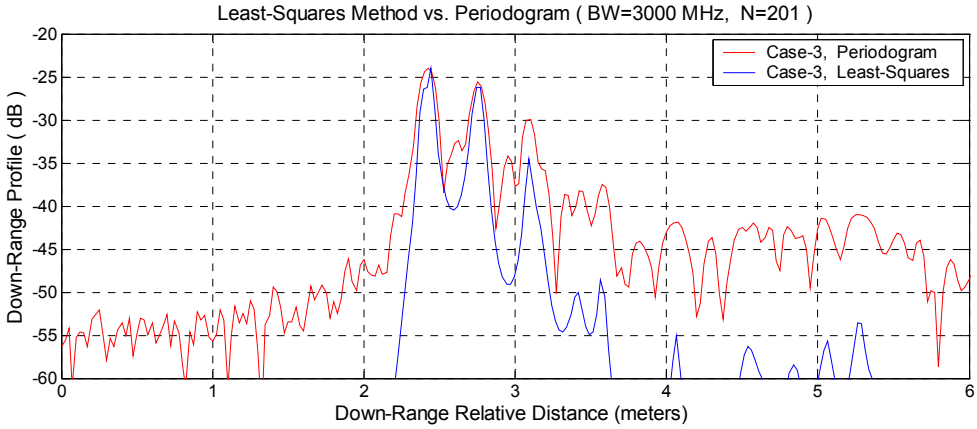

Figure 5.37. Comparison of Least-Squares method and periodogram for BOD (Case-3)

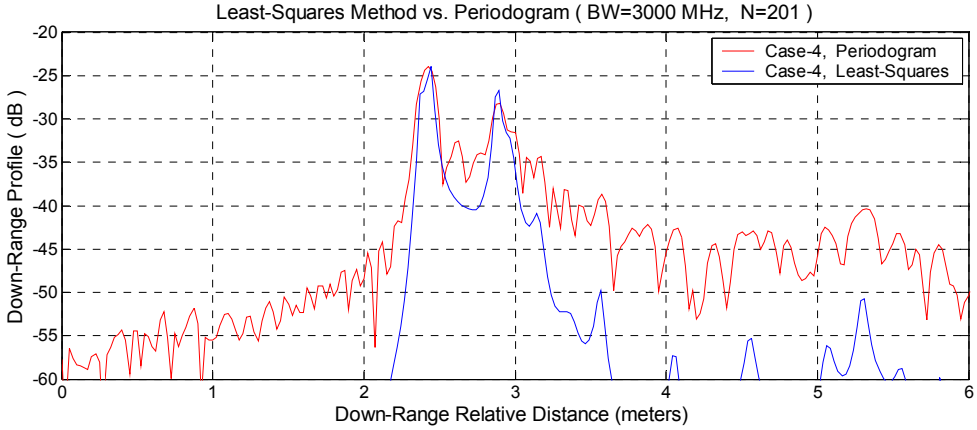

Figure 5.38. Comparison of Least-Squares method and periodogram for BOD (Case-4)

Figures 5.36-38 show that Least-Squares method provides better range profiles than periodogram method even for the small targets. Note that Least-Squares range profiles have sharper peaks at target locations and higher SCR.

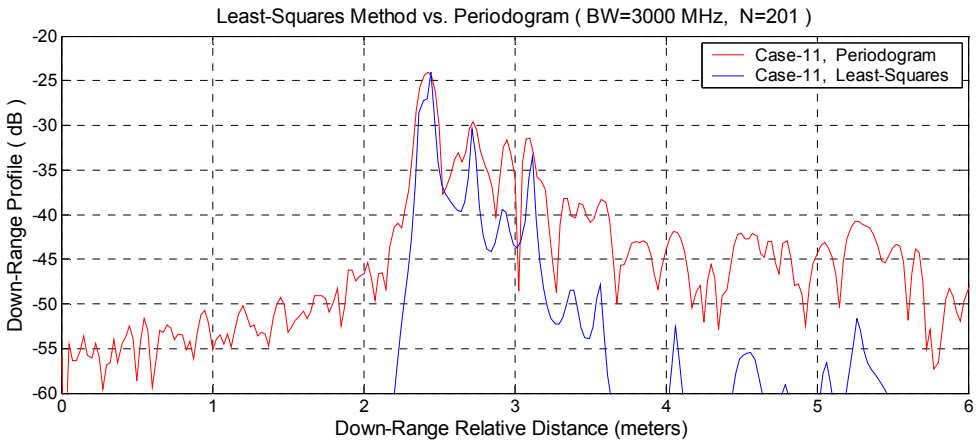

Figure 5.39. Comparison of Least-Squares method and periodogram for BOD (Case-11)

Figure 5.39 shows that Least-Squares method provides better range profiles than periodogram method even for the targets with small RCS values.

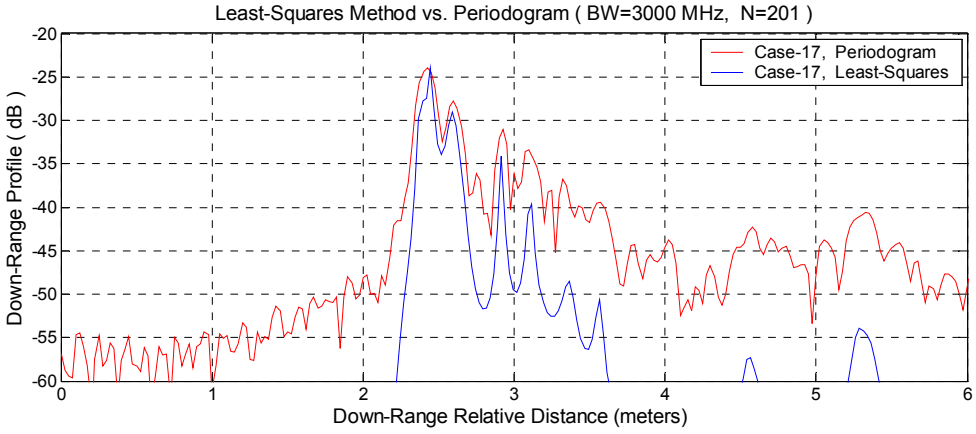

Figure 5.40. Comparison of Least-Squares method and periodogram for BOD (Case-17)

Figure 5.40 shows that Least-Squares method provides sharper peaks at target locations.

Moreover, after comparative analysis of Yule-Walker and LS methods, it has been observed that Yule-Walker method provides better and more reliable range profiles than LS method for BOD application.

5.3.3. Comparison of Line Spectra Methods and Periodogram for BOD

This section covers the performance analysis of line spectral estimators explained in detail in section 3.4 in BOD application. The parameters of the stepped-frequency radar and the target locations are given in the figures. Data collected for the case given in figure is processed using the line spectral estimators and the corresponding range estimates are given in tables below the corresponding figures.

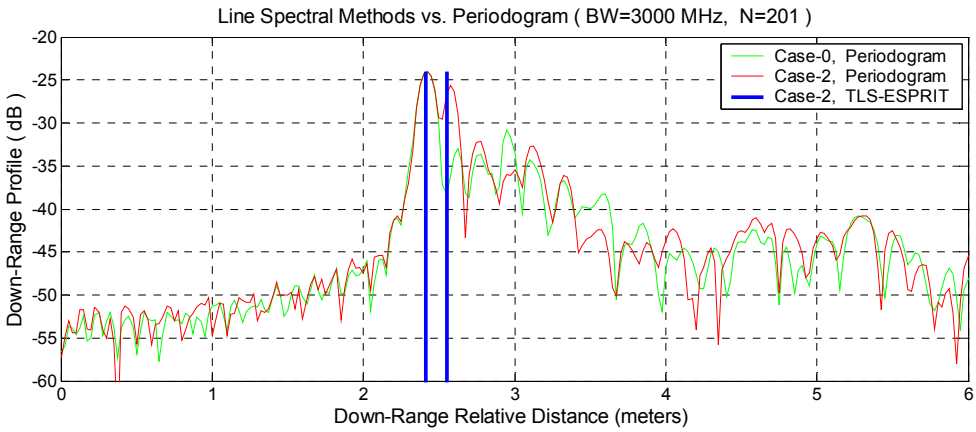

Figure 5.41. Comparison of line spectral estimators and periodogram for BOD (Case-2)

Table 5.18. Range estimates of line spectral estimators (Case-2)

Case-2	Target-1	Target-2	Difference
HOYW Method	2.4102	2.5701	0.1599
Min-Norm Method	2.4089	2.5598	0.1509
LS-ESPRIT	2.4109	2.555	**0.1441**
TLS-ESPRIT	2.4109	2.555	**0.1441**
Root-MUSIC	2.4111	2.5752	0.1641

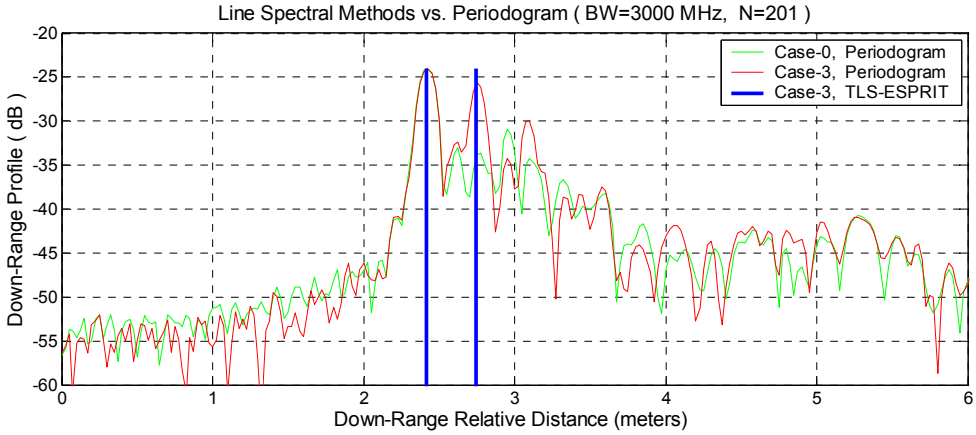

Figure 5.42. Comparison of line spectral estimators and periodogram for BOD (Case-3)

Table 5.19. Range estimates of line spectral estimators (Case-3)

Case-3	Target-1	Target-2	Difference
HOYW Method	2.4166	2.7526	0.3360
Min-Norm Method	2.4158	2.7464	0.3306
LS-ESPRIT	2.4152	2.7456	**0.3304**
TLS-ESPRIT	2.4152	2.7456	**0.3304**
Root-MUSIC	2.4191	2.7689	0.3498

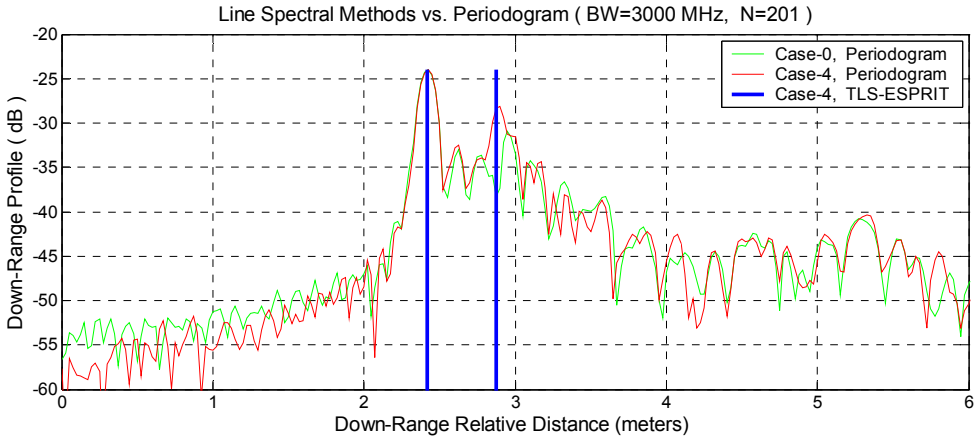

Figure 5.43. Comparison of line spectral estimators and periodogram for BOD (Case-4)

Table 5.20. Range estimates of line spectral estimators (Case-4)

Case-4	Target-1	Target-2	Difference
HOYW Method	2.4153	2.8759	0.4606
Min-Norm Method	2.4162	2.8778	0.4616
LS-ESPRIT	2.4161	2.8751	**0.4590**
TLS-ESPRIT	2.4161	2.8751	**0.4590**
Root-MUSIC	2.4151	2.8664	0.4513

Figures 5.41-43 and tables 5.18-20 show that all the line spectral estimation methods find the ranges of the targets. Note that ESPRIT solutions provide the most accurate range estimates.

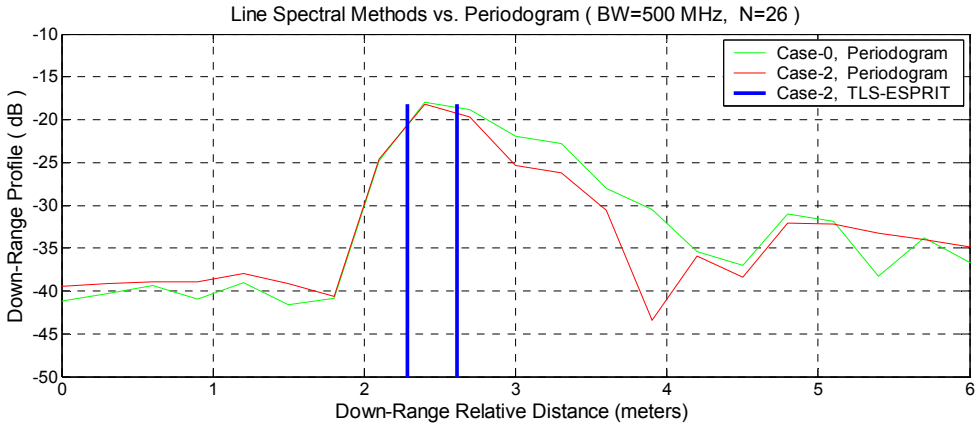

Figure 5.44. Comparison of line spectral estimators and periodogram for BOD (Case-2)

Table 5.21. Range estimates of line spectral estimators (Case-2)

Case-2 (Small BW, N)	Target-1	Target-2	Difference
HOYW Method	2.3032	2.6068	0.3036
Min-Norm Method	2.2831	2.624	0.3409
LS-ESPRIT	2.2885	2.6106	**0.3221**
TLS-ESPRIT	2.2881	2.611	**0.3229**
Root-MUSIC	2.2686	2.5989	0.3303

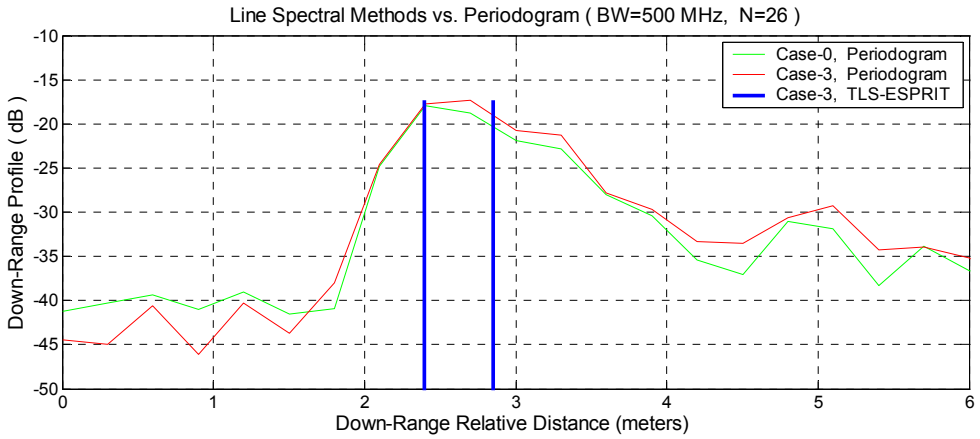

Figure 5.45. Comparison of line spectral estimators and periodogram for BOD (Case-3)

Table 5.22. Range estimates of line spectral estimators (Case-3)

Case-3 (Small BW,N)	Target-1	Target-2	Difference
HOYW Method	2.4208	2.8902	0.4694
Min-Norm Method	2.389	2.8739	0.4849
LS-ESPRIT	2.3973	2.8485	**0.4512**
TLS-ESPRIT	2.397	2.8487	**0.4517**
Root-MUSIC	2.4011	2.8917	0.4906

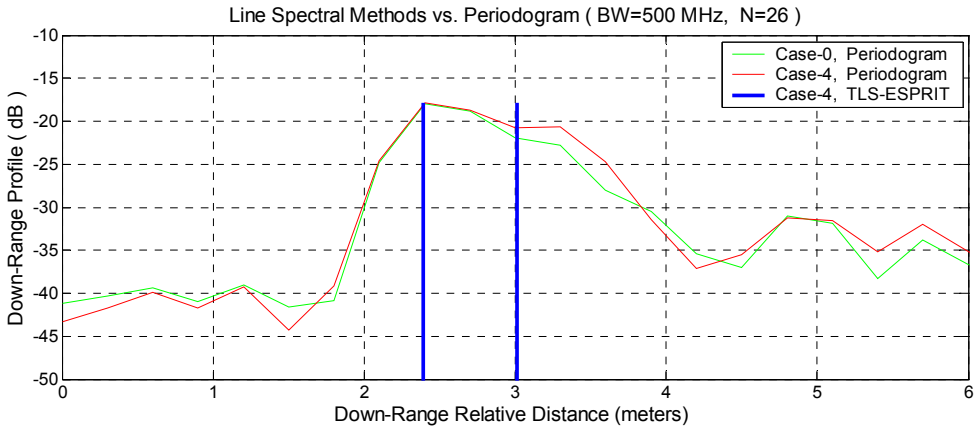

Figure 5.46. Comparison of line spectral estimators and periodogram for BOD (Case-3)

Table 5.23. Range estimates of line spectral estimators (Case-4)

Case-4 (Small BW, N)	Target-1	Target-2	Difference
HOYW Method	2.394	3.0151	0.6211
Min-Norm Method	2.3825	3.0372	0.6547
LS-ESPRIT	2.3905	3.0133	**0.6228**
TLS-ESPRIT	2.3904	3.0134	**0.6230**
Root-MUSIC	2.3754	3.0341	0.6587

Figures 5.44-46 and tables 5.21-23 show the range profile and range estimates, respectively, for the data with 26 points and 500 MHz stepped-frequency radar bandwidth. It is not possible to determine the number of targets and the target positions from the periodogram range profile. However, note that even when the number of points and the bandwidth is very small, line spectral estimators can find the target ranges.

The advantages explained in TWOD application are also valid in BOD application, i.e, less number of steps in the stepped-frequency radar waveform will be required to achieve desired range resolution which decreases the operation time and complexity, and smaller bandwidths can be used to achieve desired range resolution which in turn decreases the cost of the system and improves the performance.

Even for smaller bandwidth and number of points, ESPRIT has provided the most accurate range estimates among the line spectral estimators. Note that the ESPRIT range estimates have the minimum range estimation error in all cases.

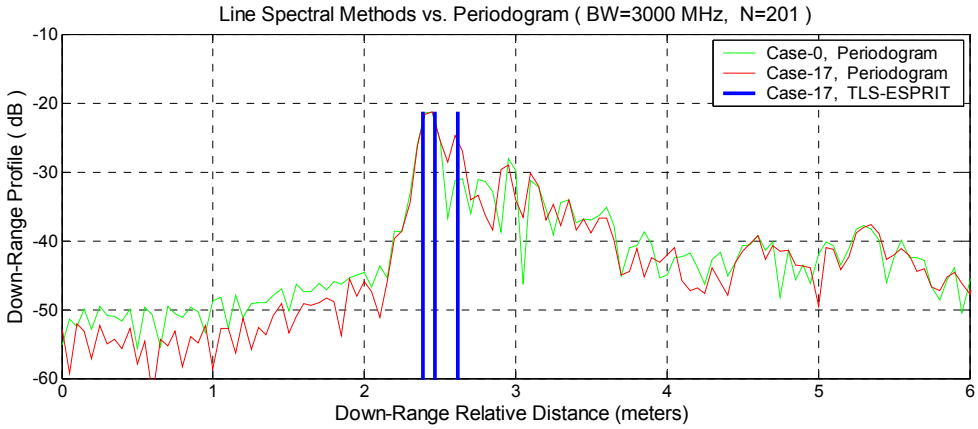

Figure 5.47. Comparison of line spectral estimators and periodogram for BOD (Case-17)

Table 5.24. Range estimates of line spectral estimators (Case-17)

Case-17	Target-1	Target-2	Target-3	Difference (Betw. 1&2)	Difference (Betw. 1&3)	Difference (Betw. 2&3)
HOYW Method	2.3759	2.4436	2.5971	0.0677	0.2212	0.1535
Min-Norm Method	2.3858	2.4608	2.6122	0.0750	0.2264	0.1514
LS-ESPRIT	2.3897	2.467	2.6182	0.0773	0.2285	0.1512
TLS-ESPRIT	2.3897	2.467	2.6183	0.0773	0.2286	0.1513
Root-MUSIC	2.4108	2.6217	3.0682	0.2109	0.6574	0.4465

In case-17, target-A is at location-4 and target-B is at location-2. As can be seen from table 5.24 and figure 5.47, most of the line spectral estimators resolve the closely placed targets; however, periodogram method does not provide enough resolution to resolve them.

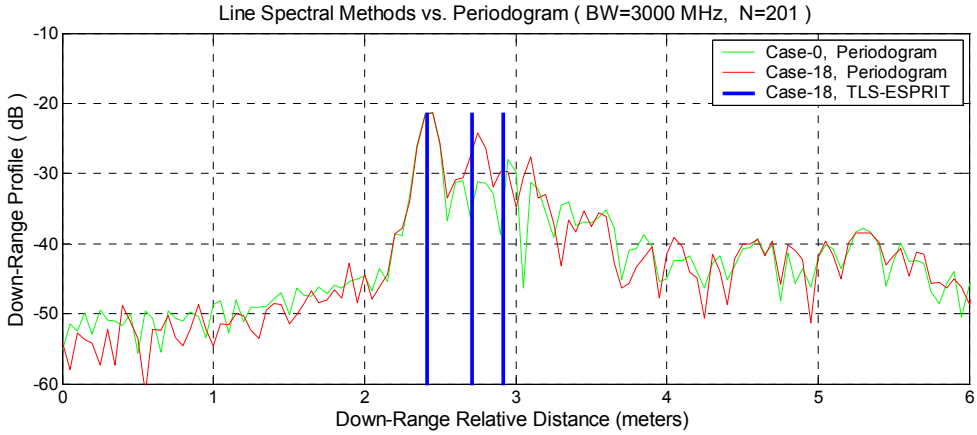

Figure 5.48. Comparison of line spectral estimators and periodogram for BOD (Case-18)

Table 5.25. Range estimates of line spectral estimators (Case-18)

Case-18	Target-1	Target-2	Target-3	Difference (Betw. 1&2)	Difference (Betw. 1&3)	Difference (Betw. 2&3)
HOYW Method	2.4141	2.7147	3.0532	0.3006	0.6391	0.3385
Min-Norm Method	2.4134	2.718	2.9634	0.3046	0.5500	0.2454
LS-ESPRIT	2.4148	2.7114	2.9202	0.2966	0.5054	0.2088
TLS-ESPRIT	2.4148	2.7114	2.9203	0.2966	0.5055	0.2089
Root-MUSIC	2.4099	2.7109	3.0216	0.3010	0.6117	0.3107

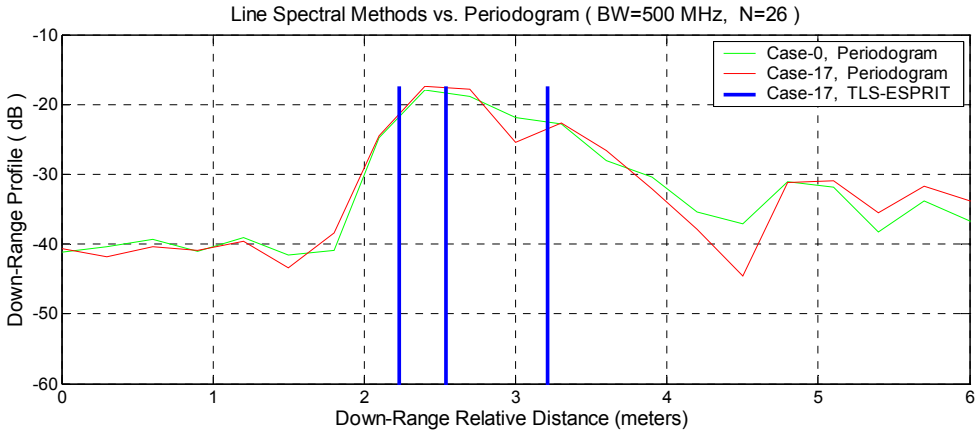

Figure 5.49. Comparison of line spectral estimators and periodogram for BOD (Case-17)

Table 5.26. Range estimates of line spectral estimators (Case-17)

Case-17 (Small BW, N)	Target-1	Target-2	Target-3	Difference (Betw. 1&2)	Difference (Betw. 1&3)	Difference (Betw. 2&3)
HOYW Method	2.2538	2.56	3.0459	0.3062	0.7921	0.4859
Min-Norm Method	2.2257	2.5369	3.2225	0.3112	0.9968	0.6856
LS-ESPRIT	2.2317	2.5383	3.2146	0.3066	0.9829	0.6763
TLS-ESPRIT	2.2317	2.5383	3.2147	0.3066	0.9830	0.6764
Root-MUSIC	2.2317	2.5448	3.2326	0.3131	1.0009	0.6878

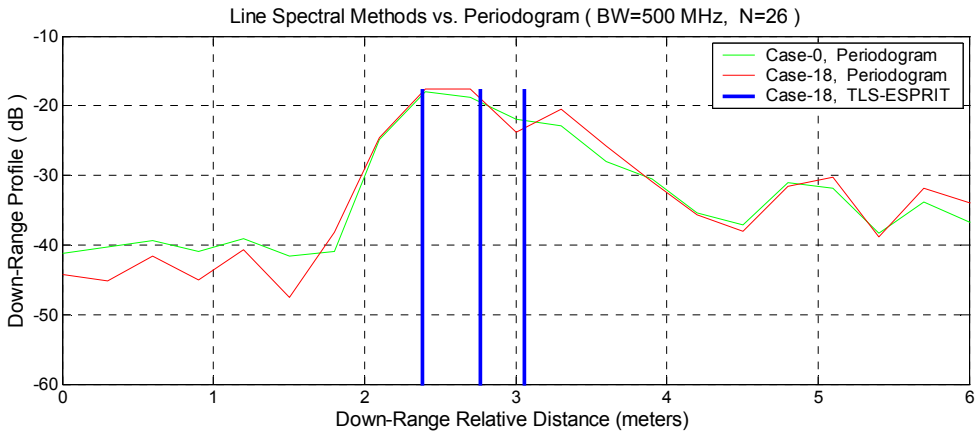

Figure 5.50. Comparison of line spectral estimators and periodogram for BOD (Case-18)

Table 5.27. Range estimates of line spectral estimators (Case-18)

Case-18 (Small BW, N)	Target-1	Target-2	Target-3	Difference (Betw. 1&2)	Difference (Betw. 1&3)	Difference (Betw. 2&3)
HOYW Method	2.2867	2.611	3.127	0.3243	0.8403	0.516
Min-Norm Method	2.3608	2.7318	3.0852	0.3710	0.7244	0.3534
LS-ESPRIT	2.3852	2.7636	3.0555	0.3784	0.6703	0.2919
TLS-ESPRIT	2.3843	2.7637	3.0563	0.3794	0.6720	0.2926
Root-MUSIC	2.2491	2.5844	3.2298	0.3353	0.9807	0.6454

Figures 5.47-50 and tables 5.24-27 show that periodogram method provides very poor range profiles and can not resolve closely separated targets when the number of points and bandwidth are very small whereas line spectral estimators resolve the closely separated targets even when the number of points and bandwidth are very small.

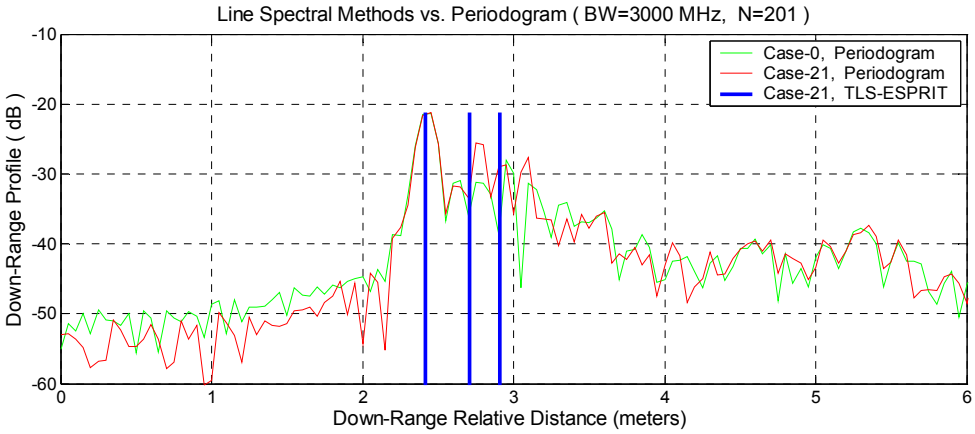

Figure 5.51. Comparison of line spectral estimators and periodogram for BOD (Case-21)

Table 5.28. Range estimates of line spectral estimators (Case-21)

Case-21	Target-1	Target-2	Target-3	Difference (Betw. 1&2)	Difference (Betw. 1&3)	Difference (Betw. 2&3)
HOYW Method	2.4141	2.7189	3.0754	0.3048	0.6613	0.3565
Min-Norm Method	2.4131	2.7199	2.9416	0.3068	0.5285	0.2217
LS-ESPRIT	2.4144	2.7086	2.9084	0.2942	0.4940	0.1998
TLS-ESPRIT	2.4144	2.7085	2.9085	0.2941	0.4941	0.2
Root-MUSIC	2.409	2.7077	2.9989	0.2987	0.5899	0.2912

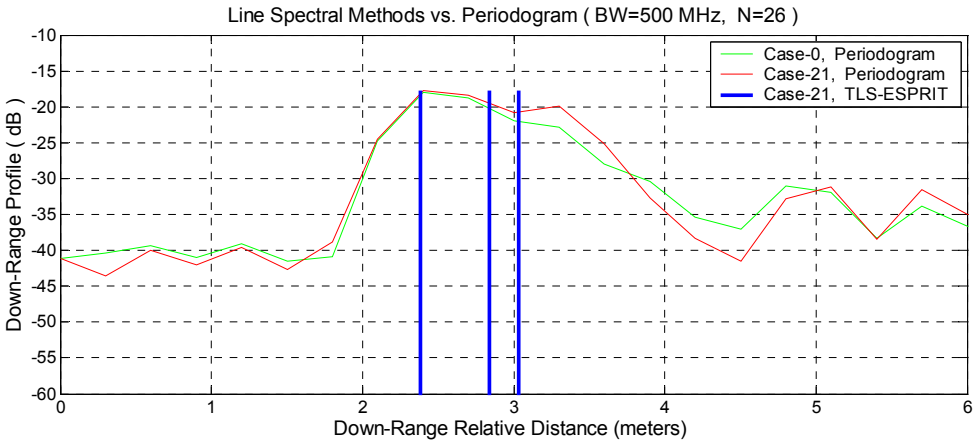

Figure 5.52. Comparison of line spectral estimators and periodogram for BOD (Case-21)

Table 5.29. Range estimates of line spectral estimators (Case-21)

Case-21 (Small BW, N)	Target-1	Target-2	Target-3	Difference (Betw. 1&2)	Difference (Betw. 1&3)	Difference (Betw. 2&3)
HOYW Method	2.2898	2.603	3.1338	0.3132	0.8440	0.5308
Min-Norm Method	2.3764	2.836	3.0887	0.4596	0.7123	0.2527
LS-ESPRIT	2.3833	2.8399	3.0296	0.4566	0.6463	0.1897
TLS-ESPRIT	2.3827	2.8391	3.031	0.4564	0.6483	0.1919
Root-MUSIC	2.256	2.6213	3.2135	0.3653	0.9575	0.5922

Figures 5.51 and 5.52 and tables 5.28 and 5.29 show that line spectral estimators resolve the closely separated targets even when the number of points and bandwidth are very small and the difference between the RCS values of the targets increases.

From the figures and tables in this section, it can be concluded that line spectral estimators provide consistent and high resolution range estimates even when the number of points and bandwidth are very small and the targets have different RCS values. These experiments show that using line spectral estimators as range estimator tool in BOD applications provides important advantages. Since less number of steps will be required to achieve desired range resolution, processing time will decrease. Moreover, since smaller bandwidth will be sufficient, cost of the stepped-frequency radar system will decrease and it will be possible to use narrowband components in the radar system which in turn improve the performance.

6. CONCLUSIONS

This study has explored the target detection and range extraction performance of parametric and non-parametric methods in through-the-wall and buried object detection applications using synthetic stepped-frequency and FMCW radar signals and experimental stepped-frequency radar data. Range estimates of the parametric methods are compared with non-parametric methods.

The synthetic and experimental data are processed via ESPRIT, Root-MUSIC, Higher Order Yule-Walker, Minimum-Norm, Yule-Walker, and Least-Squares methods and their performance are compared with the conventional periodogram. The results show that all the parametric methods provide much better range profiles than non-parametric methods.

When Yule-Walker and Least-Squares methods are compared with periodogram, it is observed that they provide much narrower peaks at the target locations and their range profiles have higher signal-to-clutter ratio. The simulations and experimental results show that Yule-Walker and Least-Squares methods can resolve the targets that are closer than the resolution limit imposed by FFT processing.

When ESPRIT, Root-MUSIC, Higher Order Yule-Walker and Minimum-Norm methods are compared with periodogram, it can be concluded that all the line spectral estimators provide much better range resolution than periodogram even when the SNR is low, the data size is small, targets are too close and targets have very different RCS values.

Experimental and simulative resolution studies showed that ESPRIT can distinguish close targets with better resolution than the other methods. Also, it is worth to note that total least squares solution of ESPRIT provided better range estimates than least squares solution. The worst resolution capability and the range estimates were demonstrated by Root-MUSIC. Also, Min-Norm method outperformed the HOYW method.

Also, the performance of spatial smoothing techniques was analyzed using synthetic and experimental data and it is observed that modified spatial smoothing processing

performs better than spatial smoothing processing. Also, line spectral estimators' range estimates had large bias when any decorrelation process was performed. These observations show that the radar data should be preprocessed by spatial smoothing techniques in order to decorrelate the individual signals and improve the accuracy of the range estimates.

To sum up, experimental and simulative results show that using parametric spectral estimators as radar signal processing tool relaxes the constraints on stepped-frequency radar waveform. First, less number of steps in the stepped-frequency radar waveform will be required to achieve desired range resolution, which decreases the operation time and system complexity. Secondly, bandwidth of stepped-frequency radar waveform can be decreased which in turn decreases the cost of the system and improves the performance. For future work, these algorithms can be implemented in digital signal processors or field programmable gate arrays and portable stepped-frequency radar can be implemented.

REFERENCES

1. Ahmad, F., and M.G. Amin, " A Noncoherent Radar System Approach for Through-the-Wall Imaging", *Proceedings of SPIE*, Vol. 5778, pp. 196-207, November 2005

2. Currie, N. and K. Stiefvater, "Evaluation of a MMW Active Through-the-Wall Surveillance System", *Proceedings of SPIE*, Vol. 4708, pp. 161-172, November 2002.

3. Frazier, L., "Surveillance Through Walls and Other Opaque Materials", *IEEE AES Systems Magazine*, pp. 6-9, October 1996.

4. Ferris, D. and N. Currie, "A Survey of Current Technologies for Through-the-Wall Surveillance (TWS)", *Proceedings of SPIE*, Vol. 3577, pp. 62-72, 1998.

5. Greneker, E., "Radar flashlight for through-the-wall detection of humans", *Proceedings SPIE*, Vol. 3375, pp. 280-285, 1998.

6. Hunt, A. R., "Image Formation Through Walls Using a Distributed Radar Sensor Network", *Proceedings of SPIE*, Vol. 5778, pp. 169-174, 2005.

7. Currie, N., D. Ferris, R. McMillan and M. Wicks, "New Law Enforcement Applications of Millimeter Wave Radar", *Proceedings of SPIE*, Vol. 3066, pp. 10-23, 1997.

8. Hunt, A. R., "Stepped-Frequency CW Radar for Concealed Weapon Detection and Through-The-Wall Surveillance," *Proceedings of SPIE*, Vol. 4708, pp. 99-105, 2002.

9. Mahafza, B. R., *Radar Systems Analysis and Design Using MATLAB*, Chapman & Hall / CRC, New York, 2000.

10. Taylor, J. D., *Ultra-Wideband Radar Technology*, CRC, New York, 2001.

11. Meikle, H., *Modern Radar Systems*, Artech House, Boston, 2001.

12. Skolnik, M. I., *Radar Handbook*, McGraw Hill, New York, 1990.

13. Curry, G. R., *Radar System Performance Modeling,* Artech House, Maryland, 2005.

14. Stoica, P. and R. Moses, *Introduction to Spectral Analysis*, Prentice-Hall, New Jersey, 1997.

15. Shan, T. J., M.Wax, and T. Kailath, "On Spatial Smoothing for Direction-of-Arrival Estimation of Coherent Signals", *IEEE Transactions on Acoustics, Speech, Signal Processing*, Vol. ASSP-33, pp. 806-811, August 1985.

16. Williams, R.T., S. Prasad, A.K. Mahalanabis, and L.H. Sibul, "An Improved Spatial Smoothing Technique for Bearing Estimation in a Multipath Environment", *IEEE Transactions on Acoustics, Speech, Signal Processing*, Vol. 36, pp. 425-432, April 1988.

17. Wax, M. and T. Kailath, "Detection of Signals by Information Theoretic Criteria", *IEEE Transactions on Acoustics, Speech, Signal Processing*, Vol. ASSP-33, pp. 387-392, 1985.

18. Wax, M. and I. Ziskind, "Detection of Number of Coherent signals by the MDL principle", *IEEE Transactions on Acoustics, Speech, Signal Processing*, Vol. 37, pp. 1190-1196, 1989.